Folded Functional Foams

Samuel Eli Calisch

B.A., Grinnell College, 2010
M.S., Massachusetts Institute of Technology, 2014

Submitted to the Program in Media Arts and Sciences, School of Architecture and Planning, in partial fulfillment of the requirements for the degree of

Doctor of Philosophy

at the

Massachusetts Institute of Technology

September 2019

Author .....
Sam Calisch
Program in Media Arts and Sciences
August 9, 2019

Certified by .....
Neil Gershenfeld
Director, MIT Center for Bits and Atoms
Program in Media Arts and Sciences

Accepted by .....
Tod Machover
Academic Head
Program in Media Arts and Sciences

Folded Functional Foams

Samuel Eli Calisch

Submitted to the Program in Media Arts and Sciences,
School of Architecture and Planning,
on August 9, 2019 in partial fulfillment of the
requirements for the degree of Doctor of Philosophy.

Abstract

Materials with effective properties dominated by geometric structure rather than composition, or architected materials, are used in nature and engineering to maximize performance subject to constraints of mass and energy. Conventional engineering examples have included textiles, polymer and metal foams, and honeycombs, but developments in digital fabrication have vastly expanded the field. The majority of this new work has focused on 3D printing for its high degree of geometric control, though production rates have been slow, material properties poor, and manufacturing costs high. An alternative, growing body of work has developed around structural origami and kirigami, where planar sheets are processed and folded to create three-dimensional architected materials. This work aims to leverage planar fabrication for scalable manufacturing, on-demand customization, and low embodied energy while exploiting the geometric richness of origami to tailor shape and maximize mechanical performance.

This thesis seeks to demonstrate the engineering potential of folded architected materials by showing scalability through automated production, structural control of three-dimensional shape and stiffness, and functional control of energy transduction. We first show a custom machine for automating cutting and folding of shaped honeycombs, illustrating the capability to prescribe large-scale geometry of an architected material in a continuous production process. We then modify this construction to make shaped architected materials with prescribed stiffness, producing shoe soles as a demonstration. Finally, we show three forms of energy transduction in folded architected materials – reflection, absorption, and transmission – and apply each to a relevant, difficult engineering problem. For energy reflection, we maximize the ratio of strain energy output to input in a collision event, taking running shoe soles as a test case and comparing performance to conventional polymer foams. For energy absorption, we maximize total energy absorbed per unit mass and apply this to vehicular crashboxes, comparing the results to aluminum honeycombs. For energy transmission, we use energy input to drive deformation modes with desired output force and geometry, taking as an application the generation of traveling waves on a hydrofoil surface (a longstanding goal of active flow control), evaluating viability under tow tank testing.

Thesis Supervisor: Neil Gershenfeld
Director, MIT Center for Bits and Atoms, Program in Media Arts and Sciences

Folded functional foams

Samuel Eli Calisch

This dissertation has been reviewed and approved by the following committee members:

Dr. Erik Demaine Professor of Computer Science MIT Electrical Engineering and Computer Science	Date

Folded functional foams

Samuel Eli Calisch

This dissertation has been reviewed and approved by the following committee members:

Dr. Michael Triantafyllou Professor of Mechanical and Ocean Engineering MIT Mechanical Engineering and Ocean Engineering	Date

Folded functional foams

Samuel Eli Calisch

This dissertation has been reviewed and approved by the following committee members:

Dr. Saul Griffith Founder and Chief Scientist Otherlab, Inc.	Date

Acknowledgements

This thesis would not have been possible without the help and support of many people.

First and foremost, I'd like to thank my advisor Neil Gershenfeld for believing in me, for pushing me to take risks, and for creating an incredible environment of exploration and exchange. The lab's orbit of intellectual and industrial giants, prioritization of first principles over status quo, and pressure for rapid reduction to practice has taught me so many things that my years in classrooms could not.

Next, I'd like to thank my thesis committee. Michael Triantafyllou, thank you for your interdisciplinary enthusiasm and great collaboration. Erik Demaine, thank you for your mentorship and friendship, infectious curiosity, and for introducing me to the structural origami community. Saul Griffith, thank you for being a mentor and dear friend over many years, for working towards compelling visions of the future, and for not tolerating bulls**t.

I'd also like to thank the entire Center for Bits and Atoms community of past, present, and future for making this place what it is. In particular, my cohort-mates Will, Prashant, and Noah, thank you for the brainstorms, encouragement, and support over the years. Also, a huge thank you goes to the lab support staff (Joe, James, Jamie, John, Ryan, Kara, Tom) for operating this complex distributed machine and helping all parts work together.

Thank you Sherry Lassiter and the Fab Foundation, for supporting Fab Labs worldwide and letting me be involved in their deployment. Thank you as well to the entire Fab Lab network, for showing me that curiosity and invention are universal.

Thank you to the huge number of industrial collaborators I've been fortunate to work with. In particular, thank you to Bryan F., Eric K., Noah M.-R., Nick L., Mike B., George S., Paul G., Gonzalo R., Matt L., Kohshi K., Umesh G., Niwa K., Álvaro J.-R., Alfonso P., Vincent L., Shawn L., Armand T., Pete A., Ted H., Bill Y., and many others.

Thank you to the Structural Origami working group: Erik D., Marty D., Tomohiro T., Rupert M., Jason K., Yves K., Kazuya S., Duks K., Klara M., Kenny C., Amanda G., Gabriel S., and others.

Thank you to the amazing MIT community for championing curiosity and open exchange. In particular, thank you to Dixia F., Gurvan J., Shuguang Z., Carlos G.-U., Jifei O., Lining Y., Guillermo B., Soma M.-B., Spencer W., Christian R., the students of *How to make (almost) Anything*, the MIT Glass Lab, and the many others who have shared inspiration and friendship.

Thank you to the great community of people I have lived with on Prentiss Street, and my friends in Boston and elsewhere.

Thank you to Nolan, Nina and Lucia, and my parents, Doug and Laura, whose unwavering love, support, and trust has made so much possible for me.

Finally, thank you Esther, for partnership, for growth, for adventure, for love.

Contents

Chapter 1

Introduction

Materials with mechanical behavior dominated by geometric structure rather than composition, or *architected materials*, have long found use in applications where no uniform material would suffice. In nature, where geometric complexity has low cost, intricate structures optimize performance subject to minimal material or energy use, including featherweight bird bones [74], resilient palm tree trunks [72], tough glass sea sponges [1, 199], and strain-stiffening tendons [13, 66] (shown in Figure 1.1). In manufactured systems, where complexity is more expensive, architected materials have relied on clever applications of physical or mechanical principles to produce the necessary geometric complexity and dynamic range. Polymer and metal foams use chemically or physically blown voids with desired statistical properties [197, 6]. Honeycomb production uses selective bonding or corrugation to form many hexagonal cells at once [22, 193]. Textile production uses shaped needles, hooks, and other elements to set tension and direction of fibers in the cellular structure of fabrics [12, 85]. These examples are shown in Figure 1.2.

As these engineered architected materials became indispensable to modern engineering, this success spawned a field of research around the design of architected materials and creation of *metamaterials*, those with effective properties not naturally occurring [43, 161, 111]. This work included the realization of negative Poisson ratios [110], negative stiffnesses [138], unbounded positive and negative thermal expansion ratios [112], and a host of unusual electric, magnetic, and optical property values [29]. Several methods showed that any positive semi-definite constitutive tensor can be realized by a two phase geometry [133, 170], and bounds on effective material properties, including elastic modulus [83], were derived. For architected materials with a material phase and an air phase, commonly called *cellular solids* or simply *foams*, fundamental scaling laws were derived from solid mechanical principles and codified into design metrics [73, 6].

This progress highlighted the need for new manufacturing methods to expand range of realizable geometry [21], and digital fabrication has begun to fill this need [153]. Computer-controlled tools have moved the field from simply creating exotic material properties to generating fully functional systems and fundamentally new material capabilities like shape-morphing, wave-guiding, and reprogrammability [16, 97, 103]. The vast majority of this new work, however, has exceeded the clever manufacturing methods described above, instead relying on additive manufacturing for production. While 3D printing promises the ability to directly write arbitrary geometric complexity, it has generally suffered from low production rates and resolution, limited material choice, high energy intensities, and large equipment and material costs compared to conventional processes. A recent survey of additive manufacturing technologies found between

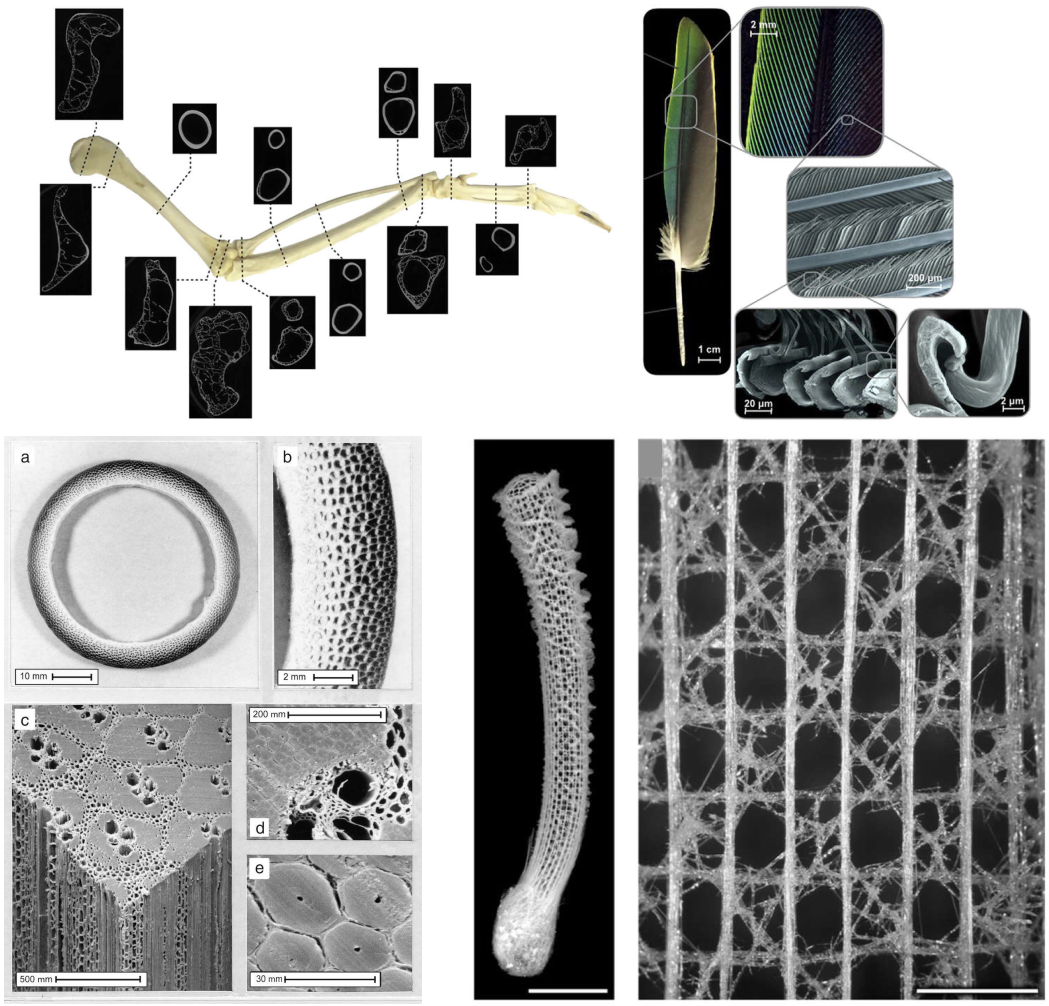

Figure 1.1: Natural architected materials. a) Internal structure of bird bones (Image from [174]), b) Interlocking barbs of feathers (Image from [174]), c) Density gradients in bamboo and palm (Image from [200]), d) Hierarchical glass skeletons of sea sponges (Image from [198]).

two and three orders of magnitude slower production rates and between one and two orders of magnitude higher energy intensities when compared to conventional manufacturing [79]. Research into improving these shortcomings has made exciting progress [191, 75, 44, 114, 120, 152], but in many cases the technologies are near their thermodynamic limits, and so improvements in any one of these metrics will likely come at the expense of the others.

While 3D printing has seen considerable development, so too has two-dimensional digital fabrication, albeit with less acclaim. At prototype scales, computer-controlled laser, waterjet, and knife cutting machines (Figure 1.3(a-e)) produce prototypes in seconds rather than the hours taken by additive manufacturing, and commodification of precision components has brought high resolution machines into the price range of consumers and small businesses. At production scales, printing presses like the one shown in Figure 1.3e now pattern ink at 15 m/s (35 mph) [126], and rotary dies like the one shown in Figure 1.3f can cut or crease at 5 m/s (12 mph) [105, 142]. Roll-to-roll manufacturing of printed circuits can pattern functional ink at rates of 10 m^2/s with features sizes of 10-100 um [55, 93]. Solar cells produced in a roll-to-roll process pay back their cost in one day of operation [58] and pay back their embodied energy several times

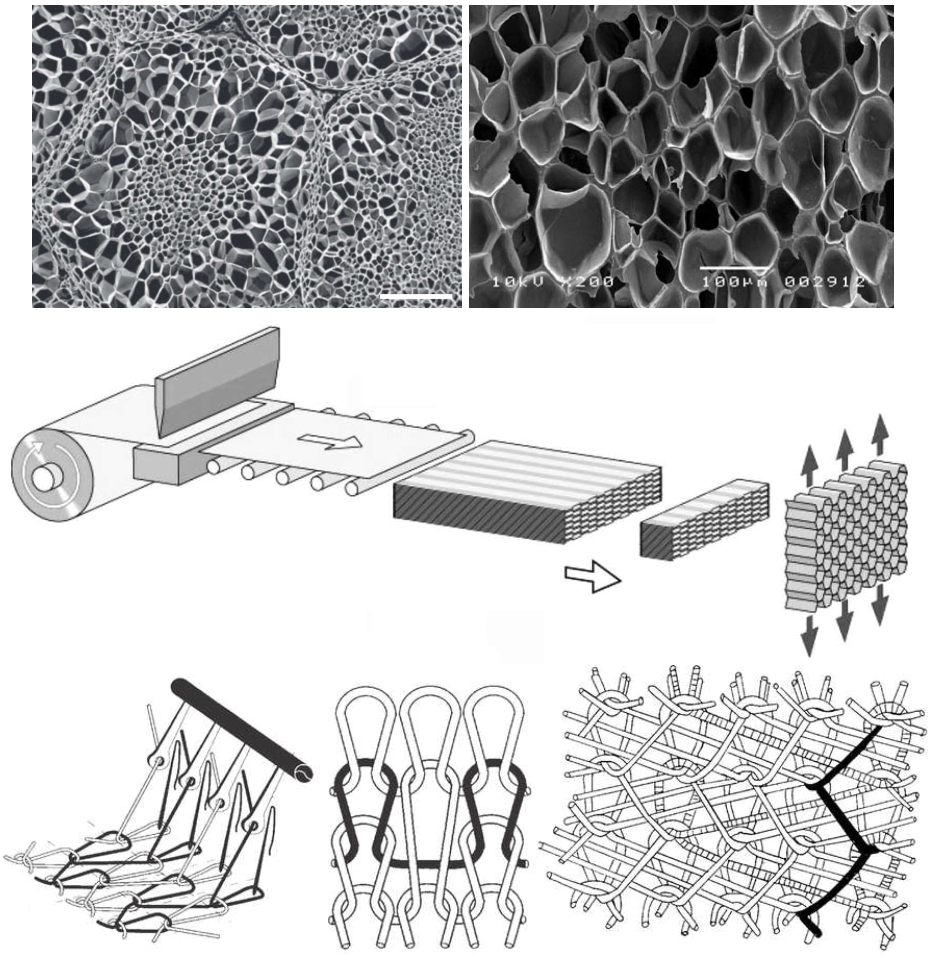

Figure 1.2: Engineered architected materials: a) Polystyrene foam (Image from [162]), b) EVA foam (Image from [192]), b) Honeycomb manufacturing (Images from [193]), c) Knitting textiles (Images from [91])

faster than conventional polycrystaline silicon cells [51, 77, 57, 157].

Critically, the output of these planar processes need not be purely two-dimensional. Conventional sheet metal fabrication transforms rolls of material into precise three-dimensional forms, and robotic process automation has massively scaled this process, for instance in automobile production [30]. Rigid-flex PCB manufacturing uses flexible substrates to fold circuit boards, bringing electronic interconnect to space-constrained, three-dimensional shapes. Corrugated cardboard, of which more than 200 billion square meters are produced annually [67], is made extremely cheaply by patterning and bonding rolls of paper in a continuous process. Continuous processes for cost-effectively producing thermoplastic honeycomb cores by thermoforming and folding have been recently developed [151, 26, 150, 166]. Sandwich panel cores have also been constructed using only folding, enabling the use of high-performance materials in these *foldcores* [136, 107, 86, 56, 81, 106].

Despite the apparent restrictions of creating three-dimensional geometry from a flat pattern, advances in algorithms for folding [49] have demonstrated that remarkable complexity and functionality can be produced this way, and the field of structural origami has grown around this observation [88]. For instance, any polyhedral mesh can be formed by folding a single flat origami pattern [50] (shown in Figure 1.4a), and an arbitrary connected three dimensional volume can be

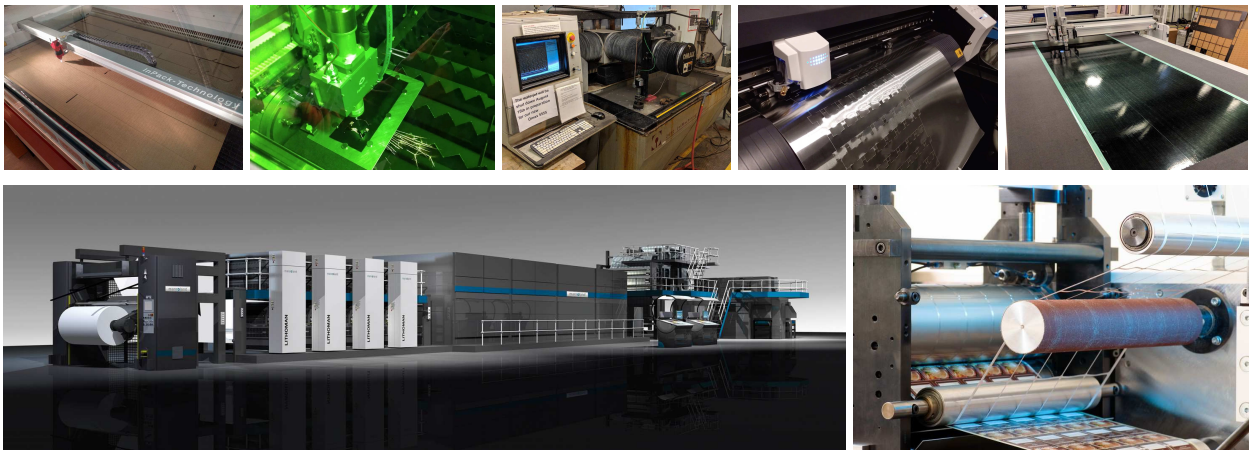

Figure 1.3: Planar processes. *a) CO2 laser cutting, b) fiber laser cutting, c) waterjet cutting, d) drag knife cutting, e) powered knife cutting, f) high speed printing press (Image from [126]), g) rotary die cutting (Image from [105]).*

filled by folding a one-dimensional chain [41]. Rigid simulation has been used for form finding [176], and considerable progress has been made to model the interplay of geometry with elasticity [164, 178, 62, 71], and of global geometry with local folds and cuts [52, 38, 37]. Exotic material capabilities have been demonstrated, including bi-directional flat-foldability [165, 163, 179, 137, 42], reconfigurable states [63, 146, 147], in-situ tunable thermal expansion [24], and acoustic waveguide behavior [11]. Particularly striking examples of complexity of folded structure come from *Pop-up MEMS* (shown in Figure 1.4b), where layers are micromachined, laminated, and folded into three dimensions based on custom design algorithms [10, 9], forming monolithic structure with high performance materials [206, 173, 201], mechanisms for transmission [129] and assembly aid [84, 60, 143, 123, 144], using a variety of actuation [99, 53, 76, 61, 115, 122] and sensing [5, 102, 27, 169, 175] technologies. Related methods enabled by atomically thin graphene kirigami [23] have produced autonomous machines on the scale of a single biological cell [134].

This thesis works to show that structural origami is not only a scalable way to manufacture architected materials, but also spans a rich enough geometric space to solve important engineering problems with those materials. In each of five case studies (shown in Figure 1.5), I build the mathematical and physical machinery necessary to meet a given functional requirement. First, in Chapter 2, I show a method to fill a desired three-dimensional shape with a structurally efficient architected material by cutting and folding a flat sheet. I then design, build, and test a machine to automate this construction. Second, in Chapter 3, I demonstrate control over the stiffness of

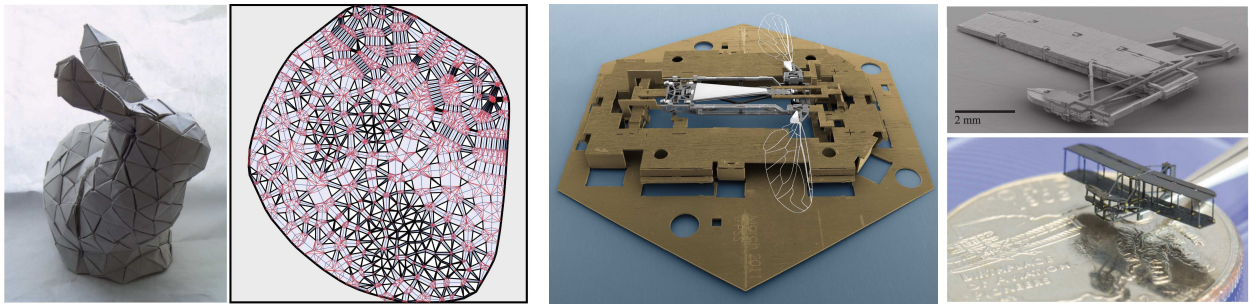

Figure 1.4: *a) Origamizer 3D model and folding pattern (Image from [50]), b) Pop-up MEMS RoboBee and Wright Flier (Image from [7])*

an architected material in addition to its shape. I apply this construction to make custom shoe soles and show that the achievable properties span a similar range as conventional foams used in footwear. Third, in Chapter 4, I maximize the resilience of an architected material, or its ability to return energy in an impact event. To this end, I develop a design method for architected materials with curved creases, a composite manufacturing technique to fabricate them, and dynamic impact test equipment to evaluate them, showing resilience approaching that of state-of-the-art polymer foams. Fourth, in Chapter 5, I maximize the toughness of an architected material, or its ability to absorb energy from an impact event, taking as an example a vehicular crashbox. I develop a hierarchical folded architected material and a machine for its construction, showing its specific energy absorption (the energy absorbed per unit mass) to be twice that of commonly used honeycombs. Fifth, in Chapter 6, I build active folded structures, taking as an application the generation of traveling waves on a hydrofoil surface (a longstanding goal of active flow control). I develop several methods of embedding actuation into folded architected materials, design and build a hydrofoil with active surface, and evaluate drag reductions in tank testing.

Each of these examples has important engineering applications in its own right, but taken together, they demonstrate the potential of folded architected materials for next-generation manufacturing. Not only can geometric design be used to increase performance, but in many cases, less material can be used to meet a design specification, and undesirable materials can be substituted for more environmentally benign ones. Energy-intensive thermal manufacturing processes can be replaced by efficient isometric operations. The cost of customization can be reduced by avoiding molds and tooling, and multiple functional parts can often be combined to simplify designs and supply chains. I discuss these implications in Chapter 7, estimating the energetic impact of adoption of architected materials.

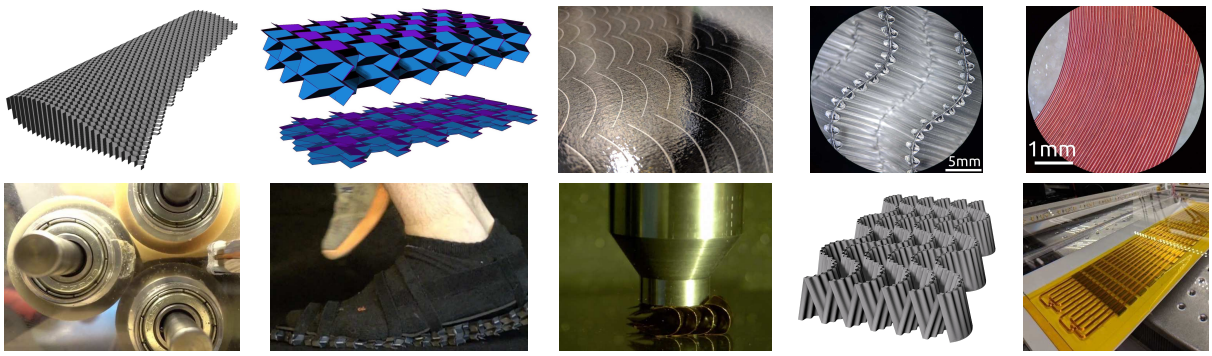

1. Shape (geometry) **Chapter 2**

2. Stiffness (quasistatics) **Chapter 3**

3. Resilience (reflection) **Chapter 4**

4. Toughness (absorption) **Chapter 5**

5. Action (transmission) **Chapter 6**

Figure 1.5: Visual table of contents of test cases

Chapter 2

Shape

2.1 Introduction

In this chapter[1], I develop a method to fill a desired three-dimensional shape with a structurally efficient architected material by cutting and folding a flat sheet. I then design, build, and test a machine to automate this construction.

This approach uses a honeycomb structure as the base geometry, as it is extremely efficient in supporting out of plane compression and shear loads. I extend a method for producing shaped honeycombs directly using cutting and folding, requiring no post-processing operations [140]. Figure 2.1 shows an example of the method, where an airfoil shape is filled with a honeycomb, decomposed into a flat pattern, laser-cut and folded, and finally skinned to create a load-bearing aerodynamic surface.

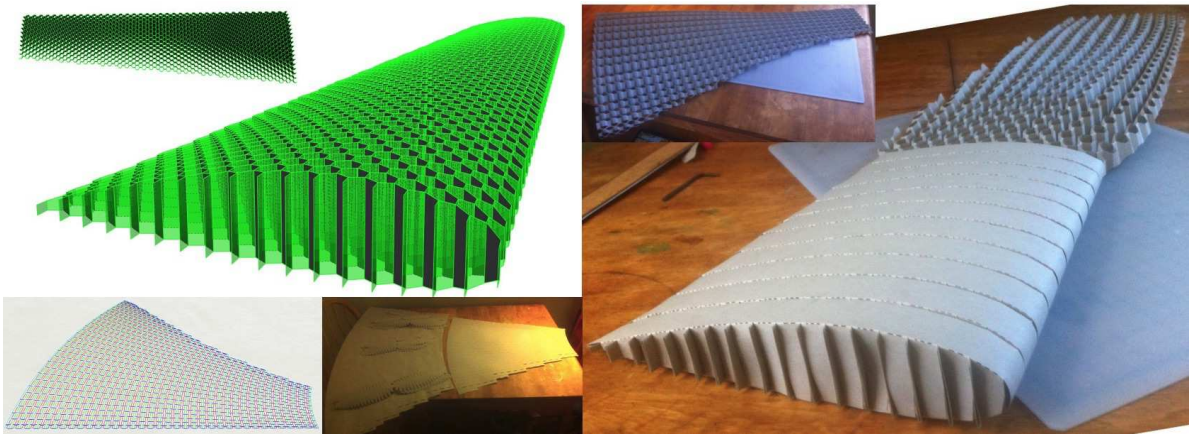

Figure 2.1: Airfoil filled with a shaped honeycomb, decomposed into a flat pattern, laser-cut and folded, and finally skinned to create a load-bearing aerodynamic surface.

Previously it had been shown that any constant-cross-section volume can be filled with a honeycomb produced by cutting and folding a flat sheet [160, 158, 139], up to a piecewise linear approximation at the pitch of the honeycomb. More recently, this technique has been extended

[1]The work of this chapter was presented at the 2018 ASME Manufacturing Science and Engineering Conference [32].

to fill a broader class of doubly-curved three-dimensional shapes [159] by describing the folding pattern in a polar coordinate system. This opens a broader class of sandwich shapes, but has the downside that many of the folds are no longer straight and parallel, significantly increasing manufacturing complexity. Researchers have also produced sandwich panel cores using only folding. These *foldcores* have been the subject of considerable research, mostly due to their advantages for ventilating the core of a sandwich panel against water ingress [107] and high compression and shear strength [86]. Batch and continuous manufacturing processes have been demonstrated [56], but only for limited panel widths, uniform thicknesses, and with a relatively large folding pitch. There has been some work on modifying patterns of creases to create shaped foldcores [81, 106] but the patterns quickly increase in manufacturing complexity. For these reasons, this work focuses on the using cutting and parallel folding only to fill volumes.

In this chapter, I first detail the approach for generating cut and fold patterns for a given three-dimensional shape. Next, I discuss motivation, design, and construction of the machine for folding these patterns, drawing on common mechanisms from the folding of paper media in industry. Finally, I characterize the crease spacings produced by this machine, show a shaped honeycomb produced on this machine, and sketch directions for future work.

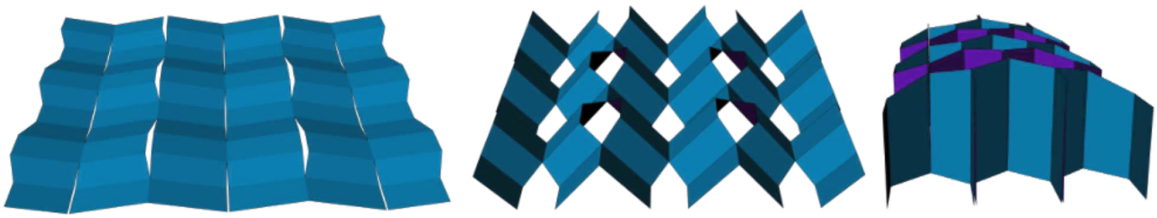

Figure 2.2: Basic folding motion from flat to three-dimensions.

2.2 Pattern construction

We begin by describing the method of constructing a cut and fold pattern for a honeycomb filling a three dimensional volume specified by two functions $t(x, y)$ and $u(x, y)$, which define upper and lower bounding surfaces of the volume (as shown in Figure 2.3). We parameterize the pitch of the desired honeycomb by its side length s and define a set of lattice coordinates

$$h(i, j) = \left(\tfrac{\sqrt{3}}{2} si, \tfrac{3}{2} s\lfloor \tfrac{j}{2} \rfloor + s(j \bmod 2)\right) \tag{2.1}$$

where $\lfloor x \rfloor$ denotes the smallest integer less than x and $j \bmod 2$ denotes the remainder upon division by 2. We use the shorthand $t_{i,j} = t(h(i, j))$ and $u_{i,j} = u(h(i, j))$ to denote the boundary functions evaluated at the coordinate $h(i, j)$. Figure 2.3 also shows a parameterized cutting and folding pattern which undergoes the transformation to become a shaped honeycomb, drawn for the case of a regular hexagonal honeycomb. For example, after folding, the line from $A_{0,0}$ to $B_{0,0}$ runs into the page at $h(0, 0)$, while the lines from $C_{0,0}$ to $D_{0,0}$ and from $A_{1,0}$ to $B_{1,0}$ run out of and into the page at $h(2, 0)$, respectively. Further, the lines from $A_{0,2}$ to $B_{0,2}$ and from $C_{0,2}$ to $D_{0,2}$ run into and out of the page at $h(1, 2)$, respectively. The task at hand is to choose the parameters

$A_{i,j}, B_{i,j}, C_{i,j}, D_{i,j}$ such that the bounding surfaces of the resulting honeycomb match the input functions t and u.

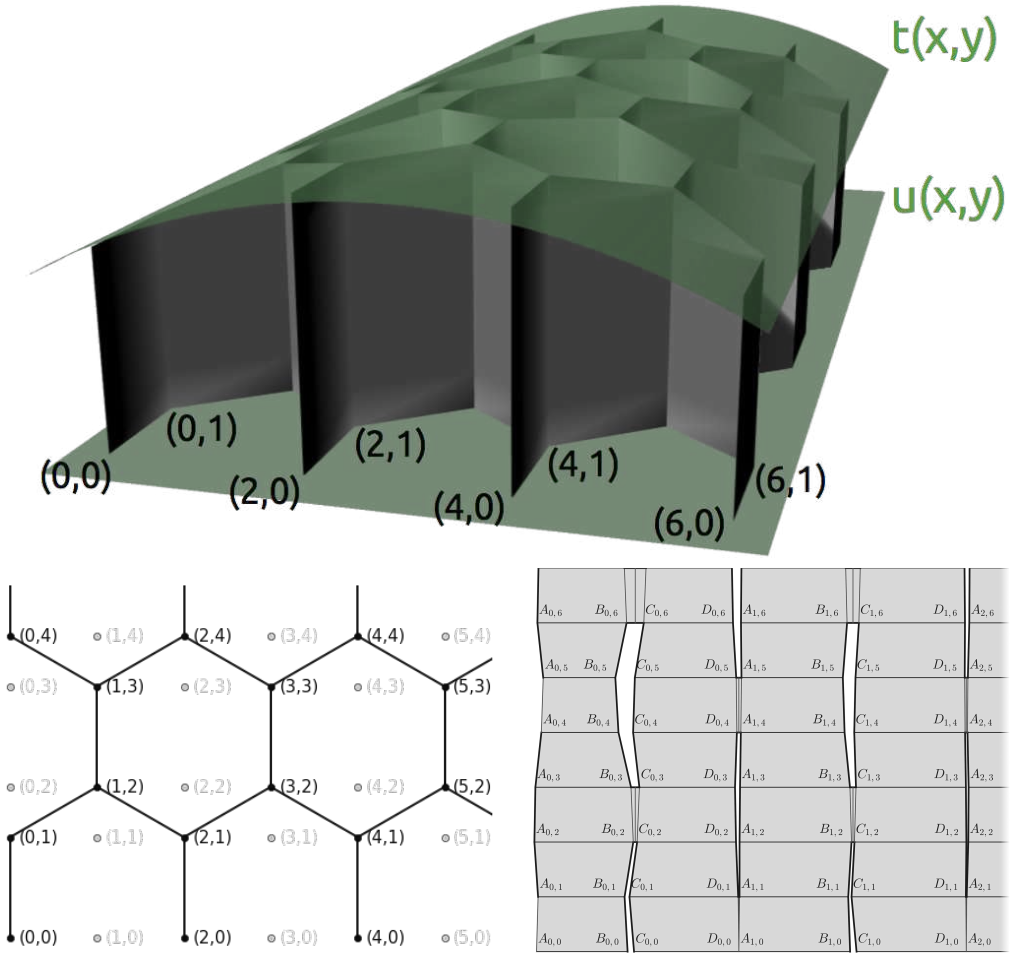

Figure 2.3: Parameterizing cut-and-fold pattern of a shaped honeycomb. a) Defining bounding surfaces and lattice coordinates, b) Lattice coordinates in two dimensions, c) Defining cut pattern parameters.

We first note that the y coordinates in the pattern are completely determined by the lattice coordinate system and hence can be computed independently from the x coordinates. The horizontal lines are parallel and simply spaced by the side length s. Without loss of generality, we let the parameters $a_{i,j}, b_{i,j}, c_{i,j}, d_{i,j}$ denote the x coordinate of these points only. To ensure that no sections of the folding pattern overlap, we first calculate parameters $a'_{i,j}, b'_{i,j}, c'_{i,j}, d'_{i,j}$ based only on the bounding surfaces t and u. Then we calculate column-wise shifts w_i and v_i such that $a_{i,j} = a'_{i,j} + w_i$, $b_{i,j} = b'_{i,j} + w_i$, $c_{i,j} = c'_{i,j} + v_i$, and $d_{i,j} = d'_{i,j} + v_i$ determine a non-overlapping pattern.

From the correspondence between Figures 2B and 2C, we have

$$a'_{i,j} = \begin{cases} u_{2i,j} & \text{if } j \equiv 0 \text{ or } j \equiv 1 \\ u_{2i+1,j} & \text{if } j \equiv 2 \text{ or } j \equiv 3 \end{cases} \pmod 4 \tag{2.2}$$

$$b'_{i,j} = \begin{cases} t_{2i,j} & \text{if } j \equiv 0 \text{ or } j \equiv 1 \\ t_{2i+1,j} & \text{if } j \equiv 2 \text{ or } j \equiv 3 \end{cases} \pmod 4 \tag{2.3}$$

We can write formulas for $c'_{i,j}$ and $d'_{i,j}$ recursively over j. Setting $c'_{i,0} = t_{2i+2,0}$, we can write

$$c'_{i,j} = \begin{cases} c'_{i,j-1} - t_{2i+2,j} + t_{2i+1,j-1} & \text{if } j \equiv 0 \\ c'_{i,j-1} - t_{2i+2,j} + t_{2i+2,j-1} & \text{if } j \equiv 1 \\ c'_{i,j-1} - t_{2i+1,j} + t_{2i+2,j-1} & \text{if } j \equiv 2 \\ c'_{i,j-1} - t_{2i+1,j} + t_{2i+1,j-1} & \text{if } j \equiv 3 \end{cases} \pmod 4 \tag{2.4}$$

Setting $d'_{i,0} = c'_{i,0} + t_{2i+2,0} - u_{2i+2,0}$, we can recurse similarly over j:

$$d'_{i,j} = \begin{cases} d'_{i,j-1} - u_{2i+2,j} + u_{2i+1,j-1} & \text{if } j \equiv 0 \\ d'_{i,j-1} - u_{2i+2,j} + u_{2i+2,j-1} & \text{if } j \equiv 1 \\ d'_{i,j-1} - u_{2i+1,j} + u_{2i+2,j-1} & \text{if } j \equiv 2 \\ d'_{i,j-1} - u_{2i+1,j} + u_{2i+1,j-1} & \text{if } j \equiv 3 \end{cases} \pmod 4 \tag{2.5}$$

Finally, to guarantee no overlaps occur in the pattern, we can set $v_0 = w_0 = 0$ and calculate recursively:

$$w_i = \max_j (d'_{i-1,j} - a'_{i,j}) + w_{i-1} \tag{2.6}$$

$$v_i = \max_j (b'_{i,j} - c'_{i,j}) + w_i \tag{2.7}$$

This parameterization is similar to that of [160], except we do not require that $d_{i,j} = a_{i+1,j}$ for $j \equiv 0, 1 \bmod 4$. and that $b_{i,j} = c_{i,j}$ for $j \equiv 2, 3 \bmod 4$. This extra freedom allows the definition of the offset parameters, which allows any bounding functions t and u to be used as bounding surfaces. This approach also maintains straight and parallel horizontal fold lines instead of using a polar coordinate system as in [159] when describing volumes with non-constant cross-section. This difference significantly simplifies the manufacturing process for these honeycombs. For instance, Figure 2.4 shows a wind turbine airfoil with a taper given by the optimal $1/R$ chord length scaling [127]. The bottom left image shows a fold pattern produced using a polar coordinate system to create a linearly tapering airfoil approximating the optimal scaling. The bottom right image shows a fold pattern for the optimal $1/R$ taper, produced with the current approach, keeping the folds linear, straight, and parallel. While the polar coordinate approach makes more efficient use of material, the current approach is easier to manufacture and allows greater control over shape.

The only penalty of this approach is that we must include extra pleats (e.g., $B_{0,2}C_{0,2}C_{0,3}B_{0,3}$) to account for the variable width of each column in the folding pattern. Depending on the application, these pleats can be simply trimmed off, or folded down between the adjacent honeycomb walls. In the case where t and u define a volume with constant cross section (normal to y), the offset parameters equal zero. In this case, the pleats have zero size and the formulas above are equivalent to those derived in [160].

2.3 Folding mechanism design

The derivation above has shown that the combination of cutting and folding operations can produce honeycombs bounded by arbitrary functions $u(x, y)$ and $t(x, y)$. For the cutting operations,

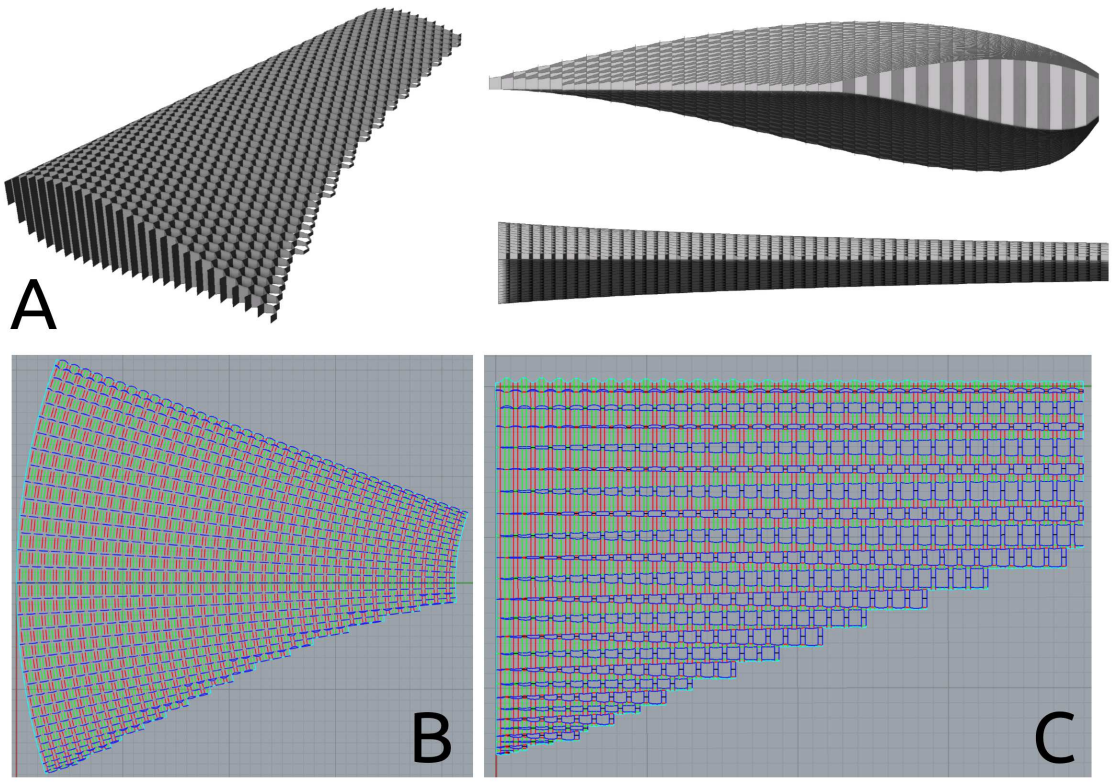

Figure 2.4: Creating folding patterns for honeycombs with non-constant cross section. a) Airfoil with optimal $1/r$ chord length, b) Linearly tapering airfoil folding pattern in polar coordinate system, c) $1/r$ tapering airfoil folding pattern with parallel creases and pleats.

there exist a large number of options for processing thin sheet materials, including passive and active knife cutting, laser cutting, abrasive waterjet machining, and die cutting. For folding, fewer options exist in industry. One recent study has shown an automated batch process for producing flat, uniform thickness kirigami honeycombs [194]. Motivated by industrial folding of maps and newspapers, I now demonstrate a folding machine for producing shaped kirigami honeycombs (shown in Figure 2.7), capable of producing a variably spaced sequence of mountain and valley folds in a roll of material. I characterize the accuracy of this fold placement using an optical scanning technique. By adding a cutting stage on this machine, I show that two of the three required steps for producing kirigami honeycombs can be realized. Finally, I sketch a mechanism for gathering the output into a finished, shaped honeycomb.

Thick or ductile materials are often folded using computer controlled press brakes or corrugation dies. Very thin materials require a small radius of curvature to reach a plastic onset strain level. Further, many papers and plastics exhibit greater elasticity than the metals which are usually folded using these methods. For these reasons, I looked to folding methods, suited to these materials and thicknesses, which correspondingly crease material to a much greater angle during forming than is required in the final, creased state. These same techniques work on thin metal foils also, provided no brittle fracture occurs. To this end, production of maps and newspapers offers an impressive example of precise, high-speed folding at industrial scales [131]. Figure 2.5 shows two folding mechanisms commonly used in this industry. In both cases, a set of rollers at the left pulls a sheet into the machine where it is folded. In the left configuration, a physical stop

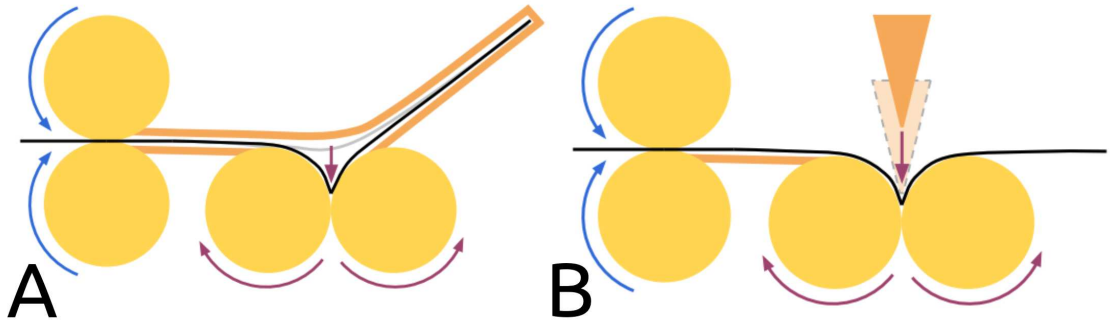

Figure 2.5: Folding mechanisms used in processing print media. a) Folding using a physical stop, b) Folding using a moving knife.

is positioned so that a moving sheet hits it, forming a buckle. Guides support the paper everywhere except the desired location for the buckle. This buckle is then grabbed and creased by a set of folding rollers. The process at the right is similar but uses a descending knife to push a buckle into the set of folding rollers. The position of the buckle on the sheet is set not by the physical position of a stop, but by the timing of the knife's movement relative to the moving sheet. In this way, fold position on the sheet can be varied in real time, unlike as with the first mechanism. The price to this functionality an additional degree of freedom as compared to the first mechanism.

To produce a set of folds, multiple versions of these mechanisms are connected in series; as a sheet travels from one to the next, a desired set of folds is produced. As the honeycomb folding patterns derived in the last section contain a large number of parallel folds, it is untenable to have

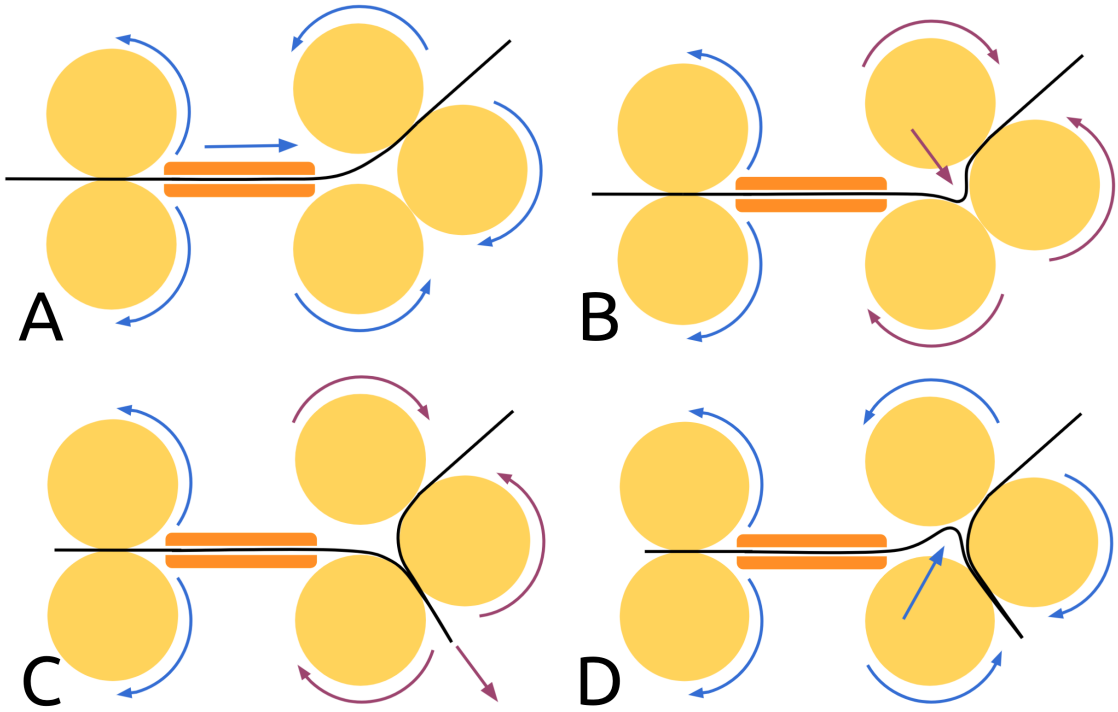

Figure 2.6: Mechanism for programmable folding with arbitrary fold spacing and orientation. a-d) Performing a move sequence to create a valley-mountain folding sequence.

Figure 2.7: a) Machine for cutting and folding used in processing shaped honeycombs. b) Voice coil drag knife cutting stage, c) Cut and folded output from machine, d) Machine processing vulcanized fiber.

such a large number of independent folding mechanisms. Further, as drawn, both mechanisms are only capable of producing upwards facing “valley" folds. If a downwards facing “mountain" fold is desired, inverted versions of the mechanisms are required.

Based on these constraints, I designed a mechanism (shown in Figure 2.6) inspired by the preceding two which is capable of forming both mountain and valley folds at locations which can be varied in real time, using only two degrees of freedom. To see this, consider the top left image where material enters through a roller at the left and exits through a roller at the top right. If these two rollers turn in the same orientation, the sheet simply moves through the machine. If they turn in opposite directions, a buckle is formed and folded by the third pair of rollers (shown at top right and bottom left). In this way, we have used the top right roller as a programmable stop, allowing us to place a valley fold at a variable position on the sheet. The symmetry of this configuration, however, also allows us to create mountain folds, provided we have first pulled the sheet into the bottom roller pair (shown at bottom right). The progressive formation of a buckle and then a fold is shown in Figure 2.8.

In fact, this mechanism is universal, in that it can fold any sequence of mountain and valley folds, provided the sequence starts with a valley, and the minimum crease spacing is lower

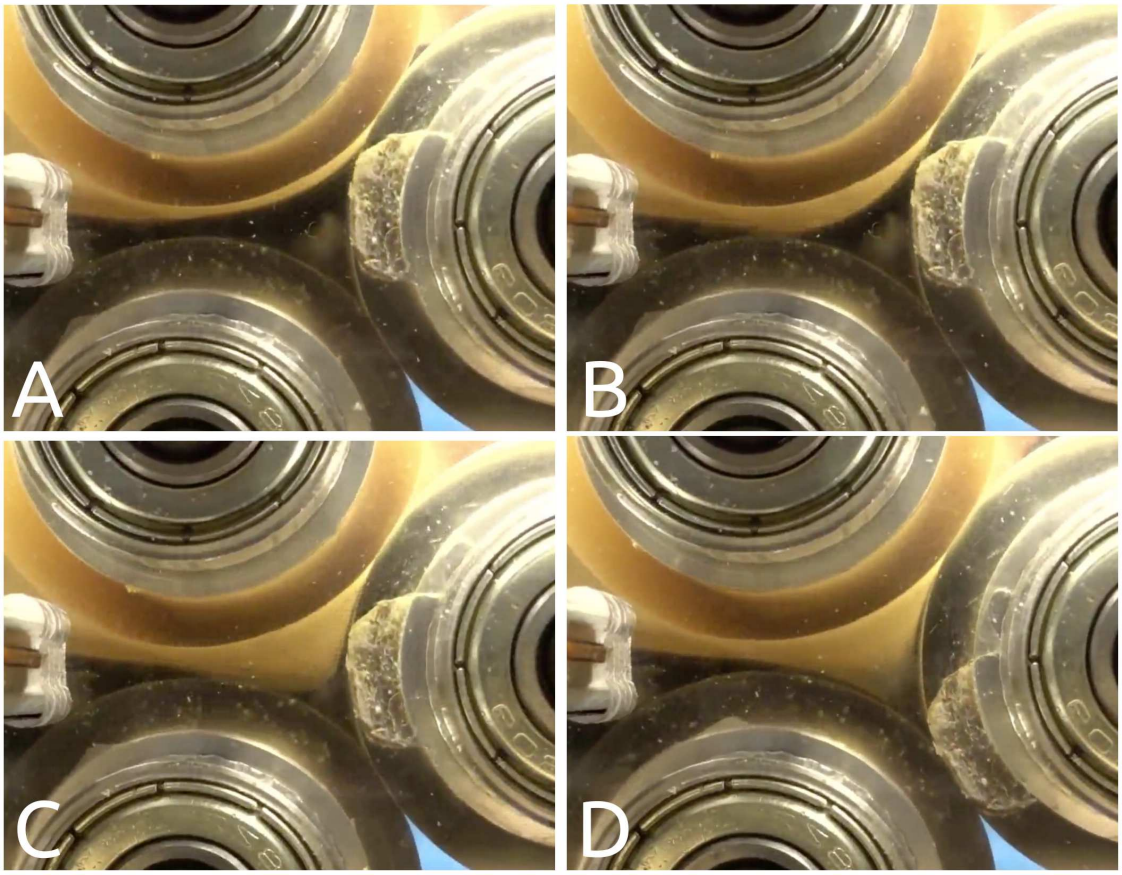

Figure 2.8: Forming a fold inside the machine. a) Sheet traveling through rollers, b) Rear roller reverses direction, causing a buckle to form, c) Curvature of buckling increases, d) Crease is formed as the buckle passes between rollers.

bounded by a constant ϵ, depending on the machine dimensions. In practice, the first condition is not a significant constraint, as we can always perform a valley fold at the start of operation, discarding the valley after all folding has been performed. The second condition is a harder constraint, as if crease spacing is less than the distance between the contact points of the folding roller pairs, consecutive creases can interact inside the machine. In practice, the exact value of ϵ depends on the orientation of the incident creases. If they have opposite orientation (one a valley and one a mountain), ϵ was determined experimentally to be roughly $d/3$, where d is the diameter of the rollers. If the incident creases have the same orientation (both valleys or both mountains), dense crease spacing presented few problems, and hence ϵ was considerably smaller than in the first case.

Given a particular pattern of creases to form with this machine, we must generate a set of commands to send to the motors driving the rollers. In the case of producing honeycomb cores, we must produce a repeating valley-valley-mountain-mountain pattern with a constant spacing s. Figure 2.9 shows a simple command set which produces this folding pattern where each command consists of the distance to drive each degree of freedom in the machine. In this commands, the variable c is a distance we drive both roller pairs to transform an initially taut sheet into a buckled, then creased state (the transition shown in Figure 2.8). We can choose any value for c as long as it is greater than $\pi d/12$, the approximate minimum distance to drive the midpoint of the taut sheet to the point of mutual tangency of the opposing rollers. In this figure, we first crease and uncrease

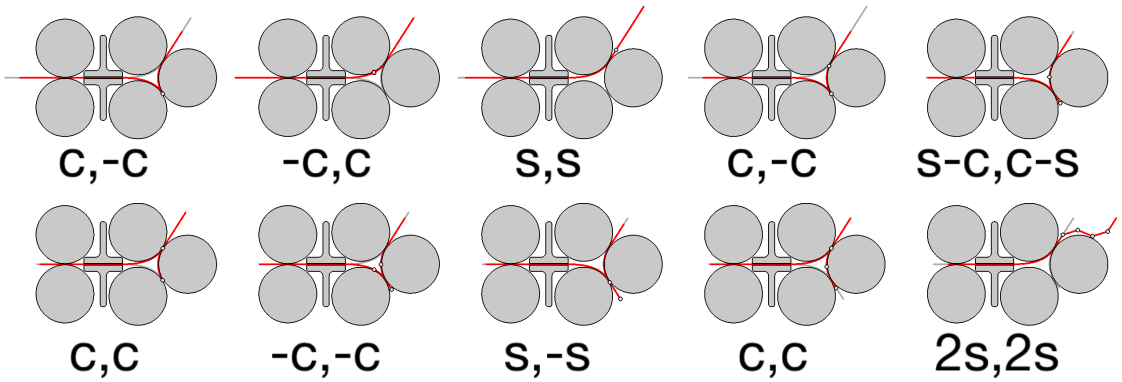

Figure 2.9: A move sequence to create a V-V-M-M fold sequence by folding creases in order.

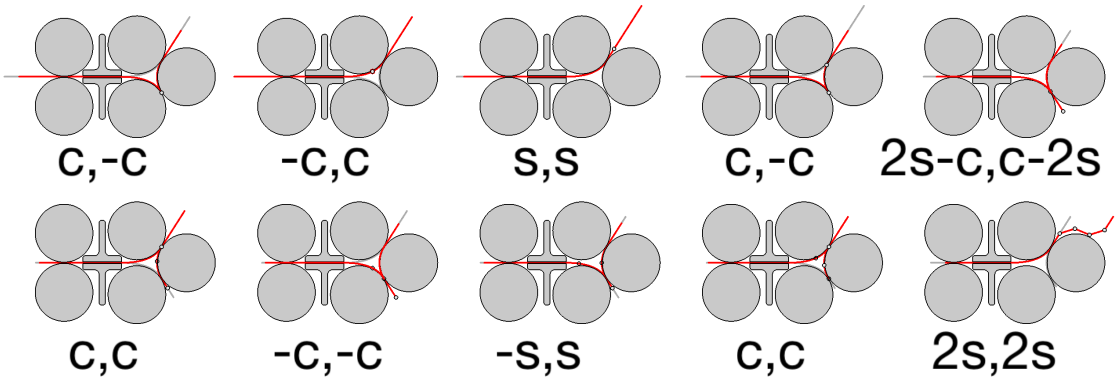

Figure 2.10: A move sequence to create a V-V-M-M fold sequence by folding creases out of order.

a valley fold, then advance by the crease spacing before creasing another valley fold. With this valley fold held, we drive to the location of the subsequent mountain fold before creasing and uncreasing it. Finally, we drive to the location of the final mountain fold, crease it, and then eject all the folds from the machine.

Figure 2.10 shows another command set which produces the same folding pattern. In contrast to the previous command set, these folds are not produced in a consecutive order. The advantage of this pattern is that the minimum distance during folding between folds of opposite orientation is $2s$, rather than s. For dense spacings, where $s < \epsilon < 2s$, this nonconsecutive sequence can be folded accurately, while the consecutive pattern cannot. This is measured empirically in Section 2.5.

2.4 Machine construction

To construct the folding machine, a set of pinch rollers were fabricated by overmolding a Shore 80A urethane rubber (Smooth-On PMC-780 Dry) onto 25 mm knurled aluminum rods. The rubber was pressure cast, demolded, rough turned, and finished ground, as shown in Figure 2.11. Two grit rollers were fabricated by knurling an aluminum rod of the same diameter as the urethane pinch rollers. All rollers had an outer diameter of 32 mm and were sized to give a 750 mm working width for the machine.

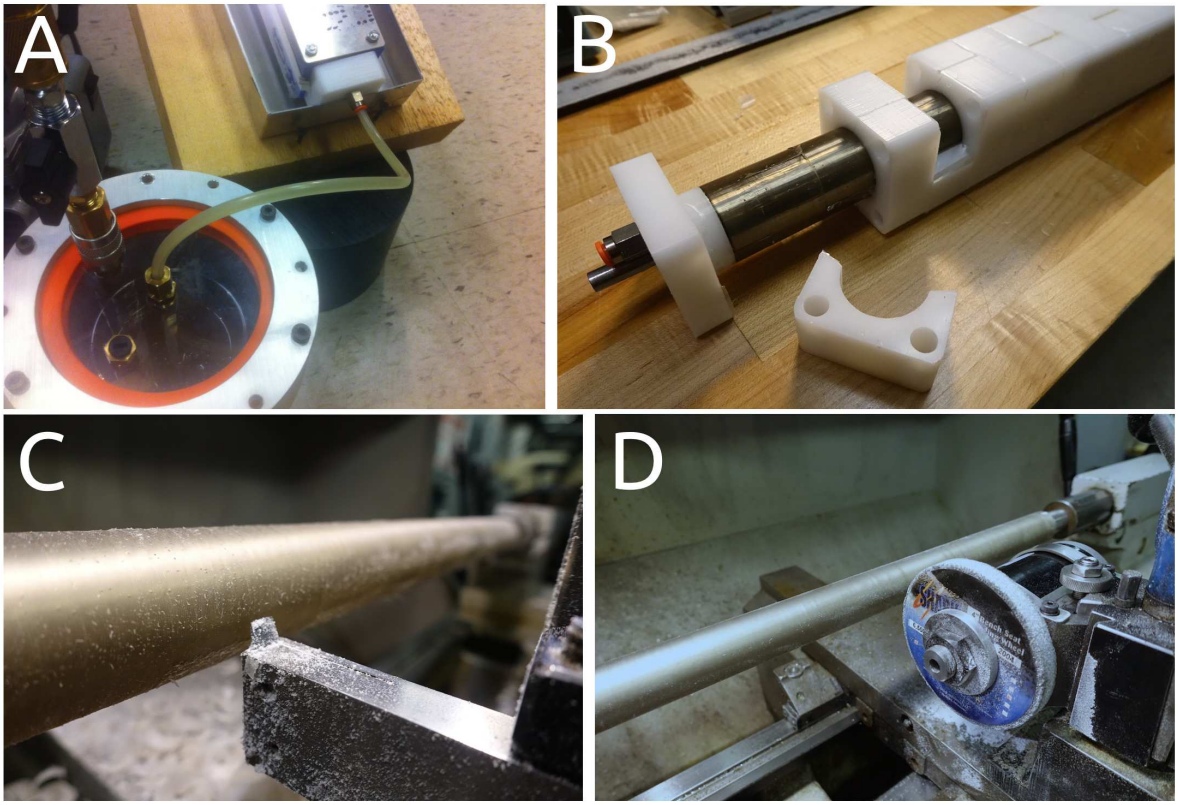

Figure 2.11: Fabrication of rollers used in the folding machine. a) Pressure molding of polyurethane rubber onto knurled aluminum rod, b) Demolding roller, c) Rough turning polyurethane surface using high-rake tool, d) Finish grinding surface to dimension.

In selecting these dimensions, I sought a balance between the maximum width material capable of being processed and the densest crease spacing possible. The wider the input material, the larger, thicker the honeycombs that can be produced. Over a large width, however, deflection of the rollers would decrease the effectiveness of the machine's creasing operation. I expected that increasing the roller diameter to compensate for this would limit the minimum spacing of creases that the machine would be capable of producing. Therefore, to balance these competing design constraints, I sized the rollers based on the expected forces per unit length required to form a plastic hinge in the material. It has been shown [154] that under a creasing force, the ratio of radius of curvature to the material thickness initially follows a plastic deformation power law. At some point, a discontinuity occurs, and additional force produces much smaller changes in residual curvature. For Tyvek of 143 micron thickness, this discontinuity was experimentally shown to occur at 200 N/m at a radius of curvature of 750 microns, while increasing the force per unit length to 1000 N/m only reduced the radius of curvature to 500 microns. Approximating the rollers as uniformly loaded beams with circular cross section, we can calculate the maximum deflection of the center point subject to these creasing loads. We can then calculate the maximum width subject to a deflection equal to the radius of curvature of the crease. Using this approach, I calculated that aluminum rollers of 25 mm diameter at 750 mm length would be able to crease this Tyvek. Given that Tyvek is a very elastic material requiring high force to induce crisp fold, I reasoned that more plastic materials would be easily creasable with rollers of these dimensions.

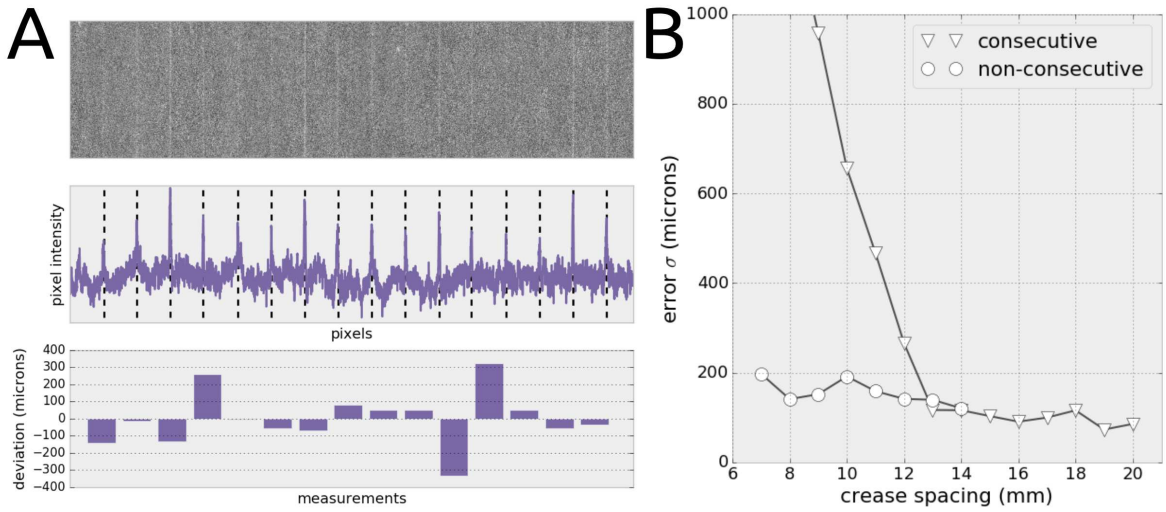

Figure 2.12: Workflow for measuring accuracy of machine-placed creases. a) Measuring crease lines for $9mm$ spacing, showing scanned image, detected creases, and calculated errors, b) Errors versus crease spacing for consecutive and non-consecutive move strategies.

These rollers were arranged into a front pair of driving rollers and a rear triple of folding rollers. The rotation of these roller groups was synchronized using spur gears and actuated using a pair of NEMA-23 bipolar stepper motors and a 3:1 timing belt reduction. These motors have 200 steps per revolution, giving a potential resolution of roughly 160 microns without microstepping, or 20 microns with 1/8th microstepping.

The cutting stage was built around a Roland drag knife holder (XD-CH2) using a 3D printed voice coil bobbin wound with 400 turns of 30 AWG magnet wire, rare earth magnets inside a 12L14 steel enclosure, and an LM8UU linear bearing with return spring. This simple voice coil actuator produced roughly 300 grams of downward cutting force, more than enough to cut a variety of sheet stocks up to 500 micron thickness.

When the sheet emerges from the machine, it has been cut according to the pattern, and the majority of creases have been folded. We call these straight and parallel folds spanning the entire pattern the *corrugation folds*. The remaining folds, which we call the *zig-zag folds*, transform the corrugated sheet into a honeycomb core. At this stage, some process for cross linking adjacent walls is necessary to retain the honeycomb in a condensed state. In the case of sandwich panels, this usually involves bonding face sheets to the core. In Figure 2.13, we bond cell walls with adhesive to avoid the need for face sheets. The machine presented above can automate the cutting and corrugation folding, but it doesn't yet automate the zig-zag folding. Later, I sketch an extension for automating the complete process.

2.5 Crease spacing evaluation

To characterize the accuracy of creasing using this folding method, a simple experiment was constructed. Vulcanized fiber sheets of $125\mu m$ thickness were prepared. These sheets crease consistently and exhibit strain whitening of the crease lines. This allows optical measurement of the spacing of crease lines. The folding machine was used to crease the sheets in a repeating valley-valley-mountain-mountain pattern, with trials for many values of the desired crease spac-

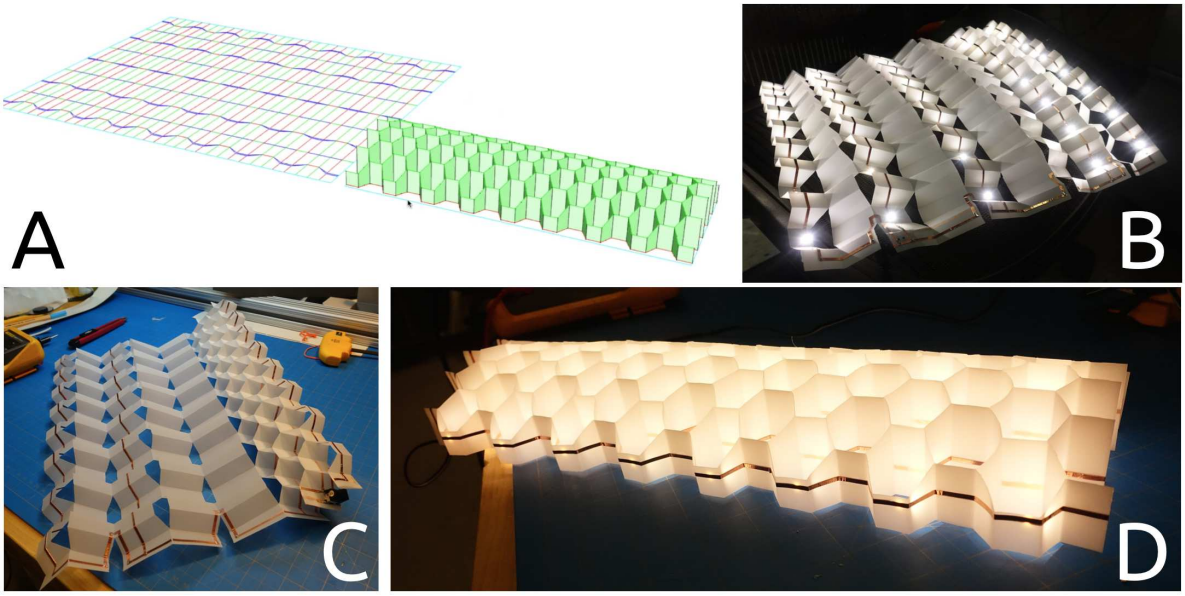

Figure 2.13: A prototype fabricated using folding machine. a) Digital design of 3D form and 2D pattern, b) After machine processing, c) During face bonding, d) Completed prototype.

ing (from $7mm$ to $20mm$). The sheets were flattened and scanned at a resolution of 100 dots per millimeter using an Epson Perfection V19 photo scanner. These images were processed using a Python script with the Numpy and OpenCV [145] libraries to detect the crease lines.

The results of this experiment are shown in Figure 2.12. At the left, I show the results from a particular trial where the desired spacing was $9mm$. The top image shows the scanned sample, the middle image shows the measured intensity values and detected peaks, and the bottom graph plots the difference between spacing of each consecutive pair and the desired value of $9mm$. The graph at right shows results over all crease spacings.

For crease spacings larger than 12 mm, a consecutive strategy for folding the creases produces errors with a standard deviation of roughly 100 microns. Below this spacing, however, the densely spaced creases can interfere with each other during folding. In this case, folding the creases out of order can avoid collisions. In the case of a repeated valley-valley-mountain-mountain pattern, folding in the order 1-2-4-3 eliminates a collision between the third crease and one of the rollers. Using this non-consecutive sequence, we can produce the same pattern down to $7mm$ crease spacing with standard deviation of error below 200 microns. The move sequences for these consecutive and nonconsecutive strategies are shown in Figure 2.9 and Figure 2.10, respectively.

2.6 Prototypes

In order to test the machine, I designed and fabricated a simple shaped honeycomb using PETE film ($130\mu m$ thickness). As shown in Figure 2.13 at top left, the shape was designed to be flat on one side and parabolic on the other based on a honeycomb with $s = 7.5mm$. In the top right image, the sample is shown after being processing by the machine, and after initial zig-zag folding has been performed manually. At bottom left, the sample is shown during bonding of adjacent faces. At bottom right, the finished sample is shown.

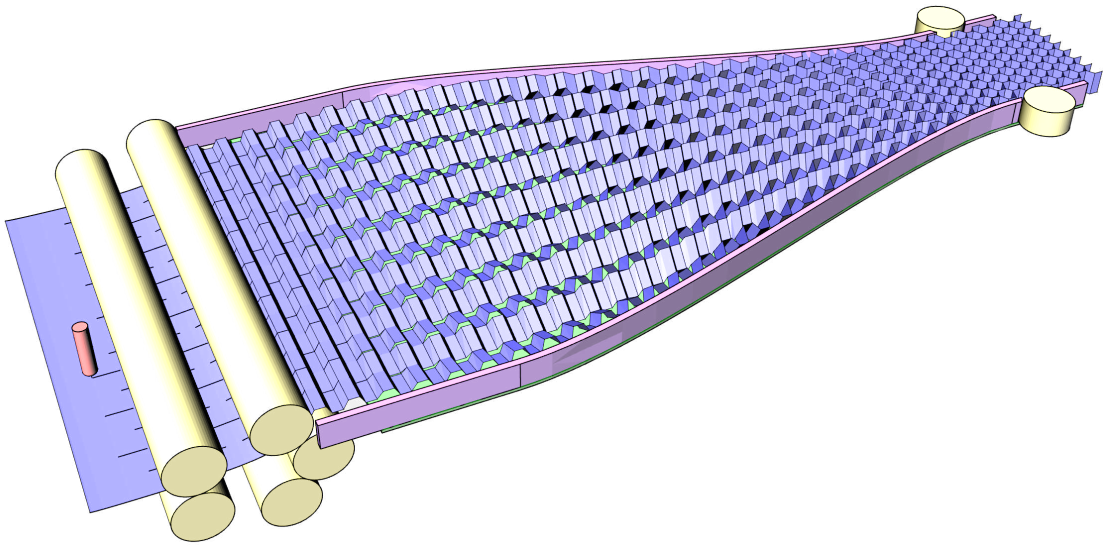

Figure 2.14: Concept for continuously gathering the folding machine output.

This sample was also used to show the viability of combining this manufacturing process with the production of flexible printed circuit boards. The shaped honeycomb acts as a carrier for an array of LEDs, positioning them accurately in three dimensional space based on their placement on the two dimensional material. The copper traces are applied using a pressure set adhesive after leaving the folding machine, but more common etching processes could be used prior to folding as well.

2.7 Conclusions

This chapter demonstrated the ability to fill a desired three-dimensional shape with a structurally efficient architected material by cutting and folding a flat sheet. First, an algorithm for computing flat patterns of cuts and folds based on three dimensional geometry was developed. Based on the large proportion of straight and parallel folds produced in these patterns, a machine was designed to both produce these folds as well as make the required cuts. This machine was then characterized by measuring the deviation of the placed folds from the desired fold locations. It was shown that with appropriate choice of crease order, the error can be kept below 200 microns over a range of desired crease spacings of 7 to 20 mm. A simple prototype was produced with this machine demonstrating its ability to combine cutting and folding to create a shaped honeycomb.

This research opens several directions for future work. First, a fully-automated continuous process for shaped honeycombs requires the addition of a final stage of this continuous process where the cut and corrugated sheet is folded in a zig-zag fashion into the final honeycomb. Depending on the application, this stage of the process may take different forms, but in the case of sandwich panels it involves gathering the cut and corrugated output from the folding machine into a honeycomb form and attaching face sheets. Similar “pattern and gather" approaches have experienced considerable success [163] in efforts to automate the folding of other origami patterns. In these techniques, a sheet is weakened along crease lines by partial cutting operations and a global contraction can cause all the creases to be folded synchronously. A sketch of this

Figure 2.15: Prototype machine for rule die creasing of aluminum honeycomb cores.

technique as applied to the shaped honeycomb problem is shown in Figure 2.14. The machine detailed above feeds its output into a narrowing passage, finally passing through its minimum width with the assistance of pulling rollers. Once started, each column of honeycomb cells imparts a bias to the next column of cells, extending the zig-zag fold. The corrugation makes each row stiff in comparison to the zig-zag crease lines, increasing the effectiveness of the gathering process. Once gathered, face sheets can be applied to fix the honeycomb in its condensed state.

A second direction for future work is to fully exploit the ability of the machine presented in this research to produce honeycomb cores of continuously varying cell size. This can be easily accomplished by changing the honeycomb cell side length s by placing corrugation folds at a different spacing. This capability could be used to provide a dense, stiff core in a region that experiences high loads (e.g., at the root of a wind turbine blade), while placing a much lighter core in regions (e.g., at the tip of the wind turbine blade) where high load capacity is not needed and weight savings has significant benefit.

Finally, alternative folding and creasing mechanisms can be incorporated into such machines to aid in processing additional materials. The folding mechanism described above was designed to crease materials like papers and polymers requiring a full 180 degree fold to create plastic deformation. For other materials like many metal foils, significantly less deformation is required, and often a full 180 degree fold can cause undesirable material fracture. Rule die creasing is often used to fold such materials. In this method, a stiff, thin metal rule, is pushed into a compliant substrate, which deforms around the rule. To investigate the use of this method in a computer controlled folding process, we build a simple rule die creasing machine, shown in Figure 2.15. Using this machine, I prototyped an array of honeycombs in aluminum, demonstrating that this method would work favorably in a version of the machine described in this chapter designed for metal foils.

Chapter 3

Stiffness

Next I demonstrate control over the stiffness of an architected material in addition to its shape[1]. To do this, the constructions for shaped kirigami honeycombs of Chapter 2 are modified to replace the hexagonal cells with Tachi-Miura polyhedral cells. The Tachi-Miura polyhedron possesses a number of useful properties, including bidirectional, rigid flat-foldability, tailorable Poisson ratio, and tileability. I analyze the rigid mechanics of these *Tachi-Miura honeycombs*, and experimentally test the elastic behavior subject to realistic materials and boundary conditions. Finally, I apply this construction to make custom shoe soles and show that the achievable properties span a similar range as conventional foams used in footwear.

In [137] and [179], several rigid-foldable origami cylinders are proposed and analyzed. One example, the Tachi-Miura polyhedra, is a rigid, bidirectionally flat-foldable cylinder which is tileable. Such foldable, space-filling cylinders open the possibility of constructing cellular materials with rigid folding mechanisms. The mechanical properties of cellular materials based on the Tachi-Miura polyhedron have been analyzed in several studies [211, 212, 213]. As these materials are rigidly flat-foldable, they can be used to create objects that undergo large reversible strains, with Poisson ratios determined by the Miura angle used to create the underlying polyhedra. This capability is a powerful tool for engineering compliant structures.

Physically constructing such cellular materials by simply joining many cylinders is difficult to implement at scale, but we can adapt strategies that were developed to efficiently construct origami honeycombs [140, 158, 160, 194]. These works show how a single sheet can be cut and folded to create a straight-walled honeycomb filling the space between two bounding surfaces. The current research extends these methods to fabricate honeycombs with Tachi-Miura polyhedra instead of hexagonal prismatic cells. These cellular materials are efficiently constructed by cutting and scoring a flat sheet which rigidly folds into the cellular material. By specifying locations of cuts, these cellular materials acquire a desired shape, just as with hexagonal honeycombs. We call such structures *Tachi-Miura honeycombs*.

In this chapter, I first describe our construction for these cellular materials and characterize the rigid folding motions of the resulting cellular materials by calculating their Poisson ratios. To validate the application of these cellular materials to engineer compliant materials, I measure the mechanical response of samples under compressive loading. By varying the Miura angle of the underlying Tachi-Miura polyhedron, the response can be tuned to match a range of common

[1]The work of this chapter was presented at the 7th International Meeting on Origami in Science, Mathematics and Education (OSME 2018) [31].

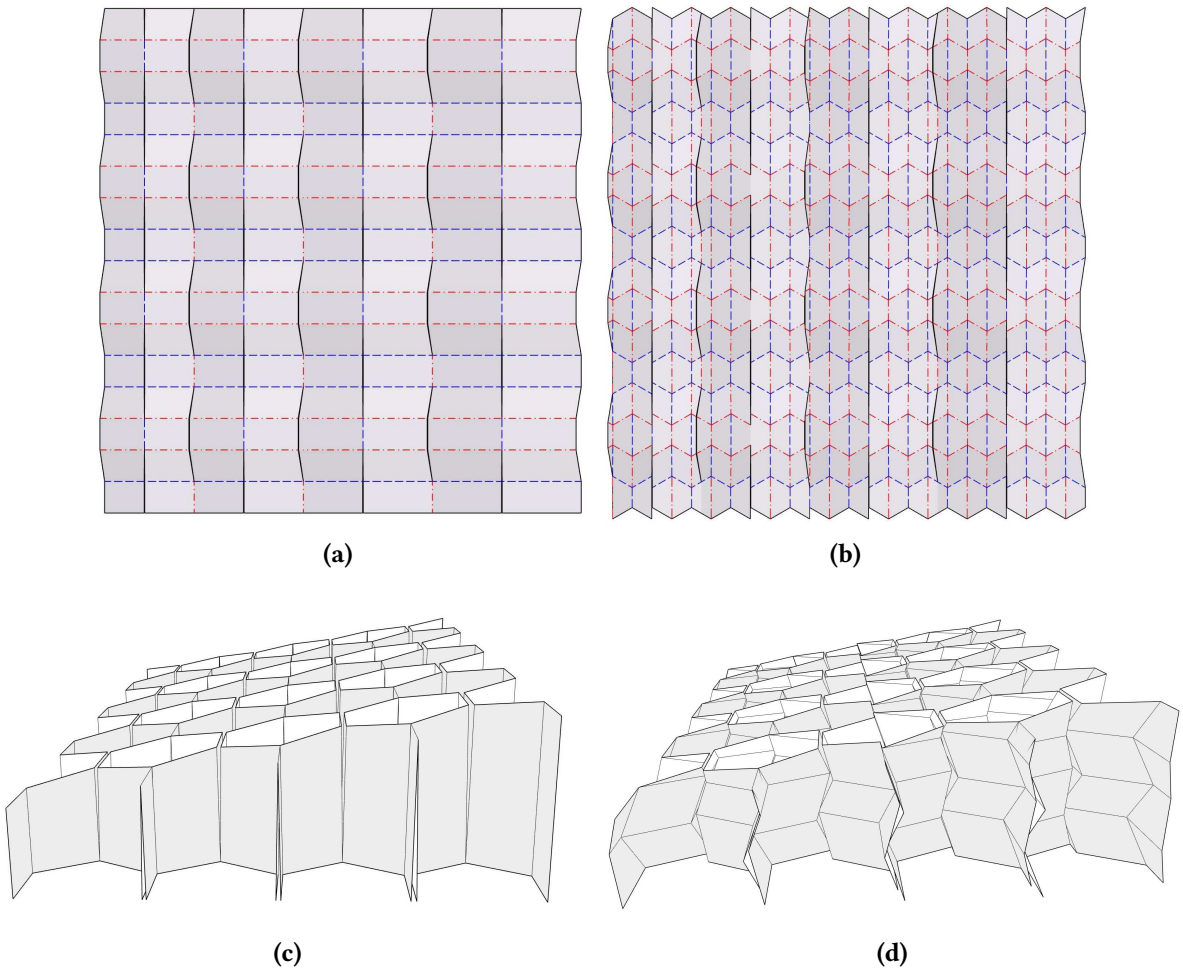

Figure 3.1: A) Cutting and folding pattern for the straight-walled honeycomb (blue dashed lines denote a valley fold, red dash-dot lines denote a mountain fold, and black solid lines denote a cut), B) Cutting and folding pattern, for Tachi-Miura honeycomb, made replacing straight folds with zig-zag folds, C) Shaped straight-walled kirigami honeycomb, D) Shaped Tachi-Miura kirigami honeycomb.

engineering foams. I then design a prototype utilizing both the large compliance of the folding mechanism and the shape control offered by the honeycomb construction: a running shoe sole. This prototype is then laser cut, folded, and tested.

3.1 Pattern generation

We begin by describing the method of constructing an origami pattern for a Tachi-Miura honeycomb filling a given volume. The volume to be filled is defined as all points $(x, y, z) \in \mathbb{R}^3$ such that $0 < x < X$, $0 < y < Y$, and

$$u(x, y) < z < t(x, y). \tag{3.1}$$

In other words, the volume is the space bounded by two functions u, t, restricted to a rectangular region of the $x - y$ plane. For instance, in Figure 3.1c, t and u are taken as linear functions describing planes.

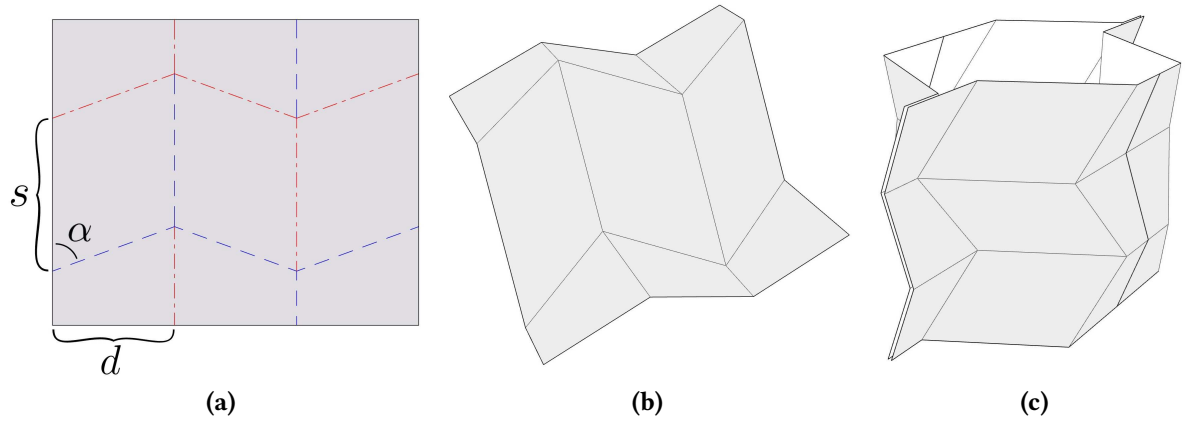

Figure 3.2: A) Parameterized Tachi-Miura unit cell folding pattern, B) Tachi-Miura unit cell three dimensional geometry. C) The unit cell and its mirror image arranged into a Tachi-Miura polyhedron.

In [160, 32], methods are derived for calculating the shape and positions of the slits in Figure 3.1a in order to produce the honeycomb shown in Figure 3.1c. These methods use evaluations of the functions t and u in recursive equations to calculate these parameters. For brevity, we do not reproduce these derivations here, but refer the reader to these articles for the details of these calculations.

This method for producing Tachi-Miura honeycombs is a direct adaptation of the method described above, motivated by modifying the cutting and folding pattern shown in Figure 3.1. First, we introduce some nomenclature. We distinguish *corrugation folds*, the horizontally-running folds in Figure 3.1a, from *strip folds*, the vertically-running folds joining adjacent cuts. Then, we conceptually subdivide the pattern into *strips*, the regions of material bounded on left and right by cuts and strip folds. For example, Figure 3.1a is composed of eight strips.

Within each strip, we can replace each corrugation fold line with a zig-zag fold of the same mountain/valley orientation. As shown in Figure 3.2, these zig-zag folds make an angle of $\pm\alpha$ with the vertical axis and has a period of $2d$. Vertical mountain and valley folds are added between each vertex of the zig-zag as shown to create a Tachi-Miura quarter cylinder [179]. We can apply this modification to each strip, taking care to adjust the phase of the zig-zag fold pattern so that adjacent strips align when the strip folds are actuated.

This modification allows Tachi-Miura honeycombs to be produced from one sheet, but to accurately determine the shape, the rigid folding mechanism of the Tachi-Miura polyhedron must be analyzed. To do this, we can use an angle parameterization, introduced and proven in [137], given by the equation:

$$\tan\alpha\cos\beta = \tan\gamma \tag{3.2}$$

where the *Miura angle* α sets the relationship between the exterior angle of each cell (2γ) and the dihedral angle of the trapezoidal faces (2β). These angles are shown graphically in Figure 3.3a.

Using these angle definitions, I define variables x, y, z for the spatial extents of a cell in each coordinate direction, shown in Figure 3.3b, and calculate:

$$x = 2s\sin 2\gamma \qquad y = s + s\cos 2\gamma \qquad z = Nd\sin\beta \tag{3.3}$$

where N is the number of zig-zag half-periods in our strip. We see that the expressions for x and y are identical to those of a standard hexagonal honeycomb cell, while the expression for z

is simply scaled by a factor of $\sin\beta$. Therefore, to accurately reproduce the shape of functions t and u, we must scale our generated patterns in the horizontal direction by a factor of $1/\sin\beta$.

We note that for functions t and u with large derivative, the intersection of the folded image of the zig-zag fold with the top or bottom surface can differ from the function's value at the base point of the zig-zag fold. This is illustrated in Figure 3.4, where the image of the zig-zag fold is shown in magenta. In this case, we can correct the function values used in the recursive equations by calculating the actual intersection of the zig-zag fold image with the bounding surfaces.

To do this, we can define the linear segments of the magenta path by vectors $\mathbf{v}_+$ and $\mathbf{v}_-$ (shown in Figure 3.4b). Using the angle parameterization of the Tachi-Miura polyhedron and the parallelogram area interpretation of the cross product, we calculate

$$\mathbf{v}_+ = d\left[\cot\alpha, \cot\alpha - \frac{\cos\beta}{\sin 2\gamma}, \sin\beta\right]^\mathsf{T} \tag{3.4}$$

$$\mathbf{v}_- = d\left[-\cot\alpha, -\cot\alpha + \frac{\cos\beta}{\sin 2\gamma}, \sin\beta\right]^\mathsf{T} \tag{3.5}$$

Thus, to calculate the intersection point we start from a point known to lie between t and u (shown in Figure 3.4 as the $z = 0$ plane). We alternatively add $\mathbf{v}_+$ and $\mathbf{v}_-$ until we leave the valid region. At this point, we have bracketed the intersection point by the end points of one linear segment of the zig-zag fold image path. Hence, we can simply perform a root search (e.g. binary search) to approximate the intersection point as accurately as is desired. For example, in Figure 3.4, the intersection point is computed to be approximately $\mathbf{v}_+ + \mathbf{v}_- + \mathbf{v}_+ - \frac{1}{2}\mathbf{v}_+ + \frac{1}{4}\mathbf{v}_+$ away from the starting point.

Finally, we also note that for functions t and u with large curvature, self-intersections of the flat folding pattern can occur as a result of the zig-zag phase shift. In practice, these are small, and for the purposes of the present work, we ignore them. With these corrections and caveats, our modification of the kirigami honeycomb pattern produces Tachi-Miura honeycombs filling the same volume.

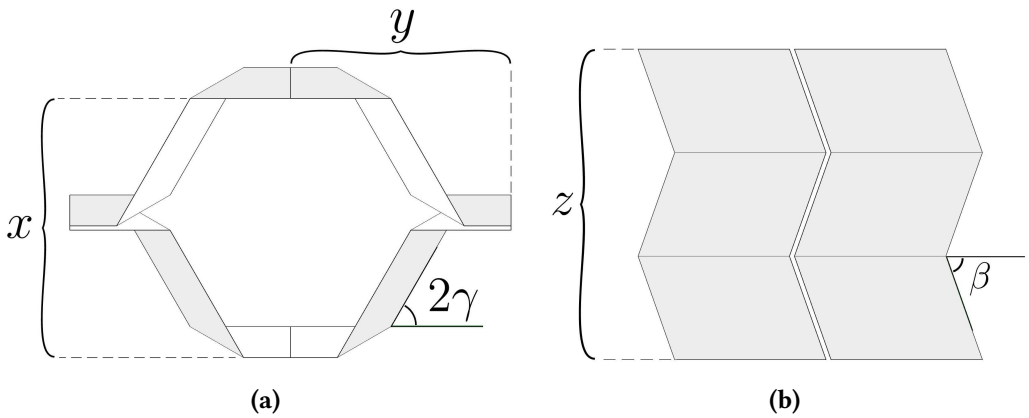

Figure 3.3: A) Plan view, defining x, y, and γ, B) Altitude view, defining z and β.

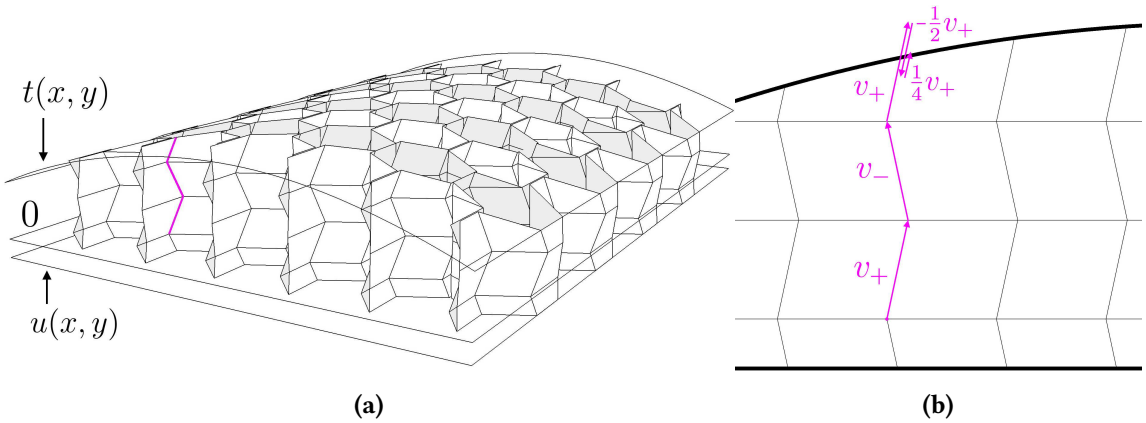

Figure 3.4: A) Bounding surfaces t and u shown in reference to the $z = 0$ plane. B) Calculating the intersection of the zig-zag fold image curve with the bounding surfaces using binary search.

3.2 Poisson Ratios

To analyze the mechanical behavior of these Tachi-Miura honeycombs, we first calculate their Poisson ratios (i.e., negative the ratio of strains between coordinate directions during the folding motion). We start from the expressions derived above for the x, y, and z extents, calculating the Poisson ratios in terms of α and γ. These expressions are similar to those derived in [212] but with a parameterization (shown in Figure 3.3) of cell extents that generalizes to volumes of adjacent cells (instead of applying to single cells).

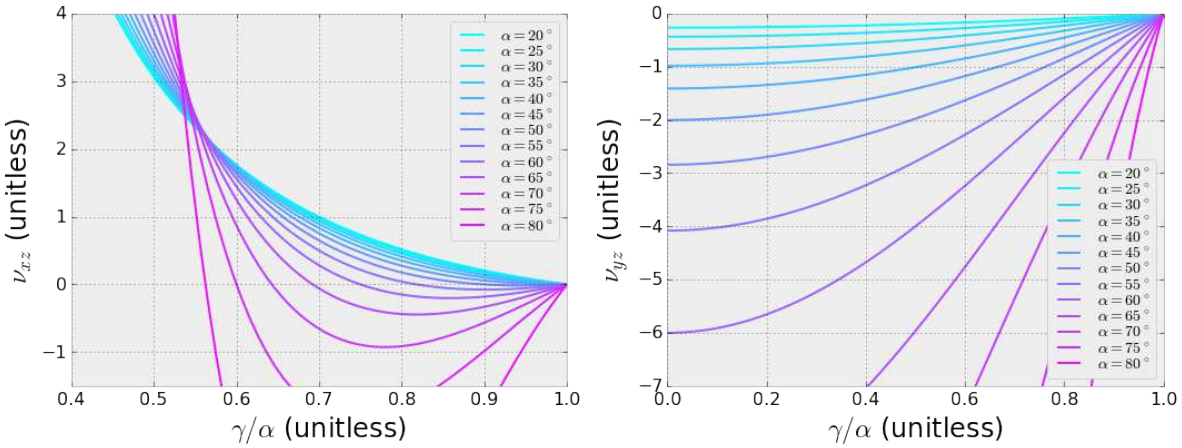

Figure 3.5: Poisson ratios of Tachi-Miura honeycomb. A) $\nu_{xz} = -\epsilon_x/\epsilon_z$, B) $\nu_{yz} = -\epsilon_y/\epsilon_z$.

To derive the poisson ratios of these structures, we must write expressions for the strains $\epsilon_x = \mathrm{d}x/x$, $\epsilon_y = \mathrm{d}y/y$, and $\epsilon_z = \mathrm{d}z/z$. Towards this end, we take derivatives of the spatial extents relative to γ:

$$\frac{\mathrm{d}x}{\mathrm{d}\gamma} = 4s\cos 2\gamma \tag{3.6}$$

$$\frac{\mathrm{d}y}{\mathrm{d}\gamma} = -2s\sin 2\gamma \tag{3.7}$$

$$\frac{\mathrm{d}z}{\mathrm{d}\gamma} = \frac{\mathrm{d}z}{\mathrm{d}\beta}\frac{\mathrm{d}\beta}{\mathrm{d}\gamma} = Nd\cos\beta\frac{\mathrm{d}\beta}{\mathrm{d}\gamma} = Nd\frac{-1}{\tan\beta\tan\alpha\cos^2\gamma} \tag{3.8}$$

where the final line follows from implicitly differentiating the governing equation. Now we calculate the strains:

$$\epsilon_x = \frac{\mathrm{d}x}{x} = \frac{\mathrm{d}x}{\mathrm{d}\gamma}\frac{\mathrm{d}\gamma}{x} = \frac{\mathrm{d}\gamma(1-\tan^2\gamma)}{\tan\gamma} \tag{3.9}$$

$$\epsilon_y = \frac{\mathrm{d}y}{y} = \frac{\mathrm{d}y}{\mathrm{d}\gamma}\frac{\mathrm{d}\gamma}{y} = -2\mathrm{d}\gamma\tan\gamma \tag{3.10}$$

$$\epsilon_z = \frac{\mathrm{d}z}{z} = \frac{\mathrm{d}z}{\mathrm{d}\gamma}\frac{\mathrm{d}\gamma}{z} = \frac{-\mathrm{d}\gamma\tan\gamma}{\tan^2\alpha\cos^2\gamma - \sin^2\gamma} \tag{3.11}$$

Figure 3.6: A) Foam sample on test platen, B) Folded sample on test platen, C) Foam sample loaded by platens, D) Folded sample loaded by platens.

These expressions can be used directly to calculate the Poisson ratios, as the factor of $\mathrm{d}\gamma$ cancels:

$$\nu_{xz} = -\frac{\epsilon_x}{\epsilon_z} \tag{3.12}$$

$$\nu_{yz} = -\frac{\epsilon_y}{\epsilon_z} \tag{3.13}$$

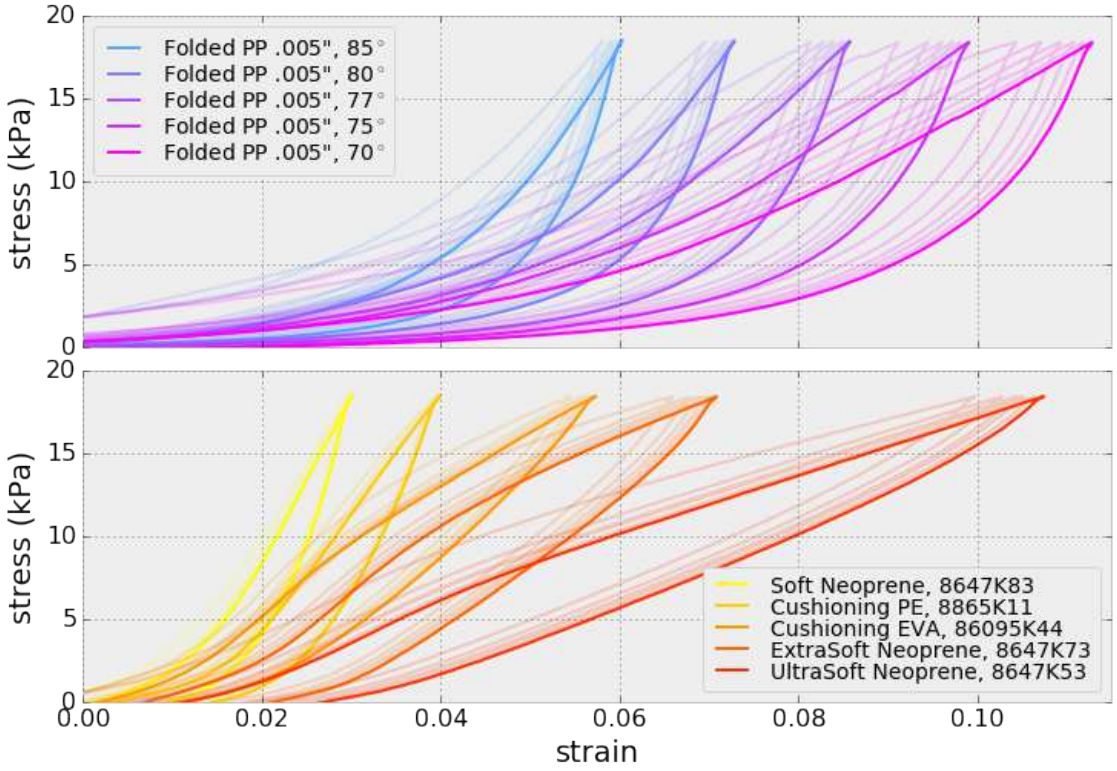

Figure 3.7: Loading curves of Tachi-Miura polyhedra compared with those of engineering foams

These values are shown in Figure 3.5. We see that the Poisson ratio depends on the choice of α, but it is independent of d and N. Further, for many choices of α and over much of the folding range, ν_{xz} is approximately zero, while ν_{yz} is very sensitive to α over this same range. This dependence between ν_{yz} and α forms the basis of the stiffness control developed in this chapter. While in this mathematical model the Tachi-Miura honeycomb is free to contract laterally when compressed vertically, in physical prototypes boundary conditions prevent this. This tension between boundary conditions and the preferred mechanism of the honeycomb cause elastic energy to be stored in deformations of the honeycomb facets. This effectively turns the entire structure into a spring. As the relative amplitude of the lateral contraction with respect to vertical compression is given by ν_{yz}, changing this Poisson ratio changes the effective stiffness of the spring. In the next section, we investigate this behavior.

3.3 Elastic behavior testing

The behavior of Tachi-Miura honeycombs under realistic boundary conditions is a combination of the rigid mechanism analyzed above and elastic deformations of the underlying material. A nonzero Poisson ratio means that fixed or frictional boundary conditions effectively resist the structure's tendency to follow its rigid mechanism under a compressive load in the z direction [213]. The larger the magnitude of the Poisson ratio, the more lateral movement is required by the rigid mechanism, and hence, the more resistance is offered from the boundary condition. As the average magnitude of the Poisson ratios ν_{xz} and ν_{yz} increases with α, we expect the effective

stiffness of Tachi-Miura honeycombs subject to fixed or frictional boundary conditions to also increase with α.

To confirm this effect, I performed compression testing of Tachi-Miura honeycombs comparing the results to those of commercially available engineering foams. Using a constant base material and sheet thickness, I prepared samples with varying Miura angles. We stitched these samples to retain the folded state of the strip folds. I applied a load of $100N$ to the samples over their full area of 54 cm^2, cycling the load six times at a rate of 1 mm per minute. I tested commercial foam samples of several materials having similar density to the pleated honeycomb samples with the same test parameters. The results (graphed in Figure 3.7) show the the pleated honeycombs span a range of average modulus from roughly 140 to 300 kPa, while the commercial foams range from roughly 170 to 500 kPa.

This shows that by using a single material and simply changing the Miura angle, a similar range of stiffness can be produced as is exhibited by a range of commercial foams. The conventional foams use a variety of materials and process parameters to achieve this range of stiffness. Thus, the reduction of material properties to geometry has the potential to simplify the manufacturing supply chains for products using foam-like materials. Further, foams are commonly made in a heat-induced expansion process, giving no ability to spatially vary material properties. Tachi-Miura honeycombs can be constructed where Miura angle varies from cell to cell, effectively giving the ability to spatially map stiffness. While polyhedra with differing Miura angle are not strictly tileable, similar methods as outlined above can work in practice to produce such honeycombs with only minor gaps between adjacent cells. Quantifying the precise limits to this approach is an active area of future research.

3.4 Shoe sole prototype

Given that Tachi-Miura honeycombs can exhibit similar compliance as commercial foams while filling a prescribed shape, I now use the construction to prototype a running shoe sole. The thermal processes involved in creating a conventional sole are responsible for the majority of the energy required to manufacture an athletic shoe [39], and so creating a sole using only cutting and folding processes is an attractive strategy for embodied energy reduction. Further, athletic soles are conventionally produced in a machined mold, requiring a large number of identical soles to be produced for economic feasibility. Specifying the sole geometry using the fold pattern instead of a mold has the potential to enable customized shoes without this overhead.

Figure 7.2 shows the steps of producing this folded running shoe sole. First, the geometry is digitally designed. In this case, the sole has a thickness of 20mm throughout the heel and tapers to 10mm through the forefoot. The footprint of cells which are populated with Tachi-Miura polyhedra are selected to fit inside the shape of common mens size 10 sole outline. The angle α is $50°$, while the lengths d and s are 2.8mm and 8.8mm, respectively. The top three images at left of Figure 7.2 show the three-dimensional design and the corresponding folding and cutting pattern.

This pattern is sent to a laser-cutter, where the outline and slits are through-cut and the creases are half-cut. The material used is 0.25mm polypropylene, which produces robust creases with this laser processing technique. This sheet is then folded with the aid of 3D printed creasing dies of progressively larger fold angles γ. The flat and folded states are shown in the bottom two

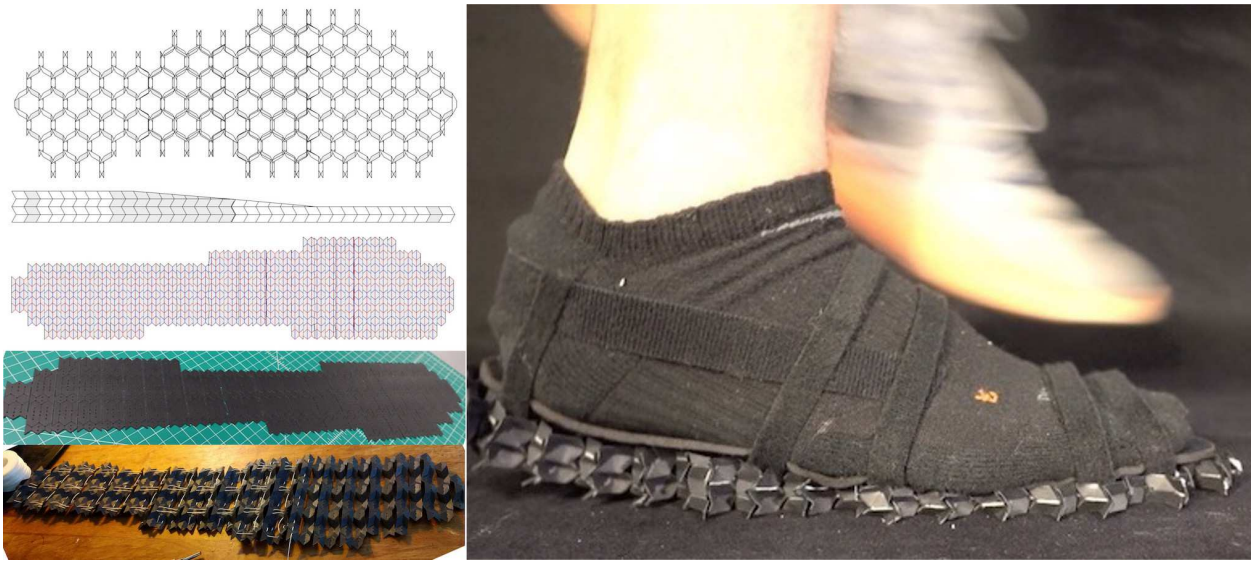

Figure 3.8: A) Plan view of digitally designed geometry for shoe sole, B) Altitude view, C) Cut and fold pattern for shoe sole, D) Laser cut polypropylene prototype, E) After initial folding, F) Testing the shoe sole at running speed.

images at the left of Figure 7.2. Finally, cotton thread is passed through laser cut holes and pulled tight in order to keep the strip folds held closed. The finished shoe is shown in Figure 7.2 at right during a running test.

When loaded by a footstep, the folded shoe sole compresses to levels similar to that of a conventional foam shoe, absorbing the impact of the foot strike. At this point, the forces arising from the Poisson effects and boundary conditions balances the force from the foot, and the Tachi-Miura honeycomb is limited from continuing its flat-folding mechanism. The deformation occurs chiefly at regions of highest force (for example, under the heel and metatarsal heads), effectively conforming to the underfoot shape. With a thin neoprene sock liner, the result was comfortable for a range of test athletes.

3.5 Automating folding

Efficiently automating the folding of Tachi-Miura honeycombs presents many of the same challenges as other origami patterns due to the bi-axial contraction of the sheet during folding. A comprehensive literature review of bending operations using in manufacturing such doubly corrugated sheets is given in [163], where the methods are roughly divided into synchronous processes, gradual processes, and pre-gathered process. The synchronous processes work in batch with low production rates with high tooling costs for each pattern, while the pre-gathered processes require more material deformation than is desirable to reach the final shape. The gradual processes occupy an interesting place between these two extremes, where folding takes place incrementally, minimizing the chances of drawing or tearing the material.

Patterned rollers are often used in these gradual processes [56]. The need for many rollers with incrementally deepening patterns is often prohibitive, and the interlocking patterns can often suffer from tooth interference if made with too small a diameter. Flat dies with incrementally deepening patterns are also used, but they can produce misalignment of the media as it contracts

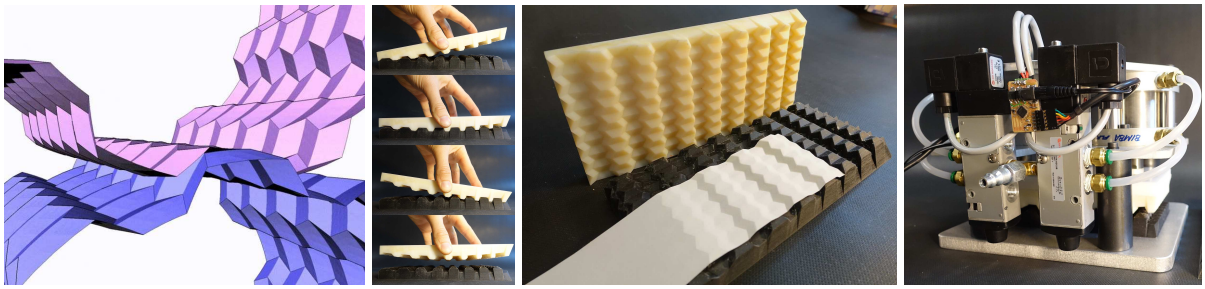

Figure 3.9: A) Tachi-Miura corrugation roller concept, B) Incremental forming die for automated folding of creases using corrugation roller sections, C) Incremental forming of paper with Tachi-Miura pattern, D) Pneumatic press prototype for incremental forming.

into the form, pulling towards wherever frictional forces are highest. In Figure 3.9, I show a combination approach, using two patterned plates with a small curvature. These plates can be thought of as sections of a patterned roller with very large diameter. As the curved plates rock over each other, the media is patterned, deterministically contracting to the single line of contact between the plates. Afterwards, the plates are separated, the media is advanced by one pattern row, and the next iteration deepens the forming pattern. I prototyped a pneumatically actuated press with electronic control of the rocking motion. This prototype proved the viability of the approach, but more development was necessary to increase throughput and reliability.

3.6 Conclusions

This chapter showed how existing techniques for producing shaped hexagonal-celled honeycombs can be adapted to produce shaped honeycombs with Tachi-Miura polyhedra as cells. The bi-directional flat folding mechanism of the Tachi-Miura polyhedron endows the resulting honeycombs with the same flat foldings. In physical prototypes, finite-thickness materials and boundary conditions turn this flat folding into an elastic mechanism, a powerful tool for building robust structures with compliance.

Motivated by this, I investigated the mechanical properties of Tachi-Miura honeycombs, first calculating the rigid Poisson ratios. Next, I compared the mechanical behavior of the structures to common engineering foams, showing it is possible to create a similar range of compliance by changing the angle α. Finally, I use these findings to design a prototype making use of both the compliance and the shape control: a running shoe sole.

This work shows how many foams used in engineering can be replaced by architected materials. Rather than relying on the stochastic structural properties generated through the chemical or physical blowing process, geometry can be explicitly designed at the cellular level with desired performance in mind. Further, the complex and often toxic supply chains required for foam production can be simplified, instead using a single recyclable sheet stock to synthesize required mechanical responses.

Chapter 4

Resilience

In this chapter, I work to maximize the resilience of an architected material, or its ability to return energy in an impact event. That is, I build folded architected materials with high modulus of resilience, storing the maximum amount of strain energy without plastically deforming. To this end, I develop a design method for architected materials with curved creases, a composite manufacturing technique to fabricate them, and dynamic impact test equipment to evaluate them, showing resilience approaching that of state-of-the-art polymer foams.

Graphically, the modulus of resilience is equivalent to the area of the hysteresis curve in a stress-strain plot subject to cycling loading. For a classical elastic material, the modulus of resilience is defined as $R = \sigma_y^2/(2E)$ where σ_y is yield strength and E is elastic modulus. Because σ_y and E usually scale directly, creating materials with high σ_y and low E is difficult [54] and amounts to filling an unoccupied region material parameter space. The creation of material properties not naturally occurring is a well-suited problem for architected materials, but prior work on this particular problem is sparse. Multi-scale hierarchy has been suggested as key to high resilience [132], but the metric evaluated was geometric recovery of initial dimensions, not actually resilience. In that study, despite loading at strain rates of only $10^{-3}s^{-1}$, the stress-strain plots have large hysteresis loops and show a great reduction in stiffness between loading cycles. Elastic energy storage in monolithic folded sheets has been investigated as a material selection problem [187], but this work focused on storing energy in hinges instead of the facets and was restricted to one geometry and used a single material for both facets and hinges.

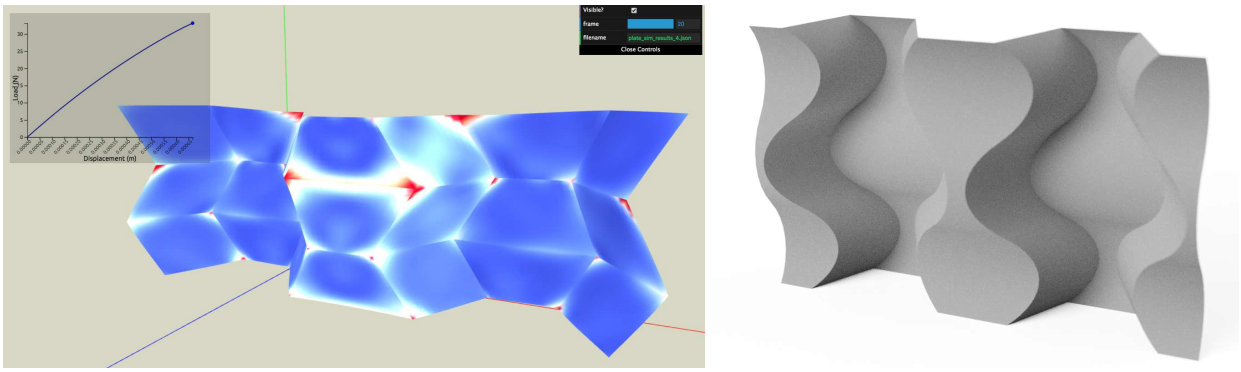

Figure 4.1: a) Vertically loaded Tachi-Miura honeycomb with strain density visualized (simulation details in Chapter B), b) A curved crease equivalent geometry

We start our work on this problem by noting that the Tachi-Miura polyhedral cells of Chapter 3 offer comparable resilience as the engineering foams tested for stiffness (shown in Figure 3.7), but fall far short of state-of-the-art foams designed for maximum energy return. If we examine sources of energy lost in compressive loading of these Tachi-Miura polyhedra, we can see a major source is plastic deformation concentrated at the vertices. Figure 4.1a shows a simulation of a vertically loaded Tachi-Miura polyhedron section, where strain density is visualized. Details of this simulation are available in Appendix B. This simulation shows stress concentrations at the vertices and near zero stress over most of rest of the material. In other words, most of the material does not contribute to the stiffness, and that which does contribute is strained past its plastic onset. A more efficient spring can be made by spreading out this strain density, allowing more of the material to participate and store energy.

To do this, we can convert the faceted Tachi-Miura polyhedron to use curved creases, shown in Figure 4.1b. The advantages of this are two-fold. First, the high strain density regions described above are effectively spread over a larger area, lowering the local material strain. Second, the flat panels of the faceted Tachi-Miura polyhedron are replaced with curved panels, allowing strain energy to be efficiently stored in a bending mode. While the mechanics of curved crease origami are far from fully understood [47, 48], we show in Section 4.1 that the required geometry can be created under a set of simplifying assumptions, allowing effective analysis and design.

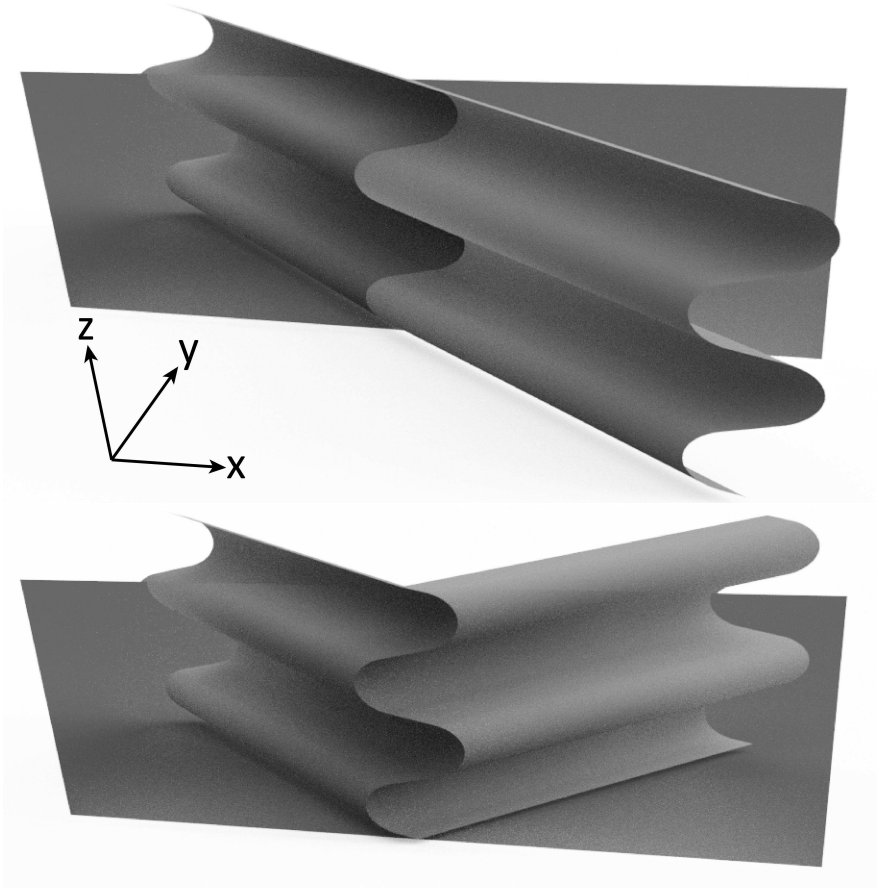

Figure 4.2: curved crease by reflection

4.1 Curved creases of reflection

In this section[1], we consider those curved creases which can be formed by a geometric reflection, shown in Figure 4.2. At top, we see a simply deformed sheet with no creases. We can reflect part of this sheet about a plane to form a curved crease of reflection, as shown at bottom. Due to the symmetry involved, this new surface with creases can be folded from a flat sheet [135]. This creates a continuous analog of a straight crease origami mechanism: the shape of the sheet's cross section is now linked to the angle it makes with the reflection plane. To effectively use such curved crease constructions in folded architected materials, we must derive relationships between their three-dimensional configurations and their two-dimensional patterns, effectively calculating their folding mechanisms.

We begin with some background and notation. All developable surfaces in three dimensions (i.e., those where every point p has a neighborhood isometric to a region in the plane), such as those created by bending sheets, are ruled. That is, through every point on the surface there is a line segment which lies in the surface. In curved crease folding patterns, these rule lines can be considered to define an infinitesimal grid of straight line folds. A curved crease pattern is said

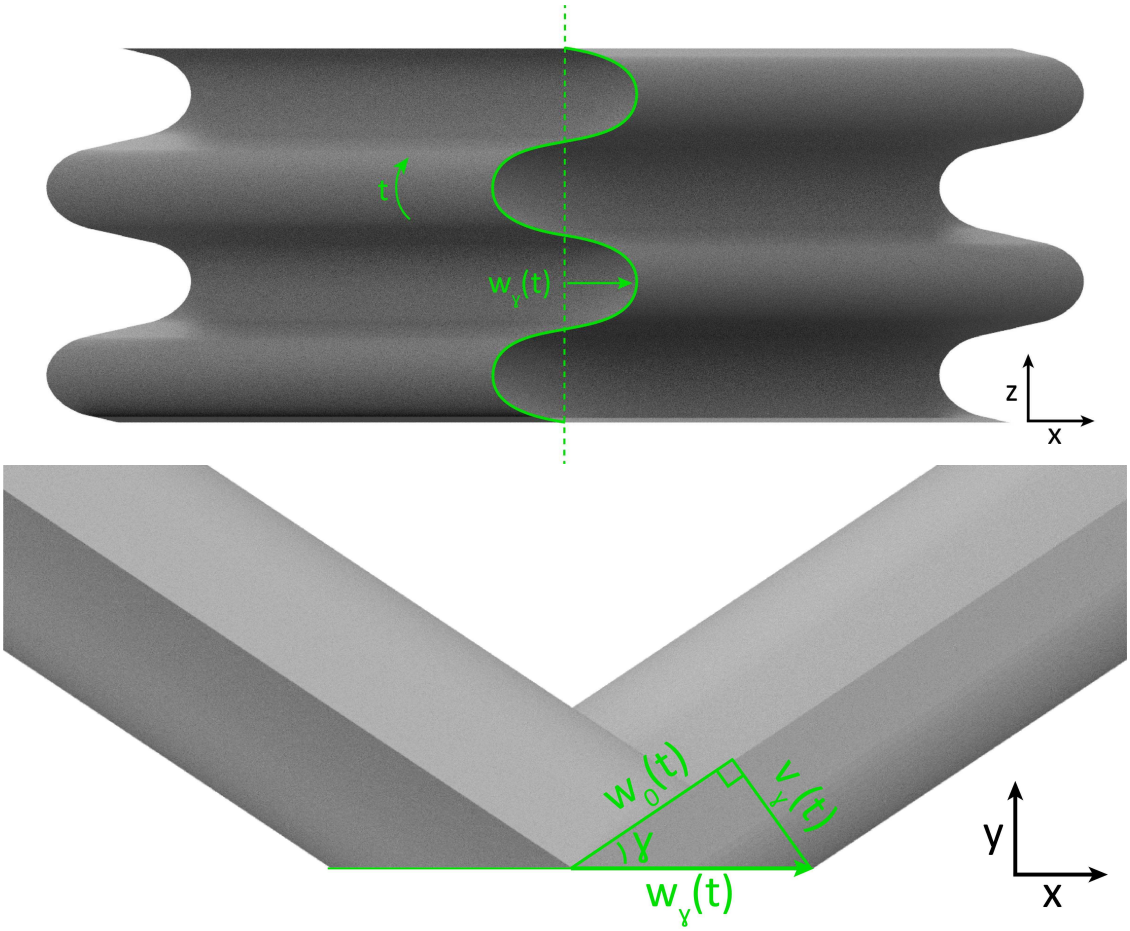

Figure 4.3: Defining t, w_γ, and v_γ.

[1]The work in this section comes from a collaboration with Tomohiro Tachi.

to be rigidly foldable if the ruling (collection of rule lines) does not move on the surface during a folding motion [47, 48]. This definition derives from the pattern being the infinite limit of a finite discretization which folds via rigid panels. These patterns are of interest because they can be realized in stiff physical materials without incurring damage [177].

The constructions considered in this section have curved faces where all rule lines are parallel to each other. For such geometries, the plane of reflection shown in Figure 4.2 is the *osculating plane* of the crease curve, as it is spanned by the curve's tangent and normal vectors. We define the fold angle γ of a crease (shown in Figure 4.3b) as the angle between all the rule lines of an incident face and the osculating plane. Note that this is an equivalent definition to Chapter 3. We establish a right-hand Cartesian coordinate system where the $x-z$ plane is the osculating plane, and y points in the direction of folding. We parameterize the surface of the incident faces using an arc-length variable t measured along a curve perpendicular to the ruling.

At every point in the folding mechanism (which has a corresponding value for γ), we define $w_\gamma(t)$ to be the x coordinate of the curved crease (shown in Figure 4.3a). When $\gamma = 0$, the sheet is flat, and so the curve $(w_0(t), t)$ defines the two-dimensional geometry of the crease. Because the folding motion is an isometry, we have the right triangle shown in Figure 4.3b, and so

$$w_\gamma(t) = \frac{w_0(t)}{\cos\gamma} \tag{4.1}$$

We define the remaining side of this right triangle to be $v_\gamma(t)$, and so

$$v_\gamma(t) = w_\gamma(t)\sin\gamma = w_0(t)\tan\gamma \tag{4.2}$$

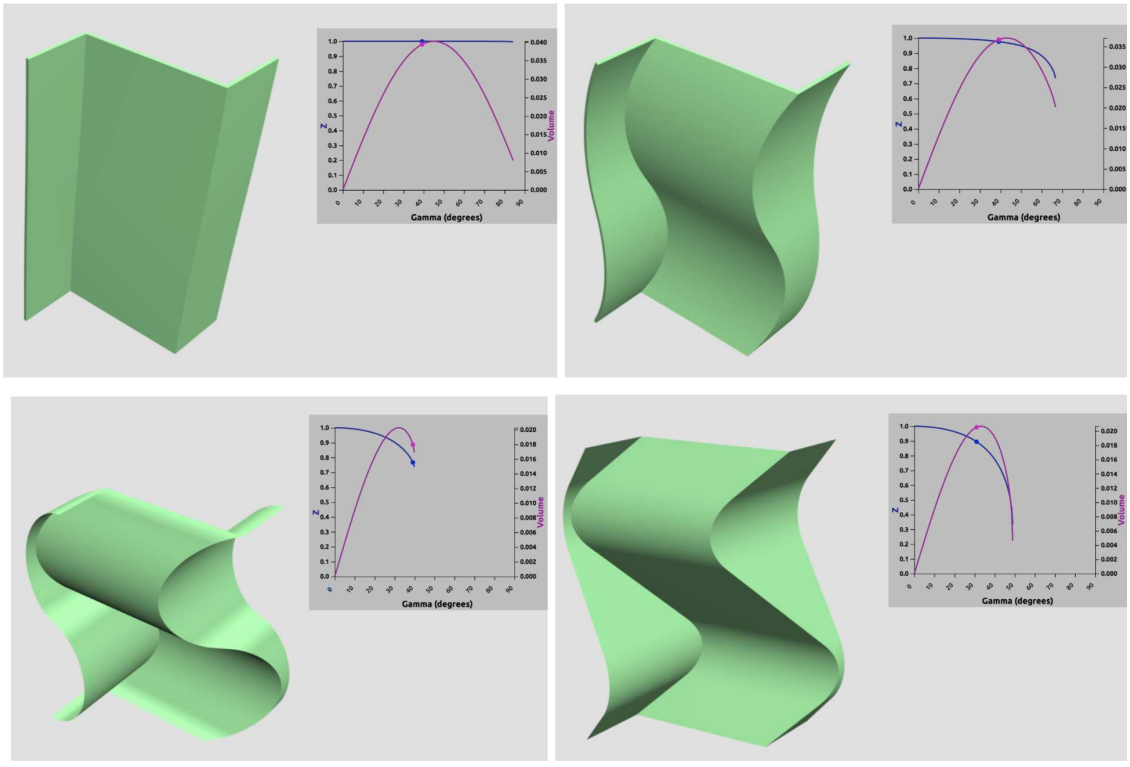

Figure 4.4: Javascript design tool for calculating two- and three-dimensional geometries.

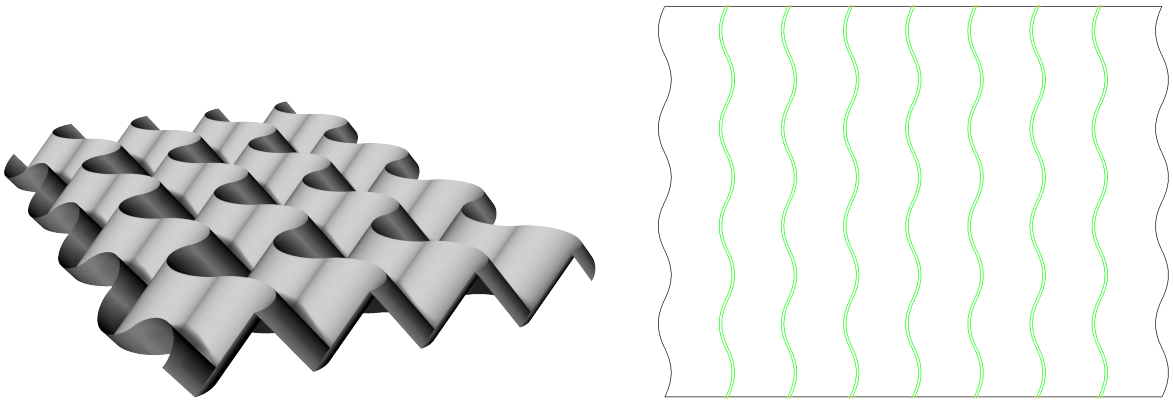

Figure 4.5: Inverting a cylinder: a) Folded architected material with cylindrical sections, b) Corresponding flat pattern with sinusoidal creases

We seek a function $z(t)$, which is the z coordinate of the surface, parameterized by the arc length variable t. Because t measures along a path perpendicular to the ruling, we have the infinitesimal relation

$$dz^2 + dv_\gamma^2 = dt^2 \tag{4.3}$$

Therefore, we have an ordinary differential equation:

$$\frac{dz}{dt} = \sqrt{1 - \left(\frac{dv_\gamma}{dt}\right)^2} = \sqrt{1 - \tan^2\gamma \left(\frac{dw_0}{dt}\right)^2} \tag{4.4}$$

This ordinary differential equation can be numerically solved to calculate $z(t)$ from $w_0(t)$. That is, it allows the three dimensional geometry to be calculated from the two dimensional geometry. This is illustrated in Figure 4.4, where three-dimensional geometry is calculated for a variety of curves w_0 and fold angles γ. In this case, I used a bi-arc parameterization for the curves (i.e., sequences of consecutively tangent line and arc segments), which is both easy to calculate function and derivative values and also conveniently interpolates between the faceted Tachi-Miura polyhedra of Chapter 3 and their curved crease analogs.

We often wish instead to decompose desired three-dimensional geometry for architected materials into flat patterns which can be efficiently manufactured. In this case, we can invert the differential equation:

$$\frac{dw_0}{dt} = \frac{1}{\tan\gamma}\sqrt{1 - \left(\frac{dz}{dt}\right)^2} \tag{4.5}$$

Similarly, this equation is easy to solve numerically to calculate the required crease pattern. In some cases, it can even be analytically solved. For instance (as shown in Figure 4.5), a folded architected material composed of panels with semi-circular normal cross section requires crease curve shapes given by sinusoidal curves. For maximizing resilience of a folded architected material, however, there are better section shapes to choose. In the next section, we derive a curve shape based on solid mechanics considerations.

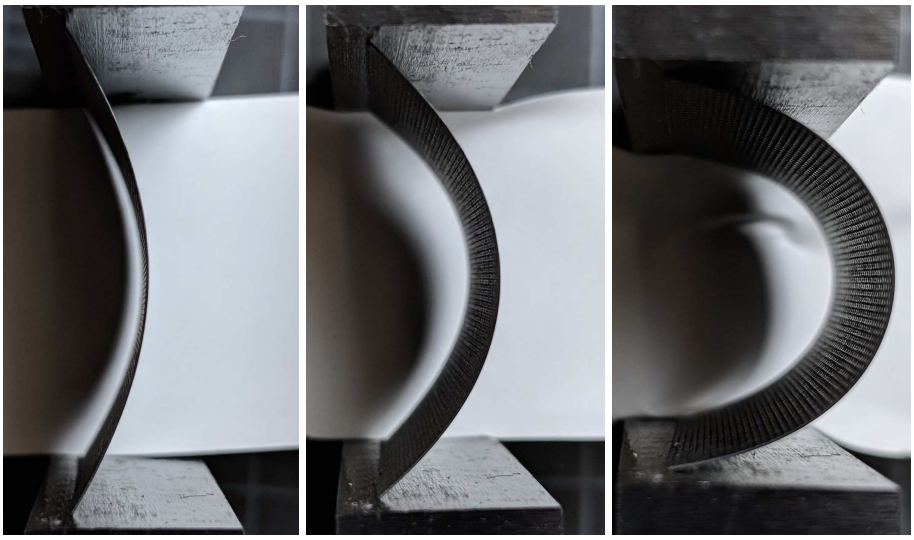

Figure 4.6: Elastic member under progressively larger end loading, demonstrating the elastica curve.

4.2 Elastica curves

In the previous section, we calculated the folding mechanics of a class of curved crease constructions with the goal of storing strain energy throughout the material. In an architected material with curved creases, this strain energy is stored in the bending of the incident panels. If the bending shape prescribed by the crease differs too much from the minimum energy shape of the bent panel, however, the creases themselves can experience significant stress concentration. To avoid this, we now calculate the minimum energy shape of the panels.

As the flexural modulus of the panels is approximately constant, we can approximate the two-dimensional surface by a one-dimensional member. The shape taken by a one-dimensional elastic member subject to end loading is a classic problem from the calculus of variations, originally solved by Euler [113]. The resulting shapes are called *elastica* curves; several are shown in Figure 4.6, as a thin elastic member is subject to increasing end loading.

We can calculate the shapes taken by this member in the same coordinate system as above, adapting the analysis of [186]. We start with the exact differential equation of an elastic curve, which states that the bending moment at all points in the member equals the flexural rigidity times the curvature:

$$EI\frac{d\theta}{dt} = -Pz \tag{4.6}$$

where E is the elastic modulus, I is the second area moment of inertia, and P is the loading force. In this derivation, the angular variable θ is more convenient to work with, but since $\sin\theta = \frac{dz}{dt}$, we can convert to Cartesian coordinates when necessary. Thus,

$$EI\frac{d^2\theta}{dt^2} = -P\sin\theta \tag{4.7}$$

It is worth noting this is the same differential equation as a dynamic pendulum, where the variable t is taken as time. This is called Kirchoff's dynamical analogy. If we set $k^2 = P/EI$, multiply

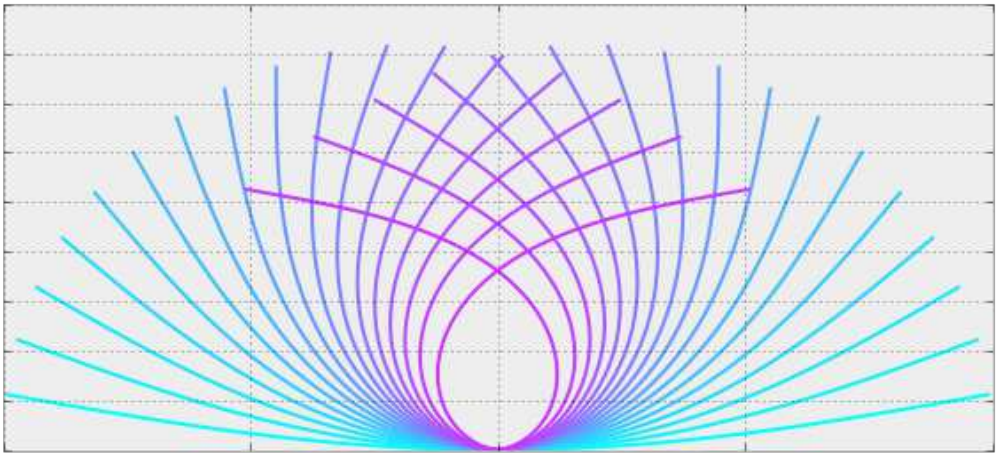

Figure 4.7: a) Plotting a family of elastica curves for various tip angles θ_0

both sides by $d\theta$ and integrate, we have:

$$\int \frac{d^2\theta}{dt^2}\frac{d\theta}{dt}dt = -k^2 \int \sin\theta d\theta \tag{4.8}$$

By undoing the chain rule, this is the same as

$$\frac{1}{2}\int \frac{d}{dt}\left(\frac{d\theta}{dt}\right)^2 dt = -k^2 \int \sin\theta d\theta \tag{4.9}$$

and so

$$\frac{1}{2}\left(\frac{d\theta}{dt}\right)^2 = k^2\cos\theta + C \tag{4.10}$$

where C is a constant of integration. We know that the bending moment at $t = 0$ (the end of the bent member) is zero, so $d\theta/dt|_{t=0} = 0$. Hence, $C = -k^2\cos\theta_0$, where $\theta_0 = \theta(0)$. Taking the negative root without loss of generality,

$$\frac{d\theta}{ds} = -k\sqrt{2(\cos\theta - \cos\theta_0)} \tag{4.11}$$

This is now a first order nonlinear ordinary differential equation, which can be easily solved numerically, or computed exactly in terms of elliptic integrals. In Figure 4.7a, we show a family of elastica curves with various values for θ_0, the tip angle.

As $\sin\theta = \frac{dz}{dt}$, we can use this differential equation to calculate the required crease curves so the incident panels take on an elastica shape about an operating angle γ. This equation also allows us to calculate the stiffness of an architected material made this way, by relating the load carried by the elastic member to the tip angle θ_0. For this, we note that the length l of the member must satisfy

$$l = \int_0^l ds = \int_0^{\theta_0} \frac{d\theta}{k\sqrt{2(\cos\theta - \cos\theta_0)}} = \frac{1}{2k}\int_0^{\theta_0} \frac{d\theta}{\sqrt{\sin^2\frac{\theta_0}{2} - \sin^2\frac{\theta}{2}}} \tag{4.12}$$

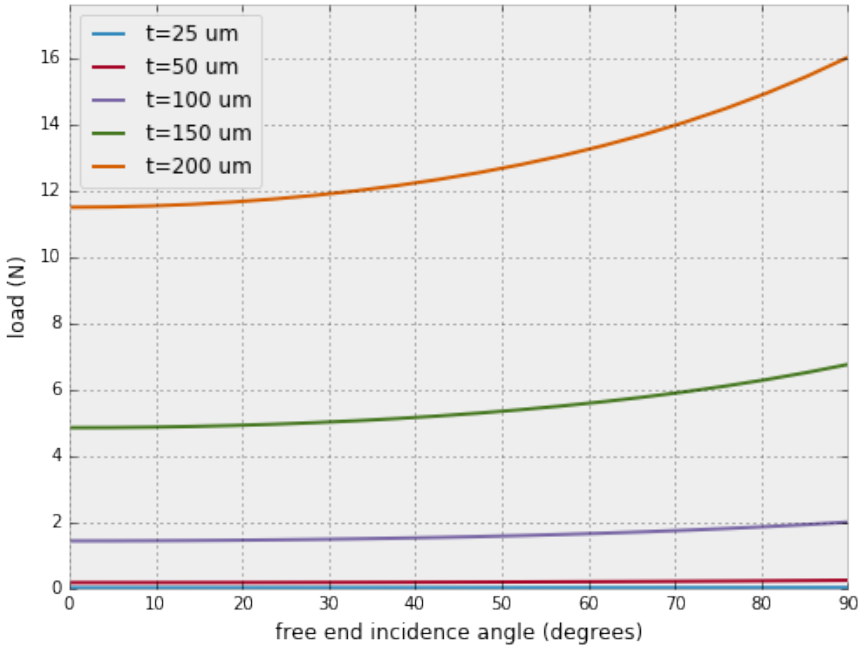

Figure 4.8: Elastica load as a function of tip angle for various member thicknesses

That is,

$$l = \frac{1}{k} K(\sin(\theta_0/2)) \tag{4.13}$$

where K is the complete elliptic integral of the first kind. Substituting the definition of k, we have an expression for the supported load:

$$P(\theta_0) = \frac{EI}{l^2} K(\sin(\theta_0/2))^2 \tag{4.14}$$

In Figure 4.8 we plot the load as a function of the free end incidence angle (θ_0) for a piece of carbon fiber reinforced polymer of various thicknesses. We see that such elastic members operate as nearly constant force springs. These curves approach a fixed value as $\theta_0 \to 0$, that is, as the elastic member straightens. This value at $\theta_0 = 0$ is the Euler buckling load of the member. As $K(0) = \pi/2$, we have derived the familiar equation for this quantity:

$$P_0 = \frac{\pi^2 EI}{4l^2} \tag{4.15}$$

In this section, we have derived expressions for calculating the crease curve shapes necessary for elastica-shaped panels, as well as for the forces experienced by these panels. In the next section, we develop a composite lamination technique for making high performance architected materials which implement these calculations.

4.3 Composite lamination process

We now develop a composite lamination technique to implement elastica-shaped folded architected materials using high performance materials, namely carbon fiber reinforced polymer. For a

Figure 4.9: a) Cutting prepreg with an oscillating knife to form hinge lines, b) Cured prepreg between polymer sheets, c) Optically registering and cutting of additional features in the cured laminate

fiber-reinforced laminate to have reasonably isotropic properties, several plies with different fiber orientation must be combined. Overall thickness can accumulate quickly, limiting the curved crease folding mechanism. Because of this, we make use of very thin carbon plies, the production of which is a surprisingly active area of recent research. The challenge of producing such plies comes in spreading the carbon fiber tows (i.e., the bundles of thousands of individual fibers in which carbon is produced) consistently and without damaging the fibers. Generally the tows pass over rollers under the influence of pneumatic or ultrasonic agitation. This gently spreads the fibers, and modern process control can produce consistent webs with average thickness approaching that of a single fiber diameter (roughly 10 μm). The fiber webs are stabilized by impregnating them with resin and applying a paper liner. The result is a very thin *prepreg*, a form commonly used in the composites manufacturing industry. Such thin prepregs have been demonstrated to produce better material properties in the resulting laminates than conventional thicker plies [4].

To use such laminates in folded architected materials, we need a means to produce accurate and robust creases. Fiber reinforced laminates are stiff and brittle, so we create a composite system utilizing a polymer to make compliant hinges, adapting methods from microrobotics [90]. In these methods, laser machining is used to pattern the prepregs to cut away thin strips where a hinge is desired. The patterned prepregs are then sandwiched around a thin polymer film and cured to form a laminate. Instead of using laser machining, we instead use an oscillating driven knife to pattern the prepregs, which is faster than laser machining and operates over larger scales (at the expense of a larger minimum feature size). Hinge cycle lifetimes approaching 10^7 have been shown in microrobotics applications with significant angular deflection, and an exponential relationship between hinge bending length and cycle life has been identified [124]. At larger scales where hinge lengths can be greater and angular deflections can be smaller, significantly

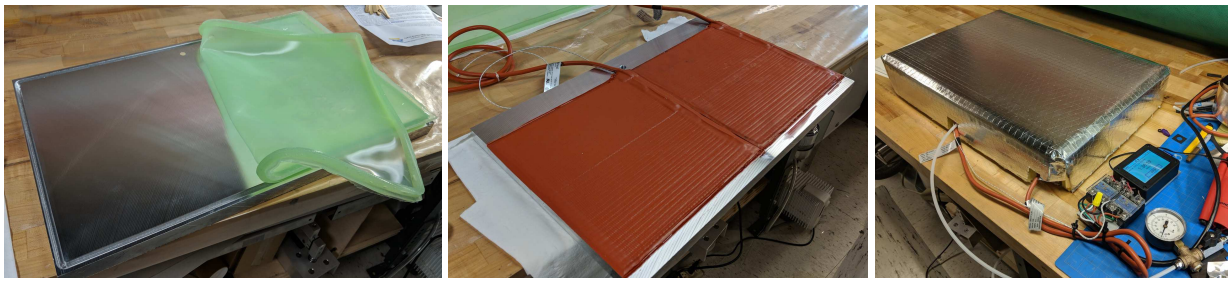

Figure 4.10: Fabrication of programmable heated vacuum platen. a) Silicone vacuum bag, b) Pad heaters on underside of vacuum platen, c) Fiberglass insulation shell with vacuum plumbed and temperature controller.

Figure 4.11: Making carbon-polymer curved crease architected materials a) Cured laminate with patterned hinges, b) Laminate cut into strips, c) Strips folded in frames, d) Strips assembled and bonded into volume.

increased lifetimes are expected and indefinite operation may be attained by staying below the material fatigue limit.

In microrobotics applications, the polymer layer is usually sandwiched between two layers of fiber reinforcement to minimize its required bending radius. In larger scale applications with wider hinges, a single layer of fiber reinforcement can be sandwiched by two polymer layers. The wider hinge maintains safe polymer bending radii, and placing the continuous polymer layers outside of the fiber reinforcement layer makes the resulting structure more robust to delamination. As resin-impregnated carbon fiber sheets are usually available in substantially thicker dimensions than polymers like PET, this layer inversion allows for thinner resulting laminates. Finally, when a polymer is sandwiched by two fiber layers that have been precisely machined, performance is sensitive to alignment of these layers. With a single machined fiber layer, no alignment is necessary, simplifying the fabrication process.

This process is illustrated in Figure 4.9. First, five plies of 15 g/m^2 prepreg (North Thin Ply Technology TP402) are layered in a 0°-90°-0°-90°-0° layup schedule, for a combined thickness of approximately 60 μm. This assembly is sandwiched between paper liner sheets to stabilize the fibers and the hinges are cut away using a Zünd Systemtechnik large format cutter with an oscillating knife tool. Additional optical registration features are also cut into the prepreg. The paper liners are removed and the patterned prepreg is sanwiched between two sheets of 12 μm PET or polyimide film and thermally cured under vacuum compaction. The cured sheets are then optically registered on the Zünd cutter and the desired parts are cut out.

To consistently cure these laminates, I built a programmable heated vacuum platen, shown

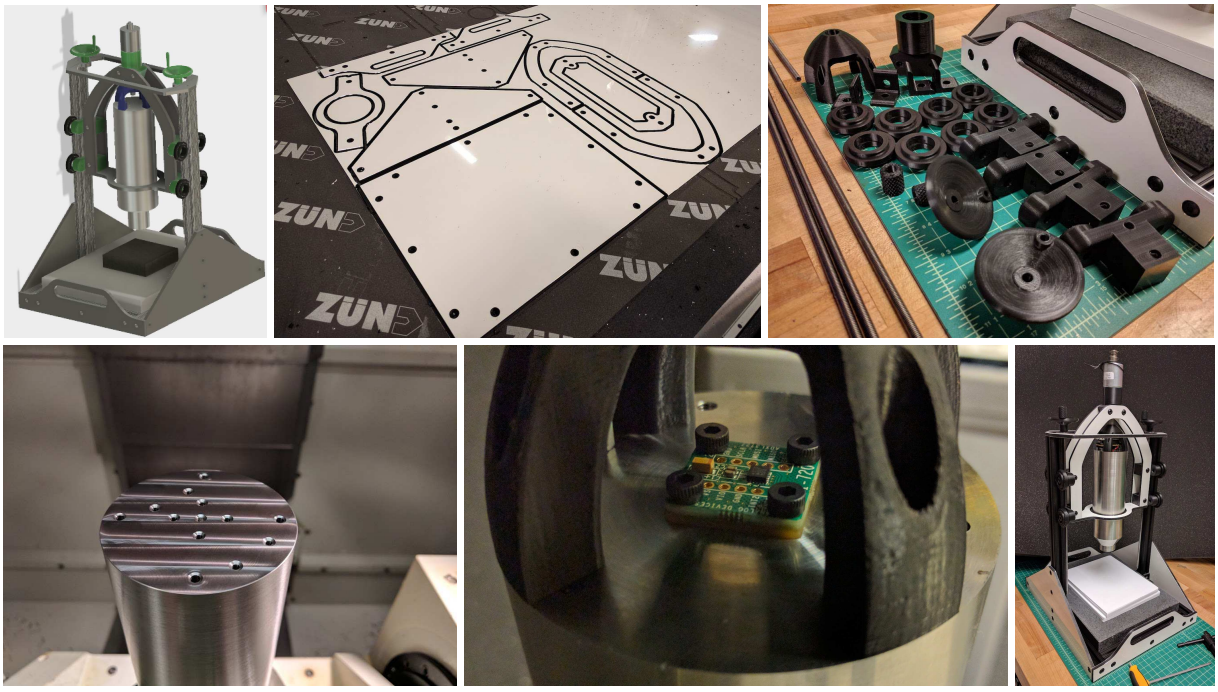

Figure 4.12: Dynamic impact test apparatus: a) CAD, showing test mass and frame for adjusting release height. b) Routed aluminum-polyethylene composite for machine frame, c) 3D printed parts for vertical rails, release mechanism, and hand wheels, d) Machining the test mass for mounting electronics and release mechanism, e) ADXL372 accelerometer mounted on test mass, f) Assembled test apparatus.

in Figure 4.10. I first routed a channel around the edges of an aluminum plate, and applied a brush-on silicone rubber (Smooth-On EZ-Brush Vac Bag Silicone) to form a reusable vacuum bag with a sealed bead in the channel. A pair of 360W silicone pad heaters were then bonded to the back side of the aluminum plate and the entire assembly was enclosed with rigid fiberglass insulation panels. A vacuum line was plumbed into the plate, and a thermocouple and temperature controller (Controleo3) added.

This composite lamination technique and equipment was used to make folded architected materials, as shown in Figure 4.11. A carbon-polymer composite sheet is patterned with hinges as described above, and then cut into strips. The strips are folded according to the curved crease folding motion and temporarily retained using laser-cut frames. These folded strips are bonded using Dow Corning 734 flowable RTV silicone, using the laser-cut frames for alignment. After removing the frames, the resulting honeycombs stay in their curved state, producing a volume with elastic energy stored in bent fiber-reinforced facets.

4.4 Dynamic test equipment

To evaluate the resilience of these folded architected materials, I developed a dynamic impact test apparatus. This consists of a known mass, released from a known distance above the sample, instrumented with a high speed accelerometer to record the impact dynamics. This apparatus is shown in Figure 4.12. The test mass (of approximately 8 kg) is positioned by a vertical linear axis for adjusting the release height. A solenoid actuator is used to press a quick-release mechanism

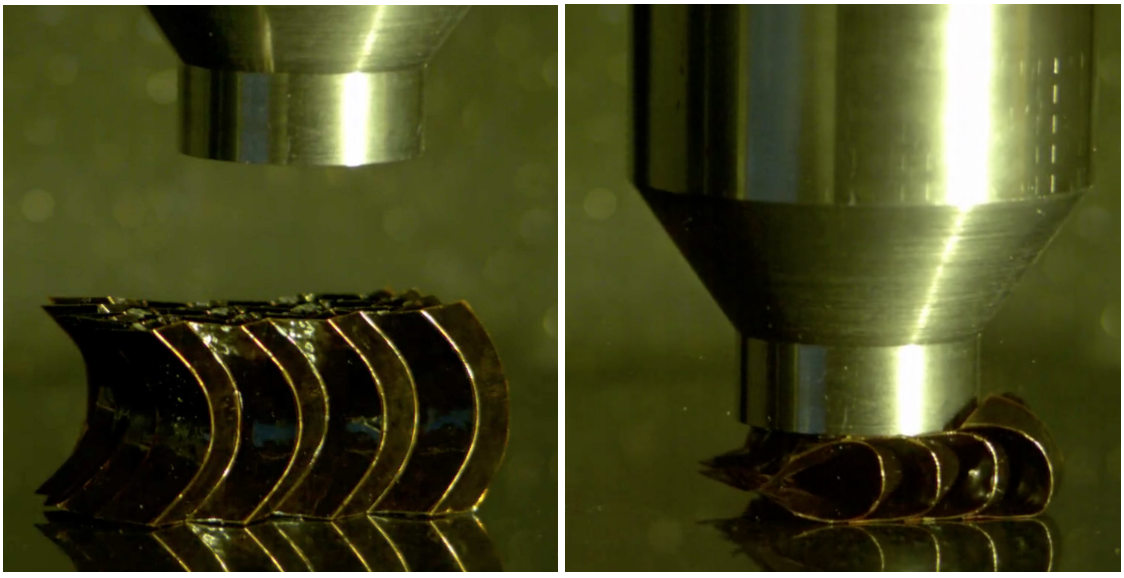

Figure 4.13: Testing the resilience of carbon-polymer elastica architected materials: a) Test mass approaching, b) Point of maximal compression.

on the frame, which releases a bushing on the test mass. A granite tile forms an underlay for the tests, its high density acting to null the effects of outside factors (e.g., the response of the table on which the testing is performed). The test mass is instrumented with an ADXL372 MEMS accelerometer, capable of measuring $\pm 200g$ of acceleration in 3 axes with a bandwidth of 3.2 kHz. The accelerometer is controlled by an ATSAMD21 ARM Cortex M0 processor using an SPI interface, and data is written to an SD card for later analysis.

4.5 Testing and Comparison

With this infrastructure in place, I tested the resilience of the carbon-polymer elastica architected materials. I prepared two samples with elastica tip angles of $45°$ and $55°$. To compare the resilience of these samples with other foams, I also tested an array of commonly used footwear foams which are designed for high energy return. The test mass was released from a height of $\frac{1}{2g} \approx 51mm$ above the samples, so as to impact with a velocity of 1 m/s (correponding to an impact energy of $8J$). Figure 4.13 shows two frames from high speed video of the elastica samples being tested. The left image shows the test mass approaching, while the right image shows the point of maximal compression.

In Figure 4.14, acceleration of the test mass is plotted versus time. For clarity, the acceleration values are normalized by the peak value during the first impact. The times of first impact are synchronized across all samples, so we can measure resilience by the time between the first and second bounces. That is, a second peak further right implies a higher energy return.

The carbon-polymer elastica architected materials samples are shown in greens. We see that these samples surpass a range of foams advertised to be “cushioning" and “resilient" (shown in blues), approaching the resilience of state-of-the-art blown phylon foams (shown in reds).

To check these results, we compare the energy returned as calculated by integrating the acceleration over an impact event (to produce a change in velocity, and in turn kinetic energy),

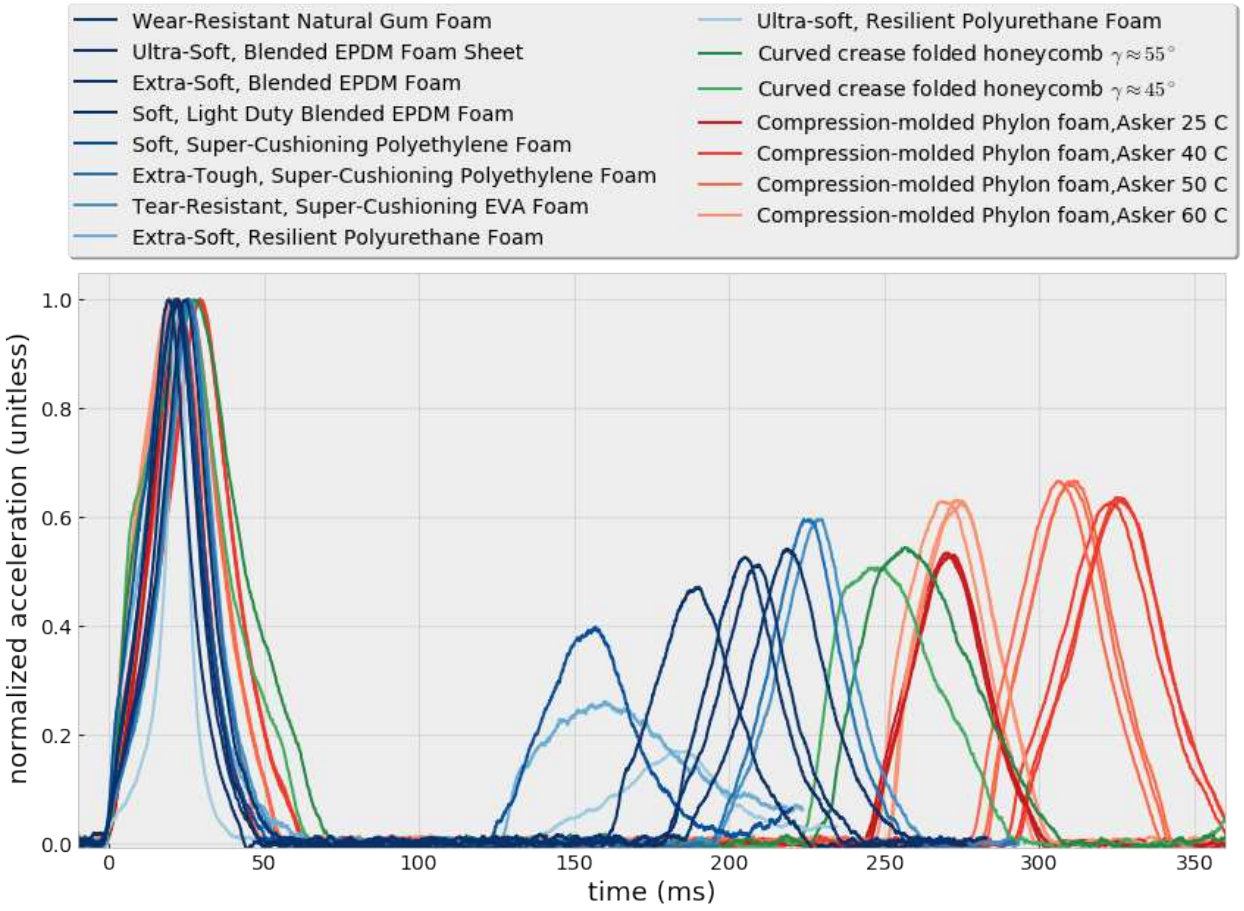

Figure 4.14: Graph of normalized acceleration of the test mass versus time. Initial impacts are synchronized, so more resilient samples have the second impact later (further right).

compared to measuring the timing between impacts (to produce a flight time, and in turn the peak potential energy of the bounce). In Figure 4.15, we see good agreement between the two methods.

4.6 Conclusions

In this chapter, I built folded architected materials with high modulus of resilience, developing a design method for architected materials with curved creases, a composite manufacturing technique to fabricate them, and dynamic impact test equipment to evaluate them. The composite curved-crease samples showed increased resilience over initial Tachi-Miura samples and conventional engineering foams at strain rates representative of shoe sole compression (roughly $10^1 s^{-1}$). Their performance approached that of state-of-the-art blown phylon foams, which are the result of decades-long development efforts by shoe companies. Because this resilience is the result of prescribed geometry, it can easily be spatially varied, something that is very difficult with conventional polymer foams.

These high-resilience origami architected materials can be applied to shoe soles, using the net shape techniques in Chapter 2 to directly control shape while also achieving superior ener-

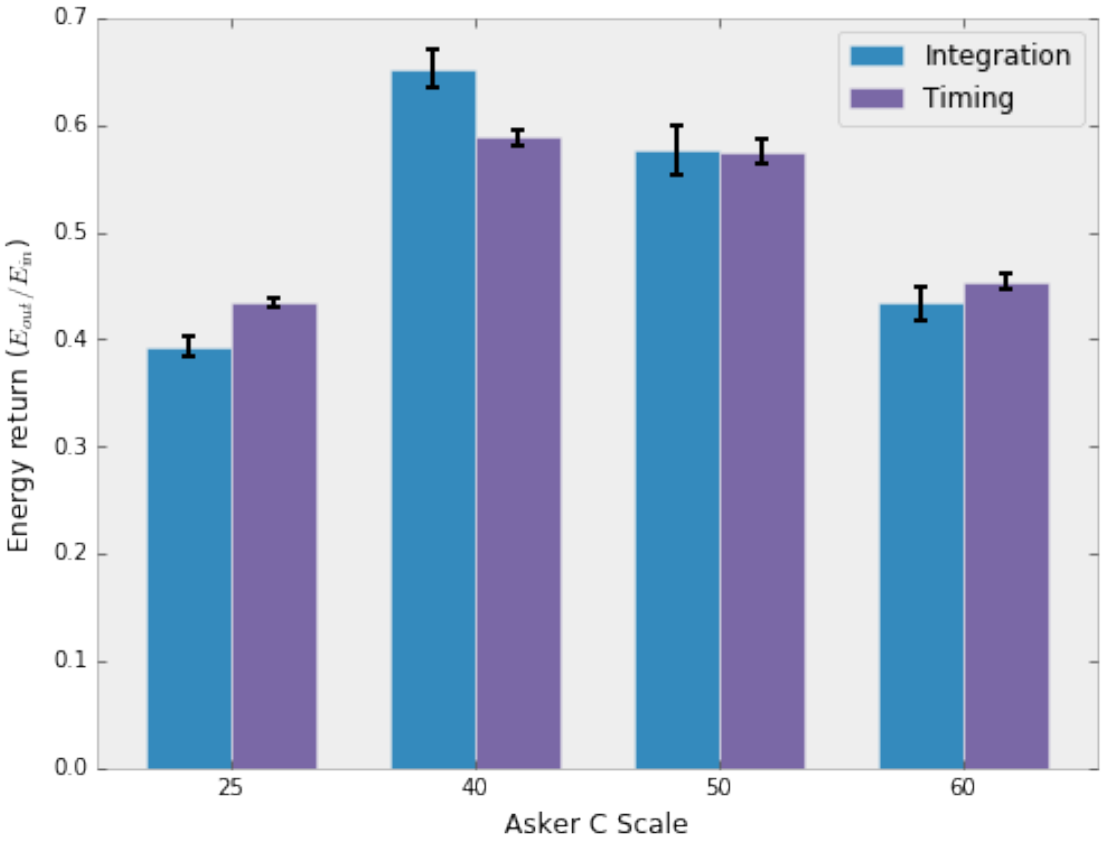

Figure 4.15: Comparing energy return calculated by integration versus timing.

getic performance. Indeed, the most efficient shoe soles made today incorporate large composite springs into a foam to store and release energy [89] (shown in Figure 4.16), though the exact mechanism of biomechanical efficiency increase is complex [14]. Besides shoe soles, other applications could include reusable cushioned packaging, efficient prosthetics and orthotics, and non-pneumatic tires with low rolling-resistance.

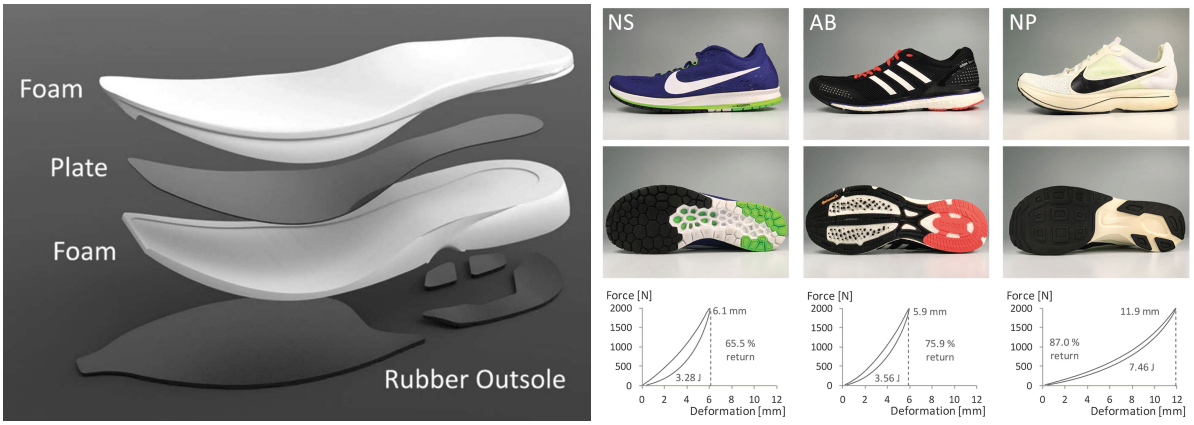

Figure 4.16: Nike's Vaporfly running shoe, which incorporates structural elements to improve energy return over that of foams alone. a) Exploded view, b) Hysteresis curves for several shoes, including the Vaporfly (Images from [89]).

Chapter 5

Toughness

The fourth task of this thesis is maximizing energy absorption per unit mass, the opposite challenge of Chapter 4. In this chapter, I build folded architected materials with high specific modulus of toughness, that is, an area inside the stress-strain hysteresis curve which is large relative to the material mass. To this end, I design and fabricate a hierarchical folded architected material and a machine for its construction, developing an analytical model to predict performance, and show its specific energy absorption to be twice that of commonly used honeycombs.

This problem is much more studied than the reflection problem, as energy absorbing elements have long been used in passenger vehicles to mitigate the damage caused by a crash. These elements transform kinetic energy into plastic deformation or brittle fracture with a bounded reaction force, maximal stroke, and stable failure modes [121]. One of the most famous applications of energy absorbing elements was in the legs of the Apollo landing module where the kinetic energy of touchdown was absorbed by a honeycomb instead of damaging the module or its occupants [45]. These elements worked beautifully but occupied considerable volume and required telescoping elements to control how forces were transmitted from the feet to the energy absorbers. In many applications, like vehicular crashboxes, there is great incentive to eliminate such overhead, as space and mass both come at a high price.

One strategy to make higher performing energy absorbers is to design them around one very specific load case. These elements often use discrete tubes, rings, cones, spheres (even beer cans [205]) which are arranged to absorb energy efficiently in response to force from a specific direction or with a specific distribution. The persistent issue with such absorbers is how sensitive their performance is to deviations from the expected loads or from the prescribed geometry [121, 185]. Small changes in either one can dramatically reduce performance. Stress-concentrating features called *triggers* (for instance chamfers, bevels, grooves, or holes) are often incorporated to stabilize the failure around the desired mode [98], but their effect is limited and they increase manufacturing complexity.

Architected materials like honeycombs and rigid foams are also used as energy absorbers because they tend to be less sensitive to such variations. Unfortunately these structures also tend to have considerably lower specific energy absorption. For example, Figure 5.1 shows section views of thin-walled and thick-walled aluminum honeycombs after being crushed by an impact. We observe in both cases that the honeycomb buckles with a characteristic wavelength. Plastic work takes place at the hinge lines, while the material between contributes very little to the absorption. Thus, decreasing this buckling wavelength would seem to increase the material uti-

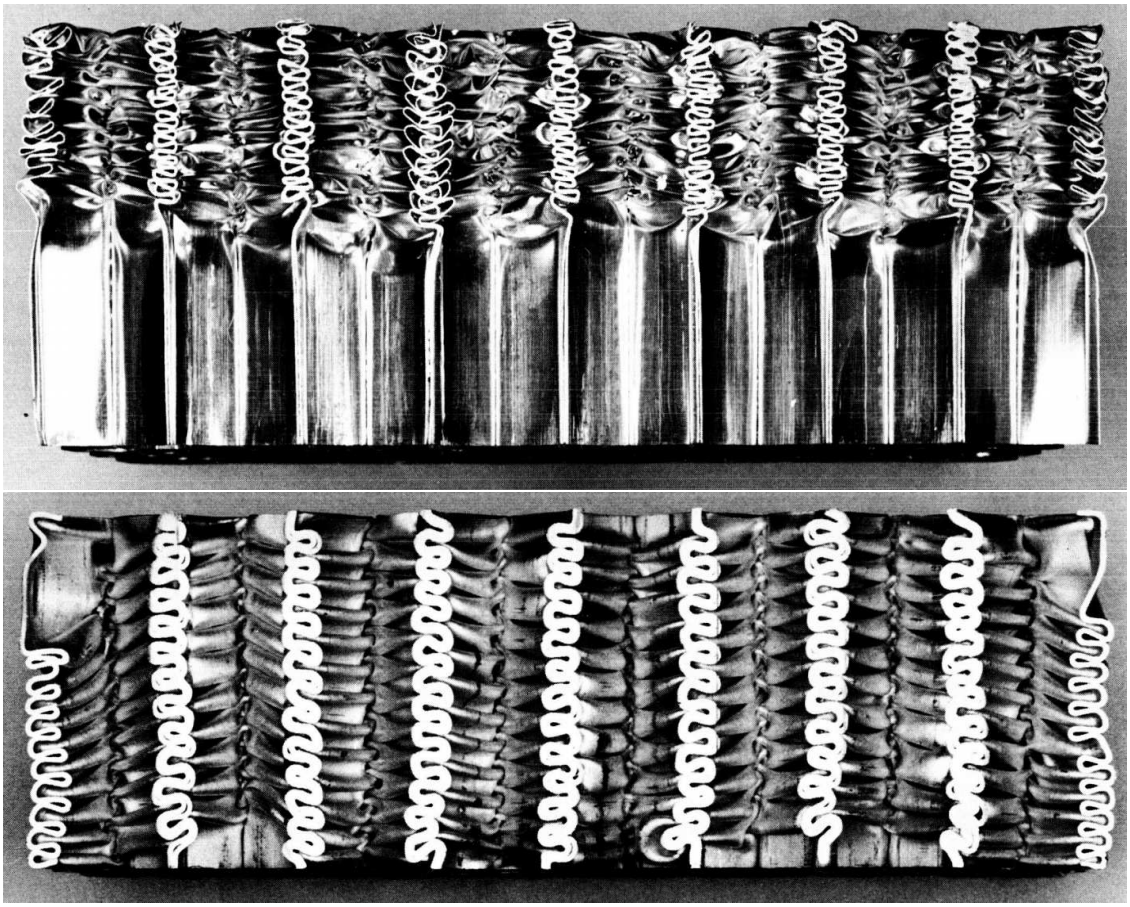

Figure 5.1: Section views after crushing of aluminum honeycombs with thin walls (a) and thick walls (b). (Images from [130])

lization and hence the specific energy absorption. Unfortunately, this wavelength depends on the honeycomb cell geometry [130, 203], and so cannot be changed without changing other features of the honeycomb like the average crushing force or the density. The crushed honeycomb also packs inefficiently, with material stacking up in some places and voids remaining in others. Thus, even if we could create a very small buckling wavelength, the stroke over which energy can be absorbed would become limited, lowering the total absorption.

There has been research from the structural origami community on using folded sheets to make better energy absorbers. Much of this focused on single elements made by folding [116, 117, 68], rather than space-filling architected materials. Of the space-filling approaches, there has been a considerable amount of work [188, 87, 215, 118, 59] on using the Miura-Ori folding pattern and its variants to construct energy absorbing foldcores [64] like those shown in Figure 5.2a. These foldcores can avoid the stackup issue mentioned above, but they usually suffer from an even larger buckling wavelength than honeycombs. Figure 5.2b shows the crushing response of a foldcore, where induced creases are formed near the medial axis, allowing the rest of the material to remain largely unstrained. The resulting stress-strain curve is shown in Figure 5.2c, the integral of which is the energy absorbed per volume. We see the induced creases form an initial peak, but over the rest of the stroke the stress is very low. As a result, the material utilization, and hence specific energy absorption, has generally been low in foldcores.

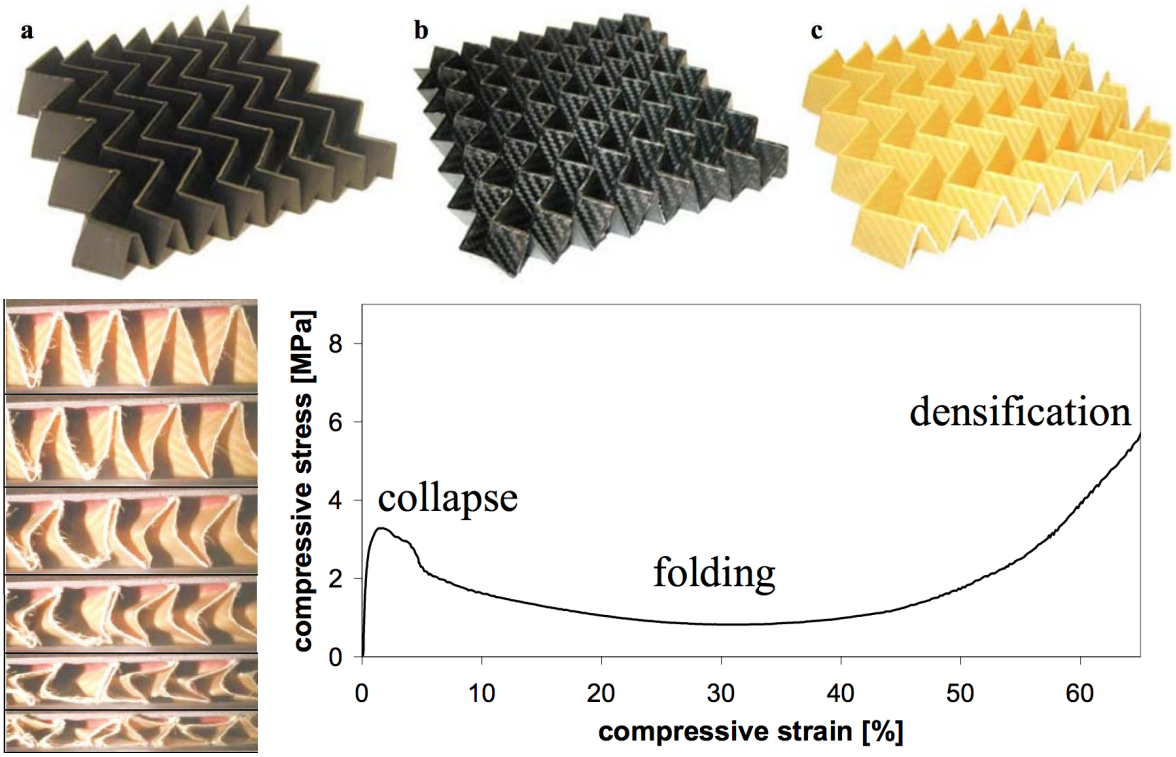

Figure 5.2: Foldcore energy absorbers, showing induced creases and valley in the stress-strain plot. (Images from [87])

In contrast, an ideal mechanical response could consist of a traveling hinge line, which sequentially extracts mechanical work from the entire material as it is crushed. To induce this behavior, the buckling load should be considerably higher than the load required for local material yield. As a curved shell is much more resistant to buckling than a flat plate, it is natural to consider curve crease foldcores as a way to accomplish this parameter combination. Simulation studies have predicted a factor of two improvement over honeycombs in the energy absorption of honeycombs per volume [70]. Experimental work to validate this prediction has been lacking, as fabricating these curved crease foldcores has typically used progressive forming of aluminum sheets. The produced geometries deviate from the ideal shape, and these deviations significantly reduce the energy absorbing capability by changing the failure mode. The inclusion of triggering features improved this performance [69], but not to the level predicted theoretically. In the next section, we attempt to realize this potential by using the carbon-polymer lamination technique developed in Chapter 4 to produced curved crease foldcores with much better geometric accuracy.

5.1 Curved crease foldcores

In this section, I use the carbon-polymer lamination method developed in Chapter 4 to produce curved crease foldcore energy absorbers. Because the crease curves can be accurately patterned in the prepreg, this approach offers greater geometric accuracy than the incremental forming techniques used in [70]. This process can be adapted to use a variety of materials, but because the use of carbon prepress had already been developed, we continued to use it.

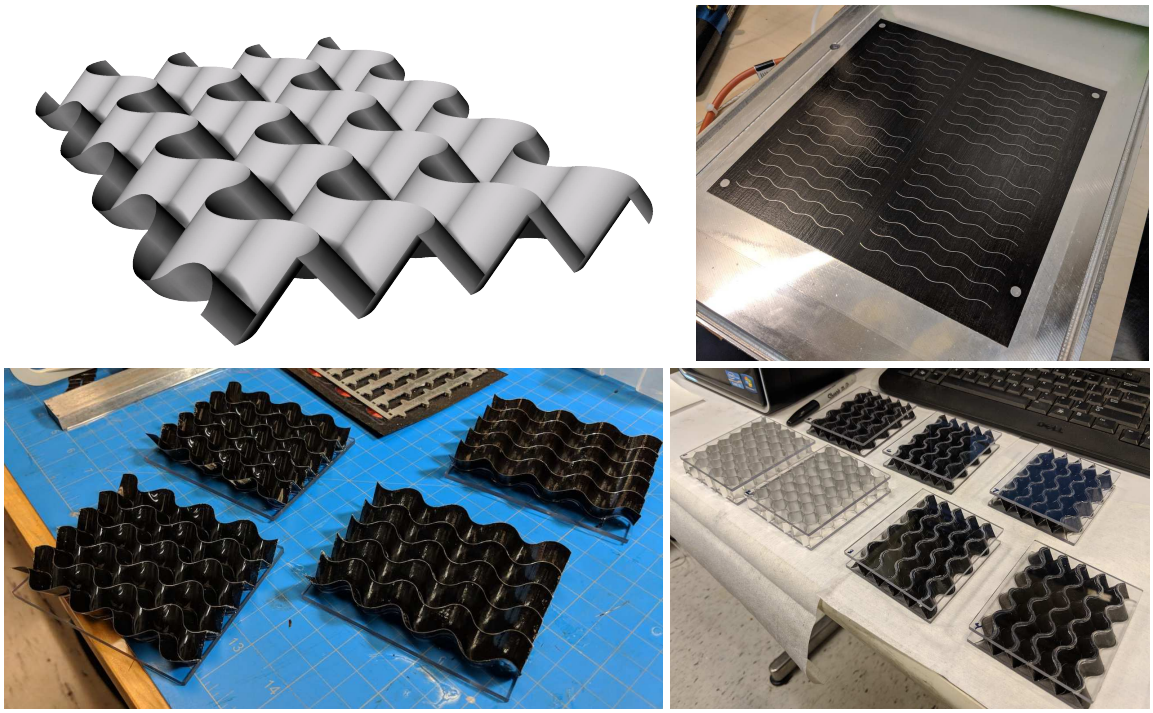

Figure 5.3: Creating cylinder-section curved crease foldcores. a) Prescribed three-dimensional geometry, b) Compute crease pattern cut from carbon prepreg and cured with PET film, c) Folded samples, bonded to polycarbonate face plates, d) Samples ready for testing.

We begin by designing the three-dimensional geometry of the energy absorbers with the goal to increase the buckling resistance as much as possible. The buckling behavior of a shell with one direction of curvature is analyzed by Timoshenko [186]. Assuming the length parallel to the axis of curvature is of the same order as the length along the curvature, the critical buckling stress is given by

$$\sigma_{cr} = \frac{\pi^2 E h^2}{3(1-\nu^2)(r\beta)^2} + \frac{E\beta^2}{4\pi^2} \tag{5.1}$$

where E is the elastic modulus, ν the Poisson ratio, h the shell thickness, β the angle subtended by the curved shell, and r the radius of curvature. Note that $r\beta$ is simply the arc length of the shell and the first term is the same as that for the critical stress of a flat rectangular shell of length $r\beta$. Thus, the second term is the contribution of curvature to the buckling resistance. With a constant arc length, greater curvature implies a greater subtended angle, and hence greater contribution to buckling resistance. As the buckling resistance of a shell with variable curvature will be limited by the minimum curvature region, we can expect a constant curvature shell to have greatest buckling resistance. Therefore, a foldcore with the greatest buckling resistance will have three-dimensional geometry consisting of cylinder sections.

Using the derivation of Chapter 4, we can calculate the required creases for a foldcore of cylindrical sections (shown in Figure 5.3a). These creases were cut from carbon fiber prepreg using a Zünd Systemtechnik large format cutter and cured between sheets of $12\mu m$ PET film. After curing the foldcore samples were trimmed on the Zünd cutter and folded into shape with the aid of a 3D printed jig. To hold the samples during testing, $3mm$ polycarbonate face sheets were engraved to fit the peaks of the foldcore and bonded to the samples.

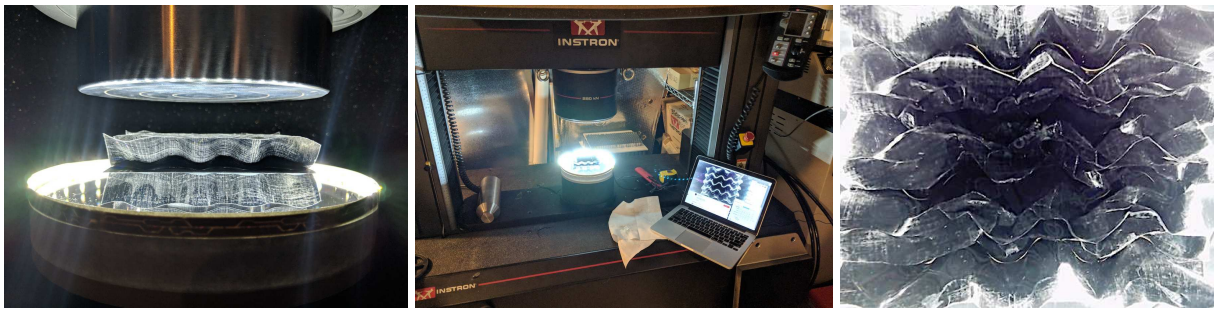

Figure 5.4: Crush test viewing apparatus. a) Curved crease sample ready for testing on the polycarbonate window, b) Crush test viewer on the Instron 5895 test frame, c) View from the camera underneath the window during crush testing.

In order to analyze the crushing modes of these structure during testing, it is important to observe the failure modes of the samples. As the interesting phenomena occur in the center region of these relatively flat samples, viewing from above or below is ideal. To accomplish this, I made a load bearing window with a camera and lights underneath and mounted it on the Instron 5895 test frame. To support the window, I turned a cone shape at the viewing angle of the webcam from a large piece of PVC rod. The camera is a Logitech C920, which enumerates as a USB universal video class device and has manual controls of focus and exposure. The window itself was routed from 20mm polycarbonate. This experimental setup is shown in Figure 5.4a-b and the view from the camera is shown in Figure 5.4c.

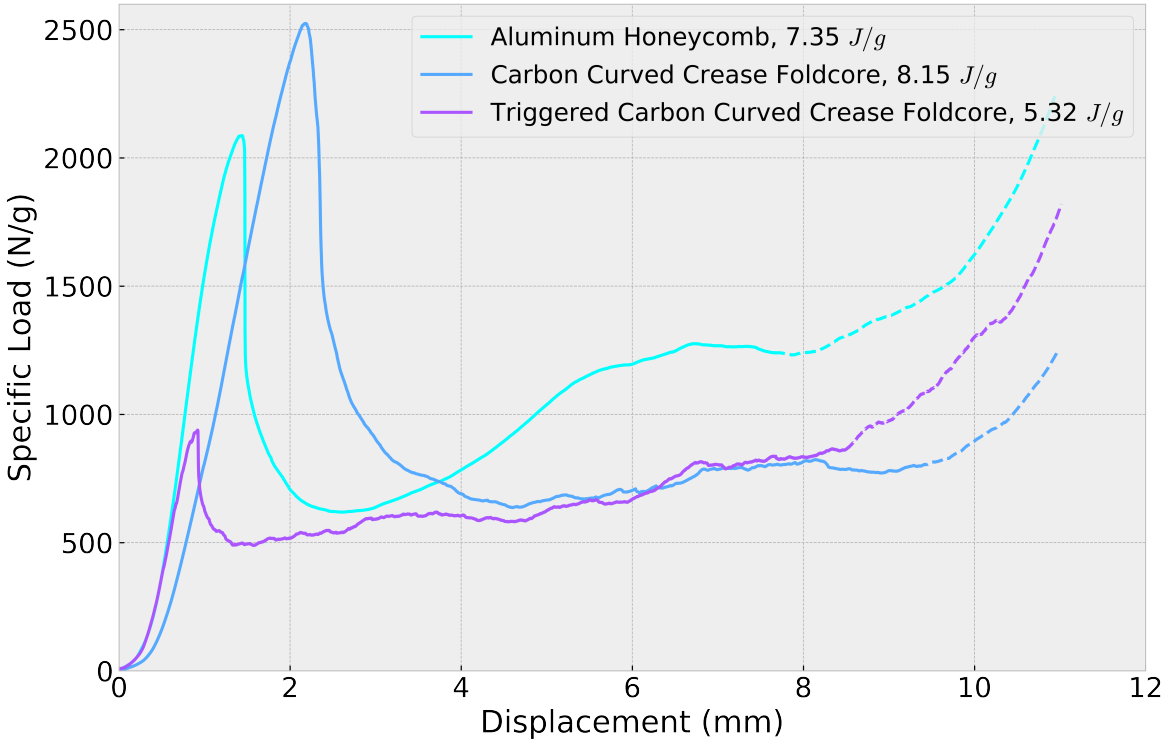

Figure 5.5: Results of quasistatic crush testing showing specific load (N/g) versus displacement of aluminum honeycomb (teal), carbon fiber curved crease foldcore (blue), and carbon fiber curved crease foldcore with triggers (purple).

The graph in Figure 5.5 shows the results of quasistatic crush testing aluminum honeycombs (teal) and carbon fiber curved crease foldcore (blue). The samples have the same geometric dimensions, and the aluminum honeycomb was selected to have a similar density to the foldcore in order to be comparable. These tests demonstrated that carbon fiber curved crease foldcores can surpass the specific energy absorption of aluminum honeycombs, but the achieved value is far from the simulation-based predictions of [70]. The densification strain is increased over honeycombs, but the curve still shows the characteristic shape of initial buckling (indicated by a peak in stress) followed by folding along the induced creases (indicated by the long valley after the peak). The images from the crush test viewer (shown in Figure 5.4c) confirm this, as the large buckling wavelength of the failure mode is clearly visible. This implies the hypothesis of [70] that geometric inaccuracies are responsible for the underperformance of curved crease honeycombs may not be the full explanation. In the following sections, we investigate methods to improve the specific energy absorption of this construction by increasing the ratio of buckling load to crushing load of the curved crease foldcore.

5.2 Triggers for progressive failure

To control this buckling wavelength we next implement a common strategy from energy absorber design in our curved crease foldcores: the use of selective weakening to stabilize a crushing failure mode. This selective weakening is implemented using *triggers*, parts of the material that have been removed. Figure 5.6a shows a rendering of a cylinder section with triggering features cut away. The tapered shape of the trigger initially localizes crushing at the very top of the fold core, performing work on the material there. After this material has yielded, load is transferred slightly further down the taper, which is now the weakest part of the foldcore. This front continues downward, progressively deforming all of the material, until at some point the length parallel to curvature axis is much smaller than the arc length (shown in Figure 5.6b) and Equation (5.1) no longer applies. At this point, the buckling resistance is high enough to eliminate the need for triggering features, and the material continues progressively deforming without them.

The lamination method developed in Chapter 4 easily allows portions of the prepreg to be cut away before curing to create such triggers. Figure 5.6c shows a sheet of carbon prepreg cut and cured with $12\mu m$ PET film. Tapered triggers were cut away using the Zünd Systemtechnik large format cutter at the same time as the hinge lines were cut. The shape of these tapers was designed qualitatively, though the optimal shape could likely be computed using finite element simulation and an optimization loop. Figure 5.6d shows this sample folded into three dimensions.

Figure 5.6e-g shows views from the crush test viewer during the testing of these samples. We can see that the triggers are successful in creating a progressive front of crushing, as these test images closely resemble the rendered ones. The stress strain curve for this test is plotted in Figure 5.5 in purple. We can see that as the large-scale buckling has been eliminated, the initial peak is almost completely removed from the curve. This demonstrates that such trigger features can provide control over the failure mechanism of a folded energy absorber. Unfortunately, in this implementation, the triggering features also reduce the ratio of active material (carbon fiber) to hinge material (PET). As the hinge material does not contribute significantly to the energy absorption, this reduced ratio creates a penalty in the specific energy absorption of the samples with triggers. We see in the graph that the curved crease foldcore with triggers absorbed less

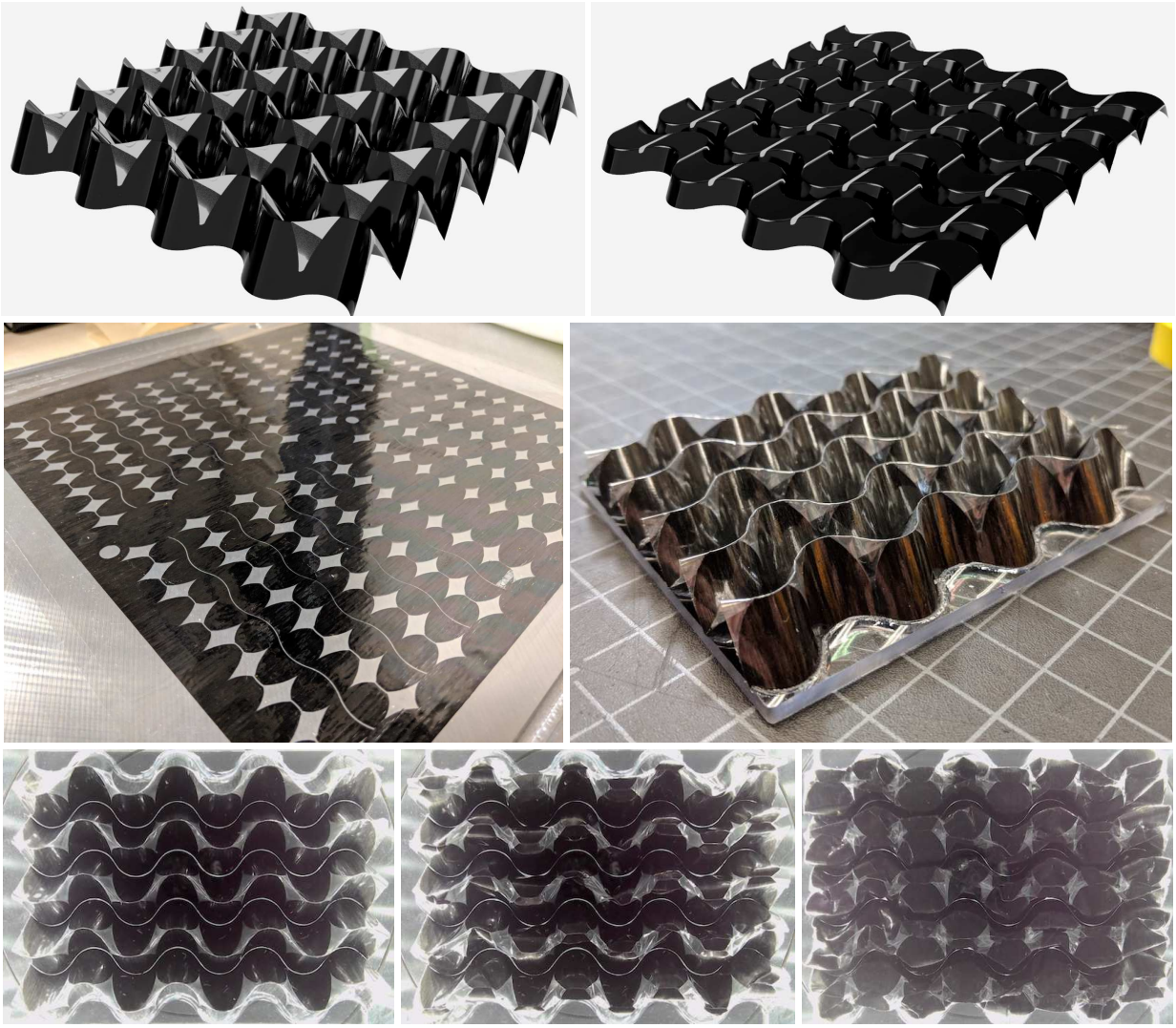

Figure 5.6: Curved crease foldcores with triggers. a-b) Render of trigger features and progressive crease crushing mode, c) Carbon prepreg cut with creases and trigger features, then cured with PET film, d) Folded sample, e-g) Snapshots from crush test viewer during testing showing progressive front of deformation.

energy per mass than both the honeycomb and the curved crease foldcore without triggers.

This issue could likely be solved by cutting the triggers away from both the active and hinge materials. I chose not to do this, however, because the folding of prototype scale samples would be made more difficult. Instead, I turned to investigate an alternative way to increase the ratio of buckling load to crushing load, described in the next section.

5.3 Foldcores with rule line corrugation

To increase the ratio of buckling load to local crushing load of these foldcores, I now apply a strategy from the packing industry: corrugation. More than 200 billion square meters of corrugated cardboard are produced annually [67]; this widespread adoption is precisely because the corrugated sandwich construction provides high buckling resistance using a minimal amount of

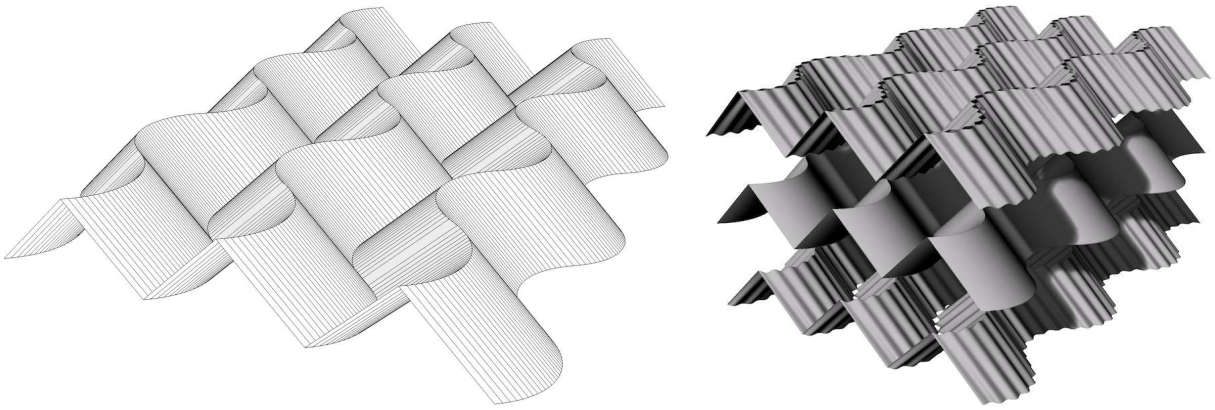

Figure 5.7: Instantiating the ruling of a curved crease foldcore. a) Cylinder section curved crease foldcore with ruling drawn in, b) Sandwiching the foldcore with corrugated layers aligned to the ruling.

material and a low manufacturing complexity.

Recall from Chapter 4 that curved crease patterns are characterized by their rulings (i.e., the set of line segments contained completely in the surface). Figure 5.7a shows one of our curved crease foldcores with its ruling drawn in. Curved crease patterns are said to be *rigid foldable* if their ruling remains constant during their folding motion [177]. Curved creases of reflection, like those comprising these foldcores, are rigid foldable. Because they do not shift on the surface during folding, these rulings can be given physical instantiation. For instance, in Figure 5.7b, we show a curved crease foldcore sandwiched by corrugated sheets aligned with the ruling.

This is a powerful construction, as it allows additional structure to be attached to a flat sheet and folded into the prescribed three dimensional geometry of the foldcore. Figure 5.8 shows two corrugated curved crease foldcores. The corrugation significantly increases the second area moment of inertia about the crushing direction, while leaving the second area moment of inertia about the perpendicular direction largely unchanged. The effect is two-fold. First, the corrugation greatly increases the buckling load of the foldcore without significantly increasing the local material crushing load. Second, the corrugations enforce the curved crease pattern, allowing the required curved panels to be bent while disallowing other deformations. This limiting of extrane-

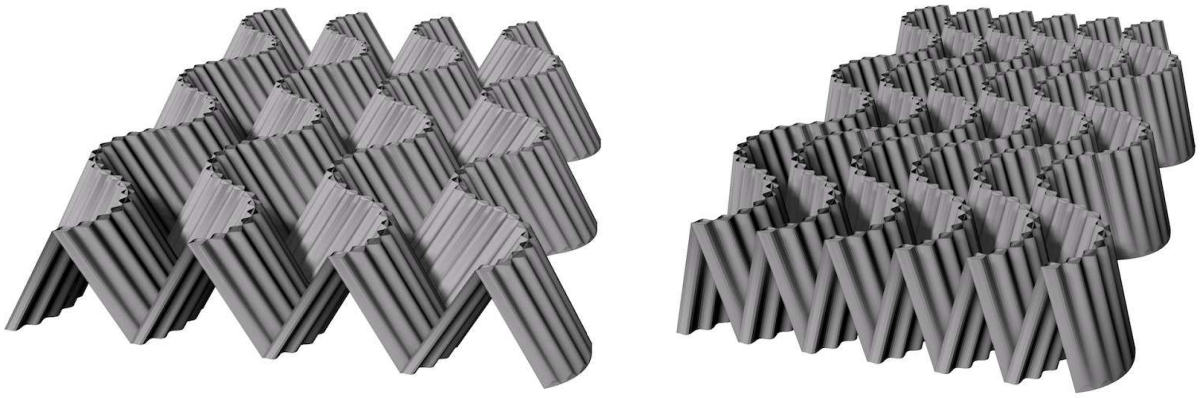

Figure 5.8: Corrugated curved crease foldcore variants.

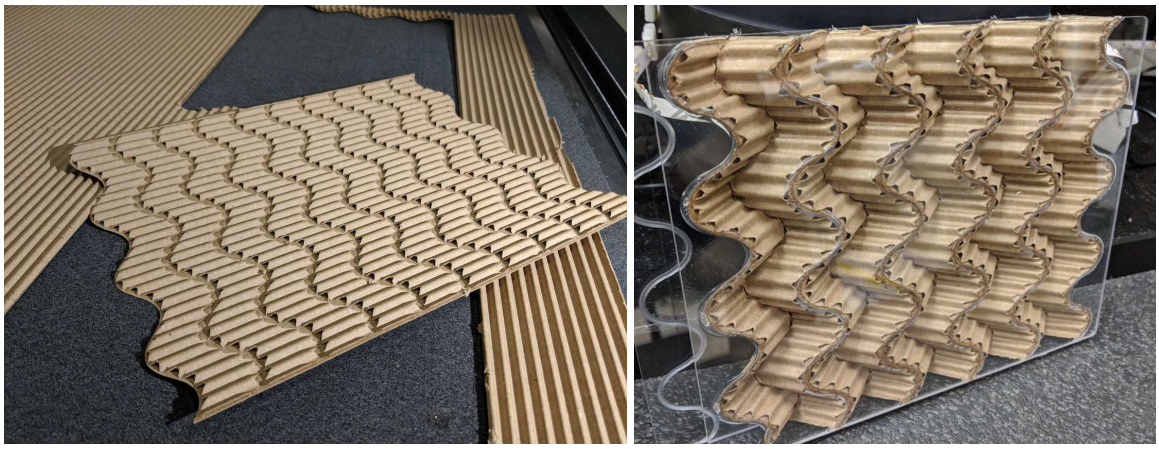

Figure 5.9: Corrugated curved crease foldcore prototypes in cardboard. a) Flat pattern after cutting crease curves from the corrugated layer, b) Folded and sandwiched between polycarbonate plates.

ous deformation aids in manufacturing, as a global boundary conditions can more readily enforce prescribed folding.

In these constructions, the rule lines of the entire sheet lie parallel to each other when the foldcore is in its flat state. This allows significant reduction in manufacturing complexity because the corrugated layers can be produced from a single sheet each and bonded to the foldcore layer while flat. Figure 5.9 shows an example, prototyped in commercially available corrugated cardboard with only one liner sheet (instead of the usual two liners). First, the creases are patterned into the corrugation layer using a 45° bevel knife tool using a Zünd Systemtechnik large format cutter. This patterned corrugate was then folded and bonded to polycarbonate plates sheets (shown in Figure 5.9).

To extend this construction to higher performance materials and geometries, I designed and built a corrugation machine, shown in Figure 5.10. In commercial production, corrugation is performed by machined rollers with interleaved teeth. The design of the profiles of these teeth is a complex task, involving balancing the desired corrugation shape with the constraints of tooth

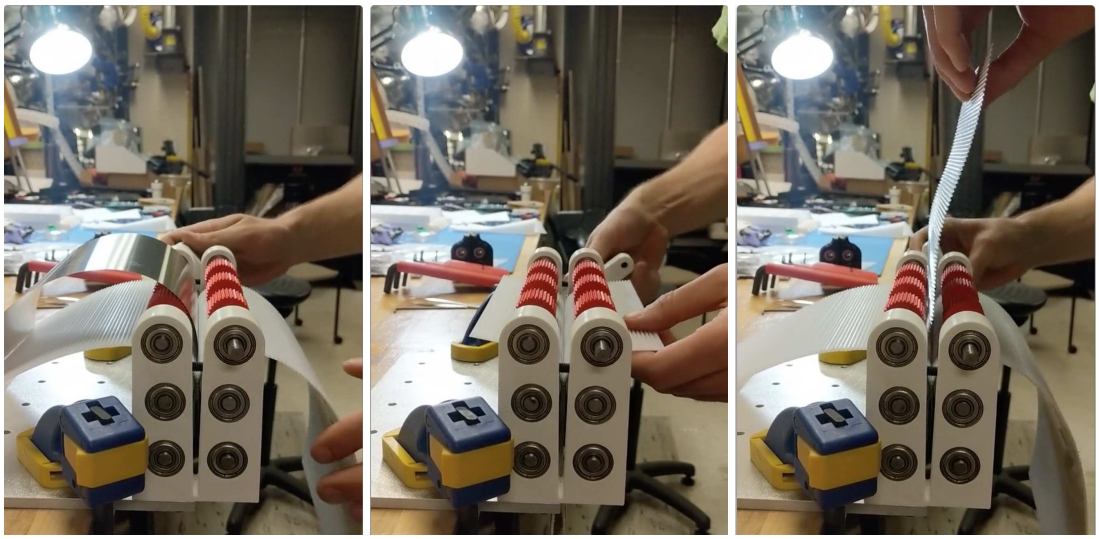

Figure 5.10: Corrugating aluminum sheet on our corrugate prototyping machine.

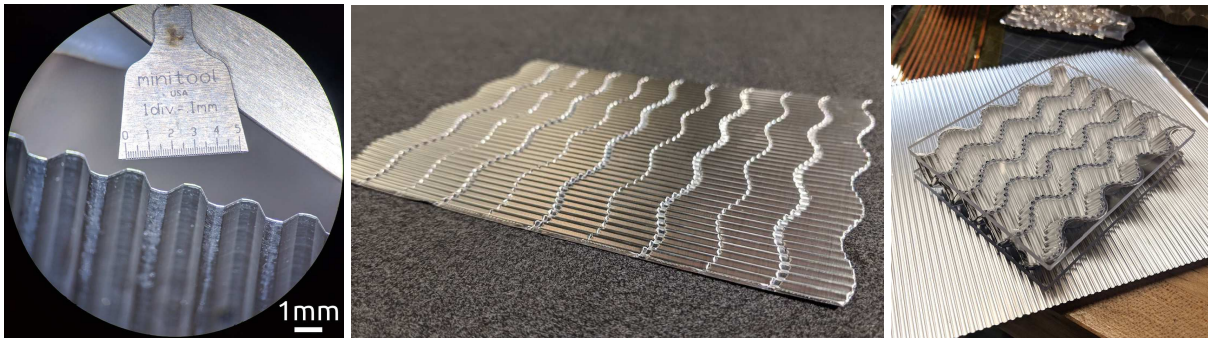

Figure 5.11: Prototyping corrugated curved crease foldcores in aluminum. a) Microscope image of $2mm$ pitch corrugated aluminum sheet. b) Corrugated layer bonded to foldcore layer and patterned with curved creases. c) Folded corrugated curved crease foldcore, constrained by polycarbonate plates.

interference and frictional interactions between the teeth and corrugation medium. To accelerate the prototyping cycle, I split the functions performed by the corrugation rollers into two components. First, I use a set of $25mm$ cylindrical steel rollers with adjustable separation to apply consistent pressure across the width of corrugation. Over these rollers, I use flexural acetal sheets with machined tooth profiles to perform the corrugation. This separation of functionality allows the tooth profile to be rapidly iterated, as machining the acetal sheets is much faster and more cost effective than machining steel rollers. Using this approach, I designed a tooth profile to produce a corrugation pitch of $2mm$, a corrugation angle of $60°$, and equal horizontal and inclined side lengths.

Using this corrugate prototyping machine, I corrugated aluminum 1100-H19 foils with thicknesses of $25\mu m$ and $50\mu m$. Figure 5.11a shows a microscope image of one of these corrugated foils. A thin film of two-part epoxy (Loctite 60HP) was spread on a glass plate and the corrugated sheet was used to pick up a small amount on each corrugation peak. These corrugated sheets were then bonded to uncorrugated sheets of the same material, which form the foldcore layer of the construction. In these tests, a single corrugated layer was used, but the same process can be used to apply corrugated layers to both sides of the foldcore layer.

After curing, curved creases were patterned in the corrugated layers using the Zünd cutter. I successfully tested several processes for patterning the corrugate, including bevel cutting, os-

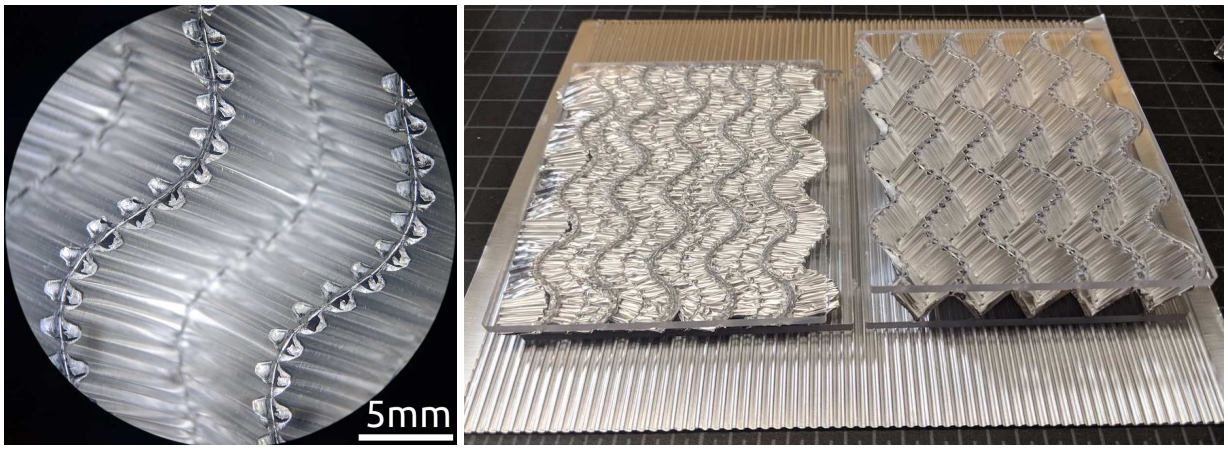

Figure 5.12: ea

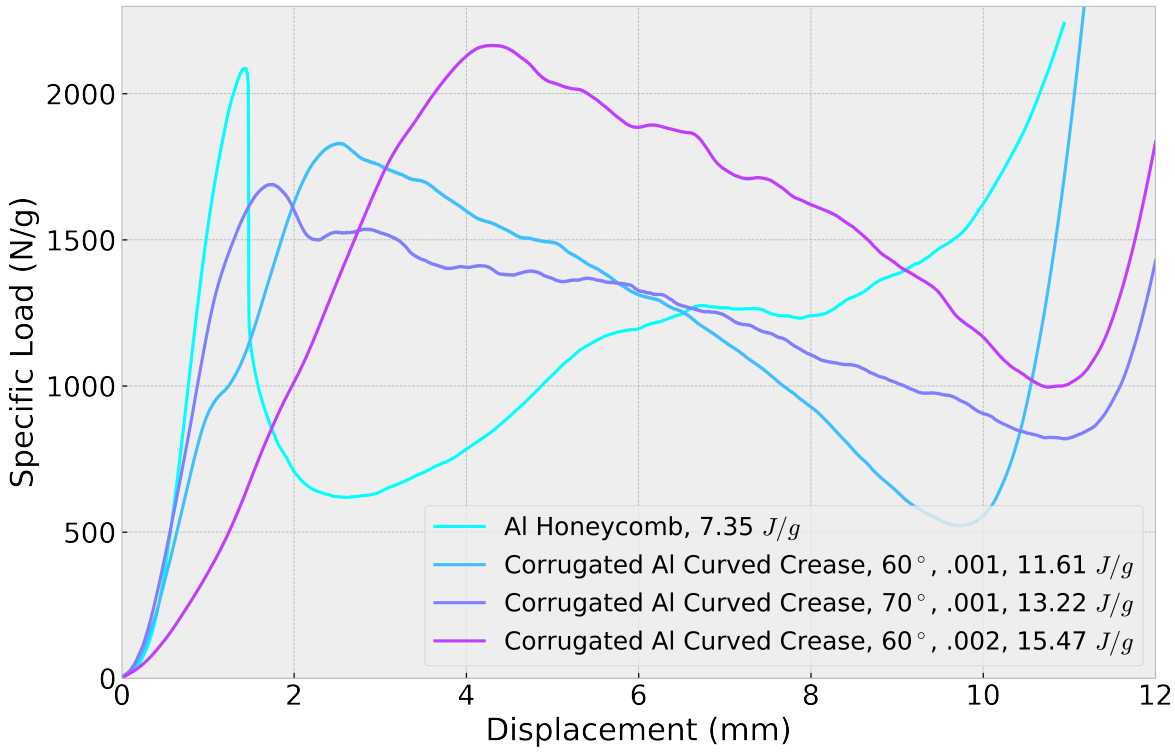

Figure 5.13: Quasistatic crush test results comparing aluminum honeycomb and aluminum corrugated curved crease foldcores. The corrugated foldcores achieved specific energy absorptions over twice that of the honeycombs.

cillating knife cutting, creasing, and routing. It is critical to remove or deform the corrugated layer enough to avoid collisions during folding but leave enough of it intact to accurately set the geometry of the crease. For prototyping, routing using a chamfer mill proved the most reliable process, but at production scales creasing would likely be the most efficient option. One of these patterned corrugates is shown in Figure 5.11b. These patterned corrugates were then folded and bonded to face sheets to hold them in their folded states, as shown in Figure 5.11c.

Using the process described, I prepared samples using aluminum of $25\mu m$ and $50\mu m$ thickness and with the angle γ taking values of $60°$ and $70°$. These aluminum corrugated curved crease energy absorbers were tested on an Instron materials characterization machine to determine their energy absorption capacity. A platen was used to crush the samples at 1 mm/min and the crushing load was recorded as a function of displacement. These quantities were converted to stress and strain and the energy absorbed was calculated as the area under this curve until the densification strain. Figure 5.13 shows these results. Compared to both aluminum honeycombs and conventional curved crease foldcores, the corrugated samples exhibited much more constant loads (i.e., no high peak followed by valley). The corrugated samples also exhibited impressive specific energy absorption capacities (15 J/g), approximately twice that of aluminum honeycombs (7 J/g).

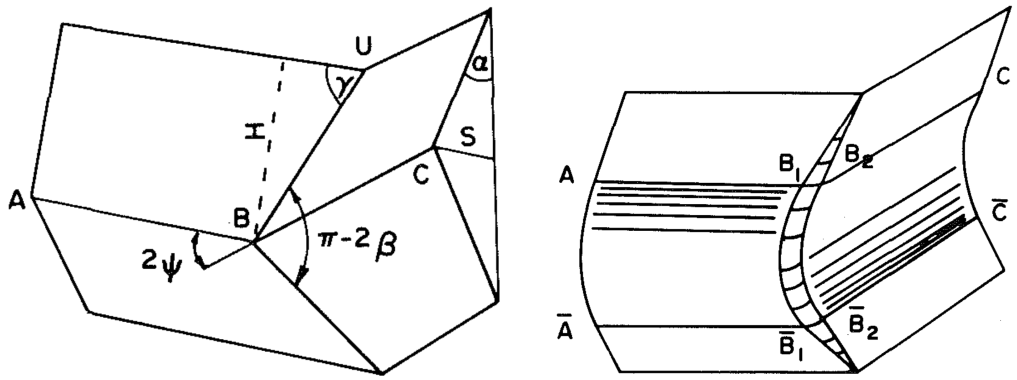

Figure 5.14: Overlaying a plasticity model of material behavior on a geometric model of crushing behavior. a) geometric crushing model, b) plasticity model (Images from [202])

5.4 Plasticity modeling

To verify these results, I now construct a model of the average crushing forces of our samples. This estimate, together with an estimation of the densification strain allows us to estimate the energy absorbing capacity of our samples. This problem was studied for honeycomb structures first by McFarland [128], and later in more rigor by Wierzbicki [202, 203]. If we assume that the average crushing force of corrugated curved crease foldcores is below the buckling load of the walls, we can simplify the analysis considerably and adapt the derivation of [202]. In this way, we exploit the hierarchical nature of these constructions to separate the analysis of the different scales.

The analysis of [202] begins by considering a characteristic unit of the induced folding mechanism of a thin-walled structure, formed by the crushing of an initially straight vertical crease. After crushing, a unit resembling Figure 5.14a is formed (this also happens to be a unit of the ubiquitous Miura-Ori folding pattern). With some reasonable assumptions on continuity and solid mechanical behavior, a more realistic picture of this unit is given by Figure 5.14b. This picture allows us to analyze sources of mechanical work, classifying it into three types. First, the surface patch bounded by $B_1\bar{B}_1\bar{B}_2B_2$ can be shown to be a section of a torus. During crushing, this patch produces an energy dissipation $\dot{E}_1$ that is equivalent to that of drawing a flat sheet over a torus, a quantity can be calculated analytically. Second, the horizontal hinge lines AB_1, B_2C, $\bar{A}\bar{B}_1$, and $\bar{B}_2\bar{C}$ move vertically during crushing, producing a known dissipation $\dot{E}_2$. Finally, the inclined hinges running from the top and bottom surfaces to the points B_1, B_2, $\bar{B}_1$, and $\bar{B}_2$ move across the surface during crushing, also producing a known dissipation $\dot{E}_3$.

It can be shown that

$$E_1 = \int \dot{E}_1 = 16 M_0 \lambda \frac{b}{t} I_1(\psi_0) \tag{5.2}$$

where t is the material thickness, b is the minor radius of the torus, λ is the half-wavelength of buckling, M_0 is the plastic moment ($M_0 = \frac{1}{4}\sigma_0 t^2$ where σ_0 is the plastic flow stress), and I_1 is a purely geometric integral over the folding motion. This integral can be evaluated using only the information in Figure 5.14a, namely the initial angle ψ_0 between the two plates (See [202] for formula). Further,

$$E_2 = 2\pi M_0 \ell \tag{5.3}$$

where ℓ is the length of segment AB. Finally,

$$E_3 = 4M_0 I_3(\psi_0)\frac{\lambda^2}{b} \tag{5.4}$$

where I_3 is again a purely geometric integral over the folding motion which depends on ψ_0.

Using these expressions for crushing energy dissipation over a distance of 2λ, we can calculate the average crushing force F, using the energy balance equation

$$2F\lambda = E_1 + E_2 + E_3 \tag{5.5}$$

Letting $A_1 = 8I_1(\psi_0)$, $A_2 = \pi$, $A_3 = 2I_3(\psi_0)$, we have

$$\frac{F}{M_0} = A_1\frac{b}{t} + A_2\frac{\ell}{\lambda} + A_3\frac{\lambda}{b} \tag{5.6}$$

This equation includes the buckling half-wavelength λ and torus minor radius b, two quantities that we do not know a priori. Assuming that the crushing force (and hence energy) is minimized with respect to these quantities, we can set $\partial_\lambda F = 0$ and $\partial_b F = 0$ and solve for them as

$$b = \left(\frac{A_2A_3}{A_1^2}\right)^{\frac{1}{3}}\left(\ell t^2\right)^{\frac{1}{3}} \qquad \lambda = \left(\frac{A_2^2}{A_1A_3}\right)^{\frac{1}{3}}\left(\ell^2 t\right)^{\frac{1}{3}} \tag{5.7}$$

and hence

$$\frac{F}{M_0} = 3\left(A_1A_2A_3\right)^{\frac{1}{3}}\left(\frac{\ell}{t}\right)^{\frac{1}{3}} \tag{5.8}$$

This elegant result implies that buckling wavelength, torus minor radius, and crushing force can all be computed simply from a geometric description of a characteristic unit of a thin-walled structure. The same form is valid when we expand the definition of the characteristic unit to include more structural detail than shown in Figure 5.14, provided we update our definitions of A_i.

For instance, in the case of a hexagonal honeycomb with double thickness on one third of the walls (a characteristic of the manufacturing process), we take as a unit cell the region around a single vertex (which includes two single thickness walls and one double thickness wall). The deformed configuration includes two moving vertices contributing to E_1, eight horizontal creases of thickness h and four horizontal creases of thickness $2h$ which contribute to E_2, and eight inclined hinges which contribute to E_3. Assuming a regular hexagonal honeycomb so $\psi = 30°$, this counting argument implies $A_1 = 16I_1(\psi_0)$, $A_2 = 3\pi$, $A_3 = 4I_3(\psi_0)$, and hence

$$\lambda_{honeycomb} \approx 0.82\sqrt[3]{tS^2} \quad F_{honeycomb} \approx 8.61\sigma_0 t^{5/3}S^{1/3} \tag{5.9}$$

where S is the side length of the hexagon cell shape.

We can perform the same analysis on a unit cell of the corrugated structure, in which we define the characteristic unit to include half of one corrugation pitch. The deformed configuration includes two moving vertices, 20 horizontal creases of thickness h, four horizontal creases of thickness $2h$, and eight inclined hinge lines. Therefore $A_1 = 16I_1(\psi_0)$, $A_2 = \frac{9}{2}\pi$, $A_3 = 4I_3(\psi_0)$ and hence

$$\lambda_{corrugate} \approx 0.94\sqrt[3]{tS^2} \quad F_{corrugate} \approx 9.86\sigma_0 t^{5/3}S^{1/3} \tag{5.10}$$

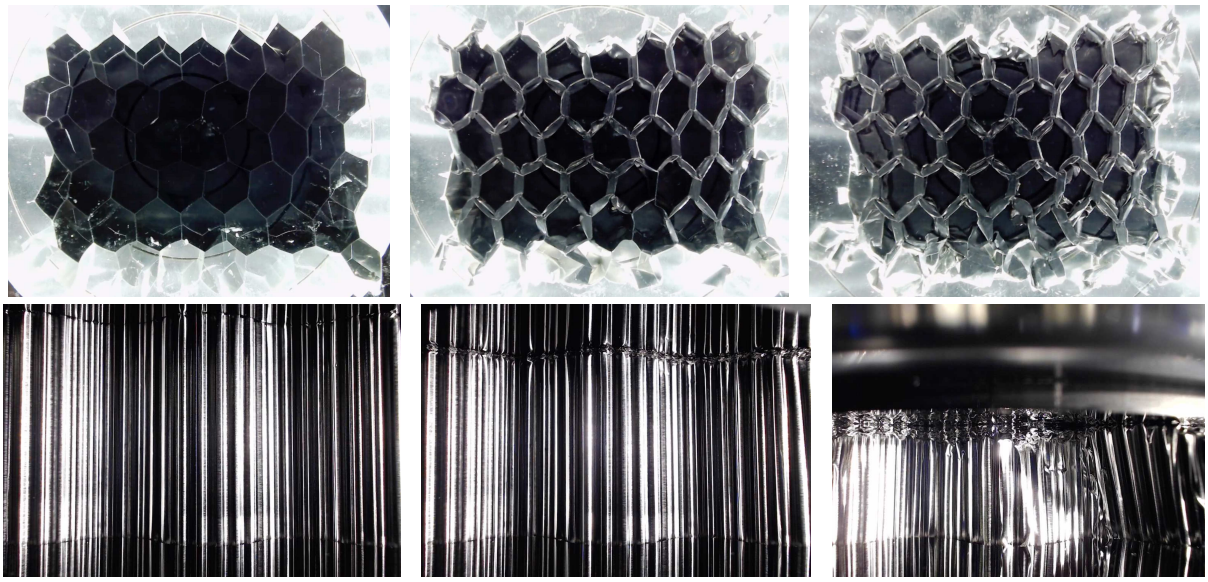

Figure 5.15: Observing buckling wavelength of crushed honeycombs and curved corrugates. a-c) Honeycomb ($12.7mm$ cell width) viewed from below, showing half wavelength λ of approximately $3mm$. d-f) Curved corrugate ($2mm$ corrugation pitch) viewed from front, showing half wavelength λ of a few hundred microns.

where here S is the side length of the corrugation.

We see that the scaling of both wavelength and crushing force is approximately the same for the honeycomb and corrugate with respect to t and S. The key difference, however, is because the corrugate structure has multiple levels of hierarchy, the parameter S can be varied freely, without affecting the relative density of the architected material. Therefore, we can lower the buckling wavelength by decreasing S. In contrast, decreasing S in a honeycomb increases relative density (unless t is also varied, but this is bounded by manufacturing constraints). For instance, the samples tested in Section 5.3 have nearly the same relative densities, but for the honeycomb $S \approx 7mm$ while for the corrugated samples $S \approx 1mm$. This implies that the buckling wavelengths differ by approximately an order of magnitude:

$$\lambda_{honeycomb} \approx 2.3mm \quad \lambda_{corrugate} \approx 0.23mm \tag{5.11}$$

In Figure 5.15, we observe the buckling wavelength in our experimental samples. Comparing against the honeycomb cell width of $12.7mm$, we estimate $\lambda_{honeycomb} \approx 3mm$. Similarly, comparing against the corrugation pitch of $2mm$, we estimate $\lambda_{corrugate}$ at a few hundred microns. These observations agree well with our theoretical predictions.

Finally, we use this analysis to verify the experimentally measured energy absorption. For honeycombs, we can integrate the average crushing force estimate over the stroke to estimate energy absorption. For corrugated curved crease foldcores, we must account for the changing relationship between crushing stroke measured by the test frame and the crushing stroke in the axis of the foldcore walls. If $F_{instron}$ is the force measured by the test frame, γ is the foldcore apex angle as defined in Chapter 4, h is the initial height, and z is the stroke, some trigonometry shows

$$\frac{F_{instron}}{F} = \frac{h\cos(\gamma) - z}{\sqrt{h^2 + z^2 - 2hz\cos(\gamma)}} \tag{5.12}$$

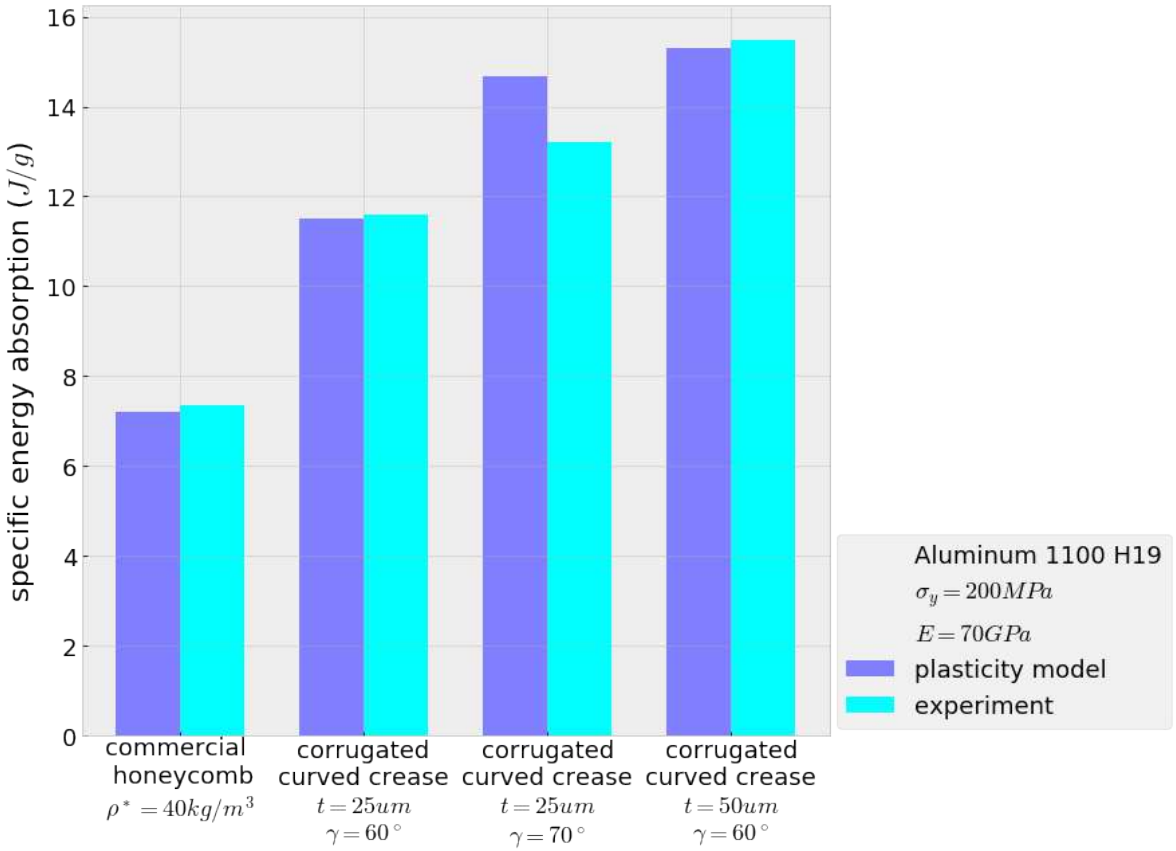

Figure 5.16: Comparing measured specific energy absorption of honeycomb and corrugated foldcores with model predictions. This model confirms the factor of two improvement of the corrugated foldcores over honeycombs.

This equation explains the negative slopes of the load-displacement curves of the corrugated foldcores shown in Figure 5.13.

Using this equation, we can estimate a force displacement curve for our corrugated curved crease foldcore samples and integrate the area under it. Further, we can write formulas for the density for the honeycomb and foldcores by multiplying all side lengths by the thickness and the material density. Combining all these ingredients in Figure 5.16, we show estimates of specific energy absorption and compare against the experimentally measured values. We can see that the analytical model confirms the measured results well, confirming the factor of two increase in specific energy absorption.

5.5 Conclusions

In this chapter, I built folded architected materials with high specific modulus of toughness, that is, with high energy absorption per mass. After a review of prior work, I iterated through some early designs noting the lessons learned. With this experience, I then designed and fabricated a hierarchical folded architected material and a machine for its construction, developed an analytical model to predict performance, and showed its specific energy absorption to be twice that of commonly used honeycombs. These energy absorbers can replace components in vehicles and

increase fuel efficiency by eliminating mass, while also increasing factors like crashworthiness, cabin size, and other measures that are often framed as a trade-off with efficiency. As corrugation is a scalable process (used at extreme scale in the packaging industry worldwide), such energy absorbers can be cost-effectively manufactured.

This is an exciting result, and suggests several directions for future work. First, based on the characterization of failure modes, the demonstrated performance of these energy absorbers can likely still be improved. Despite the improved material utilization compared to honeycombs, a significant amount of material is still not full utilized. Particularly, at the end of the stroke, the apex angle γ has effectively increased so much that a change in the test frame stroke no longer produces much change in the length of the foldcore wall. Starting with steeper foldcores can likely minimize this effect without risking the stroke-shortening observed in vertical-walled honeycombs. Also, moving from single-sided to double-sided corrugate constructions should further increases buckling resistance and energy absorption.

Next, while all the fabricated samples have a constant thickness, a key advantage of this approach is the ability to fill complex shapes [81, 107] much like the net shape honeycombs of Chapter 2. In many cases, the volumes available for energy absorption in vehicles are not uniformly shaped, and so efficiently packing a foldcore is a useful capability. Relatedly, demonstrating strategies to create tall volumes by stacking corrugated foldcores while preserving the crushing response is a useful direction for further research.

Future work should also explore the use of base materials other than aluminum in corrugated curve crease foldcores. Another key advantage of the folding-base fabrication technique used to make these foldcores is the significant freedom in material choice. In cost-sensitive and safety critical applications, like helmets, the use of polymers like PET and polycarbonate is an attractive option. In these applications, foldcores can displace the use of polystyrene and other foams, improving performance, reducing use of toxic constituent chemicals, and avoiding the long-lived waste stream associated with these foams.

In applications where reducing component mass is most important, the use of carbon fiber reinforced polymers could provide significantly higher specific energy absorption than that demonstrated in this chapter. In vehicular applications, carbon energy absorbers have shown nearly five times the specific energy absorption compared to both aluminum and steel [3], reaching hundreds of Joules per gram on a raw material basis [121, 82]. The use of carbon fiber is often dismissed due to high costs, but [155] suggests that material costs for carbon fiber dropped in price by 50% between 2012 and 2018 (from 30 \$/kg to 15 \$/kg, within a factor of 3 or 4 of the cost of raw aluminum foils). Fifty percent of this material cost currently comes from the precursors (usually polyacrilonitrile) while the balance comes from the refining these precursors into carbon fiber [196]. There is considerable work on developing the refining processes to make carbon fiber from other precursors, including from the abundant natural resource lignin [141]. Besides being a renewable resource, lignin-based carbon fiber is expected to reduce costs by at least 35%, according to [172]. Manufacturing costs of carbon components vary considerably depending on the processes used. According to [155], for standard autoclave processes, manufacturing costs encompass roughly 60% of total costs, 55% for resin-transfer molding, but only 17% for compression molding. The folded constructions described in this chapter are prime candidates for compression molding, requiring no autoclave or vacuum bagging, and many components can be stacked and cured in parallel. Because of this, adapting the methods for corrugated curved crease foldcore energy absorbers to use composite materials is an exciting direction for future research.

Chapter 6

Active Structures

In this chapter, I build active folded architected materials with embedded actuation to drive deformation modes of the structure. I take as the main test case a hydrodyncamic flow control strategy where small amplitude traveling waves are driven on the surface of a hydrofoil in the direction of fluid flow. As described in Section 6.1, reliable implementations of this strategy have been a longstanding goal in active flow control, as the requirement for distributed, high-bandwidth actuation has been elusive. In this chapter, I develop several methods of embedding actuation into folded architected materials, design and build a hydrofoil with an active surface for driving traveling waves, and evaluate drag reductions in tank testing.

6.1 Background on traveling wave flow control

Research into this mode of fluid-structure interaction dates to early studies of locomotion of fishes, where a paradoxical discrepancy was observed between the muscular power output of dolphins and the power required to tow an equivalent rigid body at comparable speeds [78]. It was suggested that the dolphin's traveling wave swimming motion was responsible for laminarizing the flow, hence reducing the power required for swimming. This model was subsequently explored in many other studies of efficient swimming [183, 208]. While it is now understood that dolphins are actually capable of much higher power output than thought at the time [65, 35], the discrepancy from rigid body analysis spurred significant research into interactions between fluids and compliant structures with traveling waves. This subject has grown to include rich phenomenology, including collective behavior [182], chaotic bifurcation [214], and inverted drafting [156], and many biomimetic flow control mechanisms for efficient robotic swimming [15, 184].

In addition to highly compliant fish-like swimming, traveling waves also provide a means of flow control when driven on the surface of plates, foils, and other rigid structures commonly used in aerodynamic and hydrodynamic applications. This was investigated in a set of beautiful experimental studies by Taneda [181, 180] using a "wave machine" composed of a rubber sheet and a set of pistons and cams (shown in Figure 6.1). It was observed that boundary layer separation is eliminated when the wave speed c exceeded the flow speed U. Experimental studies across a range of Reynolds numbers [190, 210, 40] have confirmed this, noting significant drag reductions in both water and air, and on both plates and cylinders. Computational work has provided further support for this flow control strategy [168, 207, 209, 189], showing that the energy saved by

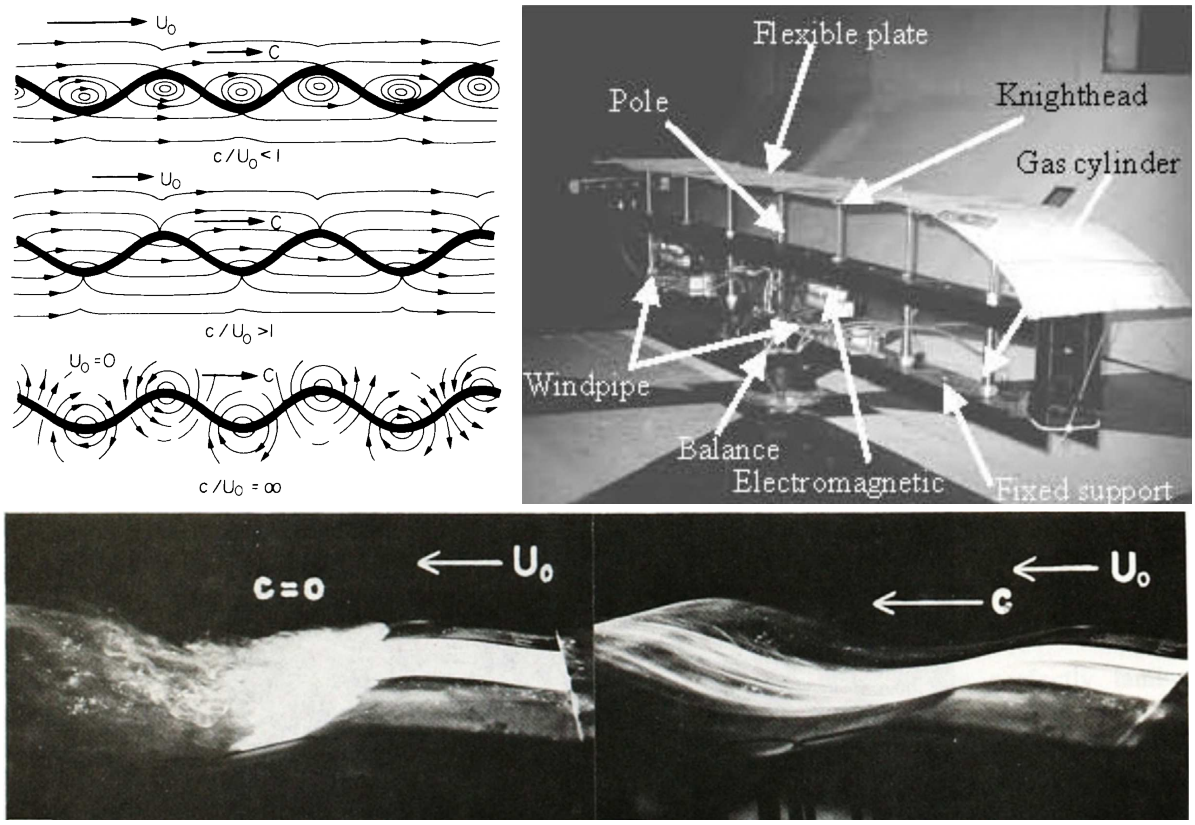

Figure 6.1: Traveling wave flow control. a) Streamlines as a function of relative wave speed (Image from [181]), b) Wind tunnel traveling wave apparatus (Image from [210]), c) Smoke study on rubber sheet "wave machine" (Image from [180])

reducing drag can be significantly greater than that required to drive the traveling waves. In particular, [189] shows through direction numerical simulation that relatively small amplitude traveling waves can be used ($a = .25\lambda/(2\pi)$, where a is amplitude, and λ is wavelength), and that net power input is minimized when $c/U \approx 1.2$. If used on the trailing edge of a foil or other streamlined body under nonzero angle of attack, it is hypothesized that separation can be delayed using traveling waves, significantly reducing turbulent drag, the major contribution of drag in this regime. For instance, [2] performed large eddy simulations over a NACA18 airfoil at $Re = 50,000$ at an angle of attack of $10°$, showing for optimal wave parameter choice, drag is decreased by 10% and lift increased by 5%.

Despite these promising results, viable fabrication of embedded devices supporting traveling waves on operable aerodynamic and hydrodynamic surfaces, rather than experimental apparatuses, has remained elusive for several reasons. First, any surface interacting with a fluid must have a high mechanical stiffness to withstand pressure loads of operation (for instance, those responsible for the generation of lift), yet be soft enough in the desired deformation mode (a wave with fixed wavelength λ) to be efficiently actuated. These opposing demands rule out most monolithic materials, but generating such anisotropic mechanical responses is a strength of architected materials [16]. For instance, such anisotropy has been exploited to actuate torsional modes while maintaining bending stiffness [103], as well as to actuate in-plane longitudinal waves without sacrificing bending stiffness [19, 18, 20, 17]. In this chapter, I leverage this capability of architected

materials to meet the design requirements for traveling wave flow control.

Second, the space afforded by the trailing edge of an airfoil or hydrofoil to contain the actuation and transmission components for driving a traveling wave is very limited, in contrast to the relatively bulky experimental apparatuses cited above. To satisfy this constraint, I use the planar processing of folded architected materials to distribute the actuation and transmission along the traveling wave surface. This significantly reduces the size and mass of the components needed to transmit force from a single large actuator to the point of application.

Finally, the prototype must be able to drive waves at speeds exceeding the free stream velocity in the harsh underwater environment, which places nontrivial demands on the actuation frequency and stroke. For relevant chordwise Reynolds numbers ($Re \approx 10^5$) and wave steepnesses ($2\pi/\lambda a \approx 0.3$), the required actuation frequencies are approximately 10-100 Hz and actuations strokes are approximately 100-1000 μm. These requirements immediately exclude a large number of actuation technologies, including un-amplified piezoelectric, magnetostriction, shape memory alloy, and thermal expansion actuators [94]. Piezoelectric ceramic and polymer bimorph actuators have been demonstrated to meet these requirements [99, 100, 101], but were discounted due to fragility and high costs. Instead, in this chapter, I show how cost-effective and robust electromagnetic actuation can be embedded in an architected material to meet these application requirements.

Next, I detail the design, fabrication, and characterization of several prototypes for driving traveling waves on a hydrofoil surface.

6.2 Folded honeycomb with distributed actuation

In this section[1], I describe a system for constructing structural airfoils and hydrofoils composed of a folded honeycomb with embedded electromagnetic actuators for driving high velocity traveling waves. Like the construction described in Chapter 2, this approach allows the specification of the shape of the honeycomb's bounding surfaces, but adds features for embedded actuators and interfaces to the skin of the hydrofoil. A concept drawing is shown in Figure 6.2. Because the honeycomb is fabricated from a planar substrate, the actuators and electrical signals can be efficiently placed before folding into three dimensions. I then detail the development of a miniaturized single-phase linear motor which is compatible with this approach. The predicted and measured forces produced by these linear motors are compared and trajectories for a $200Hz$ driving frequency are measured. Finally, performance characteristics based on hydrodynamic requirements are specified and compared with those achieved.

6.2.1 Fabrication

In this section, I first adapt the composite-polymer process developed in Chapter 4, to the fabrication of honeycombs with embedded actuation for driving traveling waves, as shown in Figure 6.3. In Figure 6.3a, a stack of resin-impregnated carbon fiber layers is cut with an oscillating knife on a flatbed cutting machine. The stack consists of three layers of unidirectional carbon with a 0-90-0 layup schedule. This cutting step removes hinge lines with a width of approximately $400\mu m$.

[1]The work of this section was presented at the 2018 IUTAM Symposium on *Critical flow dynamics involving moving/deformable structures* [33] and was published in the Journal of Fluids and Structures [34].

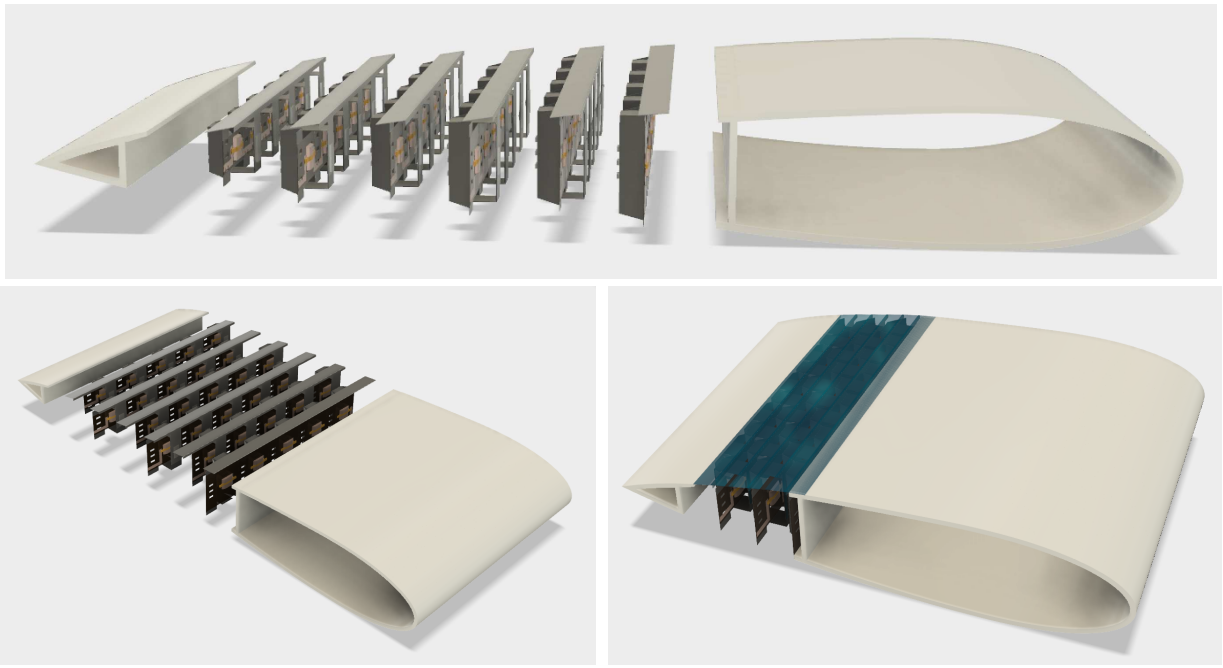

Figure 6.2: Traveling wave elements included near the 3/4 chord position of a foil. A) Exploded side view, B) Exploded perspective view, C) Assembled perspective view.

Next in Figure 6.3b, the carbon layer is placed between two sheets of $12\mu m$ PET film and cured under a vacuum bag at $200°C$ for two hours. In Figure 6.3c, this cured laminate is optically registered on the flatbed cutting machine and cut again using an oscillating knife to form registration features and an outline. The composite strips produced in one cycle are shown in Figure 6.3d. A scan of a single strip is shown Figure 6.3e and a microscope image of two hinge lines is shown in Figure 6.3f. For this prototype, the finished thickness of carbon fiber layers was roughly 150um, while the combined PET hinge layer thickness was 25um.

When assembled, the strip produced in Figure 6.3 will form one layer of a hexagonal-celled honeycomb with integrated actuators and flexure bearings. The physical example produced here has a uniform size, and so the resulting honeycomb will have a constant thickness. To produce honeycombs filling a desired shape, however, we can apply the geometric derivations of Chapter 2 to contour a given shape such as the foil shape shown in Figure 6.2.

To actuate the traveling waves, I now describe the design of a small, single phase linear motor ideal for embedding in folded structures. Linear motors often use three phases to extend actuation forces to large strokes, but because the required amplitudes for this application are only on the order of one millimeter, we use a single phase to simplify driving and wiring requirements and miniaturize the size of the actuator. As a large number of these actuators are required, I selected an "E" core shape which can be wound simply and fits inside a hexagonal honeycomb cell efficiently. Further, this core design can be parameterized easily to include any number $N > 2$ of electrical poles, where the force produced scales linearly with the number of poles (assuming the number of magnetic poles is always $N - 1$).

Figure 6.4 shows the fabrication of these linear motors. First, in Figure 6.4a, core shapes are cut from round stock of Vimvar, a relatively inexpensive electrical iron with high permeability ($\mu_r \approx 10,000$) and high saturation induction ($B_s \approx 2.1T$). Two wire cuts are make at 90 degrees

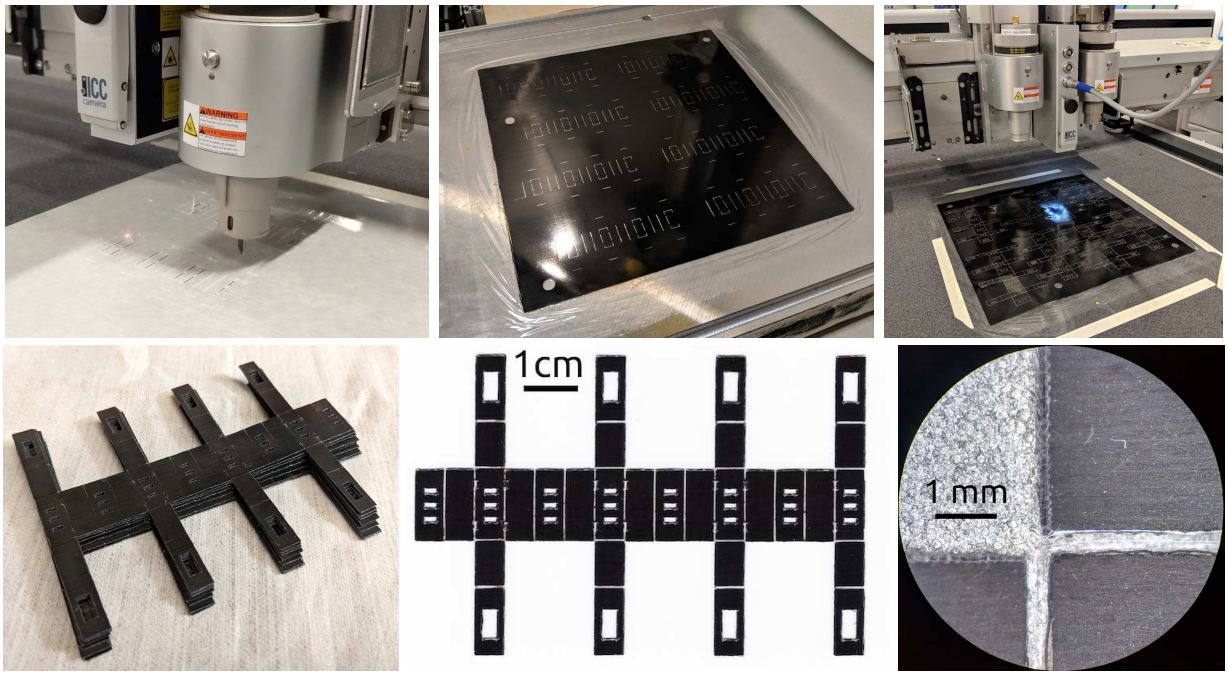

Figure 6.3: Fabrication of fiber-reinforced polymer composite laminates. A) Cutting resin-impregnated carbon fiber using oscillating knife to form hinges, B) Curing resin-impregnated carbon fiber between two sheets of 12 micron PET film, C) Optically registering and cutting cured laminate using oscillating knife, D) Batch of fiber-reinforced parts produced, E) Optical scan of part, showing clear hinges void of fiber reinforcement, F) Microscope image of two incident hinge lines.

from each other, enabling three dimensional features and producing many cores in a single machining operation. In Figure 6.4b, the produced magnetic cores are parted off and prepared for winding with 34 AWG magnet wire. A custom-built precision coil winder head is used to lay two opposing coils of 90 wraps each. The coil winder uses a Luer-Lok dispensing tip for accurate wire placement and high packing density, shown in Figure 6.4c. The coil winding head allows the coils to be placed automatically, requiring operator intervention only when starting or finishing a coil. This significantly decreases the time required to wind a core and reduces error and inconsistencies in the actuator construction. The coils are heat-set using a hot air gun and the wire ends are terminated and wrapped around a central winding guide made of paper phenolic, shown in Figure 6.4d. These terminations can be tinned with a standard soldering iron and connected with the copper traces used in our construction, shown in Figure 6.4e and Figure 6.4f.

These wound cores constitute the stator of our linear motor. The rotor consists of two neodymium permanent magnets (N50, 3mm x 3mm x 0.5mm) magnetized through thickness and oriented with opposite polarity. A wedge of Vimvar acts as a backiron flux return for this magnet pair. When the phase is energized with current, magnetic flux is directed alternately in and out of the legs of the magnetic core. This produces a force on the rotor that seeks to align the field of produced by the permanent magnets with that of the magnetic core. By alternating the direction of current periodically, the rotor can be made to oscillate at the driving frequency.

To create a functional unit, fiber-reinforced composite substrates and the magnetic components of the linear motor are combined in a set of assembly steps, shown in Figure 6.5. In Figure 6.5a, the wound magnetic cores, magnets, and back-iron components are populated on the composite substrate while in the flat state. This step is currently performed manually, but can be

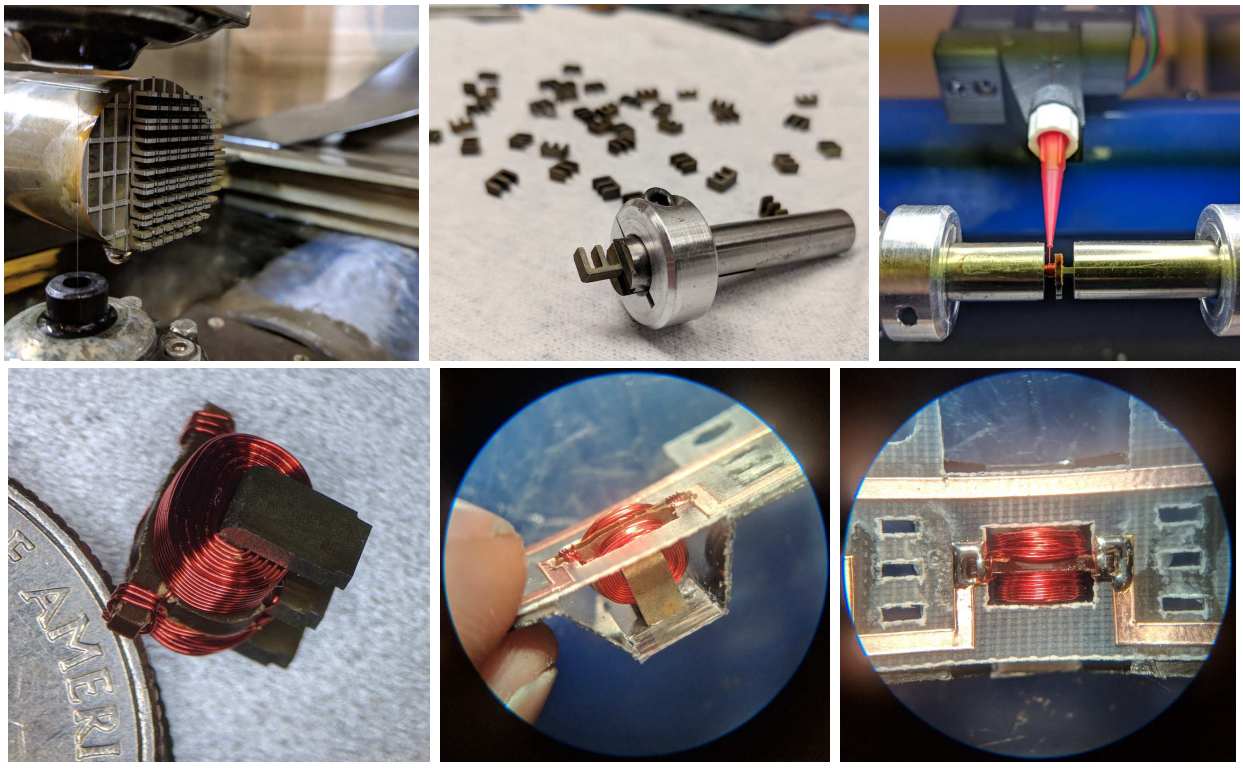

Figure 6.4: A) Electric discharge machining cores from round Vimvar stock, B) Released cores with winding clamp, C) Core during winding, D) Wound core with terminations (U.S. Quarter coin for scale), E) Wound core placed in honeycomb scaffolding, F) Wound core soldered for electrical connection.

automated in much the same manner as industrial PCB manufacturing for high production rates.

In Figure 6.5b, a wiring strip is attached using the magnetic cores for alignment, constraining the corrugation hinges and supplying soldered electrical connection to the motors. The wiring strips are produced using a simplified flex-PCB manufacturing process, where adhesive-backed copper foil is kiss-cut and transferred to 125um Garolite G10. The copper traces are optically registered, and additional features and an outline are cut. Again, while soldering was performed manually, this is amenable to reflow or wave soldering such as is used in industrial PCB manufacturing. At this stage, a skin strip is attached with cyanoacrylate glue, using magnet edges for registration. This skin strips are made with the same fiber-reinforced composite process described above, but with a overall thickness of roughly 100um.

In Figure 6.5c, the magnets and back-iron components are brought together with the aid of attractive forces, assembling the flexure bearings for the linear motors. This connection is strengthened with cyanoacrylate glue, completing the assembly of a full strip unit. Multiple units can be assembled to create a honeycomb with embedded linear actuators. The stator of one unit align with the rotor of an adjacent unit, loading the flexure bearings in tension and setting a consistent air gap (roughly 800 um in the prototype shown in Figure 6.5). The skin strips of each row overlaps slightly with that of the adjacent row. These skins are bonded and covered with adhesive-backed PET (50um thickness) to create a smooth hydrodynamic surface.

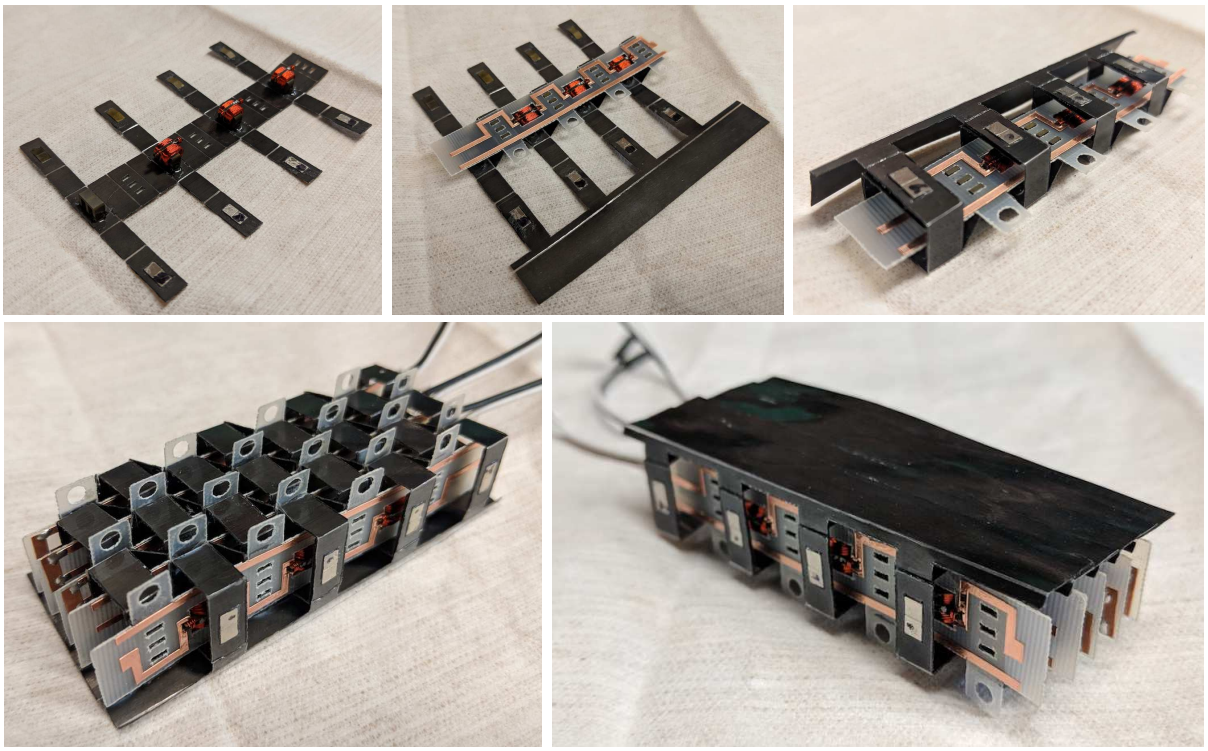

Figure 6.5: Assembly steps. A) Populate wound cores, magnets, and back-iron components, B) Apply electrical routing and skin strips to constrain corrugation hinge angles, C) Bring magnets and back-iron components together to complete flexure bearing, D) Multiple row units are stacked, E) Skin strips lap and are joined into a continuous aerodynamic skin.

6.2.2 Characterization

This section describes characterization of force and frequencies possible with the framework described above. We begin evaluating the force produced by the linear motors, comparing finite element simulation and experimental testing. The simulations were performed using COMSOL Multiphysics [96]. Figure 6.6 shows one simulation, with flux intensity and direction drawn for a linear motor in minimum (5a) and maximum (5b) configurations of the stroke when the phase current is one ampere. In Figure 6.6a, the field of the permanent magnets opposes the field produced by the coils, and flux seeks alternate paths than the iron core. In Figure 6.6b, the two flux distributions are aligned, providing a low reluctance magnetic circuit through the core. To simulate these effects, we assumed a planar flux distribution and ran a two-dimensional simulation, significantly lowering the computational burden. While the flux distributions are largely planar, this neglects fringing fields. Thus we expect simulations to slightly overestimate force produced but roughly preserve dependence on geometric parameters.

I simulated flux distributions and resulting force on the rotor for a range of coil currents, stroke positions, and core geometries. These studies indicated the size of the back-iron was significant in increasing actuator force but also in the moving mass. For these reasons, I designed the triangular back-iron shown in Figure 5, which limits magnetic saturation while avoiding unnecessary moving mass.

To compare simulated values with our physical prototypes, I measured force using a materials characterization machine (Instron 4411) with 5 N load cell, shown in Figure 6.7. I used linear slides

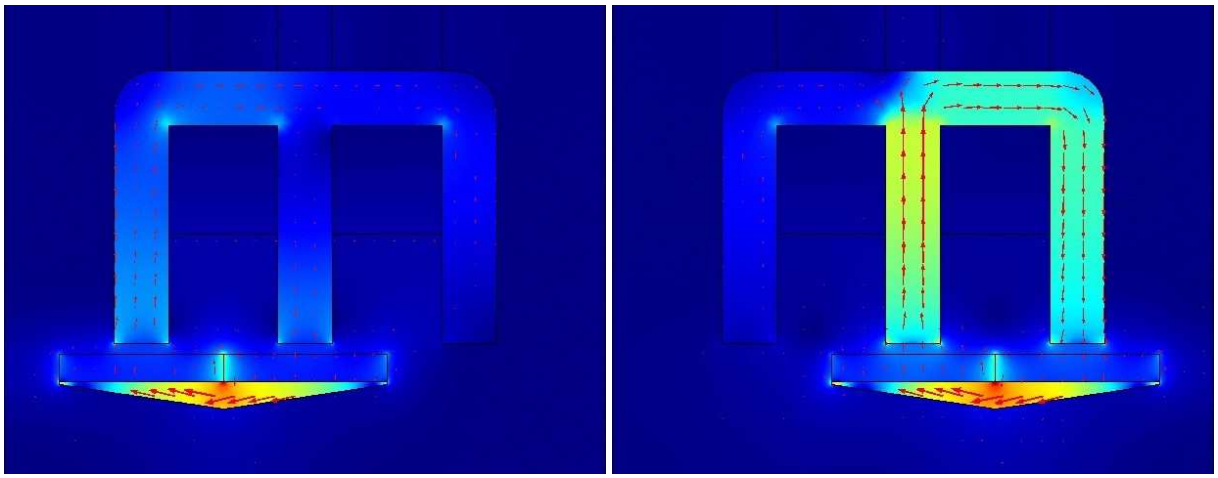

Figure 6.6: Simulated flux intensity (colormap) and direction (arrows) under positive current of 1 amp. A) A negative most stroke limit, B) At positive most stroke limit.

to precisely position the rotor and stator and transmitted force to the load cell using a Garolite flexure to avoid off-axis loads.

Figure 6.8 plots force vs. stroke and current for simulated and measured actuators with an 800um air gap. Deviations from a planar flux distribution are responsible for roughly 20% reduction in peak force at 1 ampere phase current. We note that $800\mu m$ is a conservative air gap, selected because smaller air gaps deformed rotor flexure under attractive forces. With a stiffer rotor, smaller air gaps could increase force without significantly increasing moving mass.

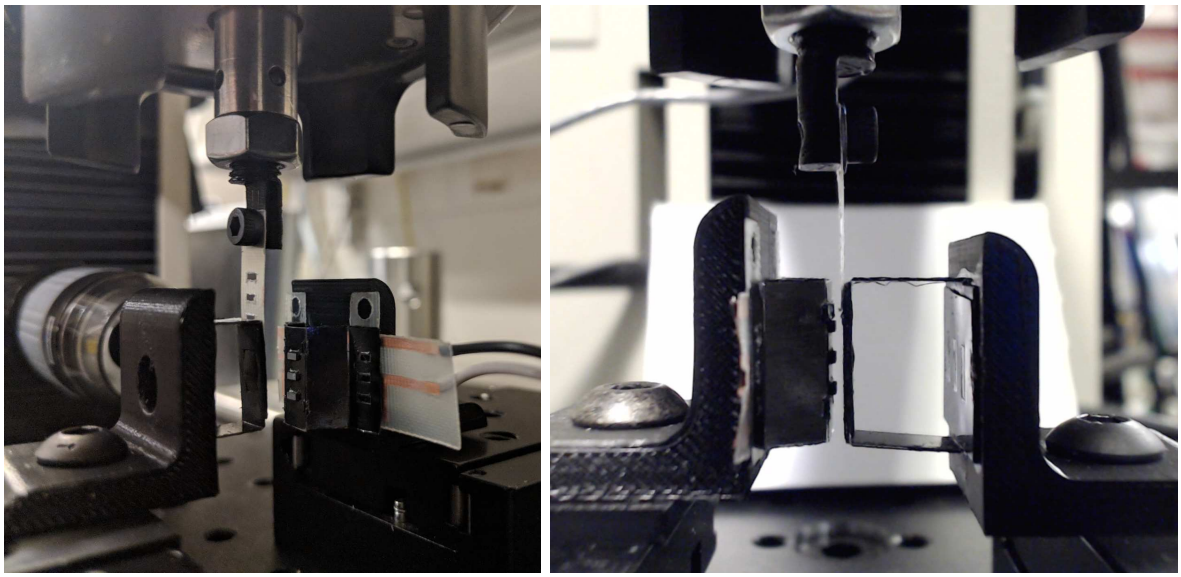

Figure 6.7: Test setup for force measurement on material characterization machine. A) Perspective view, showing 5N load cell, flexure for transmitting force, linear stages, and power wiring. B) Side view, showing prescribed gap between magnetic core and magnets.

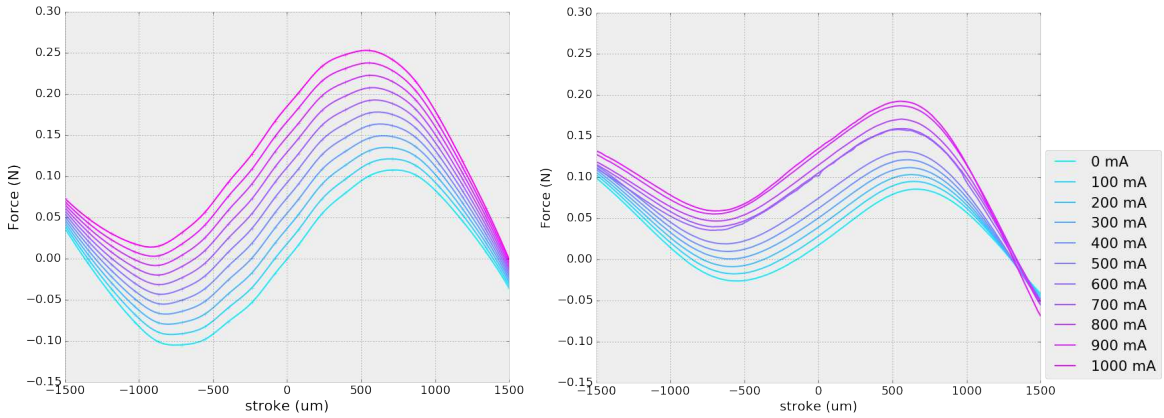

Figure 6.8: A) Two-dimensional simulation and B) measured force with 800um air gap.

6.2.3 Frequency

To characterize the maximum bandwidth of our actuators, I performed simple trials with square wave drive inputs of varying frequency using a single actuator with no skin attached. In a fully assembled honeycomb, the rotor travel is limited by the adjacent strip units, but to test variable travel limits, we implemented physical end stops using aluminum bars in these high frequency trials. Figure 6.9 shows the results of sending a 200 Hz driving frequency to the actuator with a current limit of approximately 1 ampere. The resulting trajectory was recorded using a high speed video camera (Krontech Chronos 1.4) at 3000 frames per second. I used video tracking software (Physlets Tracker) to extract the trajectory and plot it in Figure 6.9b. This simple test shows that our actuator is capable of driving its rotor at 200 Hz with an amplitude of approximately 1.2mm.

6.2.4 Fluid mechanical actuator specifications

In this section, we develope a set of specifications for a distributed actuation system for driving traveling waves on a hydrodynamic surface. For the characteristics of a desired wave shape, we

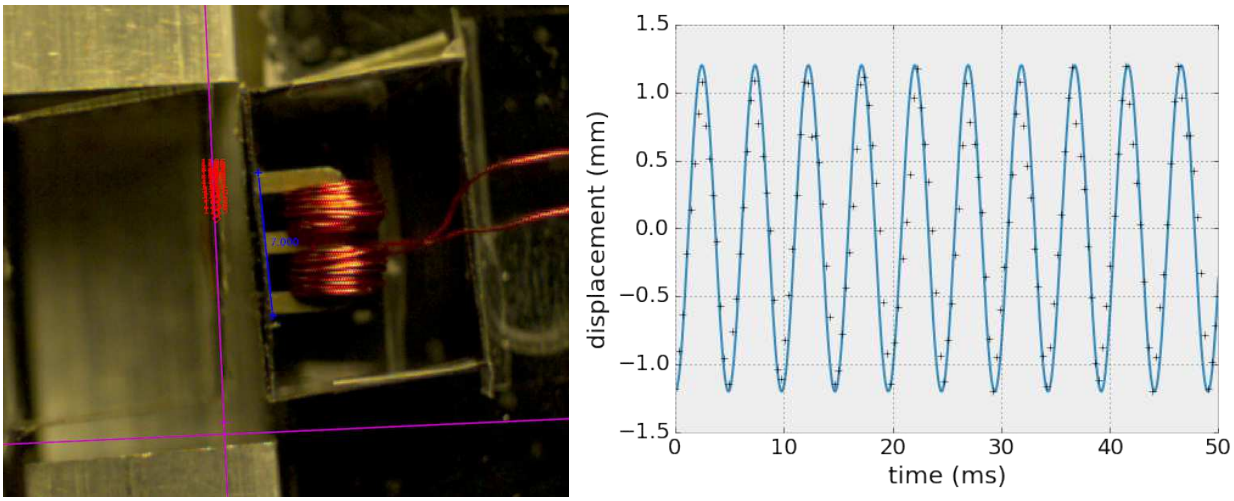

Figure 6.9: 200 Hz operation: A) High speed video with motion tracking, B) Extracted trajectory with a sinusoidal fit.

reference [168] for Reynolds number $Re = U\lambda/\nu \approx 10^4$. We use three parameters to specify the wave shape: the amplitude a, the wavelength λ and the wall motion phase speed c. The actuation frequency f of the actuators is derived as $f = c/\lambda$.

The literature uses the wave number ($k = 2\pi/\lambda$) times the amplitude to specify the wave steepness. Studies suggest values of ka of the order of 0.2 are appropriate. The wave speed is similarly prescribed by the dimensionless ratio c/U, where U is the free stream flow velocity. When this ratio is made greater than 1, separation is eliminated and the wall waves generate a thrust. At $c/U \approx 1.2$, energy optimality has been observed, as the power required to actuate the wall plus the power saved due to drag reduction is minimal. The choice of the wavelength is a tradeoff between actuator manufacturing constraints and fluid mechanic considerations.

To satisfy values from the literature and be within the constraints of a feasible actuator to design, we select an amplitude $a = 1mm$, a wavelength $\lambda = 20mm$, and frequency $f = 60Hz$, well within the $200Hz$ frequency oscillation with $1.2mm$ amplitude measured above. This gives a wave steepness of .31 and allocates four actuators per wavelength if each requires $5mm$ of chordwise extent. With a freestream velocity $U \approx 1m/s$ and a chord of $0.15m$, this gives $c/U \approx 1.2$ and chordwise $Re \approx 7.5 \times 10^4$.

To estimate the force requirements, we consider only force normal to the wall and assume a worst case estimate of actuating the suction side with maximal acceleration under the maximum pressure and inertial forces. Assuming a hexagonal packing of actuators with half-cell-span of $5mm$ as above, each actuator is responsible for a surface patch of area $A = 100mm^2$. Numerical simulation provides a pressure coefficient of 0.06, leading to $30Pa$ pressure. A typical hydrodynamic pressure is around $500Pa$. The total force produced by these pressures is around $53mN$.

To calculate the inertial forces, we must consider the actuator inertia and the fluid added mass. In general, the added mass in such a case of connected moving walls is not constant. In the case where the region under consideration has a small chordwise extent relative to λ, the force due to added mass can be written as $F = \rho akA(c-U)^2$. For the parameters identified above, this added mass force is on the order of $1mN$ (but increases greatly at larger values of c/U). Assuming a moving mass of 100 mg, the total required inertial force to operate at $60Hz$ is roughly $15mN$. This gives a total force requirement of roughly $70mN$, well within the 150mN forces measured over a significant part of the actuator stroke above.

These estimates of force and frequency requirements demonstrate a safe performance margin for our prototyped traveling wave actuation system. It is expected that this performance could be increased further by decreasing the air gap between rotor and stator and by accounting for the actuator transfer function in the driving waveforms, instead of using a simple voltage square wave. Despite these encouraging results, the task of scaling this system up to a full hydrofoil prototype was challenging due to the number of individual components which must be manufactured and assembled. Given that the traveling wave output requires many fewer degrees of freedom than the number of actuators in this prototype, we next describe a prototype which leverages this to simplify the manufacturing.

6.3 Two degree-of-freedom folded transmission

As mentioned above, the number of independent actuators in the previous design was a limiting factor for scaling. Not only does the assembly time scale with this number, but the failure of

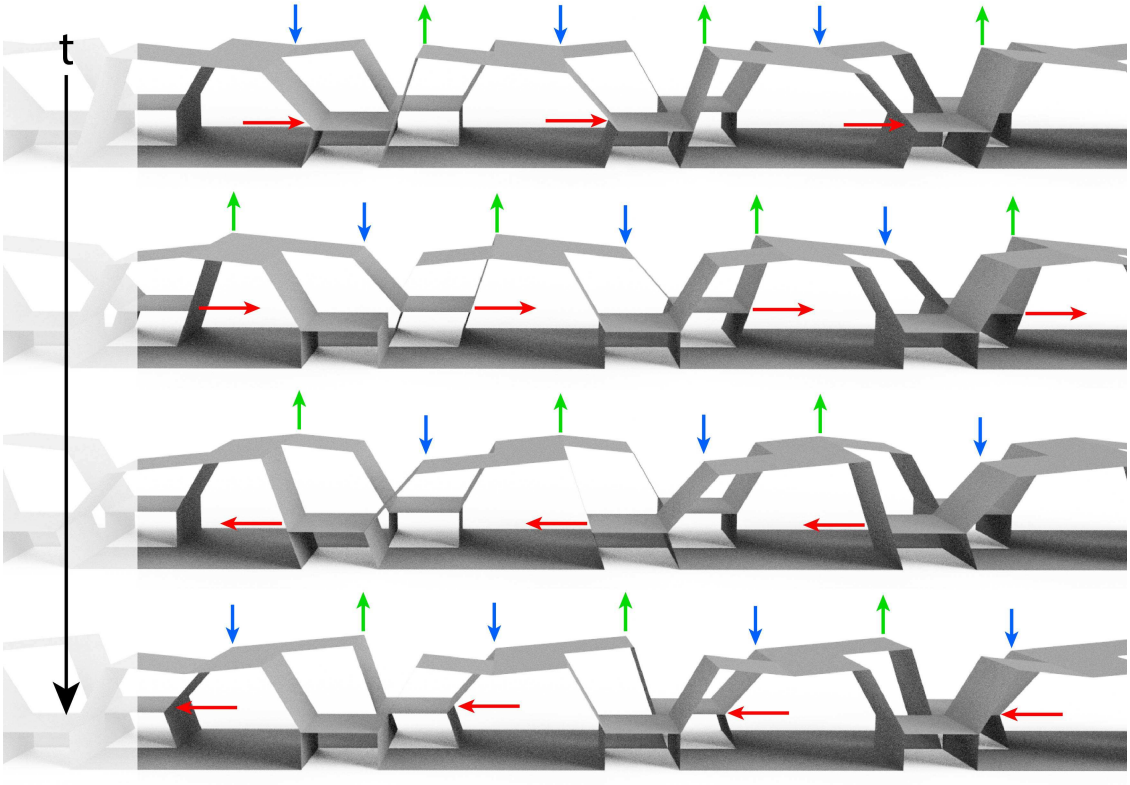

Figure 6.10: Folded structure using two degrees of freedom to drive a traveling wave. Proceeding from top to bottom in time, the sequence of peaks and valleys of the top surface (green and blue arrows) moves to the right based on the actuation of the middle surfaces (red arrows).

any one of these actuators could cause the entire prototype to stop functioning. To fix this issue, we redesigned the prototype to use just two independent actuators, which we describe in this section. In this case, we use a folded transmission to convey motion from these actuators to drive the complex traveling wave motion. Our design is shown in Figure 6.10 at four moments in time, proceeding from top to bottom. The sequence of peaks and valleys of the top surface (green and blue arrows) moves to the right based on the actuation of the middle surfaces (red arrows). Note that only two independent degrees of freedom are required, as all of the front middle surfaces move together and the rear middle surfaces move together. This can be considered a form of quadrature, as the 90° out-of-phase actuation of these two degrees of freedom sets the direction of the traveling wave.

6.3.1 System Design

Based on this folded linkage, I designed an actuated system, shown in Figure 6.11 with a NACA18 hydrofoil base. To leverage planar processing, the design is decomposed in layers, each of which spans the entire extent of the actuated region of the foil. The very top layer is a thin carbon skin layer to interpolate between the discrete oscillating points. The next outermost layers together form the linkage in Figure 6.10. The linkage is actuated by a planar Lorentz force actuator; the next two layers inwards are iron cores with magnets which create a vertically oriented flux between them. Finally, the innermost two layers are planar electromagnetic coils which produce horizontal

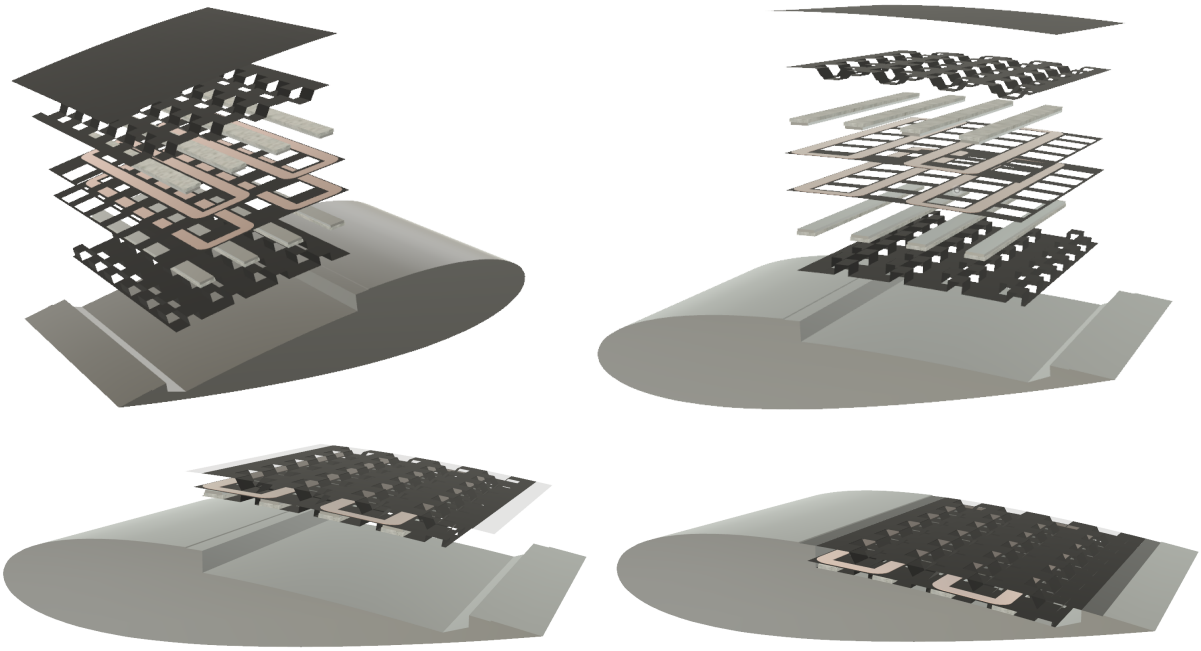

Figure 6.11: Exploded and assembled views of two degree-of-freedom prototype design.

force in the vertically oriented magnetic field when current is passed through them.

6.3.2 Simulation

Using COMSOL Multiphysics [96], I refined the electromagnetic design for the flat Lorentz force actuator, subject to the geometric constraints of the design. Figure 6.12a shows a two-dimensional view looking down the length of the planar coils (rectangles at center), where the iron core and magnets establish a vertically oriented flux field. Figure 6.12b shows a three-dimensional view, where the geometric features to keep the magnetic cores separated without causing a collision with the linkage are visible. Compared to the linear motors of the previous section, these actuators have several nice features. First, the force is nearly constant over the full stroke, simplifying the dynamics of the system. Second, there is no attraction between the rotor and stator elements,

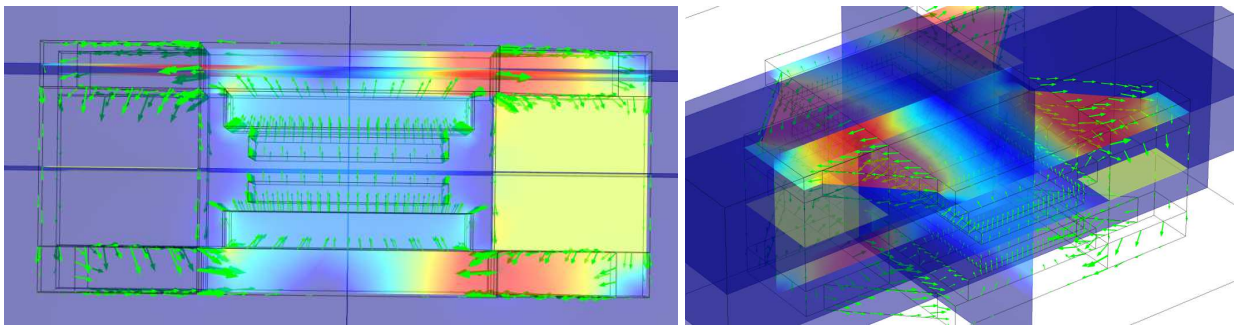

Figure 6.12: Electromagnetic finite element simulation of the flat Lorentz force actuator for the two degree-of-freedom prototype, showing magnetic flux density (colormap) and direction (arrows). a) Looking down the length of the planar coils, b) Three-dimensional view.

significantly simplifying assembly.

After this design refinement, I set out to fabricate a prototype. The linkage layers can be fabricated using the carbon-polymer process described in Chapter 4. The iron cores can be cut from a zinc-plated steel sheet by waterjet abrasive machining. The only component remaining are the planar coils forming the central two layers of the device. To make these layers, I developed a precision wire plotting technique, described in the next section.

6.3.3 Wire plotting

Electromagnetic coils are usually made by winding insulated wire around a mandrel to build up layers in both the radial and axial directions [80], as in Section 6.2.1. This approach is best suited for convex coil geometries where the number of layers in the radial direction is not significantly larger than the number of layers in the axial direction. Attempting to wind geometries with significantly more radial than axial layers (i.e., planar geometries) requires complex multi-part mandrels and usually results in poor wire packing density. Because of this, planar coils are often made using printed circuit board traces (c.f. [92, 149, 104, 28, 195]), but the constraints on small trace widths and separations limit the achievable turn density, and hence electromagnetic force.

Due to this lack of a feasible process to make dense, high quality planar coils, I developed a process for precision plotting of wire onto planar substrate with exposed pressure set adhesive. This process combines the high density of coil winding with the geometric control of printed circuit board fabrication. Figure 6.13 shows 40 AWG insulated copper wire (approximately 80 μm conductor diameter with 5 μm insulation) laid onto a 12 μm polyamide film with a silicone pressure set adhesive. Because the wire is insulated, it can be packed densely to produce a variety of actuators, sensors, and electrical interconnect. With proper wire management, this process can operate at speeds exceeding 1000 mm/s, allowing high speed fabrication of wire wound components. This process can be considered a form of additive electronics manufacturing, but significantly better material properties and much lower costs than printed ink electronics ($1.6\mu\Omega-cm$ at $\$40/kg$ for insulated copper wire versus $10\mu\Omega-cm$ at $\$1000/kg$ for silver ink). Compared to conventional circuit board manufacturing, achievable densities are an order of magnitude greater

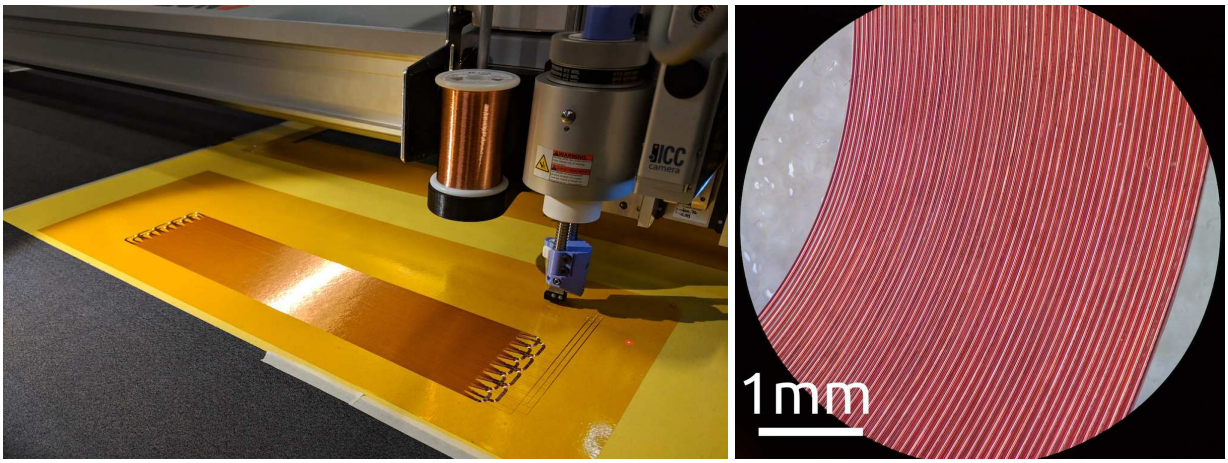

Figure 6.13: Process for plotting wire on a planar substrate. a) Spool and custom wire plotting tool on Zünd Systemtechnik large format cutter laying wire onto a substrate with exposed pressure set adhesive. b) Microscope image of the resulting planar coil, showing 25 turns of 80 μm diameter wire.

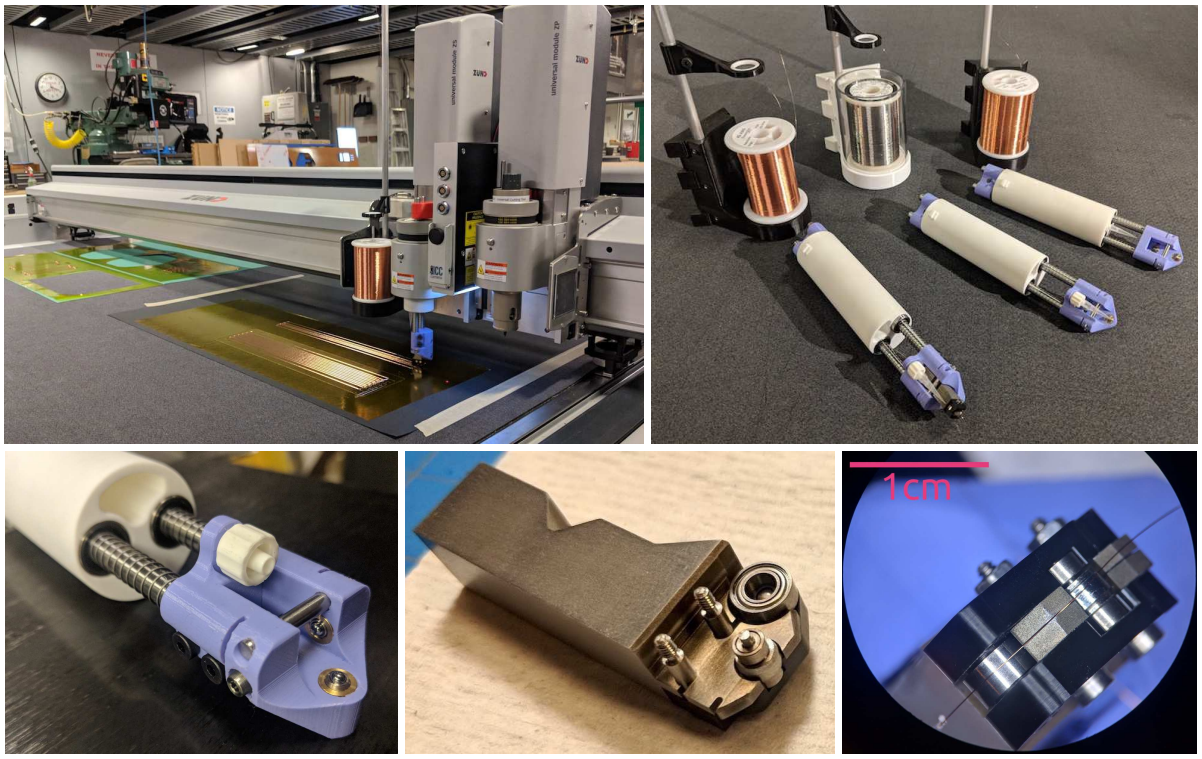

Figure 6.14: Wire plotting components. a) Zünd cutter with wire plotting tools installed, b) Spool holders, wire management, and application toolheads, c) Sprung suspension, kinematic mount, and micro-adjusting ball end screws, d) Final wire guide and application roller disassembled, e) Final guide and application roller with $80\mu m$ wire.

($2\mu m$ and $20\mu m$ conductor separation and width versus $75\mu m$ and $75\mu m$) and costs scale with volume of active materials rather than with volume of the device's bounding box. These capabilities are made possible by leveraging scalable and repeatable upstream wire fabrication processes in combination with modern motion control technology for high-speed precision plotting.

To do this, I developed custom toolheads for a Zünd Systemtechnik large format cutter, shown in Figure 6.14. These consist of a spool holder, wire management and tensioning system, and a precision application head, shown in Figure 6.14a. The spool holder accepts a standard 2.5" wire spool, one which wires of a variety of base materials, diameters, and coatings are commonly

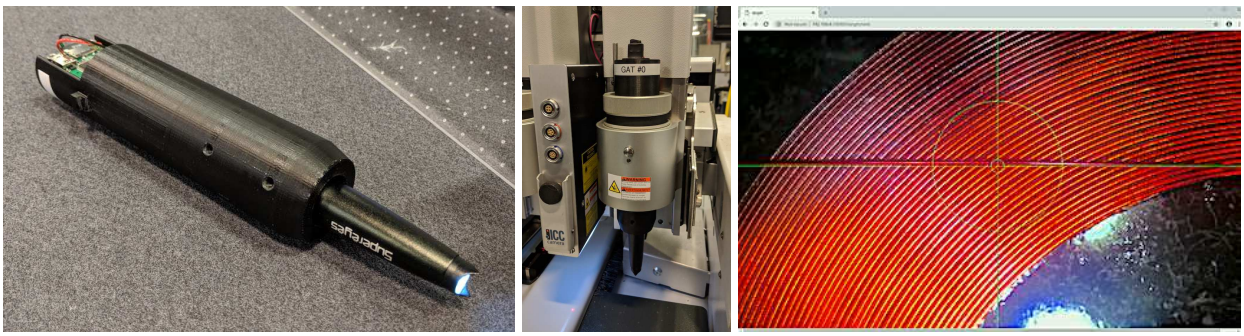

Figure 6.15: Optical calibration of wire plotting. a) Custom tool with USB microscope and Raspberry Pi single board computer to wirelessly stream video feed, b) Microscope tool installed in Zünd cutter, c) Measuring $80\mu m$ wire placement from a web browser.

available at low cost (e.g. $\$1/km$ for 40 AWG insulated copper wire). Figure 6.14b shows spools of insulated copper and nickel-plated steel wires of several sizes. Wire is taken off the spool, passes through a set of PTFE O-ring guides, between felt tensioners, and over a set of guide rollers before reaching the application head.

The wire is applied to a thin polymer film substrate (usually PET or polyamide) with a pressure set adhesive to hold the wire in place. During plotting, a piece of Bristol board with a repositionable adhesive is used underneath the polymer film to provide a firm underlay that still allows the vacuum hold-down of the Zünd cutter to pass through. After plotting, the substrate and underlay can be cut out or scored to allow folding the plotted wire into multilayer and nonplanar configurations. Finally, the open face of the substrate is covered to permanently hold the wire, usually with another piece of polymer film or a composite prepreg.

The Zünd cutter uses a rotational axis to align the application toolhead with the direction of plotting, but to plot accurately the axis of this rotation must be precisely aligned with the point of wire application on the substrate. To do this, I use a sprung suspension in the application toolhead to accurately control the application force in spite of dimensional variations in the substrate. Further, the final wire guide and application roller mount kinematically on a hardened shaft and a set of ball-ended micro-adjusting screws (Kozak Micro, 3/16"-100). The final guide spacing is set using precision shim stock to accurately constraint the lateral position of the wire without adding friction to the system. These features (shown in Figure 6.14c-e) allow the point of application to be consistently controlled to a precision of approximately 10 μm.

To accurately align the application point with the rotational axis of the tool, I developed an optical measurement tool, shown in Figure 6.15. It consists of a USB microscope (Supereyes B008), Raspberry Pi single board computer (Pi Zero W), and USB rechargeable battery mounted in a 3D printed toolholder. The Raspberry Pi acts as a wireless access point, broadcasting the MJPEG stream from the camera. By plotting a test pattern of wire and measuring the results using this optical system and the Zünd cutter's digital read-out, we can adjust the kinematic coupling of the applicator roller to align it.

6.3.4 Fabrication

Using the wire plotting process described in Section 6.5, I fabricated the planar coils for the Lorentz force actuators. This process is shown in Figure 6.16. Mirror images of the 25 turn coils are plotted on $12\mu m$ polyamide with silicone adhesive (Caplinq PIT0.5S-UT) and cut out,

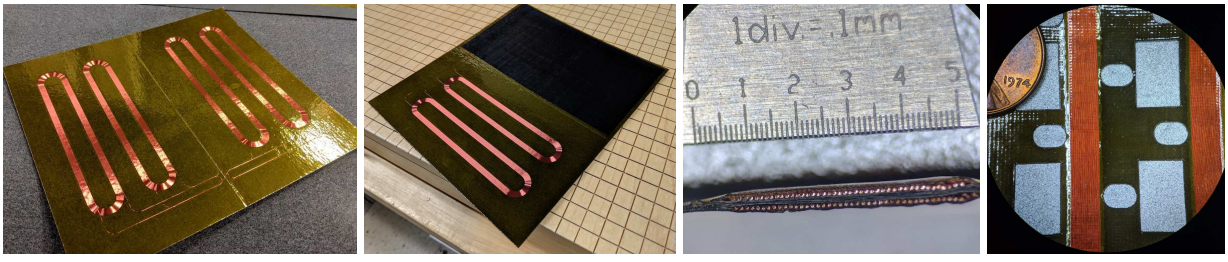

Figure 6.16: Wire plotting the planar coils for the Lorentz force actuator to drive traveling waves. a) Mirror images of the 25 turn coils are plotted and cut out, b) The plotted sections are folded around a piece of carbon prepreg and cured, c) A microscope section view of the double layered planar coils. d) Microscope image of cured planar coil, with additional features cut (U.S. penny coin for scale).

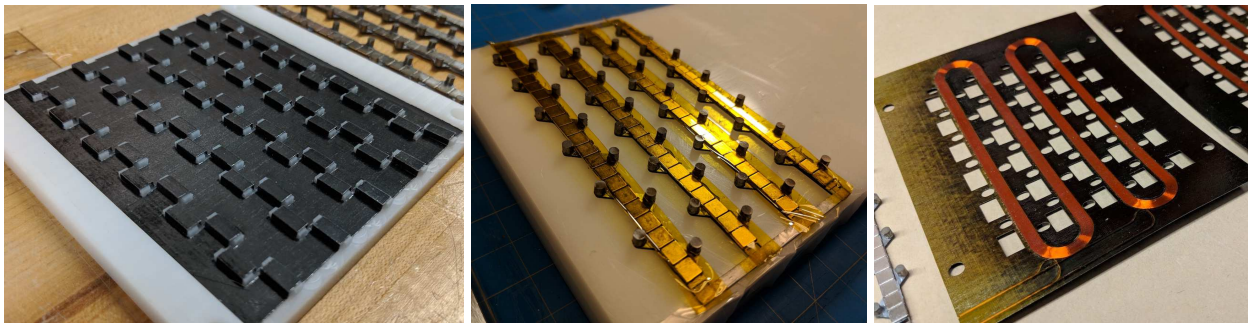

Figure 6.17: Fabricating the layers in the two degree-of-freedom prototype. a) The linkage layers used the carbon-polymer process developed in Chapter 4, b) The iron cores were waterjet and magnets were bonded on, c) The planar coils were plotted using the wire plotting process developed in Section 6.5.

keeping the Bristol board underlay in place to aid handling. A central crease is scored during the cutting process. This part is folded around a piece of carbon prepreg (shown in Figure 6.16b) to form a double layered construction with the 25 turn coils wired in parallel. A cross section of the construction is shown in Figure 6.16c. Once cured, these coil layers are taken back to the Zünd cutter, registered with the microscope tool, and additional features are cut for the traveling wave prototype, shown in Figure 6.16d.

For the two degree of freedom traveling wave prototype, the linkage layers are fabricated using the carbon-polymer process described in Chapter 4. One of these layers is shown in Figure 6.17a. To create the magnetic flux for the Lorentz force actuator, a pair of zinc-plated steel plates held apart by steel rods forms the magnetic circuit. The plates were waterjet, and the rods were positioned using a laser-cut acrylic jig plate and bonded to the plates. Neodymium magnets

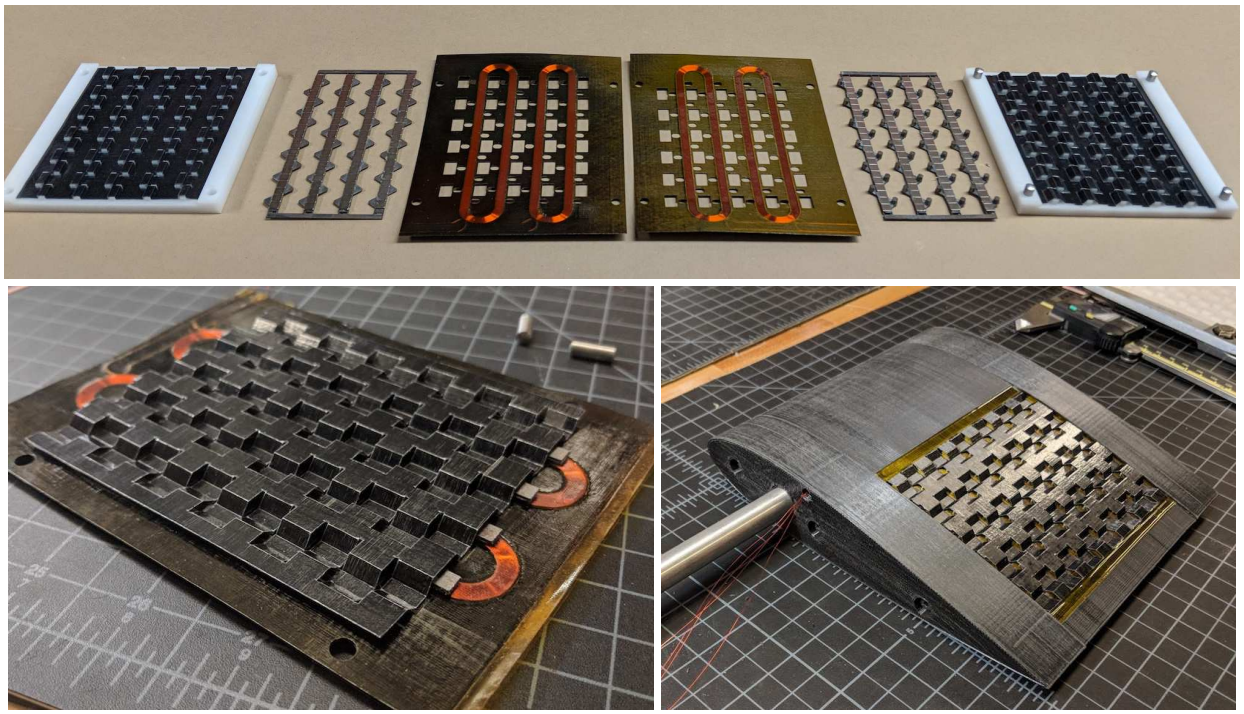

Figure 6.18: a) Layers in two degree-of-freedom prototype. From outside-in: Carbon-PET linkage layers, the iron cores and magnets, and the planar coils. b) Layer stack laminated together, c) Stack installed in hydrofoil

(N52, 5mm x 5mm x .75mm) are applied to the central axis of the plates. Theoretically, a long skinny plate magnet could perform this job, but these are difficult to source and very fragile. Instead, magnets are applied from a 3D printed dispenser to a tape and transfer the magnets and tape to the steel plates (which have had epoxy applied to them). This magnetic layer is shown in Figure 6.17b, and the finished planar coil layer is shown in Figure 6.17.

These fabricated layers are shown in Figure 6.18a and assembled in Figure 6.18b. Epoxy is applied to the linkage layers through a laser cut mask and then the stack is aligned and compressed using two milled polyethylene plates with dowel pins.

6.3.5 Characterization

To validate the simulations in Section 6.3.2, I measured the force produced by a single layer actuator as a function of stroke and phase current. To measure the force produced, I clamped the actuator in the jaws of an Instron 4411 test frame with 500 N load cell. I swept over the full stroke of $2mm$ while measuring the force. The results are shown in Figure 6.19a, showing nearly constant force over the stroke. I averaged these force values and plotted them versus current in Figure 6.19b. These results match very closely with two separate finite element models: the first using a COMSOL coil element, the second calculating the surface integral over the geometric envelope of the coil and applying the Lorentz force law. The close match between the simu-

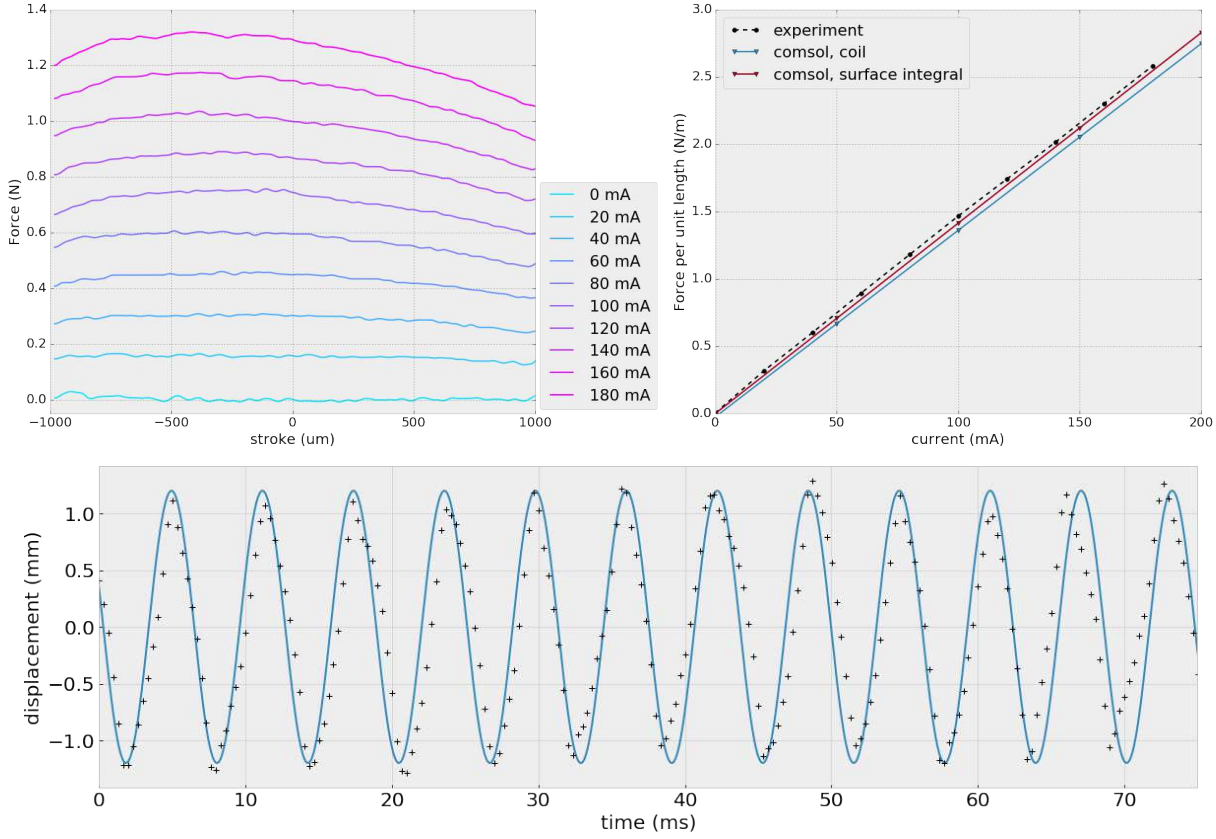

Figure 6.19: Characterizing the planar Lorentz force actuator. a) Plotting force versus stroke for a range of phase currents, b) Plotting average force over the stroke versus current and comparing against simulated values. c) Tracking amplitude at $150Hz$ actuation frequency.

lated planar Lorentz force actuator and the experimental results demonstrate a key benefit of this actuator topology: its simplicity to model and drive.

Figure 6.19c shows high speed video tracking results for the planar Lorentz actuator at a frequency of $150Hz$. This achieved frequency is well above the traveling wave bandwidth requirements.

These characterization results demonstrate the viability of this two degree-of-freedom prototype. While the number of independent actuators has been drastically reduced from the first prototype, the structural complexity is still high. In particular, the layered approach of this design requires many cut-aways and pass-throughs to function. Slight misalignments in these features can reduce performance, and the clearance required between coil layers increases the size of the magnetic air gap, lowering output force. The wire plotting process developed for this prototype worked better than expected, proving to be a very powerful prototyping workflow for embedded electromagnetic actuation. In the next section, I detail the use of wire plotting directly on a flexible membrane comprising a third traveling wave prototype.

6.4 Moving membrane traveling wave

In this section, I use the wire plotting developed in Section 6.5 to plot electromagnetic actuation directly on a membrane interacting with the flow. In Section 6.3, plotted wires in a vertically-oriented magnetic field experience a horizontal force, and folded linkage layers transmit this into force vertical oscillations of a traveling wave. Using a horizontally-oriented magnetic field, the plotted wires can experience a vertically oriented force, creating the traveling wave directly. Instead of using linkage layers to generate the directional quadrature, I use quadrature in the driving signals of the plotted coils. Figure 6.20 shows a prototype NACA12 hydrofoil with a wire plotted skin on its trailing edge. The coil arrangement is much like a linear motor, where three phases are interleaved and repeated. In Figure 6.20b, we show the terminations of these coils enabling three phase waveforms, like those used to drive common brushless motors, to be used to generate traveling waves.

6.4.1 Magnetic design

To obtain the sufficient magnetic field strength in the horizontal direction at the skin, I investigated possible magnet arrangements. Figure 6.21 shows three magnet arrangements: vertically

Figure 6.20: a) Actuated membrane applied to NACA12 hydrofoil, b) Lead connections for three-phase actuation.

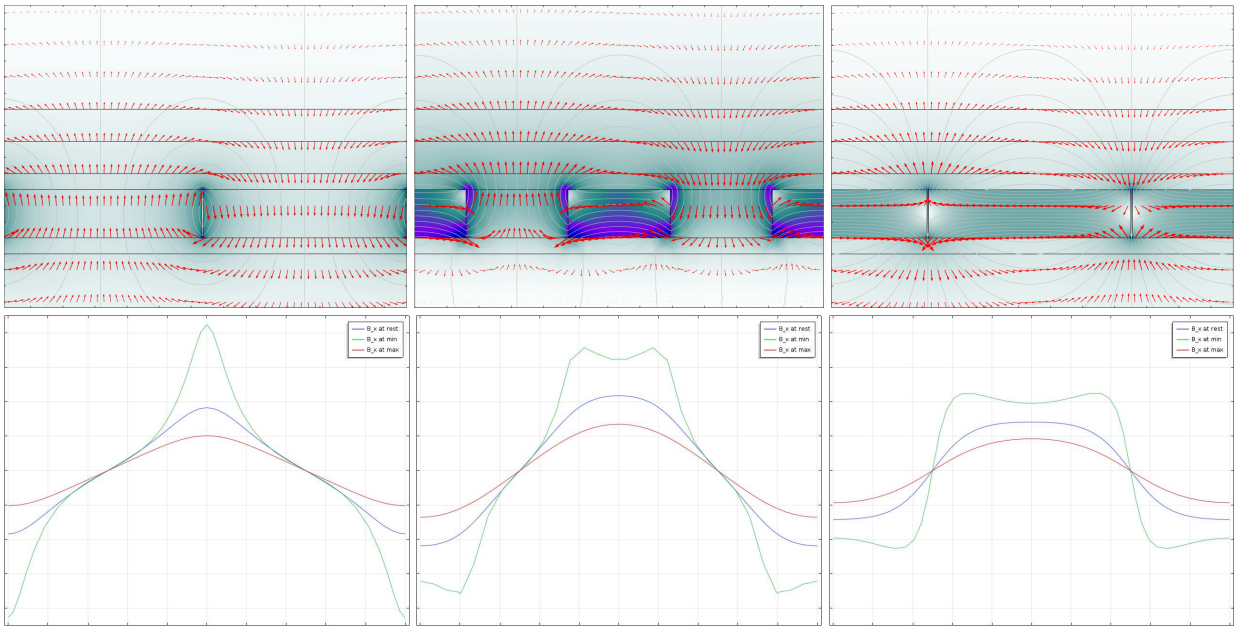

Figure 6.21: Comparing a vertically-magnetized array, Halbach array, and horizontally magnetized array. a-c) Flux density (colormap) and direction (arrows) for the three arrays, d-f) Horizontal component of magnetic field at three heights above the array (green is closest, then blue, then red). One vertical division is 0.1 Tesla.

oriented alternating, a linear Halbach array [125], and horizontally oriented alternating. In fact, the Halbach array can be considered a middle point between the other two arrangements, as it consists of interleaved alternating vertically and horizontally oriented magnets. The top row of plots graphs the magnetic flux density (colormap) and direction (arrows). In the bottom row, the horizontal component of the flux density at three heights above the array is plotted (green is closest, then blue, then red). We see that a vertically alternating array produces the highest peak field value, but only over a small spatial region. The horizontally alternating array produces a large spatial region near its maximum field value, but this value is much lower. The Halbach array is an optimal middle ground between then extremes, showing a maximum field value near that of the vertically oriented array, but with a much wider spatial distribution. In fact, if we integrate this field value over a representative volume (where we can imagine placing actuator wires), the value is roughly 150% that of either of the horizontally or vertically magnitized configurations.

Finally, I simulated the three-dimensional effects on flux density of these Halbach arrays, shown in Figure 6.22. Using neodymium magnets that were cost-effective to source (N50, 1/8" wide by 1/16" thick by 1/2" long), I plotted the flux distribution both at the coil center, as well as at the coil edge, shown in Figure 6.22a-b. Integrating over the envelope of the moving coil, I obtained an average flux density of roughly 0.12 Tesla.

The favorable magnetic properties of Halbach arrays come with a price, as they are usually difficult to fabricate because all magnets repel their neighbors. To help with this, I made an assembly aid which extrudes a Halbach array, shown in Figure 6.23. The extruder draws from four magnet cartridges, one for each orientation. Array holders are filled, holding magnets in place while a thin piece of carbon is bonded to their roughened surface with epoxy. After curing, the Halbach arrays are transferred to the hydrofoil.

6.4.2 Three phase control

Because controlling the traveling wave shape is important, the drive electronics for our prototype must allow control over the commutation waveform (e.g., to implement sinusoidal commutation), rather than being limited to six-step or trapezoidal schemes. Assuming actuation frequencies of $100Hz$ and a sine function lookup table with 100 entries, we estimate a $10kHz$ update rate for the commutation waveforms. Many brushless motor drivers have pulse-width-modulation frequencies slower than this rate, and so clearly a high speed three phase driver is required to drive our prototype. As an added benefit to high-speed modulation, the inductance of the devices can be reduced. Drive electronics for brushless motors often rely on the significant inductance of iron-cored windings or external series inductors to smooth out pulse-width-modulated waveforms. With high speed modulation, no such inductance is required, and the associate magnetic losses can be eliminated, increasing efficiency.

To meet these requirements, I designed a circuit board (shown in Figure 6.24) with three N

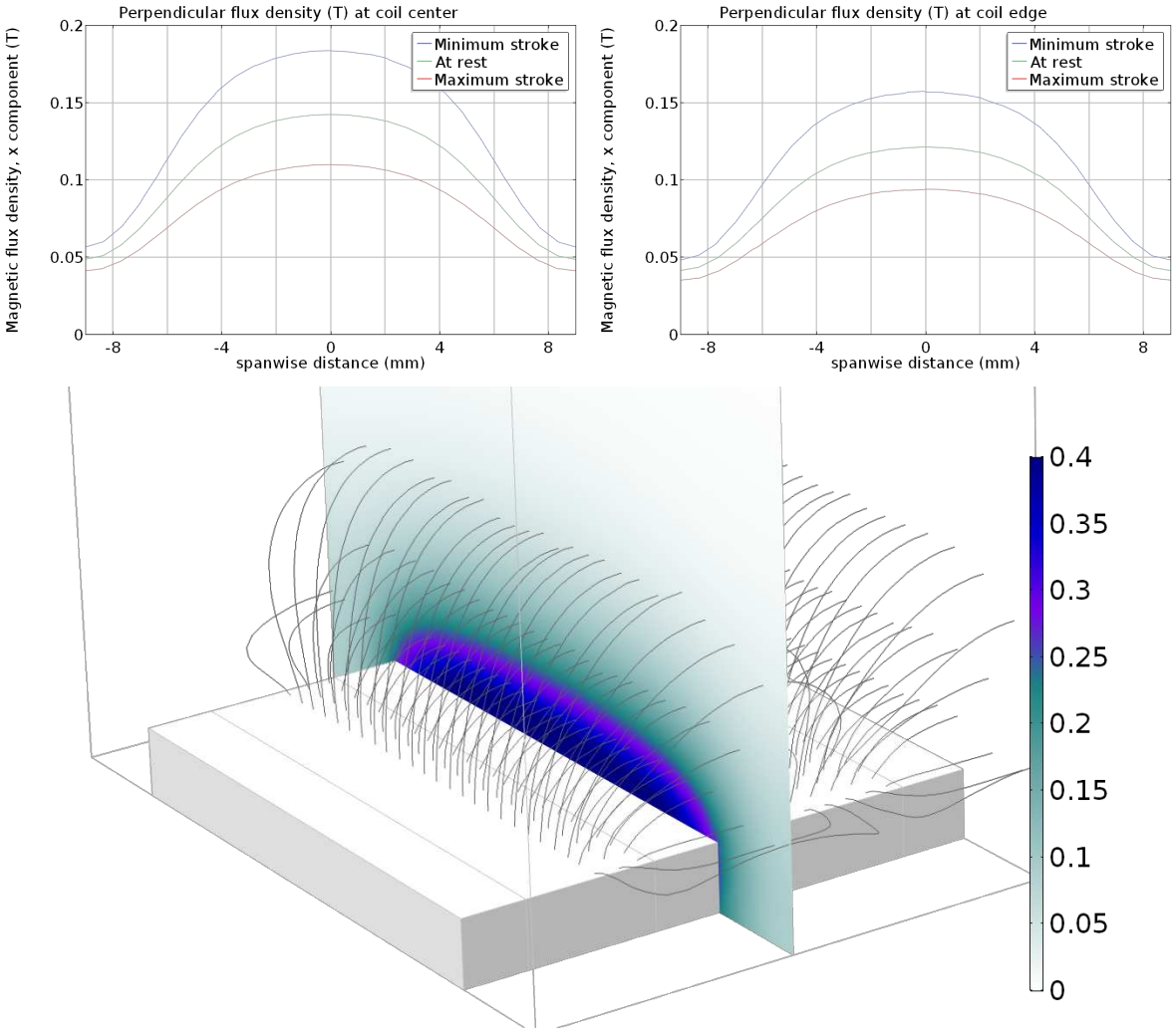

Figure 6.22: 3D simulation of Halbach magnet arrays. a) Plotting horizontal flux density at the coil center for the minimum, maximum, and rest heights of the coil, b) Plotting horizontal flux density at the coil edge for the same three heights, c) 3D view, showing flux density (colormap, units in Tesla) and direction (streamlines).

Figure 6.23: Halbach assembly aids. a) Halbach extruder draws from four cartridges of magnets, one for each orientation, b) Cartridges are filled and bonded to a thin piece of carbon, c) Halbach arrays are transferred to the hydrofoil.

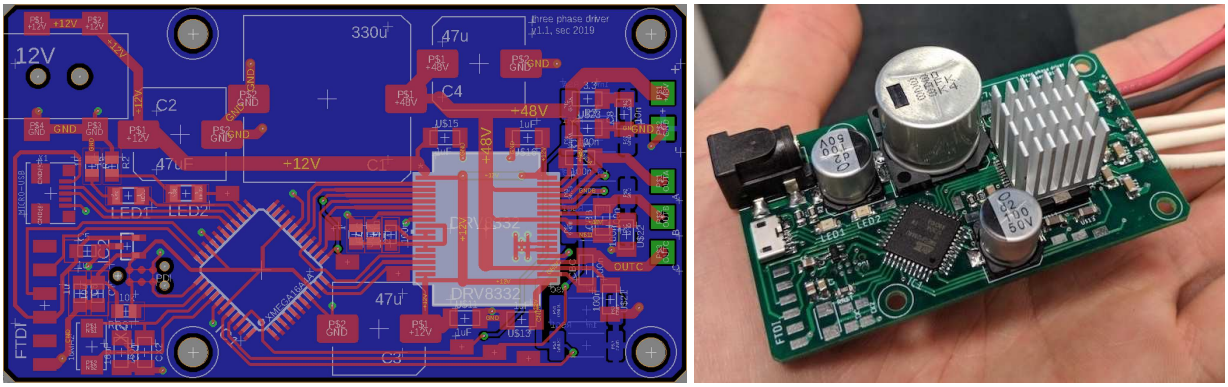

Figure 6.24: High speed three phase driver for implementing space vector modulation. a) Board design, b) Prototype.

MOSFET half-bridges and gate drives capable of $500kHz$ pulse-width-modulation frequency at voltages up to $50V$ (packaged in Texas Instruments' DRV8332). The commutation waveforms are generated on an Atmel XMega A4U microcontroller, which also includes an analog-to-digital convertor for measuring phase currents using low-side sense resistors. USB and serial host interfaces allow the device to be controlled and the sensed values to be reported. I implemented space vector modulation [171] control for the generation of complementary three-phase signals based on a sine lookup table using hardware timer/counters. This implementation is significantly simplified by using complementary waveforms (i.e., those which sum to zero at all points in time). As the sum of all n^{th} roots of unity sum to zero for all n, this holds for our sinusoidal waveforms with $120°$ phase offset ($n = 3$), as well as generalizations to $n > 3$.

6.4.3 Characterization

I fabricated many prototypes of the moving membrane design using the three-phase wire plotted skin and Halbach magnet arrays on a 3D printed NACA12 hydrofoil with $150mm$ chord length and $450mm$ span, shown in Figure 6.25a. The result of this iteration was a functional prototype, shown in Figure 6.25b. In this prototype, $80\mu m$ (40 AWG) wires were plotted onto $25\mu m$ polyamide film with silicone adhesive (GizmoDorks) and covered with $2\mu m$ PET film (DuPont Mylar C). Each of the three phase windings consists of a four planar wire 25 turn bundles in series (organized into two coils). These phases are wye-terminated for a phase resistance of 100Ω. The hydrofoil includes an adjustment mechanism for tensioning the membrane, as well as a path

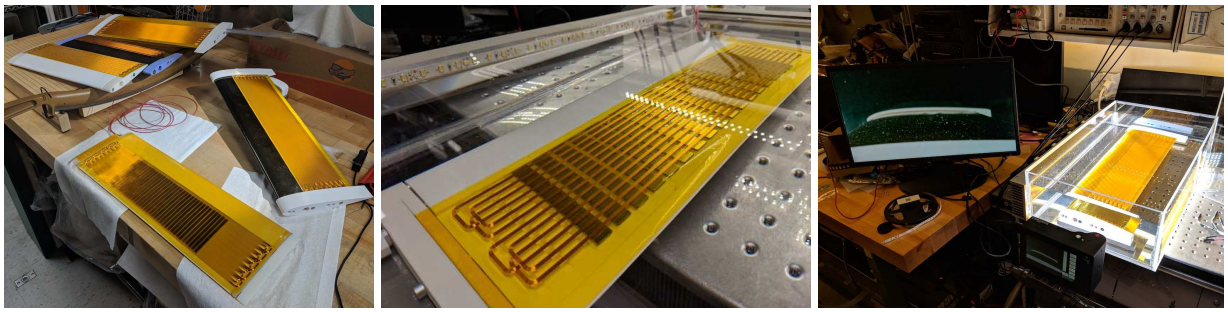

Figure 6.25: Characterizing moving membrane prototype. a) Assembled prototype underwater, showing wire plotted membrane and Halbach magnet arrays on a 3D printed NACA12 hydrofoil. b) Taking high speed underwater video.

to route the three phase leads away from the hydrodynamic surface.

To optimize the design and microcode in operating conditions, I built a small water tank designed for collecting high speed video, shown in Figure 6.25c. Using the driver described in Section 6.4.2, I actuated this prototype underwater at $f = 50Hz$ and $36V$ sinusoid amplitude, recording video at 2400 frames per second using a Chronos 1.4 high speed camera.

From this video, I measured a traveling wave amplitude of $a = \pm 500\mu m$. For this design, the wavelength is $\lambda = 19mm$, which gives a wave steepness factor of $2\pi a/\lambda \approx 0.15$. This value is the range of values covered by the simulation literature on traveling wave flow control. Characterizing the shape of these traveling waves from video is difficult due to the small amplitude, so I used dense optical flow analysis between frames to estimate the velocity of movement at every pixel. I used the `Coarse2Fine` dense optical flow algorithm [119, 148] between every five frames (a time interval of $2ms$). Figure 6.26 shows a sample frame from the video, along with three frames separated by $12ms$ each that have been blended with the calculated optical flow. Hue denotes direction (purple is upwards, green is downwards) and value denotes magnitude (brighter is faster). From this analysis, we can clearly see the propagation of wavefronts at the speed of $\lambda f \approx 1000mm/s$.

We can estimate the power required to drive these traveling waves under optimal conditions with a simple physical model incorporating the distributed actuator moving mass and the added mass from the fluid interaction. The moving mass is given almost entirely by the mass of the copper windings, which we can calculate based on the wire diameter and the plotted geometry. As a pessimal assumption, we assume all the kinetic energy of the moving mass is dissipated by the fluid. For a mass m undergoing sinusoidal oscillation $z(t) = a\sin(2\pi ft)$, its average magnitude of acceleration is given by $\langle|\ddot{z}|\rangle = 8\pi af^2$, and hence the average force required to drive the moving mass is $\langle|F_{mm}|\rangle = 8m\pi af^2$. Because the mass travels a distance of $4a$ during one period, the average power required to drive the moving mass is $\langle P_{mm}\rangle = 4a\langle|F|\rangle f = 32\pi ma^2f^3$. Now, the added mass force from fluid interaction is given by $\langle|F_{am}|\rangle = \rho\frac{2\pi}{\lambda}aA(c-U)^2$, where ρ is the fluid density, and A is the area under consideration, c is the wave speed, and U is the flow speed [33]. As before, we calculate the power required to drive this added mass as $\langle P_{am}\rangle = 4a\langle|F_{am}|\rangle f = 8\pi\rho\frac{a^2}{\lambda^2}Ac(c-U)^2$. In Figure 6.27, we use geometric dimensions from the prototype and plot the average force and mechanical required for driving traveling waves as a function of the relative speed (c/U).

Based on this estimate of required force, we can calculate the corresponding Joule heating loss in the coils of the actuated skin. Because these electromagnetic actuators have no iron core

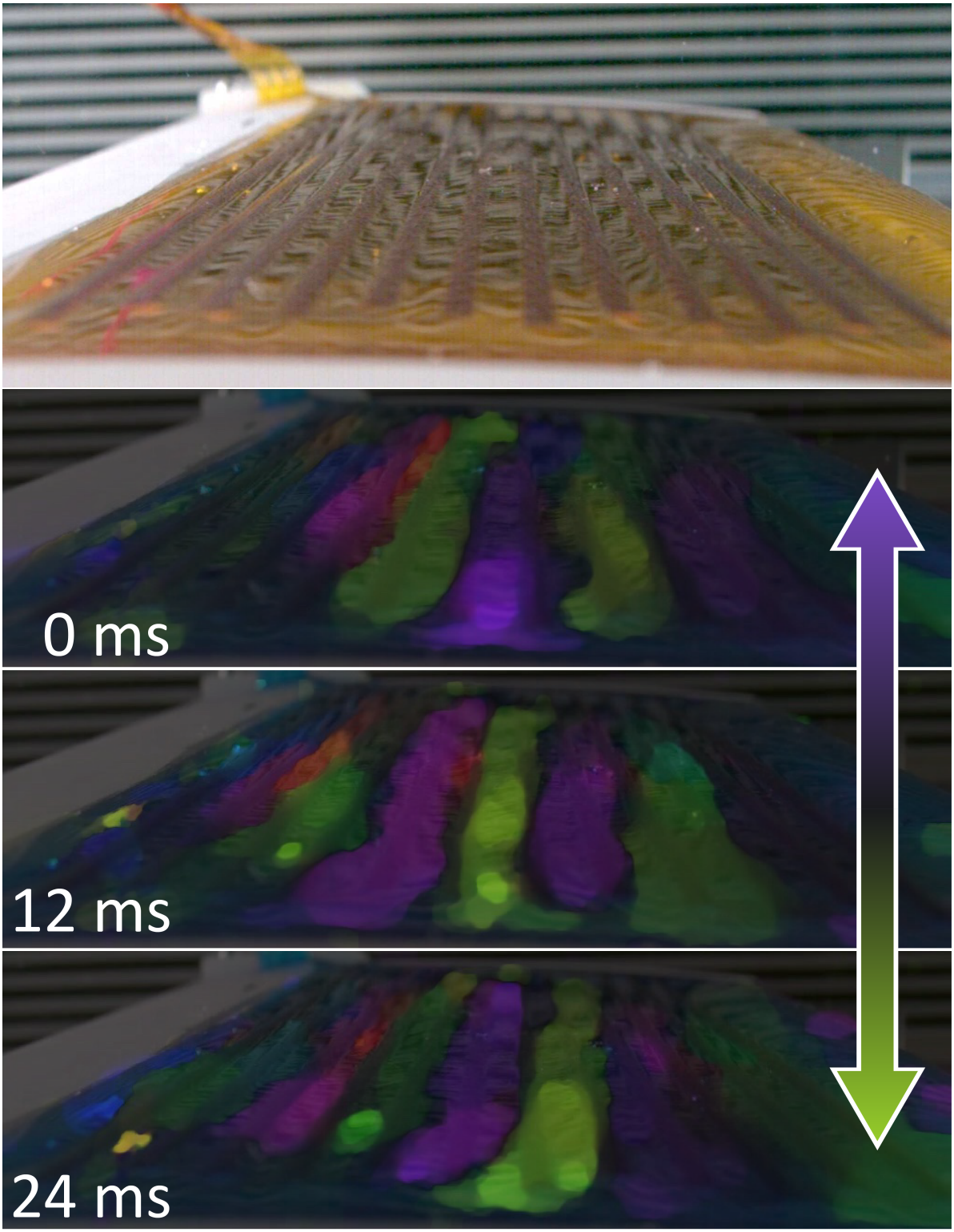

Figure 6.26: Wave characterization by high speed video and optical flow analysis. a) Frame from high speed video, showing spanwise view of flexible hydrofoil skin, b-d) Extracted frames with overlaid optical flow analysis showing rightward traveling wave fronts. Color value denotes magnitude (brighter is faster), and color hue denotes angle (purple is upwards, green is downwards).

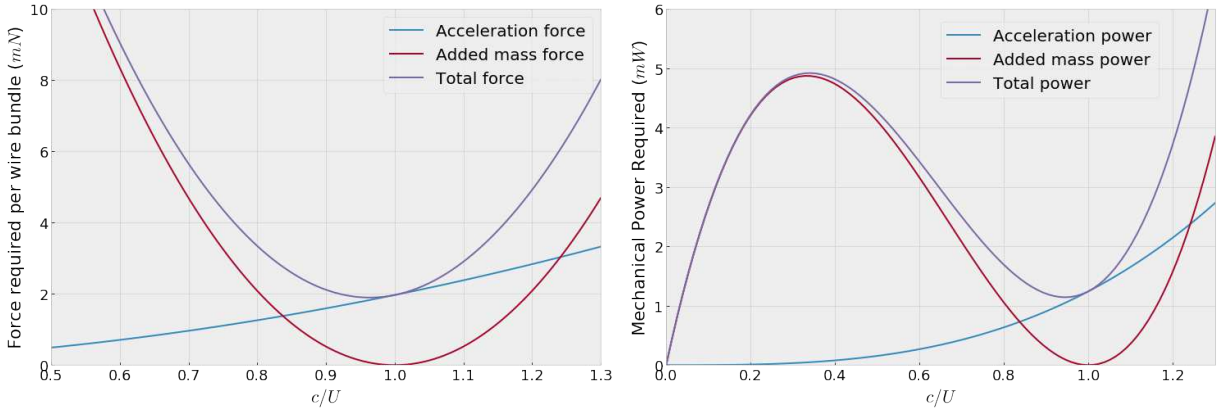

Figure 6.27: Plotting mechanical force and power requirements. a) Components of force required per wire bundle versus speed ratio c/U, b) Components of mechanical power required versus speed ratio c/U.

and the magnetic field is nearly constant in time, we do not expect magnetic hysteresis losses or eddy current losses to be significant. Assuming a required average mechanical force output of $5mN$ per wire bundle (safely above the curves in Figure 6.27) and an average horizontal component of magnetic field density of 0.1 T over the actuation envelope of the wire bundle (based on the 3D finite element modeling of Section 6.4.1), we estimate an average required current of approximately $7mA$. Based on the phase resistance, this current draw incurs a $2mW$ Joule loss per wire bundle, or a total of $20mW$ Joule loss over the entire actuated surface. There is also a loss associated with the energy stored in the magnetic field of each coil when energized, which discarded twice per period, but the coil inductances are on the order of $100\mu H$, and so the power dissipated in this way is well below $1mW$. Therefore, the Joule loss combined with the mechanical work required gives a best case estimate of approximately 25 mW of electrical power to drive the traveling waves.

6.4.4 Tow tank testing

After demonstrating traveling waves on a hydrofoil surface in a static tank, I moved to testing in a flow. For this I used the MIT Towing Tank, a hydrodynamic testing facility where models are towed through the 30 m x 2.5 m x 1.25 m volume of water using an overhead gantry track, shown in Figure 6.28a. The traveling wave prototype was mounted vertically in a cantilevered configuration using a hexagonal aluminum extrusion and a matching 5C collet. To measure drag and lift forces, a six degree-of-freedom waterproof load cell was used (ATI Gamma 15-50). The mounted prototype is shown with water level lowered in Figure 6.28.

A series of experimental trials were conducted at a flow speed $U = 0.5m/s$, giving a chordwise Reynolds number of $Re \approx 7.5 \times 10^4$. The trials were conducted across three angles of attack (3°, 5°, 7°). To precisely control angle of attack, the loadcell assembly was mounted on a rotational axis with a 3D printed globoid worm drive and stepper motor, shown in Figure 6.29a. This drive can resolve $0.01°$, but more importantly allows the adjustment of angle of attack remotely to avoid disturbing the water in the tank. The three-phase driver described in Section 6.4.2 was mounted on the carriage along with a Raspberry Pi single board computer to allow the control of traveling wave actuation through a local wireless network.

For each angle of attack, I conducted three trials at values of the speed ratio c/U of 0, 0.2,

Figure 6.28: Tow tank testing setup. a) The author installing traveling wave experiment on tow tank carriage. b) View down the tow tank with water level lowered, showing loadcell, collet-holder, and traveling wave prototype.

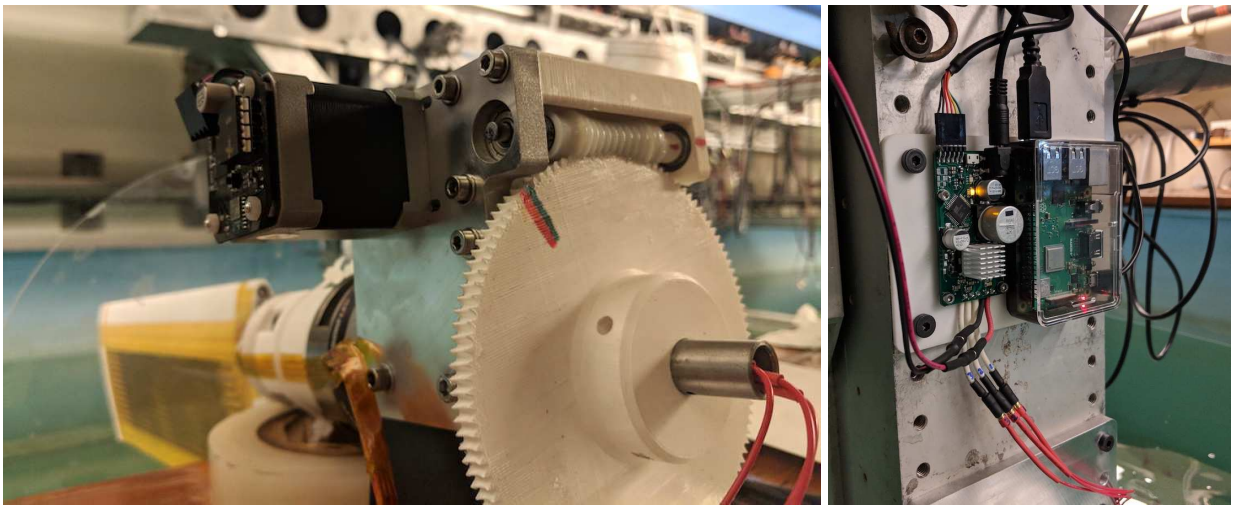

Figure 6.29: Tow tank testing setup. a) 3D printed globoid worm gear and stepper motor for controlling angle of attack. b) Three phase driver and Raspberry Pi single board computer for wireless control of traveling waves.

0.4, 0.8, 1.0, and 1.2. To establish the zero angle of attack position, we first bracketed the zero position by finding two small angles of attack which produced lift forces of opposite sign when towed. I then linearly interpolated between these values to set the zero position, towing at this setting to confirm a sufficiently small lift force. During each trial, the force was calculated by first averaging 500 samples at zero flow speed and no actuation to establish a baseline. The sample is then accelerated to the testing flow speed and the actuation is started. After a delay of a few seconds, 5000 samples are averaged to calculate the mean forces on the hydrofoil in each axis.

The results of these trials are shown in Figure 6.30, where we plot average drag force versus speed ratio c/U for the three angles of attack. Across the three angles, we see a consistent drag reduction of 5-15%. This is a significant reduction and is of a similar magnitude as those predicted by the simulations in [2]. The power saved by this drag reduction is $P_{saved} \approx (0.5m/s) \times (300mN) \approx$

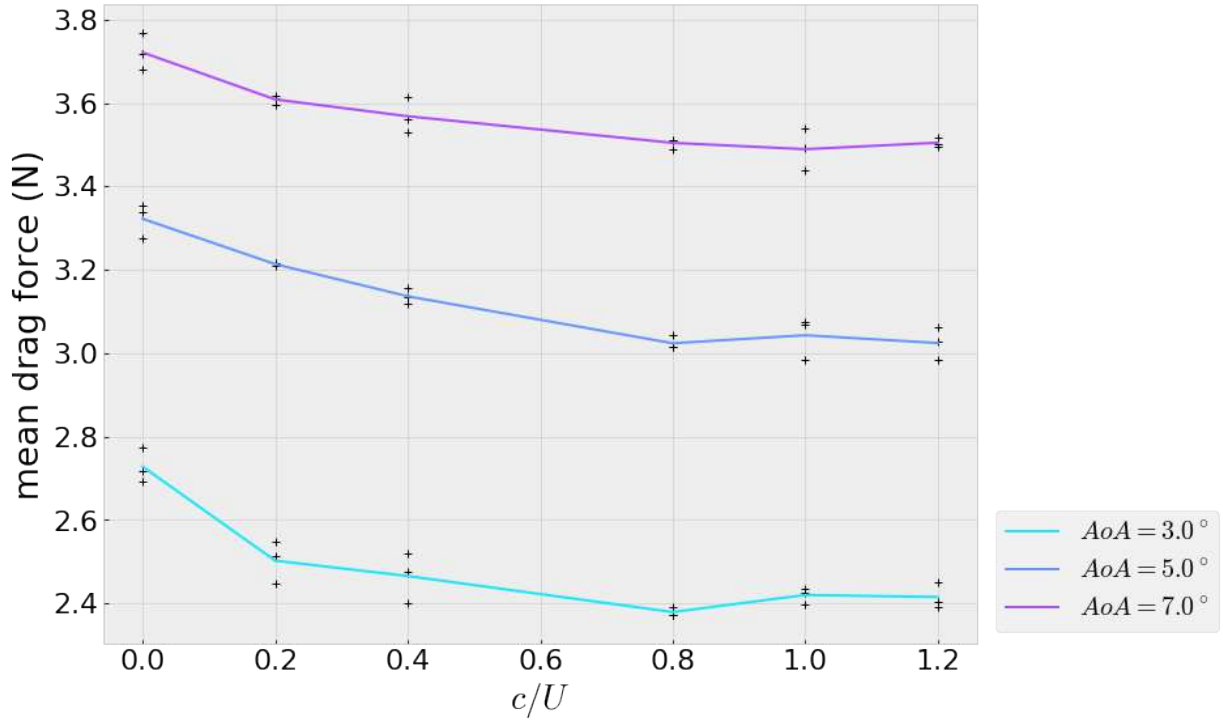

Figure 6.30: Data from tow tank trials. Plotting drag force versus speed ratio c/U for three angles of attack.

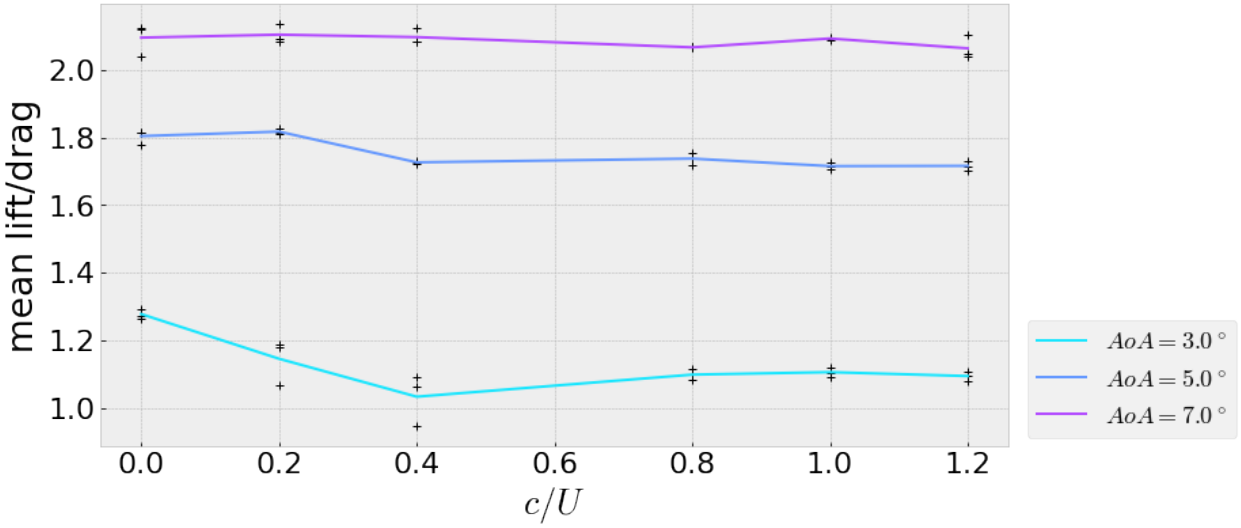

Figure 6.31: Data from tow tank trials. Plotting lift-to-drag ratio versus speed ratio c/U for three angles of attack.

$150mW$, which is significantly higher than our best-case estimate for required driving power of $25mW$. In our experimental prototype, however, the driving power for the whole system is on the order of several Watts, due to the open-loop control strategy and drive inefficiencies.

Figure 6.31 shows the average lift-to-drag ratio during these same trials. We see that in most cases tested, lift-to-drag ratio remains largely constant with respect to c/U, though in the $3°$ angle of attack case we see a reduction in this ratio. This also aligns with the predictions of [2] that show if the actuation amplitude is too large, a reduction in lift is caused. In this traveling

wave prototype, there is no feedback mechanism to precisely control the actuation amplitude, and so an increased wave amplitude is a possible explanation for the lift reduction.

6.5 Wire plotting applications

Besides the this hydrodynamic use case, the wire plotting process developed in this chapter has shown considerable potential for a range of other active structures.

As the achievable conductor placement density is an order of magnitude higher than conventional printed circuit board fabrication and the material costs scale with the volume of active materials rather than with volume of the device's bounding box, this process is a viable way to directly write electronic interconnect. Figure 6.32a shows an example of doing just this, where a netlist of component connections has been converted into a wire plotting path. To streamline the process, we can calculate a Hamiltonian path through the sites to visit (shown in purple), and then calculate a cutting path to remove the unwanted traces, or singulate the desired traces. This singulation path is shown on blue. Figure 6.32b-c show microscope images of prototypes of wire plotted circuits, where a path visiting each lead of a microcontroller with a TQFP footprint was plotted and then singulated. The pads were then stripped of their insulation using a fiber laser and the surface mount component was placed and soldered as in conventional printed circuit board population.

In addition to circuits, a range of other sensors and actuators can be plotted from wire. I demonstrated wire plotting of capacitive touch buttons and sliders, as well as inductive sensors like linear variable differential transformers for precision servo control. Figure 6.33 shows wire plotting of planar speakers for high performance audio with tailorable frequency response. First a substrate is populated with small rod magnets, then a membrane is wire plotted and stretched over the magnetic substrate and a speaker is formed. Figure 6.33c shows a microscope image of the wire plotting path, which is designed to cut the magnetic field perpendicularly.

Finally, in Figure 6.34, I show a wire plotted brushless motor. Motors without a flux concentrating core, like this prototype, are called *ironless*, and are known for high efficiency and power density. They are usually expensive due to difficulty manufacturing and cooling the stator windings, but wire plotting allows both issues to be addressed. Figure 6.34a shows the wire plotted stator windings, which are folded to accumulate turn density and wrapped around the stator body Figure 6.34b. The stator and the rotor, which consists of a Halbach array produced using the methods described in Section 6.4.1, are then joined to form the motor in Figure 6.34c-d. The stator windings are backed by wire plotted heat pipes, which keep them cool and allow the motor to operate efficiently, despite the time varying magnetic field which would cause eddy heating in a monolithic heatsink.

As these examples demonstrate, the achievable density and scaling of wire plotting allows conventionally distinct manufacturing processes for active structures to be combined into a single monolithic process. For instance, brushless servo-motors like the one described above can be made by plotting conductive wires to form electrical phases, soft magnetic wires to guide flux, thermally conductive wires to manage heat, and additional wire circuits to integrate encoders, current sensing, and drive electronics. Conventionally, such a motor would require many distinct processes (each with tooling and infrastructure costs) to produce many distinct components to be assembled (introducing uncertainty and model mismatch). Monolithic, tool-free construction

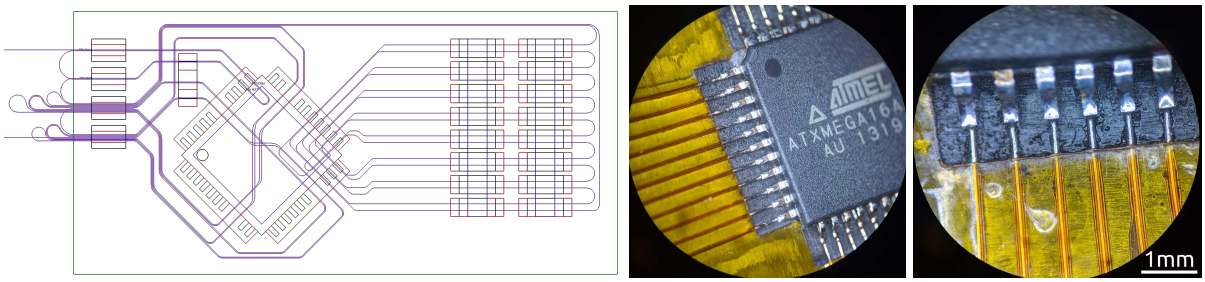

Figure 6.32: Wire plotting circuit boards. a) Board design showing Hamiltonian path routing (purple) and singulation cut paths (blue), b) Microcontroller with TQFP footprint soldered to wire plotted circuit board after laser stripping, c) Detail of wire plotted TQFP footprint after stripping and soldering.

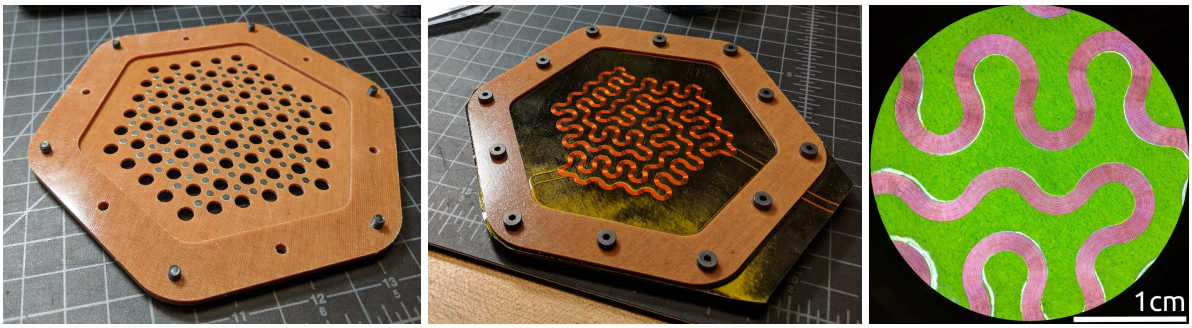

Figure 6.33: Wire plotted planar speakers, a) Phenolic substrate populated with rod magnets, b) Wire plotted carbon membrane stretched over substrate, c) Microscope image of speaker coil.

Figure 6.34: Wire plotted ironless motor. a) Three phase stator windings plotted and terminated, b) Stator folded to accumulate turn density and wrapped onto stator body, c) Stator and rotor with radial flux Halbach array, d) Assembled motor, showing wire plotted heat pipes for stator thermal management.

reduces costs of customization, shortens development cycles, and enables robust computer-aided optimization. In this way, wire plotting can significantly simply manufacturing active structures, aiding their incorporation into architected materials.

6.6 Conclusions

In this chapter, I designed and built active folded architected materials with embedded actuation to drive deformation modes of the structure. Our main application was driving traveling waves on a hydrofoil surface in order to control the flow and reduce drag. I demonstrated several approaches for embedded actuation meeting the application requirements and tested one such prototype, demonstrating a significant drag reduction of 5-15%.

This suggests many directions for future work. First, implementing amplitude control in the traveling wave prototype is a clear next step. This could likely be done by measuring back-emf waveforms to estimate the relative velocities between wire and magnets (i.e., the same way that many brushless motor controllers measure rotor position). By controlling for wave amplitude, the power required to drive the actuated surface should be significantly improved. Second, increasing the hydrofoil aspect ratio (the ratio of chord length to span length) should not only improve hydrodynamic performance and drag savings of the prototype by reducing the influence of 3D flow effects, but also increases the ratio of force-generating wire length to total wire length, reducing the effect of Joule losses. This work demonstrates manufacturable systems that could be incorporated into a variety of streamlined aerodynamic and hydrodynamic components, like airfoils sections, ship hulls, vehicle fairings, automobile panels. If separation is delayed on foils with nonzero angle of attack, the potential for turbulent drag reduction can be quite large, and the impact on these applications significant.

The method of plotting fine wire also has many applications in active structures besides the hydrodynamic test case which was the focus of this chapter. In Section 6.5, I demonstrated plotting wire for high density interconnect of commercial integrated circuits, as well as for constructing custom sensors and actuators. This approach to additive manufacturing of electronics not only provides better material properties and lower costs than conductive ink printing, but also achieves higher densities than conventional printed circuit board fabrication.

Chapter 7

Conclusions

I started this thesis by noting the engineering potential of architected materials, the limitations of additive manufacturing, and the combined manufacturing efficiency and geometric richness made possible by patterning and folding planar sheets. I then set out to show that while folded fabrication does not have the geometric universality attributed (somewhat inaccurately) to additive manufacturing, the range of geometries producible by patterning and folding flat sheets spans a rich enough space to scalably solve engineering problems of importance.

Through a set of five case studies I worked to demonstrate this capacity. In Chapter 2, I showed a mathematical construction and a custom machine for producing shaped structurally-efficient architected materials from a flat sheet, filling the volume bounded by arbitrary heightmaps using only cutting and folding operations. In Chapter 3, I demonstrated control over the stiffness of a folded architected material in addition to its shape, showing the ability to span a similar range as a wide variety of engineering foams. In Chapter 4, I demonstrated material resilience, developing a design method for architected materials with curved creases, a composite manufacturing technique to fabricate them, and dynamic impact test equipment for evaluation. The fabricated prototypes showed energy return approaching that of state-of-the-art polymer foams, and relied geometry rather than chemistry and thermal processes for achieving this performance. In Chapter 5, I showed material toughness, designing, fabricating, and testing a folded architected material with specific energy absorption twice that of commonly used honeycombs. Finally, in Chapter 6, I developed several methods for building active folded structures, capable of embedding actuation, sensing, and computation within a folded architected material. I demonstrated this potential by building a hydrofoil capable of driving traveling waves on its surface and measure its ability to reduce drag using this actuation.

Each of these examples has important engineering applications in its own right, but taken together, they demonstrate the more general potential of folded architected materials for next-generation manufacturing. Not only can geometric design be used to increase performance, but in many cases, less material can be used to meet design specifications, undesirable materials can be replaced with more benign ones, and energy-intensive thermal manufacturing processes can be replaced by efficient isometric operations. The cost of customization can be reduced by avoiding molds and tooling, and multiple functional parts can be combined to simplify designs and supply chains. These advantages can be used to solve a host of problems across the engineering and manufacturing space. To illustrate this, I turn to one of the greatest challenges of our time: the decarbonization of the global economy.

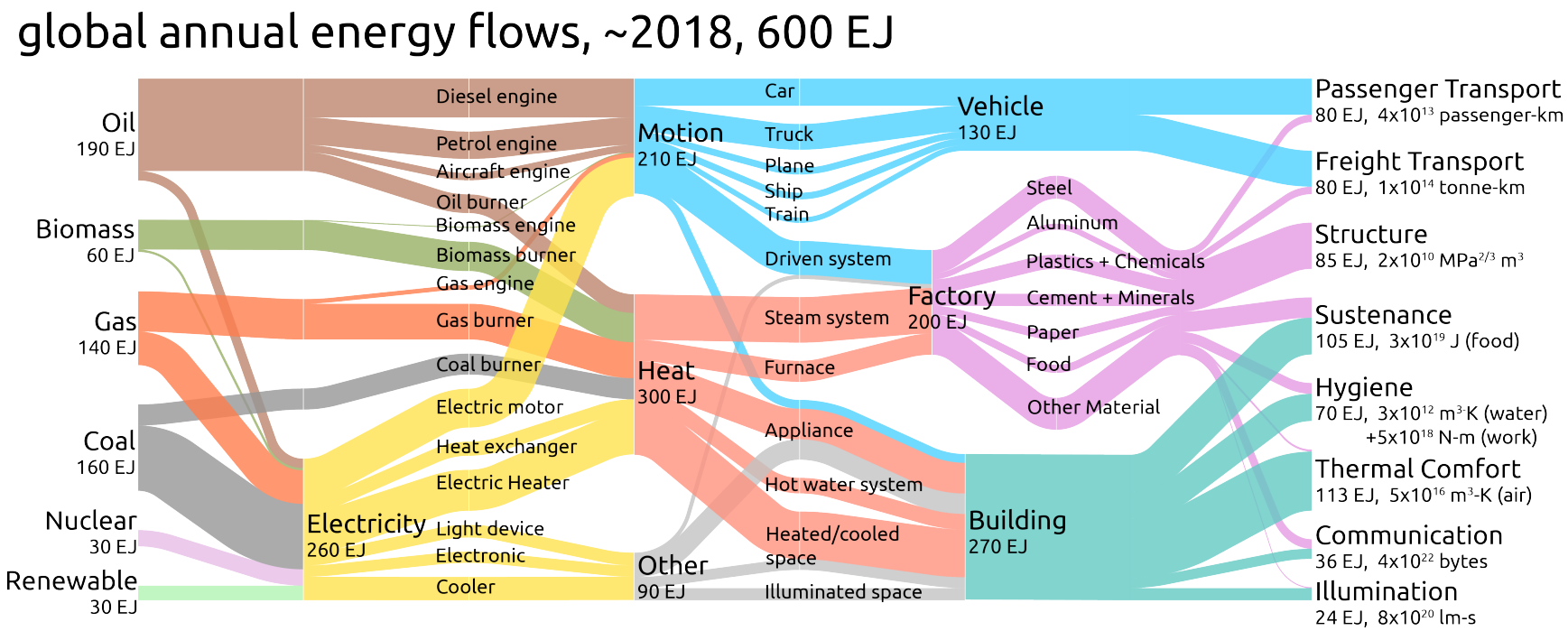

Figure 7.1: Sankey diagram of global energy economy, showing transformation steps from primary sources to final services. (Data updated and from Cullen and Allwood's diagram of the 2005 energy economy [46])

Figure 7.1 shows a graphical representation of the 2018 global energy economy, called a *Sankey diagram*, tracing the flow of energy from primary sources to final services. The width of each strand represents the magnitude of the energy flow, tabulated in terms of primary energy, so that in any vertical slice the sum of strands represents the total flow of 600 exajoules (EJ) per year. We can see that roughly one third of this energy is used in vehicles, one third in factories, and one third in buildings. Despite this breakdown, however, most energy efficiency efforts today focus only on the energy used in vehicles and buildings (e.g., electric vehicles, LED lighting, etc.). The third of energy used in factories, responsible for the refinement of raw materials into useful devices, feeds into all of the eight end use sectors and represents an enormous challenge and opportunity for energy demand reduction.

The work presented in this thesis is aimed at this neglected third of global energy usage, as increased control over geometry in architected materials can enable greater material efficiency. For instance in Chapter 2, I showed structurally-efficient net-shape production of honeycombs. Such shaped structures could be directly incorporated into structural building components, or into molds for pouring concrete elements. It is estimated that 30-40% of structural beam steel can be eliminated without any reduction in performance simply by using variable cross section beams instead of common prismatic beams which are easier to manufacture [36]. Similarly, eliminating over-design of concrete components (largely due to standardized and geometrically-limited formwork) has the potential to reduce structural cement use by 20% [167]. Both of these are enormous opportunities for energy demand reduction through material efficiency, as we can see from Figure 7.1 that steel and concrete are responsible for approximately one third of factory energy use, and the structural end use category alone requires 85 EJ per year.

In addition to material efficiency, folded architected materials offer reductions in the man-

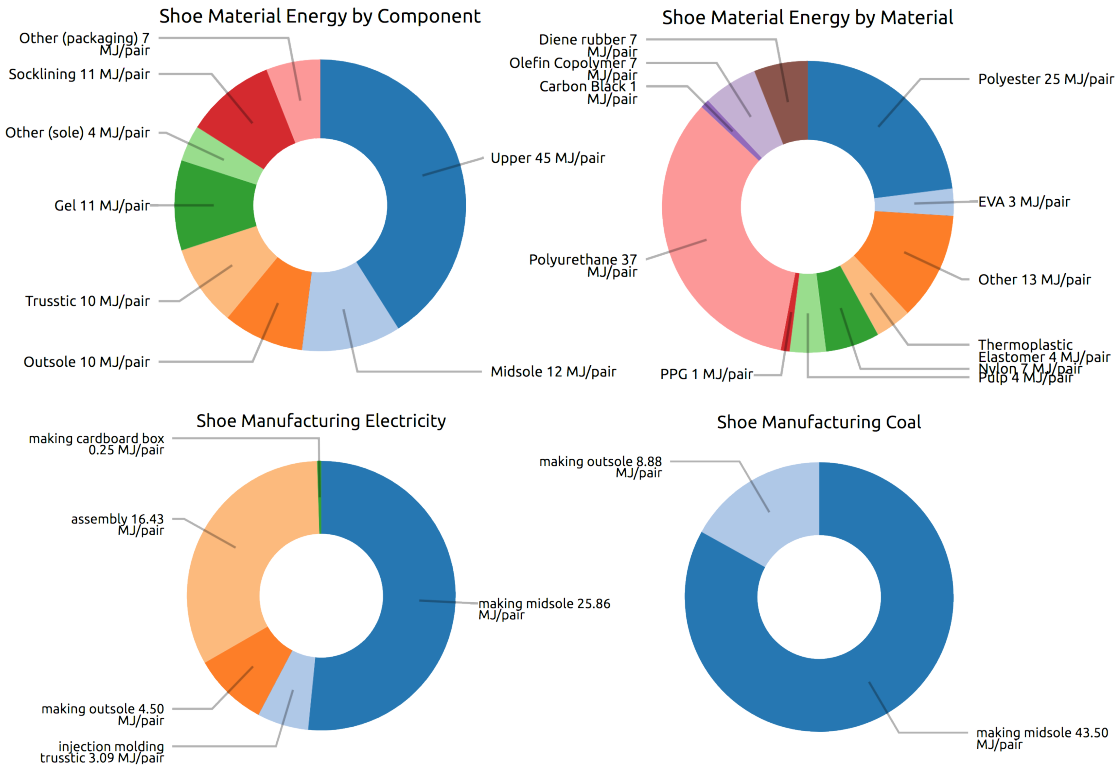

Figure 7.2: Material and manufacturing energy in footwear production. (Data derived from [39])

ufacturing energy used to process those materials. For instance, in Chapter 3 and Chapter 4, I demonstrated the capabilities necessary to replace the use of foams in the production of footwear. While this application may seem energetically insignificant, it is estimated that 10 billion pairs of athletic shoes are sold each year [95]. Each pair requires approximately 100 MJ in manufacturing energy [39], bringing the extended energy requirement to approximately one exajoule! A detailed breakdown of manufacturing energy, as well as materials energy, of footwear is shown in Figure 7.2. We see that 85% of this manufacturing energy is required to make the midsole, trusstic, and outsole; most of this goes into the heat required for injection molding, foam blowing, and compression molding. By replacing the thermal processes used for these components with cold, isometric processes enabled by folded constructions, we can greatly reduce the energy intensity of footwear. For instance, reducing the energy intensity of the footwear industry just to that of molding industry as a whole constitutes a potential savings of hundreds of petajoules [39].

Finally, as the material flows of Figure 7.1 touch all eight end-use categories, folded architected materials offer performance-based energy reductions in addition to the material and manufacturing efficiency benefits described above. In Chapter 6, I demonstrated active structures, including flow control based on driving traveling waves on a hydrofoil surface. We showed a drag reduction of 10-15%, and analysis suggests this can be made energetically viable (saving more energy from drag reduction than is required to drive the waves). If even a 5% gain were realized and deployed to hulls of ships, the savings could total hundreds of petajoules globally. In Chapter 5, I showed folded architected materials with specific energy absorption twice that of commonly used honeycombs. Such energy absorbers could aid widespread adoption of ultralight electric vehicles, which can replace cars for the 30% of vehicle miles traveled in the U.S. on trips of length shorter than 10 miles [109] (a 15 EJ electrification opportunity), but are limited by difficulties in meeting safety requirements without adding significant mass. In other energy absorbing applications, folded architected materials can replace the use of polystyrene and other foams, not only improving performance, but also reducing use of toxic constituent chemicals and hydrocarbon supply chains.

These opportunities for material efficiency, manufacturing efficiency, and performance efficiency illustrate the tremendous potential of folded architected materials to change the way things are made. By leveraging the scalability of planar processing and the geometric richness of origami, we can do explicit geometric design of desired properties, effectively putting information into materials. In this way, we not only reveal widespread opportunities to do more with less, but also enable unprecedented functionalities as we move ourselves and our things, build, eat, keep clean, warm, connected, and lit.

Appendix A

Lessons

Following the wonderful example of Ara Knaian [108], I'm including this chapter to document high-level strategies and low-level tips I've picked up during my PhD. Your mileage may vary.

A.1 Strategies

Simplify. There's no time for anything to be more complicated than it can be. Especially if you're planning to build it.
Bisect problems. Find a working instance and a non-working instance and bring them towards each other. Once you've bracketed, the problem is as good as solved.
Factor tasks. Seek out the minimum set of dependent functions and test them in isolation. Combining two working pieces is (usually) much easier than developing everything at once.
Close loops early and often. Without feedback, there is no way to evaluate. Evaluation is the only way to figure out which un-modeled parameters are actually the most important part of a problem. Test your models by building prototypes. Test your prototypes by building models.
Keep records. Write copious notes. Take a picture or screenshot every day. Use video for process debugging. Remove barriers to spur-of-the-moment documentation.
Digest and share notes in a timely manner. Packaging knowledge for others is an effective way to find and fix gaps. Having others react and free-associate is a huge productivity booster.
Create your own datasets. Compiling information from disparate sources dramatically increases its value. Don't fret over assumptions – just document them.
Grab the right tools. Clean, sharp tools and lots of light go a long way.
Use CAD as a tool, not a crutch. Only model what is necessary. Parameterize everything. Prioritize interoperability. Use APIs. Write your own.
Manage the toolmaker's regression. Great results can come from making tools to make things no one else can. Great amounts of time can be wasted making the tool that lets you make the tool to make a tool. Managing this regression requires working in parallel across dependencies, instead of stacking them serially. Augment existing tools instead of reinventing them completely. Copy reference designs. Substitute commercial components where you don't add value. Cheat any way you can.
Don't finish all the fun steps before the end of day. Leave something exciting to get you out of bed in the morning.

Be deliberate about supply-side and demand-side time management. Supply-side puts you in control. Demand-side forces action. Neither are appropriate 100% of the time.
Exercise. Duh.
Care for others and ask for care. Everyone I know well is both stronger and weaker than they originally appeared. We can help each other flourish.

A.2 Tools and Tips

Atmel XMega A4. This microcontroller will always have a very special place in my heart. Its performance routinely bests that of others that *should* be much better, and the certainty of single-cycle instruction makes sensing and controlling uncertain systems much easier.
Single board computer as wifi access point. Having an operating system in an embedded device can be really useful but headless nodes can be a pain to network when routers are inaccessible or variable. Configuring the device as an access point, rather than a client is easy and takes all the black boxes out of the equation.
Fast packet radios. Wireless doesn't have to mean high latency. Packet radios (like nRF24L01 and nRF52832) can send messages in around $100\mu s$ round trip.
Magnetic position sensing. Used differentially, Hall effect sensors give a cheap, reliable, and (when temperature compensated) remarkably accurate way to measure position across relatively large air gaps. The magnetic fields can also be shaped to give more flexibility.
Tag-Connect pogo-pin cables. Freedom from programming headers means smaller boards and less soldering.
Kozak micro-adjustment screws. Ball-end screws and bushings with 80 to 500 threads per inch for just a few dollars. Easy to incorporate for precise calibration.
Belleville washers and flexures around bearings. In prototype machines, I've found bearings are much more likely to fail from assembly forces and misalignments than from the loads of routine use. Elastic elements like Belleville washers and flexures can almost always be used to accommodate assembly uncertainty without sacrificing performance in the axes that matter.
Two-part adhesive cartridges with Luer-Lok mixing tips. A range of high performance two-part adhesives are available in cartridges with mixing tube attachments. This means you only mix what you need, and usually get a little extra working time. The Luer-Lok connection means a variety of dispensing needles and tips can be used to size the bead perfectly.
PTFE-coated fiberglass cloth. This stuff can handle plenty of heat and doesn't stick to anything. It comes in permeable and impermeable varieties – both are useful.
Freeze spray for prepreg. The thin prepregs used in this thesis are impossible to handle without carefully controlled temperature gradients. Warming under vacuum consolidates the fibers. Chilling with freeze spray makes them stick together to remove the liner.
Resin transfer molding. My best molding results have always been using vacuum or pressure assisted resin-transfer processes. Vacuum-assist minimizes plumbing – polyethylene tubing press-fit into a drilled hole can be self-sealing. Pressure-assist can transfer resin through higher resistance. Compression fittings can be drilled out so tubing can pass through while maintaining a robust seal – this can be used to drive resin from a mixing cup inside a pressure chamber.
EDM Two-Cut. Electric discharge machining is an incredibly capable process, but it becomes about twice as useful when you cut, rotate stock by 90° about a horizontal axis, and cut again.

Appendix B

Nonlinear Simulation Using Bicubic Hermite Patches

This work develops a simulation model for structural origami by modeling facets as bicubic Hermite patches. Using this polynomial form, we express the deformed shape as a function of the positions and derivatives of the facet at its corners. This parameterization is a convenient way to describe origami, and hence many relevant boundary conditions are easily implemented. We derive expressions for the bending and stretching energy densities of the facet in terms of this parameterization and combine multiple facets along creases to simulate origami patterns. Finally, we perform experimental tests and compare the results to simulation.

B.1 Introduction

As interest in structural origami and kirigami has grown, there has been a growing need for scalable methods for analyzing mechanical properties of folded sheets. Conventionally, this analysis would be involve decomposing each panel into many smaller elements and performing finite element analysis. This approach can quickly become too computationally intensive to be useful for origami design. Alternatively, several recent approaches including [164] and [62] have shown that surprisingly accurate solutions can be obtained by creating bar and hinge models of a folded sheet with with bar lengths on the order of the facet size of the folded sheet. These methods have

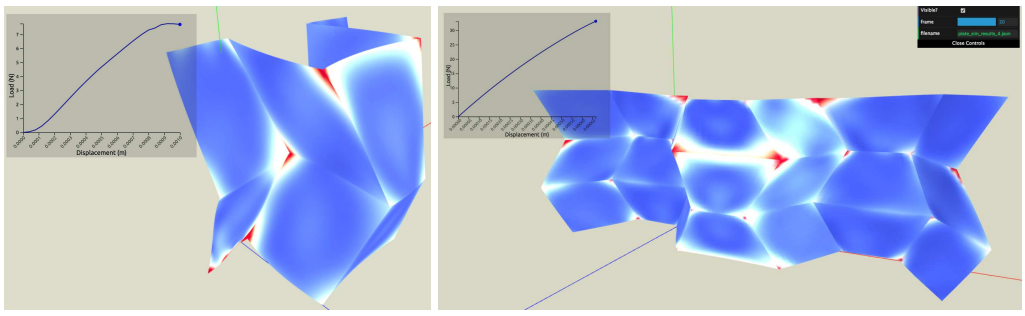

Figure B.1: Nonlinear simulation of two origami crease patterns using bicubic Hermite patches, both sections of Tachi-Miura polyhedra[137]. A) $\alpha = 75°$, B) $\alpha = 60°$. Elastic energy density is visualized over the origami pattern and the nonlinear force-displacement curves are graphed.

proven scalable and able to reveal insights about deformation modes that are difficult to see with finite element analysis [63].

Inspired by these approaches, this research develops a method of analyzing folded sheets using elements of similar physical size to the facets, but which does not approximate facets using one-dimensional elements or low-degree two dimensional elements. Instead, we use two-dimensional bicubic Hermite patches to model each facet. Because the deformation is linear with respect to bicubic coefficients, we can express quantities like material strain and curvature in terms of the positions, tangent vectors, and mixed derivatives of the patch at its corners. Thus, despite having 48 scalar degrees of freedom for each patch, the stiffness equation on Hermite patches can be solved efficiently. This allows us to frame an elastic energy minimization in terms of a system of equations which can be solved using iterative methods. We hypothesize the large number of facet degrees of freedom allows these elements to capture the complex strain fields which are common in structural origami more accurately than lower degree elements. This model captures the geometric nonlinearity [8] which is common in structural origami while being convenient to work with, as the quantities being solved for represent positions and tangents of the vertices of the origami pattern. As the origami pattern directly determines model elements, implementing boundary conditions along edges, hinge constraints between plates, and non-ideal crease behavior is easier than with subdivided facets. Further, because bicubic patches can have curved edges, this representation would easily capture curved crease origami, simulating the structural responses of such structures without the need for subdivision.

In this work, we detail our mathematical approach, starting from physically based equations for strain energy in a thin plate and deriving a system of equations with variables given by positions and spatial derivatives of the four vertices of each facet. We then extend these per-facet equations to a system for the full crease pattern by modifying the equations to attach incident edges. We also implement common boundary conditions (e.g., a force applied along an edge, or an edge constrained to move only in certain directions) which are natural to express in this framework. We also compare these methods to physical experiments applying a compressive force to cellular materials based on Tachi-Miura polyhedra.

B.1.1 Derivation

In this section, we develop the mathematical framework for our model, using bicubic Hermite patches to represent the deformed state of each origami facet. Such an Hermite patch in $\mathbb{R}^3$ is given by a bicubic polynomial with vector valued coefficients:

$$\mathbf{p}(v,w) = \sum_{i=0}^{3}\sum_{j=0}^{3} \mathbf{c}_{i,j} v^i w^j \tag{B.1}$$

where $v, w \in [0,1]$ and $\mathbf{c}_{i,j} \in \mathbb{R}^3$. We now seek to express the coefficients $\mathbf{c}_{i,j}$ in terms of the positions and derivatives of $\mathbf{p}$ at the patch corners, that is, where $v, w \in \{0,1\}$. To this end, we differentiate with respect to v and w:

$$\mathbf{p}_v(v,w) = \sum_{i=0}^{2}\sum_{j=0}^{3} \mathbf{c}_{i,j}(i+1) v^i w^j \tag{B.2}$$

$$\mathbf{p}_w(v,w) = \sum_{i=0}^{3}\sum_{j=0}^{2} \mathbf{c}_{i,j}(j+1)v^i w^j \tag{B.3}$$

and finally with respect to v then w:

$$\mathbf{p}_{v,w}(v,w) = \sum_{i=0}^{2}\sum_{j=0}^{2} \mathbf{c}_{i,j}(i+1)(j+1)v^i w^j \tag{B.4}$$

We can evaluate these four equations at each of the corners points $(v,w) \in \{(0,0),(0,1),(1,0),(1,1)\}$ to generate 16 equations in the 16 unknown coefficients. We can write this as

$$\begin{pmatrix} \mathbf{p}(0,0) \\ \mathbf{p}_v(0,0) \\ \mathbf{p}_w(0,0) \\ \mathbf{p}_{v,w}(0,0) \\ \mathbf{p}(1,0) \\ \mathbf{p}_v(1,0) \\ \mathbf{p}_w(1,0) \\ \mathbf{p}_{v,w}(1,0) \\ \mathbf{p}(0,1) \\ \mathbf{p}_v(0,1) \\ \mathbf{p}_w(0,1) \\ \mathbf{p}_{v,w}(0,1) \\ \mathbf{p}(1,1) \\ \mathbf{p}_v(1,1) \\ \mathbf{p}_w(1,1) \\ \mathbf{p}_{v,w}(1,1) \end{pmatrix} = M \begin{pmatrix} \mathbf{c}(0,0) \\ \mathbf{c}(0,1) \\ \mathbf{c}(0,2) \\ \mathbf{c}(0,3) \\ \mathbf{c}(1,0) \\ \mathbf{c}(1,1) \\ \mathbf{c}(1,2) \\ \mathbf{c}(1,3) \\ \mathbf{c}(2,0) \\ \mathbf{c}(2,1) \\ \mathbf{c}(2,2) \\ \mathbf{c}(2,3) \\ \mathbf{c}(3,0) \\ \mathbf{c}(3,1) \\ \mathbf{c}(3,2) \\ \mathbf{c}(3,3) \end{pmatrix} \tag{B.5}$$

where the summation equations have been combined into the matrix M.

Using this matrix expression, we can easily calculate and invert the matrix M using a symbolic math environment. We include the values in Appendix B.4. If $\tilde{\mathbf{p}}$ and $\tilde{\mathbf{c}}$ represent the vectors on the left and right hand side of Equation B.5, we can write

$$\tilde{\mathbf{c}} = M^{-1}\tilde{\mathbf{p}} \tag{B.6}$$

That is, we can write the coefficients of the Hermite patch as linear combinations of the positions at the plate corners (e.g., $\mathbf{p}(0,0)$), derivatives at the corners (e.g., $\mathbf{p}_v(0,0)$, $\mathbf{p}_w(0,0)$), and the mixed partial derivatives at the corners (e.g., $\mathbf{p}_{v,w}(0,0)$).

Next, we assume the Hermite patch deforms as a thin plate, and seek to write the bending and stretching energy densities of the plate in terms of the Hermite coefficients (and hence, in terms of the positions and derivatives at the corners). The solid mechanics of thin plates and derivations of energy densities is given in [204]. Assuming Hookean elasticity and plane stress, if $U_b(v,w)$ and $U_m(v,w)$ are the bending and stretching energy densities, respectively, we have

$$U_b = \frac{D}{2}\left((\kappa_{vv}+\kappa_{ww})^2 - 2(1-\nu)(\kappa_{vv}\kappa_{ww} - \kappa_{vw}^2)\right) \tag{B.7}$$

$$U_m = \frac{C}{2}\left((\epsilon_{vv} + \epsilon_{ww})^2 - 2(1-\nu)(\epsilon_{vv}\epsilon_{ww} - \epsilon_{vw}^2)\right) \tag{B.8}$$

where κ is local curvature and ϵ is local strain with subscripts defining the directions of measurement. In these equations, $D = Et^3/(12(1-\nu^2))$ and $C = Et/(1-\nu^2)$, where E is the material elastic modulus, ν is the material Poisson ratio, and t is the material thickness. With these energy densities, we can calculate total elastic energy as the integral of the sum of bending and stretching energies over the area of the patch:

$$E = \int_0^1 \int_0^1 (U_b + U_m)\, dvdw \tag{B.9}$$

To calculate these expressions, we need a deformation of the facet from its rest state. Let $\mathbf{p}_0(v,w)$ define the flat state, for which we assume total elastic energy is zero. We define the deformation as $\mathbf{u}(v,w) = \mathbf{p}(v,w) - \mathbf{p}_0(v,w)$ and the stacked vector $\tilde{\mathbf{u}} = \tilde{\mathbf{p}} - \tilde{\mathbf{p}}_0$ as in Equation B.6. We now use derivatives with respect to v and w to build a local coordinate system for expressing strain ϵ and curvature κ. We note that technically the local coordinate system should be orthogonalized, but in many cases of interest the derivatives with respect to v and w are very nearly orthogonal already. If u_v is the deformation in the direction of $\partial_v\mathbf{p}$, then $u_v = \mathbf{u}\cdot\mathbf{T}_v$, where $\mathbf{T}_v = \partial_v\mathbf{p}/|\partial_v\mathbf{p}|$ is the local unit tangent vector in the v direction. Similarly, we define $u_w = \mathbf{u}\cdot\mathbf{T}_w$, where $\mathbf{T}_w = \partial_w\mathbf{p}/|\partial_w\mathbf{p}|$ is the local unit tangent in the w direction and $\mathbf{N} = \partial_v\mathbf{p}\times\partial_w\mathbf{p}/|\partial_v\mathbf{p}\times\partial_w\mathbf{p}|$ is the local unit normal vector.

This local coordinate system will help us write the energy expressions above in a way that facilitates their minimization with respect to $\tilde{\mathbf{u}}$. In our bicubic deformation, $\mathbf{p}$ is linear in $\tilde{\mathbf{u}}$, so we have $\mathbf{u} = \partial_{\tilde{\mathbf{u}}}\mathbf{p}\cdot d\tilde{\mathbf{u}}$. The local unit coordinate vectors (T_v, T_w, N), however, are not as simple, so we do not attempt to write them in a form that can be explicitly solved for $\tilde{\mathbf{u}}$. Instead, we linearize our system by treating the coordinate vectors as constant with respect to $\tilde{\mathbf{u}}$. We then iteratively solve the linear system, line search along the solution direction to minimize energy, and update the coordinate vectors.

To write the energy density expressions above, we first compute the strain tensor [204]:

$$\epsilon_{ij} = \frac{1}{2}\left(\frac{\partial_j u_i}{|\partial_j\mathbf{p}|} + \frac{\partial_i u_j}{|\partial_i\mathbf{p}|}\right) \tag{B.10}$$

where i and j range over v and w. The summands have been normalized to create arc-length parameterizations in the coordinate directions.

$$\epsilon_{vv} = \frac{1}{|\partial_v\mathbf{p}|}\left(\mathbf{T_v}^\intercal\partial_v\partial_{\tilde{\mathbf{u}}}\mathbf{p} + \partial_v\mathbf{T}_v^\intercal\partial_{\tilde{\mathbf{u}}}\mathbf{p}\right)d\tilde{\mathbf{u}} \tag{B.11}$$

$$\epsilon_{ww} = \frac{1}{|\partial_w\mathbf{p}|}\left(\mathbf{T_w}^\intercal\partial_w\partial_{\tilde{\mathbf{u}}}\mathbf{p} + \partial_w\mathbf{T}_w^\intercal\partial_{\tilde{\mathbf{u}}}\mathbf{p}\right)d\tilde{\mathbf{u}} \tag{B.12}$$

$$\epsilon_{vw} = \frac{1}{2}\left(\frac{\mathbf{T_w}^\intercal\partial_v\partial_{\tilde{\mathbf{u}}}\mathbf{p} + \partial_v\mathbf{T}_w^\intercal\partial_{\tilde{\mathbf{u}}}\mathbf{p}}{|\partial_v\mathbf{p}|} + \frac{\mathbf{T_v}^\intercal\partial_w\partial_{\tilde{\mathbf{u}}}\mathbf{p} + \partial_w\mathbf{T}_v^\intercal\partial_{\tilde{\mathbf{u}}}\mathbf{p}}{|\partial_w\mathbf{p}|}\right)d\tilde{\mathbf{u}} \tag{B.13}$$

Similarly, we can calculate the curvature [204]:

$$\kappa_{ij} = -\frac{1}{|\partial_i\mathbf{p}||\partial_j\mathbf{p}|}\frac{\partial^2(\mathbf{u}\cdot\mathbf{N})}{\partial i\partial j} = -\left(\frac{1}{|\partial_i\mathbf{p}||\partial_j\mathbf{p}|}N^\intercal\frac{\partial^2}{\partial ij}\frac{\partial\mathbf{p}}{\partial\tilde{\mathbf{u}}}\right)d\tilde{\mathbf{u}} \tag{B.14}$$

where i and j range over v and w.

The expressions multiplied by $d\tilde{\mathbf{u}}$ in the above can be expressed as matrix functions of the Hermite patch corner positions and derivatives, as well as the values of the patch parameters v and w. We use a symbolic math environment to write these expressions and combine them as in Equation B.7 and Equation B.8. We export executable code because the expressions are quite long. We then evaluate these expressions at Gaussian quadrature points, numerically integrating over the patch. The result can be thought of as a tangent stiffness matrix, common in finite element analysis. This matrix times a vector of displacements in the positions and derivatives at the plate corners gives us an expression for total elastic energy of the facet. The energy expression itself is not linear however, as if we move to another deformation, this tangent stiffness changes and must be recalculated.

At one deformation configuration, we use standard finite element techniques to couple multiple plates along their edges and apply boundary conditions while preserving the symmetry of the stiffness matrix[25]. A convenient property of the Hermite parameterization is that two plates are joined along their full edge if and only if their positions and tangent vectors in the direction of the edge match at the two corners incident to the edge. Similarly, it is natural to express a boundary condition of an edge held against a flat surface by constraining the incident nodes' positions to lie on the surface and the incident tangents along the edge not pierce the surface.

The sparse linear system resulting from all the facets in the origami structure can be solved efficiently, yielding a vector of deformations at the facet corners which points along negative gradient of the potential energy. We use this solution in a quasi-Newton solver to minimize the elastic energy and produce a solution for the deformed state. Figure B.1 shows two example simulations of origami structures. To calculate the loading curve, we gradually apply the natural boundary condition, plotting displacements of loaded vertices. The colored field is local strain energy (i.e., $U_b + U_m$).

Besides calculating deformed states, we can also extract reaction forces at nodes and edges. The nodal reactions are calculated in a straightforward way from the linear system, but edge reactions are less obvious. To calculate this, consider the patch boundary $w = 0$ (the other boundaries are similar). We have

$$p(v,0) = p(0,0) + \frac{\partial p}{\partial v}(0,0)v \tag{B.15}$$

$$+ \left(-3p(0,0) + 3p(1,0) - 2\frac{\partial p}{\partial v}(0,0) - \frac{\partial p}{\partial v}(1,0)\right) v^2 \tag{B.16}$$

$$+ \left(2p(0,0) - 2p(1,0) + \frac{\partial p}{\partial v}(0,0) + \frac{\partial p}{\partial v}(1,0)\right) v^3 \tag{B.17}$$

To calculate the effect of reactions in the derivative terms on the output degree of freedom, we consider an equivalent point load at the midpoint, where

$$p(\frac{1}{2},0) = \frac{1}{2}p(0,0) + \frac{1}{2}p(1,0) + \frac{1}{8}\frac{\partial p}{\partial v}(0,0) - \frac{1}{8}\frac{\partial p}{\partial v}(1,0) \tag{B.18}$$

We attribute nodal reactions at the nodes, so we are interested in the displacement of the center nodes from derivative terms alone:

$$p(\frac{1}{2},0) = \frac{1}{8}\left(\frac{\partial p}{\partial v}(0,0) - \frac{\partial p}{\partial v}(1,0)\right) \tag{B.19}$$

Conservation of energy implies the generalized forces of the derivative terms can be accounted for by a force at the midpoint:

$$F_{midpoint} = 8\left(F_{\frac{\partial p}{\partial v}(0,0)} - F_{\frac{\partial p}{\partial v}(1,0)}\right) \tag{B.20}$$

The generalized forces on the right hand side can be read off directly from the minimal energy solution vector. This expression is very useful when we want to constrain a plate boundary to lie in a plane and measure the reaction on the plane.

B.2 Results

To validate the simulations above, we performed a series of experimental tests of origami structures. The samples under test were arrays of Tachi-Miura polyhedra [137], a tileable pattern with behavior with an auxetic origami mechanism with respect to compression in the direction of the cylinder axis. Because of this, the compliance of the samples when loaded in compression by a flat plate comes from a combination of the origami mechanism and elastic deformation of the underlying material. For this reason, these patterns were selected as a good target for simulation with the Hermite element method described above.

The samples were fabricated from $.25mm$ polypropylene using a laser cutter to cut the required slits and outline, and half-cut the mountain and valley folds. Patterns were designed with $\alpha = 50°, 55°, 60°, 65°, 70°$, and three samples were constructed of each angle value. The samples were tested using an Instron 4411 material characterization machine while being held at their edges and supported from below (shown in Figure B.2a). The load was applied with a rectangular plate with an area of approximately 8 cm^2. The samples were loaded cyclically between 0 N and 100 N six times. The last load cycle for each sample is shown in Figure B.2b.

Figure B.2c shows the result of simulating the loading of these samples using our Hermite patch model. We assume frictional contacts with the lower and upper surfaces, constraining the lateral displacement of the loaded nodes. We apply a displacement boundary condition to the loaded nodes in steps and calculate the reaction force at each step to extract the loading curve. The reaction force is summed over the contributions of all loaded nodes and edges.

For both experimental and simulated loading curves, we extract an estimate of stiffness by fitting a line to the loading curves and comparing the values across values of α. These values are plotted in Figure B.2d. While the exact values of these stiffnesses are likely subject to inaccuracies in experiment and modeling, the orders of magnitude are commensurate.

B.3 Conclusions

In this work, we have derived a model for simulating structural origami using bicubic Hermite patches to represent facets of our origami pattern. Leveraging the form of the bicubic function, we expressed the coefficients used to calculate the shape in terms of the positions and derivatives of the patch at its vertices, a convenient way to describe origami. Assuming the facet behaves as a thin plate, we expressed the bending and stretching energy densities in a form that can be evaluated in terms of these positions and derivatives. We implemented this facet formulation and extended the model to include multiple facets joined along crease lines. Finally, we imposed

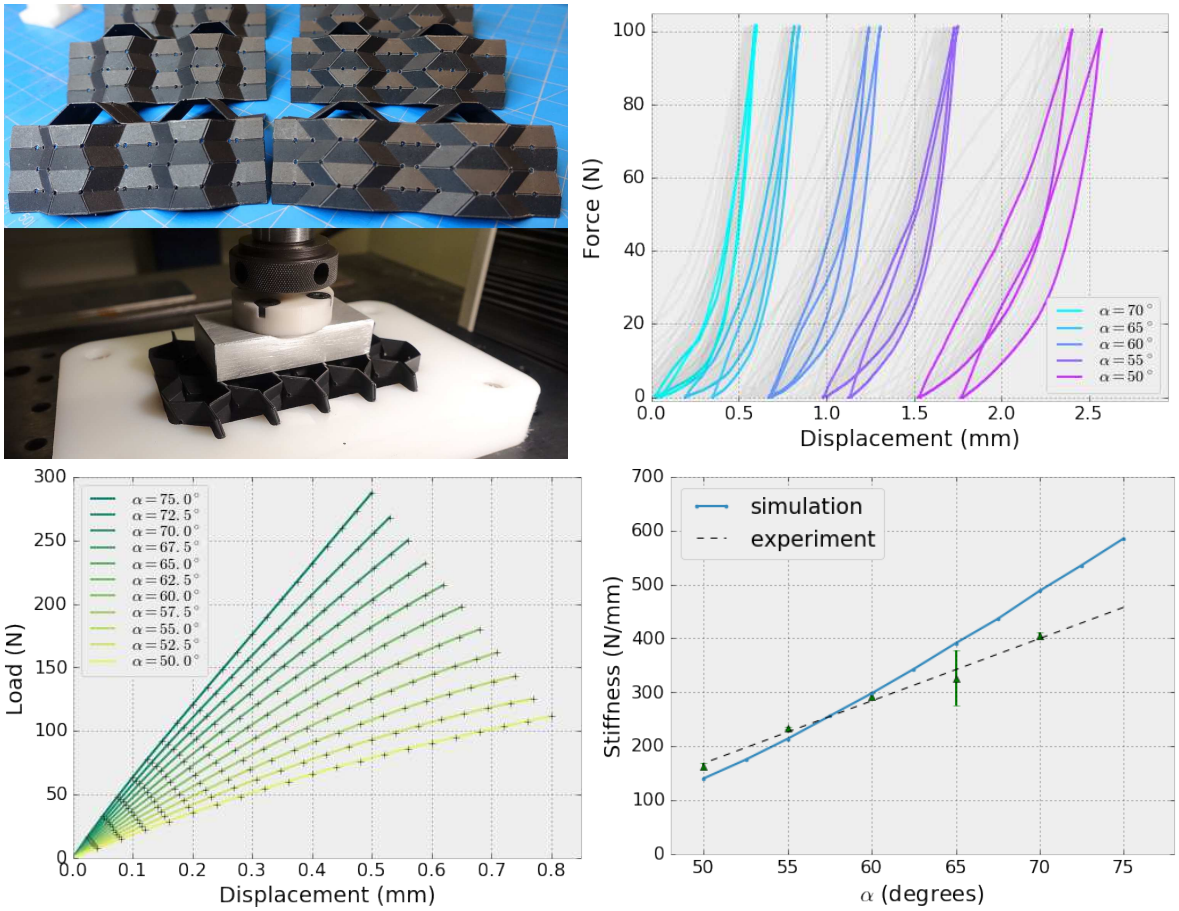

Figure B.2: A) Polypropylene samples folded and held in materials characterization machine, B) Force-displacement curves for the samples, C) Simulated force-displacement curves for a variety of Miura angles, D) Comparison of instantaneous stiffness for a variety of Miura angles between simulation and experiment.

boundary conditions and wrote a nonlinear quasi-Newton solver to produce minimum energy configurations. The results of this simulation are not only visually believable, but show a rough match with experimental data.

In future work, we plan to more fully test this formulation, comparing it against not only experimental data, but also other simulation methods. Following the example of [62], this testing will include both simple models where sources of discrepancy can be analyzed, as well as complex models where scalability can be evaluated.

Further, we also plan to move much of the computation from a CPU implementation to a GPU implementation. The majority of the computational burden of this model is not in solving the linear systems but instead in evaluating functions on the integration grid of the facets, which can be easily parallelized. Consequently, the GPU implementation would likely be considerably faster-running than the CPU version.

If this work is successful, this Hermite patch model could become a useful tool for structural origami analysis and design. Unlike simpler origami models, this approach can capture some localized deformations. The systems resulting from this model, however, are likely to be smaller than those from discretized finite element analysis. In this way, the Hermite patch model could be useful for cases when localize effects are important but finite elements are too expensive.

B.4 Matrix values

For reference, we include the values for symbolically computed matrices M and M^{-1} referenced in Section B.1.1

$$M = \begin{bmatrix}
1 & 0 & 0 & 0 & 0 & 0 & 0 & 0 & 0 & 0 & 0 & 0 & 0 & 0 & 0 & 0 \\
0 & 0 & 0 & 0 & 1 & 0 & 0 & 0 & 0 & 0 & 0 & 0 & 0 & 0 & 0 & 0 \\
0 & 1 & 0 & 0 & 0 & 0 & 0 & 0 & 0 & 0 & 0 & 0 & 0 & 0 & 0 & 0 \\
0 & 0 & 0 & 0 & 0 & 1 & 0 & 0 & 0 & 0 & 0 & 0 & 0 & 0 & 0 & 0 \\
1 & 0 & 0 & 0 & 1 & 0 & 0 & 0 & 1 & 0 & 0 & 0 & 1 & 0 & 0 & 0 \\
0 & 0 & 0 & 0 & 1 & 0 & 0 & 0 & 2 & 0 & 0 & 0 & 3 & 0 & 0 & 0 \\
0 & 1 & 0 & 0 & 0 & 1 & 0 & 0 & 0 & 1 & 0 & 0 & 0 & 1 & 0 & 0 \\
0 & 0 & 0 & 0 & 0 & 1 & 0 & 0 & 0 & 2 & 0 & 0 & 0 & 3 & 0 & 0 \\
1 & 1 & 1 & 1 & 0 & 0 & 0 & 0 & 0 & 0 & 0 & 0 & 0 & 0 & 0 & 0 \\
0 & 0 & 0 & 0 & 1 & 1 & 1 & 1 & 0 & 0 & 0 & 0 & 0 & 0 & 0 & 0 \\
0 & 1 & 2 & 3 & 0 & 0 & 0 & 0 & 0 & 0 & 0 & 0 & 0 & 0 & 0 & 0 \\
0 & 0 & 0 & 0 & 0 & 1 & 2 & 3 & 0 & 0 & 0 & 0 & 0 & 0 & 0 & 0 \\
1 & 1 & 1 & 1 & 1 & 1 & 1 & 1 & 1 & 1 & 1 & 1 & 1 & 1 & 1 & 1 \\
0 & 0 & 0 & 0 & 1 & 1 & 1 & 1 & 2 & 2 & 2 & 2 & 3 & 3 & 3 & 3 \\
0 & 1 & 2 & 3 & 0 & 1 & 2 & 3 & 0 & 1 & 2 & 3 & 0 & 1 & 2 & 3 \\
0 & 0 & 0 & 0 & 0 & 1 & 2 & 3 & 0 & 2 & 4 & 6 & 0 & 3 & 6 & 9
\end{bmatrix} \tag{B.21}$$

$$M^{-1} = \begin{bmatrix}
1 & 0 & 0 & 0 & 0 & 0 & 0 & 0 & 0 & 0 & 0 & 0 & 0 & 0 & 0 & 0 \\
0 & 0 & 1 & 0 & 0 & 0 & 0 & 0 & 0 & 0 & 0 & 0 & 0 & 0 & 0 & 0 \\
-3 & 0 & -2 & 0 & 0 & 0 & 0 & 0 & 3 & 0 & -1 & 0 & 0 & 0 & 0 & 0 \\
2 & 0 & 1 & 0 & 0 & 0 & 0 & 0 & -2 & 0 & 1 & 0 & 0 & 0 & 0 & 0 \\
0 & 1 & 0 & 0 & 0 & 0 & 0 & 0 & 0 & 0 & 0 & 0 & 0 & 0 & 0 & 0 \\
0 & 0 & 0 & 1 & 0 & 0 & 0 & 0 & 0 & 0 & 0 & 0 & 0 & 0 & 0 & 0 \\
0 & -3 & 0 & -2 & 0 & 0 & 0 & 0 & 0 & 3 & 0 & -1 & 0 & 0 & 0 & 0 \\
0 & 2 & 0 & 1 & 0 & 0 & 0 & 0 & 0 & -2 & 0 & 1 & 0 & 0 & 0 & 0 \\
-3 & -2 & 0 & 0 & 3 & -1 & 0 & 0 & 0 & 0 & 0 & 0 & 0 & 0 & 0 & 0 \\
0 & 0 & -3 & -2 & 0 & 0 & 3 & -1 & 0 & 0 & 0 & 0 & 0 & 0 & 0 & 0 \\
9 & 6 & 6 & 4 & -9 & 3 & -6 & 2 & -9 & -6 & 3 & 2 & 9 & -3 & -3 & 1 \\
-6 & -4 & -3 & -2 & 6 & -2 & 3 & -1 & 6 & 4 & -3 & -2 & -6 & 2 & 3 & -1 \\
2 & 1 & 0 & 0 & -2 & 1 & 0 & 0 & 0 & 0 & 0 & 0 & 0 & 0 & 0 & 0 \\
0 & 0 & 2 & 1 & 0 & 0 & -2 & 1 & 0 & 0 & 0 & 0 & 0 & 0 & 0 & 0 \\
-6 & -3 & -4 & -2 & 6 & -3 & 4 & -2 & 6 & 3 & -2 & -1 & -6 & 3 & 2 & -1 \\
4 & 2 & 2 & 1 & -4 & 2 & -2 & 1 & -4 & -2 & 2 & 1 & 4 & -2 & -2 & 1
\end{bmatrix} \tag{B.22}$$

Chapter 8

Bibliography

[1] Joanna Aizenberg, James C. Weaver, Monica S. Thanawala, Vikram C. Sundar, Daniel E. Morse, and Peter Fratzl. Skeleton of euplectella sp.: structural hierarchy from the nanoscale to the macroscale. *Science*, 309(5732):275–278, 2005. (Cited on page 14).

[2] Amir Akbarzadeh and Iman Borazjani. A numerical study on controlling flow separation via surface morphing in the form of backward traveling waves. In *AIAA Aviation Forum*, page 3589, 2019. (Cited on pages 74, 97, 98).

[3] Muhammad Ali, Khairul Alam, and Eboreime Ohioma. Energy absorption characteristics of a carbon fiber composite automobile lower rail: A comparative study. In *ASME International Mechanical Engineering Congress and Exposition*, volume 14, 2015. URL: http://dx.doi.org/10.1115/IMECE2015-50486. (Cited on page 72).

[4] R. Amacher, J. Cugnoni, J. Botsis, L. Sorensen, W. Smith, and C. Dransfeld. Thin ply composites: experimental characterization and modeling of size-effects. *Composites Science and Technology*, 101:121–132, 2014. (Cited on page 51).

[5] Oluwaseun A. Araromi, Conor J. Walsh, and Robert J. Wood. Hybrid carbon fiber-textile compliant force sensors for high-load sensing in soft exosuits. In *2017 IEEE/RSJ International Conference on Intelligent Robots and Systems (IROS)*, pages 1798–1803. IEEE, 2017. (Cited on page 17).

[6] Michael F. Ashby, Tony Evans, Norman A. Fleck, J.W. Hutchinson, H.N.G. Wadley, and L.J. Gibson. *Metal Foams: A Design Guide*. Elsevier, 2000. (Cited on page 14, 14).

[7] Wyss Institute at Harvard University. Pop-Up mems. URL: https://wyss.harvard.edu/technology/pop-up-mems/. (Cited on page 17).

[8] Basile Audoly and Yves Pomeau. *Elasticity and Geometry: From Hair Curls to the Non-Linear Response of Shells*. Oxford University Press, 2010. (Cited on page 109).

[9] Daniel M. Aukes, Benjamin Goldberg, Mark R. Cutkosky, and Robert J. Wood. An analytic framework for developing inherently-manufacturable pop-up laminate devices. *Smart Materials and Structures*, 23(9), 2014. (Cited on page 17).

[10] Daniel M. Aukes and Robert J. Wood. PopupCAD: a tool for automated design, fabrication, and analysis of laminate devices. In *Micro-and Nanotechnology Sensors, Systems, and Applications VII*, volume 9467. International Society for Optics and Photonics, 2015. (Cited on page 17).

[11] Sahab Babaee, Johannes T. B. Overvelde, Elizabeth R. Chen, Vincent Tournat, and Katia Bertoldi. Reconfigurable origami-inspired acoustic waveguides. *Science Advances*, 2, 2016. (Cited on page 17).

[12] Stanley Backer. The relationship between the structural geometry of a textile fabric and its physical properties: Literature review. *Textile Research Journal*, 18(11):650–658, 1948. (Cited on page 14).

[13] E. Baer, A. Hiltner, and D. Jarus. Relationship of hierarchical structure to mechanical properties. In *Macromolecular symposia*, volume 147, pages 37–61. Wiley Online Library, 1999. (Cited on page 14).

[14] Kyle R. Barnes and Andrew E. Kilding. A randomized crossover study investigating the running economy of highly-trained male and female distance runners in marathon racing shoes versus track spikes. *Sports Medicine*, pages 1–12, 2019. (Cited on page 56).

[15] D.S. Barrett, M.S. Triantafyllou, D.K.P. Yue, M.A. Grosenbaugh, and M.J. Wolfgang. Drag reduction in fish-like locomotion. *Journal of Fluid Mechanics*, 392:183–212, 1999. (Cited on page 73).

[16] Katia Bertoldi, Vincenzo Vitelli, Johan Christensen, and Martin van Hecke. Flexible mechanical metamaterials. *Nature Reviews Materials*, 2(11), 2017. (Cited on pages 14, 74).

[17] James Bird, Matthew Santer, and Jonathan Morrison. The determination and enhancement of compliant modes for actuation in structural assemblies. *International Journal of Solids and Structures*, 106-107:264–273, 2017. URL: http://www.sciencedirect.com/science/article/pii/S0020768316303237. (Cited on page 74).

[18] James Bird, Matthew Santer, and Jonathan Morrison. Compliant kagome lattice structures for generating in-plane waveforms. *International Journal of Solids and Structures*, 141-142:86–101, 2018. URL: http://www.sciencedirect.com/science/article/pii/S0020768318300593. (Cited on page 74).

[19] James Bird, Matthew Santer, and Jonathan F. Morrison. Experimental control of turbulent boundary layers with in-plane travelling waves. *Flow, Turbulence and Combustion*, 100(4):1015–1035, 2018. URL: https://doi.org/10.1007/s10494-018-9926-2. (Cited on page 74).

[20] James W. Bird, Matthew J. Santer, and Jonathan F. Morrison. Adaptive kagome lattices for near wall turbulence suppression. In *23rd AIAA/AHS Adaptive Structures Conference*. American Institute of Aeronautics and Astronautics, 2015. URL: https://doi.org/10.2514/6.2015-0270. (Cited on page 74).

[21] Josh Bishop-Moser, Christine Andres, and Chris Spadaccini. A call to action: Manufacturing architected materials. *Journal of Materials Research*, 33(3):247–248, 2018. (Cited on page 14).

[22] Tom Bitzer. *Honeycomb Technology: Materials, Design, Manufacturing, Applications and Testing.: Materials, Design, Manufacturing, Applications and Testing*. Springer, 1997. URL: http://www.springer.com/us/book/9780412540509. (Cited on page 14).

[23] Melina K. Blees, Arthur W. Barnard, Peter A. Rose, Samantha P. Roberts, Kathryn L. McGill, Pinshane Y. Huang, Alexander R. Ruyack, Joshua W. Kevek, Bryce Kobrin, David A. Muller, and Paul L. McEuen. Graphene kirigami. *Nature*, 524, 2015. URL: https://doi.org/10.1038/nature14588. (Cited on page 17).

[24] Elisa Boatti, Nikolaos Vasios, and Katia Bertoldi. Origami metamaterials for tunable thermal expansion. *Advanced Materials*, 29(26), 2017. (Cited on page 17).

[25] Allan F Bower. *Applied Mechanics of Solids*. CRC Press, 2009. URL: http://solidmechanics.org/index.html. (Cited on page 112).

[26] J. Philipp Bratfisch, Dirk Vandepitte, Jochen Pflug, and Ignaas Verpoest. Development and validation of a continuous production concept for thermoplastic honeycomb. In *Sandwich structures 7: advancing with sandwich structures and materials*, pages 763–772. Springer, 2005. (Cited on page 16).

[27] Remo Brühwiler, Benjamin Goldberg, Neel Doshi, Onur Ozcan, Noah Jafferis, Michael Karpelson, and Robert J. Wood. Feedback control of a legged microrobot with on-board sensing. In *2015 IEEE/RSJ International Conference on Intelligent Robots and Systems (IROS)*, pages 5727–5733. IEEE, 2015. (Cited on page 17).

[28] Carl Bugeja. How to print an electric motor. *IEEE Spectrum*, September 2018. URL: https://spectrum.ieee.org/geek-life/hands-on/how-to-print-an-electric-motor. (Cited on page 85).

[29] Wenshan Cai and Vladimir Shalaev. *Optical Metamaterials: Fundamentals and Applications*. Springer Science and Business Media, 2009. (Cited on page 14).

[30] Len Calderone. What super efficient manufacturing looks like, July 2016. URL: https://www.manufacturingtomorrow.com/article/2016/07/what-super-efficient-manufacturing-looks-like/8262. (Cited on page 16).

[31] Sam Calisch and Neil Gershenfeld. Kirigami fabrication of shaped, flat-foldable cellular materials based on the tachi-miura polyhedron. In *Origami^7: Proceedings of the 7th International Meeting on Origami in Science, Mathematics and Education (OSME 2018)*, volume 7, 2018. (Cited on page 33).

[32] Sam Calisch and Neil Gershenfeld. Towards continuous production of shaped honeycombs. In *ASME 2018 Manufacturing Science and Engineering Conference*, volume 3. American Society of Mechanical Engineers, 2018. (Cited on pages 19, 35).

[33] Sam Calisch, Neil Gershenfeld, Dixia Fan, Gurvan Jodin, and Michael Triantafyllou. Fabrication and characterization of folded foils supporting streamwise traveling waves. In *IUTAM Symposium on Critical flow dynamics involving moving/deformable structures with design applications*, June 2018. (Cited on pages 75, 94).

[34] Sam Calisch, Neil Gershenfeld, Dixia Fan, Gurvan Jodin, and Michael Triantafyllou. Fabrication and characterization of folded foils supporting streamwise traveling waves. *Journal of Fluids and Structures*, 2019. URL: http://www.sciencedirect.com/science/article/pii/S0889974618306091. (Cited on page 75).

[35] P.W. Carpenter, Christopher Davies, and A. Lucey. Hydrodynamics and compliant walls: Does the dolphin have a secret? *Current Science*, 79, 1999. (Cited on page 73).

[36] Mark A. Carruth, Julian M. Allwood, and Muiris C. Moynihan. The technical potential for reducing metal requirements through lightweight product design. *Resources, Conservation and Recycling*, 57:48–60, 2011. (Cited on page 104).

[37] Toen Castle, Yigil Cho, Xingting Gong, Euiyeon Jung, Daniel M. Sussman, Shu Yang, and Randall D. Kamien. Making the cut: Lattice kirigami rules. *Physical review letters*, 113(24), 2014. (Cited on page 17).

[38] Toen Castle, Daniel M. Sussman, Michael Tanis, and Randall D. Kamien. Additive lattice kirigami. *Science Advances*, 2(9), 2016. URL: http://advances.sciencemag.org/content/2/9/e1601258. (Cited on page 17).

[39] Lynette Cheah, Natalia Duque Ciceri, Elsa Olivetti, Seiko Matsumura, Dai Forterre, Richard Roth, and Randolph Kirchain. Manufacturing-focused emissions reductions in footwear production. *Journal of Cleaner Production*, 44:18–29, 2013. URL: http://www.sciencedirect.com/science/article/pii/S0959652612006300. (Cited on pages 40, 104, 105, 105).

[40] Wenli Chen, Yang Liu, Feng Xu, Hui Li, and Hui Hu. Suppression of vortex shedding from a circular cylinder by using a traveling wave wall. In *52nd Aerospace Sciences Meeting*. American Institute of Aeronautics and Astronautics, 2014. (Cited on page 73).

[41] Kenneth C. Cheung, Erik D. Demaine, Jonathan Bachrach, and Saul Griffith. Programmable assembly with universally foldable strings (moteins). *IEEE Transactions on Robotics*, 27(4):718–729, 2011. (Cited on page 17).

[42] Kenneth C. Cheung, Tomohiro Tachi, Sam Calisch, and Koryo Miura. Origami interleaved tube cellular materials. *Smart Materials and Structures*, 23(9), 2014. URL: http://iopscience.iop.org/article/10.1088/0964-1726/23/9/094012/meta. (Cited on page 17).

[43] Johan Christensen, Muamer Kadic, Oliver Kraft, and Martin Wegener. Vibrant times for mechanical metamaterials. *MRS Communications*, 5(3):453–462, 2015. (Cited on page 14).

[44] Brett G. Compton and Jennifer A. Lewis. 3D-printing of lightweight cellular composites. *Advanced Materials*, 26(34):5930–5935, 2014. URL: https://onlinelibrary.wiley.com/doi/abs/10.1002/adma.201401804. (Cited on page 15).

[45] Grumman Aerospace Corporation, the National Aeronautics, and Space Administration. Apollo news reference: Lunar module, 1972. URL: https://www.hq.nasa.gov/alsj/CSM_News_Reference_H_Missions.pdf. (Cited on page 57).

[46] Jonathan M. Cullen and Julian M. Allwood. The efficient use of energy: Tracing the global flow of energy from fuel to service. *Energy Policy*, 38(1):75–81, 2010. URL: http://www.sciencedirect.com/science/article/pii/S0301421509006429. (Cited on page 103).

[47] Erik D. Demaine, Martin L. Demaine, David A. Huffman, Duks Koschitz, and Tomohiro Tachi. Characterization of curved creases and rulings: Design and analysis of lens tessellations. In *Origami^6: Proceedings of the 6th International Meeting on Origami in Science, Mathematics and Education (OSME 2014)*, volume 1, pages 209–230. American Mathematical Society, Tokyo, Japan, August 10–13 2014. (Cited on pages 44, 46).

[48] Erik D. Demaine, Martin L. Demaine, David A. Huffman, Duks Koschitz, and Tomohiro Tachi. Conic crease patterns with reflecting rule lines. In *Origami^7: Proceedings of the 7th International Meeting on Origami in Science, Mathematics and Education (OSME 2018)*. Tarquin, Oxford, England, September 5–7 2018. (Cited on pages 44, 46).

[49] Erik D. Demaine and Joseph O'Rourke. *Geometric Folding Algorithms: Linkages, Origami, Polyhedra*. Cambridge University Press, July 2007. (Cited on page 16).

[50] Erik D. Demaine and Tomohiro Tachi. Origamizer: A practical algorithm for folding any polyhedron. In *Proceedings of the 33rd International Symposium on Computational Geometry (SoCG 2017)*, pages 34:1–34:15, Brisbane, Australia, July 4–7 2017. (Cited on pages 16, 17).

[51] Benjia Dou, James B. Whitaker, Karsten Bruening, David T. Moore, Lance M. Wheeler, John Ryter, Nicholas J Breslin, Joseph J Berry, Sean M Garner, and Frank Barnes. Roll-to-roll printing of perovskite solar cells. *ACS Energy Letters*, 2018. (Cited on page 16).

[52] Levi H. Dudte, Etienne Vouga, Tomohiro Tachi, and L. Mahadevan. Programming curvature using origami tessellations. *Nature Materials*, 15(5):583–588, 05 2016. URL: http://dx.doi.org/10.1038/nmat4540. (Cited on page 17).

[53] Mihai Duduta, David R Clarke, and Robert J Wood. A high speed soft robot based on dielectric elastomer actuators. In *IEEE International Conference on Robotics and Automation (ICRA)*, pages 4346–4351. IEEE, 2017. (Cited on page 17).

[54] Keith J. Dusoe, Xinyi Ye, Kim Kisslinger, Aaron Stein, Seok-Woo Lee, and Chang-Yong Nam. Ultrahigh elastic strain energy storage in metal-oxide-infiltrated patterned hybrid polymer nanocomposites. *Nano Letters*, 17(12):7416–7423, 12 2017. URL: https://doi.org/10.1021/acs.nanolett.7b03238. (Cited on page 43).

[55] The Economist. On a roll, July 2016. URL: https://www.economist.com/science-and-technology/2016/07/29/on-a-roll. (Cited on page 15).

[56] E.A. Elsayed and B.B. Basily. A continuous folding process for sheet materials. *International Journal of Materials and Product Technology*, 21(1-3):217–238, 2004. (Cited on pages 16, 20, 41).

[57] Nieves Espinosa, Rafael Garcia-Valverde, Antonio Urbina, and Frederik C. Krebs. A life cycle analysis of polymer solar cell modules prepared using roll-to-roll methods under ambient conditions. *Solar Energy Materials and Solar Cells*, 95(5):1293–1302, 2011. (Cited on page 16).

[58] Nieves Espinosa, Markus Hösel, Dechan Angmo, and Frederik C. Krebs. Solar cells with one-day energy payback for the factories of the future. *Energy and Environmental Science*, 5(1):5117–5132, 2012. (Cited on page 15).

[59] R.K. Fathers, J.M. Gattas, and Z. You. Quasi-static crushing of eggbox, cube, and modified cube foldcore sandwich structures. *International Journal of Mechanical Sciences*, 101:421–428, 2015. (Cited on page 58).

[60] S. Felton, M. Tolley, E. Demaine, D. Rus, and R. Wood. A method for building self-folding machines. *Science*, 345(6197):644–646, 2014. URL: http://science.sciencemag.org/content/345/6197/644. (Cited on page 17).

[61] S.M. Felton, K.P. Becker, D.M. Aukes, and R.J. Wood. Self-folding with shape memory composites at the millimeter scale. *Journal of Micromechanics and Microengineering*, 25(8), 2015. (Cited on page 17).

[62] E.T. Filipov, K. Liu, T. Tachi, M. Schenk, and G.H. Paulino. Bar and hinge models for scalable analysis of origami. *International Journal of Solids and Structures*, 124:26–45, 2017. (Cited on pages 17, 108, 114).

[63] Evgueni T. Filipov, Tomohiro Tachi, and Glaucio H. Paulino. Origami tubes assembled into stiff, yet reconfigurable structures and metamaterials. *Proceedings of the National Academy of Sciences*, 112(40):12321–12326, 2015. URL: http://www.pnas.org/content/112/40/12321.abstract. (Cited on pages 17, 109).

[64] Sebastian Fischer, Sebastian Heimbs, Sebastian Kilchert, M Klaus, and C. Cluzel. Sandwich structures with folded core: Manufacturing and mechanical behavior. In *SAMPE Europe International Conference*, 2009. (Cited on page 58).

[65] Frank E. Fish. A porpoise for power. *Journal of Experimental Biology*, 208(6):977–978, 2005. (Cited on page 73).

[66] Peter Fratzl and Richard Weinkamer. Nature's hierarchical materials. *Progress in Materials Science*, 52(8):1263–1334, 2007. (Cited on page 14).

[67] Freedonia. World corrugated boxes, study 3042. Technical report, Freedonia, 2013. URL: https://www.freedoniagroup.com/brochure/30xx/3042smwe.pdf. (Cited on pages 16, 63).

[68] Daniel Garrett, Zhong You, and Joseph M. Gattas. Curved crease tube structures as an energy absorbing crash box. In *International Design Engineering Technical Conferences and Computers and Information in Engineering Conference*, volume 5B, 2016. URL: http://dx.doi.org/10.1115/DETC2016-59784. (Cited on page 58).

[69] J.M. Gattas and Z. You. Quasi-static impact of indented foldcores. *International Journal of Impact Engineering*, 73:15–29, 2014. (Cited on page 59).

[70] J.M. Gattas and Z. You. The behaviour of curved-crease foldcores under low-velocity impact loads. *International Journal of Solids and Structures*, 53:80–91, 2015. URL: http://www.sciencedirect.com/science/article/pii/S0020768314003989. (Cited on pages 59, 59, 62, 62).

[71] Amanda Ghassaei, Erik D. Demaine, and Neil Gershenfeld. Fast, interactive origami simulation using GPU computation. In *Origami^7: Proceedings of the 7th International Meeting on Origami in Science, Mathematics and Education (OSME 2018)*. Tarquin, Oxford, England, September 5–7 2018. (Cited on page 17).

[72] Lorna J. Gibson. The hierarchical structure and mechanics of plant materials. *Journal of The Royal Society Interface*, 9(76):2749–2766, 2012. URL: http://rsif.royalsocietypublishing.org/content/9/76/2749. (Cited on page 14).

[73] Lorna J. Gibson and Michael F. Ashby. *Cellular Solids: Structure and Properties*. Cambridge university press, 1999. URL: http://www.cambridge.org/us/academic/subjects/engineering/materials-science/cellular-solids-structure-and-properties-2nd-edition?format=PB&isbn=9780521499118. (Cited on page 14).

[74] Lorna J Gibson, Michael F Ashby, and Brendan A Harley. *Cellular materials in nature and medicine*. Cambridge University Press, 2010. (Cited on page 14).

[75] Jamison Go and A. John Hart. Fast desktop-scale extrusion additive manufacturing. *Additive Manufacturing*, 18:276–284, 2017. (Cited on page 15).

[76] Benjamin Goldberg, Michael Karpelson, Onur Ozcan, and Robert J. Wood. Planar fabrication of a mesoscale voice coil actuator. In *2014 IEEE International Conference on Robotics and Automation (ICRA)*, pages 6319–6325. IEEE, 2014. (Cited on page 17).

[77] Jian Gong, Seth B. Darling, and Fengqi You. Perovskite photovoltaics: life-cycle assessment of energy and environmental impacts. *Energy and Environmental Science*, 8(7):1953–1968, 2015. (Cited on page 16).

[78] J. Gray. Studies in animal locomotion: The propulsive powers of the dolphin. *Journal of experimental biology*, 13(2):192–199, 1936. (Cited on page 73).

[79] Timothy Gutowski, Sheng Jiang, Daniel Cooper, Gero Corman, Michael Hausmann, Jan-Anders Manson, Timo Schudeleit, Konrad Wegener, Matias Sabelle, and Jorge Ramos-Grez. Note on the rate and energy efficiency limits for additive manufacturing. *Journal of Industrial Ecology*, 21(S1):S69–S79, 2017. (Cited on page 15).

[80] Jürgen Hagedorn, Florian Sell-Le Blanc, and Jürgen Fleischer. *Handbook of Coil Winding*. Springer, 2018. (Cited on page 85).

[81] Falk Hahnel, Klaus Wolf, Andreas Hauffe, Kirill A. Alekseev, and Il'dus M. Zakirov. Wedge-shaped folded sandwich cores for aircraft applications: from design and manufacturing process to experimental structure validation. *CEAS Aeronautical Journal*, 2(1):203–212, 2011. URL: http://dx.doi.org/10.1007/s13272-011-0014-8. (Cited on pages 16, 20, 72).

[82] H. Hamada, J.C. Coppola, D. Hull, Z. Maekawa, and H. Sato. Comparison of energy absorption of carbon/epoxy and carbon/PEEK composite tubes. *Composites*, 23(4):245–252, 1992. URL: http://www.sciencedirect.com/science/article/pii/001043619290184V. (Cited on page 72).

[83] Z. Hashin and S. Shtrikman. A variational approach to the theory of the elastic behaviour of multiphase materials. *Journal of the Mechanics and Physics of Solids*, 11(2):127–140, 1963. URL: http://www.sciencedirect.com/science/article/pii/0022509663900607. (Cited on page 14).

[84] E. Hawkes, B. An, N. M. Benbernou, H. Tanaka, S. Kim, E. D. Demaine, D. Rus, and R. J. Wood. Programmable matter by folding. *Proceedings of the National Academy of Sciences of the United States of America*, 107(28):12441–12445, 2010. (Cited on page 17).

[85] John W.S. Hearle, Percy Grosberg, and Stanley Backer. Structural mechanics of fibers, yarns and fabrics. *Wiley Interscience*, 1969. (Cited on page 14).

[86] Sebastian Heimbs. Foldcore sandwich structures and their impact behaviour: an overview. In *Dynamic failure of composite and sandwich structures*, pages 491–544. Springer, 2013. URL: http://link.springer.com.libproxy.mit.edu/chapter/10.1007%2F978-94-007-5329-7_11. (Cited on pages 16, 20).

[87] Sebastian Heimbs, Jörg Cichosz, Sebastian Kilchert, and M. Klaus. Sandwich panels with cellular cores made of folded composite material: Mechanical behaviour and impact performance. In *ICCM International Conferences on Composite Materials*, 07 2009. (Cited on pages 58, 59).

[88] Sarah Holt and François-Xavier Vives. Nova: The origami revolution. Public Broadcasting Service (PBS), 2017. (Cited on page 16).

[89] Wouter Hoogkamer, Shalaya Kipp, Jesse H. Frank, Emily M. Farina, Geng Luo, and Rodger Kram. A comparison of the energetic cost of running in marathon racing shoes. *Sports Medicine*, 48(4):1009–1019, Apr 2018. URL: https://doi.org/10.1007/s40279-017-0811-2. (Cited on page 56, 56).

[90] Aaron M. Hoover and Ronald S. Fearing. Fast scale prototyping for folded millirobots. In *2008 IEEE International Conference on Robotics and Automation*, pages 886–892. IEEE, 2008. (Cited on page 51).

[91] A. Horrocks and S. Anand. *Handbook of Technical Textiles*. Woodhead, 2000. (Cited on page 16).

[92] A. Hsu, A. Wong-Foy, B. McCoy, C. Cowan, J. Marlow, B. Chavez, T. Kobayashi, D. Shockey, and R. Pelrine. Application of micro-robots for building carbon fiber trusses. In *2016 International Conference on Manipulation, Automation and Robotics at Small Scales (MARSS)*, pages 1–6, July 2016. (Cited on page 85).

[93] Guohua Hu, Joohoon Kang, Leonard WT Ng, Xiaoxi Zhu, Richard C.T. Howe, Christopher G. Jones, Mark C. Hersam, and Tawfique Hasan. Functional inks and printing of two-dimensional materials. *Chemical Society Reviews*, 47(9):3265–3300, 2018. (Cited on page 15).

[94] J.E. Huber, N.A. Fleck, and M.F. Ashby. The selection of mechanical actuators based on performance indices. *Proceedings of the Royal Society of London. Series A: Mathematical, physical and engineering sciences*, 453(1965):2185–2205, 1997. (Cited on page 75).

[95] Inc. IBISWorld. Ibisworld industry report: Global footwear manufacturing: C1321-gl. Technical report, IBISWorld, Inc., 2010. URL: https://clients1.ibisworld.com/reports/gl/industry/default.aspx?entid=500. (Cited on page 105).

[96] COMSOL Inc. Comsol multiphysics reference manual, version 5.3. URL: www.comsol.com. (Cited on pages 79, 84).

[97] Alexandra Ion, Johannes Frohnhofen, Ludwig Wall, Robert Kovacs, Mirela Alistar, Jack Lindsay, Pedro Lopes, Hsiang-Ting Chen, and Patrick Baudisch. Metamaterial mechanisms. In *Proceedings of the 29th Annual Symposium on User Interface Software and Technology*, pages 529–539. ACM, 2016. (Cited on page 14).

[98] George C. Jacob, John F. Fellers, Srdan Simunovic, and J. Michael Starbuck. Energy absorption in polymer composites for automotive crashworthiness. *Journal of Composite Materials*, 36(7):813–850, 2002. URL: https://doi.org/10.1177/0021998302036007164. (Cited on page 57).

[99] Noah T. Jafferis, Mario Lok, Nastasia Winey, Gu-Yeon Wei, and Robert J. Wood. Multilayer laminated piezoelectric bending actuators: design and manufacturing for optimum power density and efficiency. *Smart Materials and Structures*, 25(5):055033, 2016. (Cited on pages 17, 75).

[100] Noah T. Jafferis, Howard A. Stone, and James C. Sturm. Traveling wave-induced aerodynamic propulsive forces using piezoelectrically deformed substrates. *Applied Physics Letters*, 99(11):114102, 2011. URL: https://doi.org/10.1063/1.3637635. (Cited on page 75).

[101] Noah Thomas Jafferis. *The flying carpet and other tales.* PhD thesis, Princeton University, 2012. (Cited on page 75).

[102] Kaushik Jayaram, Noah Thomas Jafferis, Neel Doshi, Benjamin Goldberg, and Robert J. Wood. Concomitant sensing and actuation for piezoelectric microrobots. *Smart Materials and Structures*, 2018. (Cited on page 17).

[103] Benjamin Jenett, Sam Calisch, Daniel Cellucci, Nick Cramer, Neil Gershenfeld, Sean Swei, and Kenneth C. Cheung. Digital morphing wing: Active wing shaping concept using composite lattice-based cellular structures. *Soft Robotics*, 2016. URL: http://dx.doi.org/10.1089/soro.2016.0032. (Cited on pages 14, 74).

[104] Lincoln M. Jore and Matthew B. Jore. Conductor optimized axial field rotary energy device, Oct 2004. URL: https://patents.google.com/patent/US7109625B1/en. (Cited on page 85).

[105] Andreas Keller. Basics of rotary die-cutting, October 2018. URL: https://narrowwebtech.com/dossiers/basics-of-rotary-die-cutting/. (Cited on pages 15, 17).

[106] Yves Klett. Realtime rigid folding algorithm for quadrilateral-based 1-dof tessellations. In *International Design Engineering Technical Conferences and Computers and Information in Engineering Conference*, 2013. URL: http://dx.doi.org/10.1115/DETC2013-12659. (Cited on pages 16, 20).

[107] Yves Klett and Klaus Drechsler. Designing technical tessellations. In *Origami^5: Proceedings of the 5th International Meeting of Origami Science, Math, and Education*, pages 305–322, 2011. URL: http://www.crcnetbase.com/doi/abs/10.1201/b10971-28. (Cited on pages 16, 20, 72).

[108] Ara Nerses Knaian. *Electropermanent Magnetic Connectors and Actuators: Devices and Their Application in Programmable Matter*. PhD thesis, Massachusetts Institute of Technology, 2010. (Cited on page 106).

[109] Oak Ridge National Lab. National household travel survey. Technical report, U.S. Department of Transportation, 2017. URL: https://nhts.ornl.gov/. (Cited on page 105).

[110] Roderic Lakes. Foam structures with a negative poisson's ratio. *Science*, pages 1038–1040, 1987. (Cited on page 14).

[111] Roderic Lakes. Materials with structural hierarchy. *Nature*, 361(6412):511–515, 1993. URL: http://www.nature.com/nature/journal/v361/n6412/abs/361511a0.html. (Cited on page 14).

[112] Roderic Lakes. Cellular solids with tunable positive or negative thermal expansion of unbounded magnitude. *Applied Physics Letters*, 90(22):221905, 2007. URL: https://doi.org/10.1063/1.2743951. (Cited on page 14).

[113] Raph Levien. The elastica: a mathematical history. Technical Report UCB/EECS-2008-103, EECS Department, University of California, Berkeley, Aug 2008. URL: http://www2.eecs.berkeley.edu/Pubs/TechRpts/2008/EECS-2008-103.html. (Cited on page 48).

[114] J.âĂĽA. Lewis. Direct ink writing of 3d functional materials. *Advanced Functional Materials*, 16(17):2193–2204, 2006. URL: https://onlinelibrary.wiley.com/doi/abs/10.1002/adfm.200600434. (Cited on page 15).

[115] Shuguang Li, Daniel M Vogt, Daniela Rus, and Robert J Wood. Fluid-driven origami-inspired artificial muscles. *Proceedings of the National Academy of Sciences*, page 201713450, 2017. URL: https://www.pnas.org/content/114/50/13132. (Cited on page 17).

[116] Yang Li and Zhong You. Thin-walled open-section origami beams for energy absorption. In *International Design Engineering Technical Conferences and Computers and Information in Engineering Conference*, volume 3, 2014. URL: http://dx.doi.org/10.1115/DETC2014-35204. (Cited on page 58).

[117] Yang Li and Zhong You. Corrugated tube inversion for energy absorption. In *International Design Engineering Technical Conferences and Computers and Information in Engineering Conference*, 2015. URL: http://dx.doi.org/10.1115/DETC2015-47135. (Cited on page 58).

[118] Yang Li and Zhong You. Multi-corrugated indented foldcore sandwich panel for energy absorption. In *International Design Engineering Technical Conferences and Computers and Information in Engineering Conference*, 2015. URL: http://dx.doi.org/10.1115/DETC2015-47269. (Cited on page 58).

[119] Ce Liu. *Beyond pixels: exploring new representations and applications for motion analysis*. PhD thesis, Massachusetts Institute of Technology, 2009. URL: https://people.csail.mit.edu/celiu/Thesis/CePhDThesis.pdf. (Cited on page 94).

[120] Lonnie J. Love, Chad E. Duty, Brian K. Post, Randall F. Lind, Peter D. Lloyd, Vlastsimil Kunc, William H. Peter, and Craig A. Blue. Breaking barriers in polymer additive manufacturing. Technical report, Oak Ridge National Lab.(ORNL), Oak Ridge, TN (United States). Manufacturing Demonstration Facility (MDF), 2015. (Cited on page 15).

[121] Guoxing Lu and T.X. Yu. *Energy Absorption of Structures and Materials*. Elsevier, 2003. (Cited on pages 57, 57, 72).

[122] Kevin Y. Ma, Pakpong Chirarattananon, Sawyer B. Fuller, and Robert J. Wood. Controlled flight of a biologically inspired, insect-scale robot. *Science*, 340(6132):603–607, 2013. (Cited on page 17).

[123] Kevin Y. Ma, Pakpong Chirarattananon, and Robert J. Wood. Design and fabrication of an insect-scale flying robot for control autonomy. In *IEEE/RSJ International Conference on Intelligent Robots and Systems (IROS)*, pages 1558–1564. IEEE, 2015. (Cited on page 17).

[124] Ronit Malka, Alexis Lussier Desbiens, Yufeng Chen, and Robert J. Wood. Principles of microscale flexure hinge design for enhanced endurance. In *2014 IEEE/RSJ International Conference on Intelligent Robots and Systems (IROS 2014)*, pages 2879–2885. IEEE, 2014. (Cited on page 51).

[125] J. Mallinson. One-sided fluxes – a magnetic curiosity? *IEEE Transactions on Magnetics*, 9(4):678–682, December 1973. (Cited on page 91).

[126] Manroland. Manroland web systems, February 2015. URL: https://www.manroland-web.com/en/newsroom/press-release/1280/new-lithoman-for-ctp-printers-in-cape-town. (Cited on pages 15, 17).

[127] James F. Manwell, Jon G. McGowan, and Anthony L. Rogers. *Wind Energy Explained: Theory, Design and Application*. John Wiley and Sons, 2010. (Cited on page 22).

[128] R.K. Mc Farland. Hexagonal cell structures under post-buckling axial load. *AIAA journal*, 1(6):1380–1385, 1963. URL: https://arc.aiaa.org/doi/pdf/10.2514/3.1798. (Cited on page 68).

[129] Hayley McClintock, Fatma Zeynep Temel, Neel Doshi, Je-sung Koh, and Robert J. Wood. The millidelta: A high-bandwidth, high-precision, millimeter-scale delta robot. *Science Robotics*, 3(14), 2018. URL: https://robotics.sciencemag.org/content/3/14/eaar3018. (Cited on page 17).

[130] R.K. McFarland Jr. The development of metal honeycomb energy-absorbing elements. *Jet Propulsion Laboratory, Pasadena, California*, Technical Report No. 32-63, 1964. URL: https://ntrs.nasa.gov/archive/nasa/casi.ntrs.nasa.gov/19640023989.pdf. (Cited on page 58, 58).

[131] Kristof Mertens. Folding and scoring: Finishing of coated papers after sheet-fed offset printing. Technical report, Sappi, 2001. URL: https://www.sappietc.com/sites/default/files/Sappi-Technical-Series-Folding-and-Scoring.pdf. (Cited on page 23).

[132] Lucas R. Meza, Alex J. Zelhofer, Nigel Clarke, Arturo J. Mateos, Dennis M. Kochmann, and Julia R. Greer. Resilient 3D hierarchical architected metamaterials. *Proceedings of the National Academy of Sciences*, 112(37):11502–11507, 2015. URL: http://www.pnas.org/content/112/37/11502. (Cited on page 43).

[133] Graeme W. Milton and Andrej V. Cherkaev. Which elasticity tensors are realizable? *Journal of Engineering Materials and Technology*, 117(4):483–493, 10 1995. URL: http://dx.doi.org/10.1115/1.2804743. (Cited on page 14).

[134] Marc Z. Miskin, Kyle J. Dorsey, Baris Bircan, Yimo Han, David A. Muller, Paul L. McEuen, and Itai Cohen. Graphene-based bimorphs for micron-sized, autonomous origami machines. *Proceedings of the National Academy of Sciences*, 115(3):466–470, 2018. URL: http://www.pnas.org/content/115/3/466. (Cited on page 17).

[135] Jun Mitani. Interactive design of planar curved folding by reflection. In *Proceedings of Pacific Graphics 2011.*, 2011. URL: https://www.jst.go.jp/erato/igarashi/publications/001/PG2011.pdf. (Cited on page 45).

[136] Koryo Miura. New structural form of sandwich core. *Journal of Aircraft*, 12(5):437–441, 1975. URL: http://arc.aiaa.org/doi/abs/10.2514/3.44468?journalCode=ja. (Cited on page 16).

[137] Koryo Miura and Tomohiro Tachi. Synthesis of rigid-foldable cylindrical polyhedral. *Symmetry: Art and Science, International Society for the Interdisciplinary Study of Symmetry, Gmuend*, 2010. URL: http://www.tsg.ne.jp/TT/cg/FoldableCylinders_miura_tachi_ISISSymmetry2010.pdf. (Cited on pages 17, 33, 35, 108, 113).

[138] B. Moore, T. Jaglinski, D. S. Stone, and R. S. Lakes. Negative incremental bulk modulus in foams. *Philosophical Magazine Letters*, 86(10):651–659, 2006. URL: https://doi.org/10.1080/09500830600957340. (Cited on page 14).

[139] Robin M Neville and Fabrizio Scarpa. Design of shape morphing cellular structures and their actuation methods. In *ICAST2015: 26th International Conference on Adaptive Structures and Technologies, Kobe, Japan.*, volume 10, 2015. (Cited on page 19).

[140] Taketoshi Nojima and Kazuya Saito. Development of newly designed ultra-light core structures. *JSME International Journal Series A Solid Mechanics and Material Engineering*, 49(1):38–42, 2006. URL: http://adsabs.harvard.edu/abs/2006JSMEA..49...38N. (Cited on pages 19, 33).

[141] Ida Norberg. *Carbon fibres from kraft lignin*. PhD thesis, KTH Royal Institute of Technology, 2012. URL: http://www.diva-portal.org/smash/get/diva2:513032/FULLTEXT01.pdf. (Cited on page 72).

[142] Mikael Nygards. Rate effects during rotary die creasing: Testing of paperboards with different zd compression properties. Technical report, Innventia, 2013. URL: http://www.innventia.com/Documents/Rapporter/report416.pdf. (Cited on page 15).

[143] Cagdas D. Onal, Michael T. Tolley, Robert J. Wood, and Daniela Rus. Origami-inspired printed robots. *IEEE/ASME transactions on mechatronics*, 20(5):2214–2221, 2015. (Cited on page 17).

[144] Cagdas D. Onal, Robert J. Wood, and Daniela Rus. Towards printable robotics: Origami-inspired planar fabrication of three-dimensional mechanisms. In *2011 IEEE International Conference on Robotics and Automation (ICRA)*, pages 4608–4613. IEEE, 2011. (Cited on page 17).

[145] OpenCV. Open source computer vision library. https://github.com/opencv/opencv, 2017. (Cited on page 30).

[146] Johannes T. B. Overvelde, Twan A. de Jong, Yanina Shevchenko, Sergio A. Becerra, George M. Whitesides, James C. Weaver, Chuck Hoberman, and Katia Bertoldi. A three-dimensional actuated origami-inspired transformable metamaterial with multiple degrees of freedom. *Nature Communications*, 7, 03 2016. URL: http://dx.doi.org/10.1038/ncomms10929. (Cited on page 17).

[147] Johannes T.B. Overvelde, James C. Weaver, Chuck Hoberman, and Katia Bertoldi. Rational design of reconfigurable prismatic architected materials. *Nature*, 541(7637):347–352, 2017. URL: http://www.nature.com/nature/journal/v541/n7637/full/nature20824.html. (Cited on page 17).

[148] Deepak Pathak. Python dense optical flow. Github. URL: https://github.com/pathak22/pyflow. (Cited on page 94).

[149] R. Pelrine, A. Wong-Foy, B. McCoy, D. Holeman, R. Mahoney, G. Myers, J. Herson, and T. Low. Diamagnetically levitated robots: An approach to massively parallel robotic systems with unusual motion properties. In *2012 IEEE International Conference on Robotics and Automation*, pages 739–744, May 2012. (Cited on page 85).

[150] Jochen Pflug. Coretinium®: a new tata steel material based on econcore's innovative thermhex technology. *Reinforced Plastics*, 60(2):107–109, 2016. URL: http://www.sciencedirect.com/science/article/pii/S0034361715008875. (Cited on page 16).

[151] Jochen Pflug, B. Vangrimde, Ignace Verpoest, Dirk Vandepitte, M. Britzke, and A. Wagenführ. Continuously produced paper honeycomb sandwich panels for furniture applications. In *5th Global Wood and Natural Fibre Composites Symposium. Kassel, Germany, April*, pages 27–28, 2004. (Cited on page 16).

[152] Brian Post, Peter D. Lloyd, John Lindahl, Randall F. Lind, Lonnie J. Love, and Vlastimil Kunc. The economics of big area additive manufacturing, 2016. (Cited on page 15).

[153] Jordan R. Raney and Jennifer A. Lewis. Printing mesoscale architectures. *MRS Bulletin*, 40(11):943–950, 2015. (Cited on page 14).

[154] Abhinav Rao, Sameh Tawfick, Matthew Shlian, and A. John Hart. Fold mechanics of natural and synthetic origami papers. In *ASME 2013 International Design Engineering Technical Conferences and Computers and Information in Engineering Conference*, pages V06BT07A049–V06BT07A049. American Society of Mechanical Engineers, 2013. URL: http://proceedings.asmedigitalcollection.asme.org/proceeding.aspx?articleid=1830770. (Cited on page 28).

[155] Shama Rao, T.G.A. Simha, and K.P. Rao. Carbon composites are becoming competitive and cost effective. Technical report, Infosys, 2018. URL: https://www.infosys.com/engineering-services/white-papers/Documents/carbon-composites-cost-effective.pdf. (Cited on page 72, 72).

[156] Leif Ristroph and Jun Zhang. Anomalous hydrodynamic drafting of interacting flapping flags. *Physical Review Letters*, 101:194502, Nov 2008. URL: https://link.aps.org/doi/10.1103/PhysRevLett.101.194502. (Cited on page 73).

[157] A.L. Roes, E.A. Alsema, K. Blok, and Martin Kumar Patel. Ex-ante environmental and economic evaluation of polymer photovoltaics. *Progress in Photovoltaics: Research and Applications*, 17(6):372–393, 2009. (Cited on page 16).

[158] Kazuya Saito, Fabio Agnese, and Fabrizio Scarpa. A cellular kirigami morphing wingbox concept. *Journal of intelligent material systems and structures*, 22(9):935–944, 2011. URL: http://jim.sagepub.com/content/22/9/935.refs. (Cited on pages 19, 33).

[159] Kazuya Saito, Akinobu Fujimoto, and Yoji Okabe. Design of a 3D wing honeycomb core based on origami techniques. In *International Design Engineering Technical Conferences and Computers and Information in Engineering Conference*, 2016. URL: http://dx.doi.org/10.1115/DETC2016-60419. (Cited on pages 20, 22).

[160] Kazuya Saito, Sergio Pellegrino, and Taketoshi Nojima. Manufacture of arbitrary cross-section composite honeycomb cores based on origami techniques. *Journal of Mechanical Design*, 136(5), 2014. URL: http://pressurevesseltech.asmedigitalcollection.asme.org/article.aspx?articleid=1831332. (Cited on pages 19, 22, 22, 33, 35).

[161] Tobias A. Schaedler and William B. Carter. Architected cellular materials. *Annual Review of Materials Research*, 46(1):187–210, 2016. URL: https://doi.org/10.1146/annurev-matsci-070115-031624. (Cited on page 14).

[162] Jürgen Schellenberg and Mario Wallis. Dependence of thermal properties of expandable polystyrene particle foam on cell size and density. *Journal of Cellular Plastics*, 46(3):209–222, 2010. URL: https://doi.org/10.1177/0021955X09350803. (Cited on page 16).

[163] Mark Schenk. *Folded shell structures*. PhD thesis, University of Cambridge, 2012. URL: http://www.markschenk.com/research/files/PhD%20thesis%20-%20Mark%20Schenk.pdf. (Cited on pages 17, 31, 41).

[164] Mark Schenk and Simon D. Guest. Origami folding: A structural engineering approach. In *Origami 5: Fifth International Meeting of Origami Science, Mathematics, and Education*, pages 291–304. CRC Press, Boca Raton, FL, 2011. URL: http://www2.eng.cam.ac.uk/~sdg/preprint/5OSME.pdf. (Cited on pages 17, 108).

[165] Mark Schenk and Simon D. Guest. Geometry of miura-folded metamaterials. *Proceedings of the National Academy of Sciences*, 110(9):3276–3281, 2013. URL: http://www.pnas.org/content/110/9/3276.short. (Cited on page 17).

[166] John Sewell, Tomasz Czarnecki, and Jochen Pflug. Continuous thermoplastic honeycomb sandwich panel process technology for cost optimal lightweight composites. *Reinforced Plastics*, 60(3):146–150, 2016. URL: http://www.sciencedirect.com/science/article/pii/S0034361716300029. (Cited on page 16).

[167] W. Shanks, Cyrille Francois Dunant, Michał P. Drewniok, Richard Charles Lupton, Andre Serrenho, and Julian M. Allwood. How much cement can we do without? lessons from cement material flows in the uk. *Resources, Conservation and Recycling*, 141:441–454, 2019. (Cited on page 104).

[168] Lian Shen, Xiang Zhang, Dick K.P. Yue, and Michael S. Triantafyllou. Turbulent flow over a flexible wall undergoing a streamwise travelling wave motion. *Journal of Fluid Mechanics*, 484:197–221, 2003. (Cited on pages 73, 82).

[169] ByungHyun Shin, Samuel M. Felton, Michael T. Tolley, and Robert J. Wood. Self-assembling sensors for printable machines. In *2014 IEEE International Conference on Robotics and Automation (ICRA)*, pages 4417–4422. IEEE, 2014. (Cited on page 17).

[170] Ole Sigmund. Materials with prescribed constitutive parameters: An inverse homogenization problem. *International Journal of Solids and Structures*, 31(17):2313–2329, 1994. URL: http://www.sciencedirect.com/science/article/pii/0020768394901546. (Cited on page 14).

[171] Yngve Solbakken. Space vector PWM introduction. URL: https://www.switchcraft.org/learning/2017/3/15/space-vector-pwm-intro. (Cited on page 93).

[172] Felipe Souto, Veronica Calado, and Nei Pereira Jr. Lignin-based carbon fiber: a current overview. *Materials Research Express*, 5(7), 2018. (Cited on page 72).

[173] Pratheev S. Sreetharan, John P. Whitney, Mark D. Strauss, and Robert J. Wood. Monolithic fabrication of millimeter-scale machines. *Journal of Micromechanics and Microengineering*, 22(5), 2012. (Cited on page 17).

[174] Tarah N. Sullivan, Bin Wang, Horacio D. Espinosa, and Marc A. Meyers. Extreme lightweight structures: avian feathers and bones. *Materials Today*, 20(7):377–391, 2017. URL: http://www.sciencedirect.com/science/article/pii/S136970211730072X. (Cited on page 15, 15).

[175] Xu Sun, Samuel M Felton, Robert J. Wood, and Sangbae Kim. Printing angle sensors for foldable robots. In *2015 IEEE/RSJ International Conference on Intelligent Robots and Systems (IROS)*, pages 1725–1731. IEEE, 2015. (Cited on page 17).

[176] Tomohiro TACHI. Simulation of rigid origami. *Origami^4: Proceedings of the 4th International Meeting of Origami Science, Math, and Education (OSME 2006)*, pages 175–187, 2009. (Cited on page 17).

[177] Tomohiro Tachi. Composite rigid-foldable curved origami structure. In *1st International Conference on Transformable Architecture*, 2013. (Cited on pages 46, 64).

[178] Tomohiro Tachi. Interactive form-finding of elastic origami. In *Proceedings of IASS Annual Symposia*, pages 1–4. International Association for Shell and Spatial Structures (IASS), 2013. (Cited on page 17).

[179] Tomohiro Tachi and Koryo Miura. Rigid-foldable cylinders and cells. *J. Int. Assoc. Shell Spat. Struct*, 53(4):217–226, 2012. URL: http://origami.c.u-tokyo.ac.jp/~tachi/cg/RigidFoldableCylindersCellsTachiMiuraJournalIASS2012.pdf. (Cited on pages 17, 33, 35).

[180] Sadatoshi Taneda. Visual study of unsteady separated flows around bodies. *Progress in Aerospace Sciences*, 17:287–348, 1976. URL: http://www.sciencedirect.com/science/article/pii/0376042176900117. (Cited on pages 73, 74).

[181] Sadatoshi Taneda and Yoshimasa Tomonari. An experiment on the flow around a waving plate. *Journal of the Physical Society of Japan*, 36(6):1683–1689, 1974. URL: https://doi.org/10.1143/JPSJ.36.1683. (Cited on pages 73, 74).

[182] Geoffrey I. Taylor. Analysis of the swimming of microscopic organisms. *Proceedings of the Royal Society of London A: Mathematical, Physical and Engineering Sciences*, 209(1099):447–461, 1951. URL: http://rspa.royalsocietypublishing.org/content/209/1099/447. (Cited on page 73).

[183] Geoffrey I. Taylor. Analysis of the swimming of long and narrow animals. *Proceedings of the Royal Society of London A: Mathematical, Physical and Engineering Sciences*, 214(1117):158–183, 1952. URL: http://rspa.royalsocietypublishing.org/content/214/1117/158. (Cited on page 73).

[184] Alexandra H. Techet, Franz S. Hover, and Michael S. Triantafyllou. Separation and turbulence control in biomimetic flows. *Flow, Turbulence and Combustion*, 71(1):105, Mar 2003. URL: https://doi.org/10.1023/B:APPL.0000014923.28324.87. (Cited on page 73).

[185] P. H. Thornton and C. L. Magee. The interplay of geometric and materials variables in energy absorption. *Journal of Engineering Materials and Technology*, 99(2):114–120, 04 1977. URL: http://dx.doi.org/10.1115/1.3443419. (Cited on page 57).

[186] Stephen P. Timoshenko and James M. Gere. *Theory of Elastic Stability*. Courier Corporation, 2009. (Cited on pages 48, 60).

[187] Sean S. Tolman, Isaac L. Delimont, Larry L. Howell, and David T. Fullwood. Material selection for elastic energy absorption in origami-inspired compliant corrugations. *Smart Materials and Structures*, 23(9), 2014. URL: http://stacks.iop.org/0964-1726/23/i=9/a=094010. (Cited on page 43).

[188] Sean S. Tolman, Spencer P. Magleby, and Larry L. Howell. Elastic energy absorption of origami-based corrugations. In *International Design Engineering Technical Conferences and Computers and Information in Engineering Conference*, 2017. URL: http://dx.doi.org/10.1115/DETC2017-67081. (Cited on page 58).

[189] M.S. Triantafyllou, F.S. Hover, A.H. Techet, and D.K. Yue. Review of hydrodynamic scaling laws in aquatic locomotion and fishlike swimming. *Applied Mechanics Reviews*, 58(4):226–237, 2005. (Cited on pages 73, 74).

[190] M.S. Triantafyllou, A.H. Techet, Q. Zhu, D.N. Beal, F.S. Hover, and D.K.P. Yue. Vorticity control in fish-like propulsion and maneuvering. *Integrative and comparative biology*, 42(5):1026–1031, 2002. (Cited on page 73).

[191] John R. Tumbleston, David Shirvanyants, Nikita Ermoshkin, Rima Janusziewicz, Ashley R. Johnson, David Kelly, Kai Chen, Robert Pinschmidt, Jason P. Rolland, Alexander Ermoshkin, Edward T. Samulski, and Joseph M. DeSimone. Continuous liquid interface production of 3D objects. *Science*, 2015. URL: http://science.sciencemag.org/content/early/2015/03/18/science.aaa2397. (Cited on page 15).

[192] R. Verdejo and N.J. Mills. Heel–shoe interactions and the durability of eva foam running-shoe midsoles. *Journal of Biomechanics*, 37(9):1379–1386, 2004. URL: http://www.sciencedirect.com/science/article/pii/S0021929003004858. (Cited on page 16).

[193] Haydn N.G Wadley. Multifunctional periodic cellular metals. *Philosophical Transactions of the Royal Society of London A: Mathematical, Physical and Engineering Sciences*, 364(1838):31–68, 2006. URL: http://rsta.royalsocietypublishing.org/content/364/1838/31. (Cited on pages 14, 16).

[194] Lijun Wang, Kazuya Saito, You Gotou, and Yoji Okabe. Design and fabrication of aluminum honeycomb structures based on origami technology. *Journal of Sandwich Structures and Materials*, 2017. URL: https://doi.org/10.1177/1099636217714646. (Cited on pages 23, 33).

[195] Xiaoyuan Wang, Huaidong Lu, and Xiang Li. Winding design and analysis for a disc-type permanent-magnet synchronous motor with a PCB stator. *Energies*, 11(12):3383, 2018. (Cited on page 85).

[196] C. David Warren. Low cost carbon fiber overview. Technical report, Oak Ridge National Laboratory, May 2011. URL: https://www.energy.gov/sites/prod/files/2014/03/f11/lm002_warren_2011_o.pdf. (Cited on page 72).

[197] Denis L. Weaire and Stefan Hutzler. *The Physics of Foams*. Oxford University Press, 2001. (Cited on page 14).

[198] James C. Weaver, Joanna Aizenberg, Georg E. Fantner, David Kisailus, Alexander Woesz, Peter Allen, Kirk Fields, Michael J. Porter, Frank W. Zok, Paul K. Hansma, Peter Fratzl, and Daniel E. Morse. Hierarchical assembly of the siliceous skeletal lattice of the hexactinellid sponge euplectella aspergillum. *Journal of Structural Biology*, 158(1):93 – 106, 2007. URL: http://www.sciencedirect.com/science/article/pii/S1047847706003352. (Cited on page 15).

[199] James C. Weaver, Garrett W. Milliron, Peter Allen, Ali Miserez, Aditya Rawal, Javier Garay, Philipp J. Thurner, Jong Seto, Boaz Mayzel, and Larry Jon Friesen. Unifying design strategies in demosponge and hexactinellid skeletal systems. *The Journal of Adhesion*, 86(1):72–95, 2010. (Cited on page 14).

[200] Ulrike G.K. Wegst. Bending efficiency through property gradients in bamboo, palm, and wood-based composites. *Journal of the Mechanical Behavior of Biomedical Materials*, 4(5):744–755, 2011. Special Issue on Natural Materials / Papers from the Third International Conference on the Mechanics of Biomaterials and Tissues. URL: http://www.sciencedirect.com/science/article/pii/S175161611100035X. (Cited on page 15).

[201] J.P. Whitney, P.S. Sreetharan, K.Y. Ma, and R.J. Wood. Pop-Up book mems. *Journal of Micromechanics and Microengineering*, 21(11), 2011. URL: http://stacks.iop.org/0960-1317/21/i=11/a=115021. (Cited on page 17).

[202] T. Wierzbicki and W. Abramowicz. On the crushing mechanics of thin-walled structures. *Journal of Applied Mechanics*, 50(4a):727–734, 12 1983. URL: http://dx.doi.org/10.1115/1.3167137. (Cited on page 68, 68, 68, 68, 68).

[203] Tomasz Wierzbicki. Crushing analysis of metal honeycombs. *International Journal of Impact Engineering*, 1(2):157–174, 1983. URL: http://www.sciencedirect.com/science/article/pii/0734743X83900040. (Cited on pages 58, 68).

[204] Tomasz Wierzbicki. MIT OCW 2.080J Structural Mechanics, Fall 2013, 2013. URL: https://ocw.mit.edu/courses/mechanical-engineering/2-080j-structural-mechanics-fall-2013/index.htm. (Cited on pages 110, 111, 111).

[205] P. H. Wirsching and R. C. Slater. The beer can as a shock absorber. *Journal of Engineering Materials and Technology*, 95(4):224–226, 10 1973. URL: http://dx.doi.org/10.1115/1.3443157. (Cited on page 57).

[206] Robert J. Wood, Srinath Avadhanula, Ranjana Sahai, Erik Steltz, and Ronald S. Fearing. Microrobot design using fiber reinforced composites. *Journal of Mechanical Design*, 130(5), 2008. (Cited on page 17).

[207] Chui-Jie Wu, Liang Wang, and Jie-Zhi Wu. Suppression of the von kármán vortex street behind a circular cylinder by a travelling wave generated by a flexible surface. *Journal of Fluid Mechanics*, 574:365–391, 2007. (Cited on page 73).

[208] T. Yao-Tsu Wu. Swimming of a waving plate. *Journal of Fluid Mechanics*, 10(3):321–344, 1961. (Cited on page 73).

[209] Feng Xu, Wen-Li Chen, Wei-Feng Bai, Yi-Qing Xiao, and Jin-Ping Ou. Flow control of the wake vortex street of a circular cylinder by using a traveling wave wall at low reynolds number. *Computers and Fluids*, 145:52–67, 2017. (Cited on page 73).

[210] Yan Yao, Chuan jing Lu, Ting Si, and Kun Zhu. Experimental investigation on the drag reduction characteristics of traveling wavy wall at high reynolds number in wind tunnel. *Journal of Hydrodynamics, Ser. B*, 22(5):719–724, 2010. (Cited on pages 73, 74).

[211] H. Yasuda, C. Chong, E. G. Charalampidis, P. G. Kevrekidis, and J. Yang. Formation of rarefaction waves in origami-based metamaterials. *Phys. Rev. E*, 93, Apr 2016. URL: https://link.aps.org/doi/10.1103/PhysRevE.93.043004. (Cited on page 33).

[212] H. Yasuda and Jinkyu Yang. Reentrant origami-based metamaterials with negative poisson's ratio and bistability. *Physical review letters*, 114(18):185502, 2015. URL: http://faculty.washington.edu/jkyang/research/publication/2015_PRL_origami.pdf. (Cited on pages 33, 37).

[213] Hiromi Yasuda, Thu Yein, Tomohiro Tachi, Koryo Miura, and Minoru Taya. Folding behaviour of Tachi–Miura polyhedron bellows. In *Proc. R. Soc. A*. The Royal Society, 2013. URL: http://rspa.royalsocietypublishing.org/content/469/2159/20130351.short. (Cited on pages 33, 39).

[214] Jun Zhang, Stephen Childress, Albert Libchaber, and Michael Shelley. Flexible filaments in a flowing soap film as a model for one-dimensional flags in a two-dimensional wind. *Nature*, 408, 12 2000. URL: http://dx.doi.org/10.1038/35048530. (Cited on page 73).

[215] H.Z. Zhou and Z.J. Wang. Application of foldcore sandwich structures in helicopter subfloor energy absorption structure. *IOP Conference Series: Materials Science and Engineering*, 248(1), 2017. URL: http://stacks.iop.org/1757-899X/248/i=1/a=012033. (Cited on page 58).